Karlsruher Institut für Technologie

ETP-KA/2025-09

Irradiation Testing of Silicon Sensors for Future CMS Upgrades

Umut Elicabuk

Zur Erlangung des akademischen Grades eines
DOKTORS DER NATURWISSENSCHAFTEN (Dr. rer. nat.)
von der KIT-Fakultät für Physik des
Karlsruher Instituts für Technologie (KIT)

angenommene

Dissertation

von

M.Sc. Umut Elicabuk
aus Pforzheim

Tag der mündlichen Prüfung: 25.07.2025

Referent: Prof. Dr. Thomas Müller Institut für Experimentelle Teilchenphysik
Korreferent: Prof. Dr. Ulrich Husemann Institut für Experimentelle Teilchenphysik

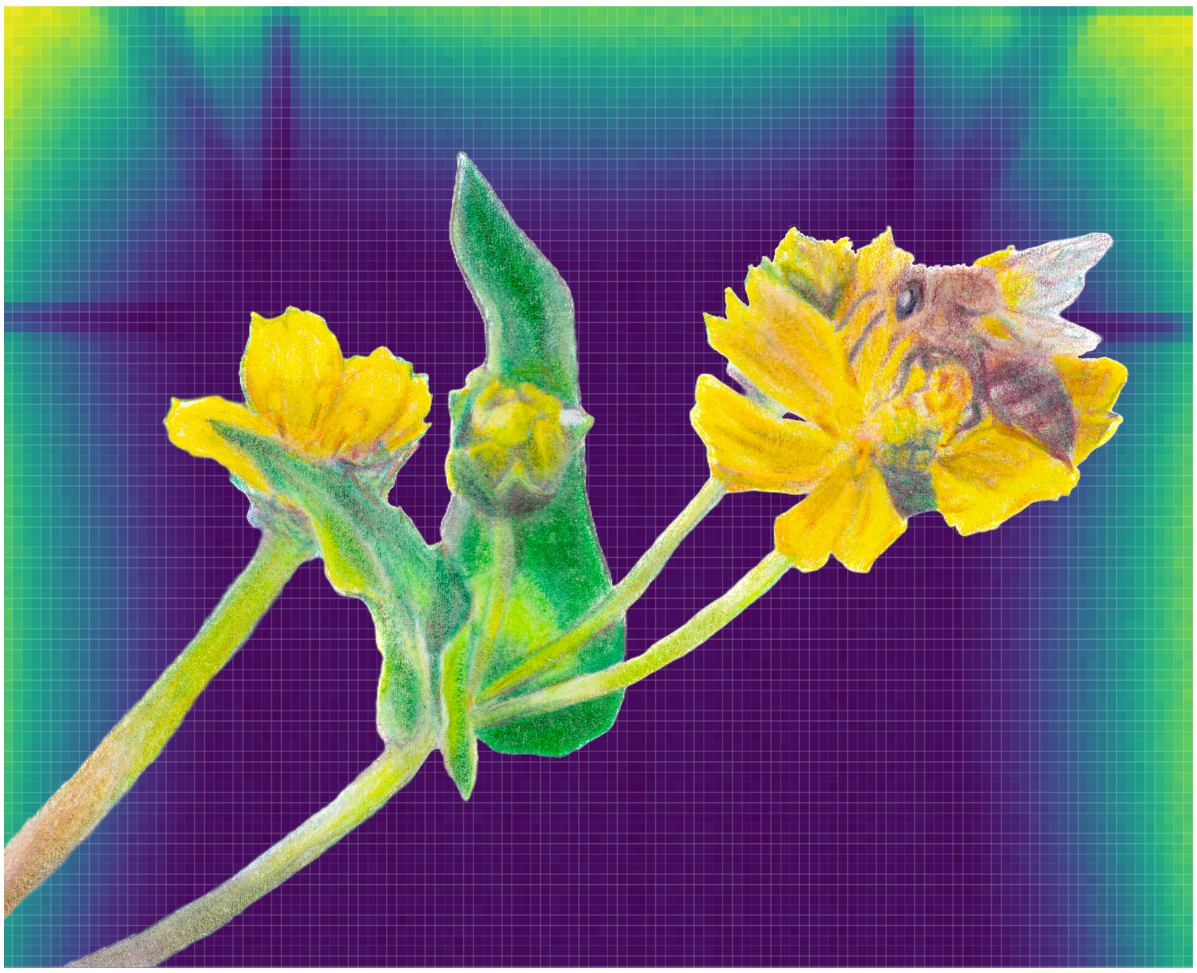

Cover painting by Franziska Petkau, 2025

Umut Elicabuk:
Irradiation Testing of Silicon Sensors for Future CMS Upgrades
June 2025

Contents

1 Introduction

What are we made of? The answer to this question surely depends on whom you ask. A psychologist could say we are made of thoughts and emotions, a biologist might answer that we are made of cells, a chemist would likely say that we are made of molecules. Carl Sagan, a well-known scientist and science communicator, answered the question more poetically: *"The cosmos is within us. We are made of star-stuff. We are a way for the universe to know itself."* Considering all of these answers suddenly makes the question more complex but also simple at the same time. All are correct in their own way, and all deserve to be seen as equally valid — a thought that is not only often forgotten in the scientific community in the face of specialization, but also in society as a whole in the face of the fascist and discriminatory ideologies that have plagued humanity for centuries. This thesis will contribute to answering the question in a very specific way, breaking the initial question down to the fundamental level: the elementary particles that make up atoms, which in turn make up the chemist's molecules, the biologist's cells, and finally the psychologist's thoughts and emotions.

The Standard Model of Particle Physics (SM) is the theory that describes these elementary particles and their interactions, distinguishing between two main classes of particles: fermions, which make up physical matter, and bosons, which mediate the interactions between them. As a quantum field theory, the SM describes particles as excitations of quantum fields that permeate all of space-time. The SM has been very successful in describing nature at the smallest scales, probing it with high precision using particle detectors and colliders like the Large Hadron Collider (LHC) at CERN in Geneva, Switzerland. Despite its success, it is far from being a complete theory of nature. Numerous open questions remain, such as the nature of dark matter, the origin of neutrino masses, and the matter-antimatter asymmetry in the universe. The thesis you are reading is a contribution to the detectors at the Compact Muon Solenoid (CMS) experiment at the LHC, which is used to search for new physics beyond the SM and to measure the properties of known particles, such as the Higgs boson discovered in 2012 [Cha+12; Aad+12].

To increase the physics potential at the LHC, the accelerator complex is being upgraded to the High-Luminosity LHC (HL-LHC) [Abe+20], which will increase the integrated luminosity by a factor of ten compared to the current LHC. In order to fully exploit the increased luminosity and cope with the numerous challenges that come with it, the CMS experiment is also being upgraded. The silicon tracker, at the heart of the detector, is one of its key components, which is used to precisely measure the trajectories of charged particles produced in collisions. It will have to be fully replaced and extended in the following years, which is where this thesis fits in.

The main foci of this thesis are testing the radiation hardness of the silicon sensors produced for the new CMS tracker in Part I, and studying the radiation effects on ultrafast silicon devices for future upgrades in Part II. To introduce the reader to the topics covered in this work first, Chapter 2 will give a brief overview of all basic concepts needed to understand the rest of the thesis. Chapter 3 will then introduce the topic of radiation damage, which is crucial to understand the radiation-induced effects on the silicon sensors. Chapter 4 will give a brief overview of the LHC and the CMS experiment, as well as the upgrades that are planned during

the HL-LHC era. All measurement and irradiation facilities and software used or developed as part of this thesis are described in Chapter 5.

2
Basics of Silicon Sensors

The year is 2025. Data centers as big as villages are processing the data of the world. With the rise of technology in the last decades, the amount of data that is generated is increasing exponentially and one element is at the center of it all: silicon. Although silicon used to be a material that was never thought to cease, the demand for it is increasing and the resources are limited. Today, silicon is used in an unimaginable amount of applications, ranging from electronics, over photonics to particle physics. Manufacturers of silicon devices are nowadays very experienced in producing silicon devices with high precision and quality. High-energy physics (HEP) can benefit from this experience and use silicon sensors in their experiments in new and inventive ways. As a semiconductor, silicon has a lot of properties that qualify it for use in HEP experiments. The following sections will give an overview of the basics of solid state semiconductor physics and modern silicon sensors. Unless stated otherwise, the formulae used throughout this chapter will use natural units $\hbar = c = \mathrm{k_B} = 1$.

2.1. The Band Model

In solid state physics, the band model is used to describe the electronic properties of a material. To introduce this concept, let us consider electrons inside of an atomic lattice; a periodic potential $V(\vec{r}) = V\left(\vec{r} + \vec{R}\right)$, where $\vec{R}$ denotes a translation vector of the lattice that takes us from one lattice site to another. Then, solutions to the stationary Schrödinger equation can be written as *Bloch waves*

$$\psi_{\vec{k}}(\vec{r}) = e^{i\vec{k}\cdot\vec{r}} u_{\vec{k}}(\vec{r}),$$

according to the Bloch theorem [Blo29], where $\psi_{\vec{k}}$ is the wave function, $\vec{k}$ is the wave vector and $u_{\vec{k}}$ is a periodic function with the same periodicity as the lattice: $u_{\vec{k}}\left(\vec{r} + \vec{R}\right) = u_{\vec{k}}(\vec{r})$. Such a wave function is only unique up to a reciprocal lattice vector $\vec{G}$, i.e. $\psi_{\vec{k}}(\vec{r}) = \psi_{\vec{k}+\vec{G}}(\vec{r})$. Hence, it is common to restrict the wave vector to the *first Brillouin zone*, which is a primitive cell of the same lattice in reciprocal space. In this periodic lattice, the wave vector $\vec{k}$ is quantized and the dispersion relation of an electron feeling the lattice potential is given by

$$E_{\vec{k}} = \frac{1}{2m_{\mathrm{e}}^*}\left|\vec{k} + \vec{G}\right|^2,$$

where m_{e}^* is the effective mass of the electron. Electrons that scatter off the lattice potential must satisfy the *Bragg condition*

$$\left(\vec{k} + \vec{G}\right)^2 = k^2,$$

according to the previous dispersion relation. At the edges of the first Brillouin zone, this Bragg condition is satisfied, yielding two solutions for the electronic probability density function. These solutions accumulate electrons either directly on the lattice sites or between them, resulting in two different energy levels. Therefore, the parabolic, free electron dispersion relation is either lowered, or raised at the edges of the first Brillouin zone, which leads to a zone with

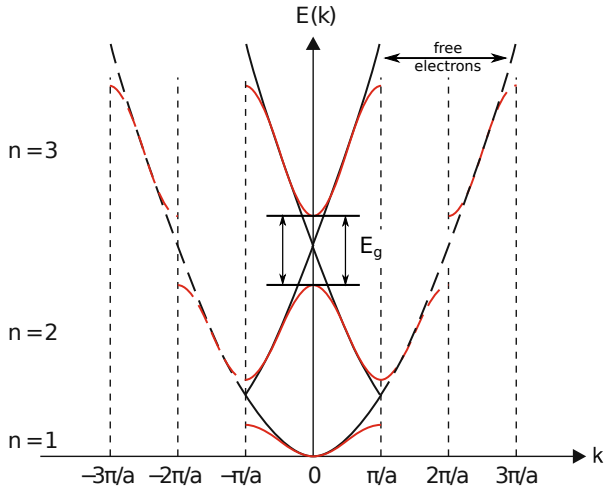

Figure 2.1.: The band structure evolves by lowering or raising the energy at the edges of the first Brillouin zone. This leads to the formation of a *band gap*. Graphic adapted from [Dem00].

forbidden states, the *band gap*. The evolution of the band structure as described is illustrated in Fig. 2.1. For a crystal lattice with many lattice sites, as is the case for a macroscopic solid, this discrete energy spectrum transitions into continuous *(energy) bands*. The band above the band gap is called the *conduction band*, while the band below is called the *valence band*. The energy difference between the valence and conduction bands is called the *band gap energy* E_G. In reality, the derivation of the band structure of a real crystal is far more involved, leading to band structures that are more complex than described here. However, the underlying principle remains the same. Following the Pauli exclusion principle, the energy states in the band structure are filled with electrons. As fermions, electrons occupying a state λ with an energy ϵ_λ must follow *Fermi-Dirac statistics* with the occupation probability

$$\overline{n_\lambda} = \left(e^{\frac{\epsilon_\lambda - E_\mathrm{F}}{T}} - 1 \right)^{-1}$$

at a temperature T. At absolute zero, electrons occupy states starting from the ground state up until the *Fermi energy* E_F, where all electrons occupy a state. At a non-zero temperature, electrons may also occupy higher energy states in the conduction band, which leaves vacancies in the valence band that are called *holes*. Although holes, in principle, are nothing more than a mathematical formalism and as such, are classified as quasi-particles, they are a very useful concept to consider within the framework of this model. As for electrons, an effective mass m_h^* can be introduced for holes. Considering the density of electrons that have been excited into the conduction band n and the hole concentration in the valence band h, the number of free charge carriers for a temperature T is

$$n_\mathrm{i} = \sqrt{nh} = 2 \left(\frac{T}{2\pi} \right)^{3/2} (m_\mathrm{e}^* m_\mathrm{h}^*)^{3/4} \, \mathrm{e}^{-E_\mathrm{G}/(2T)}. \tag{2.1}$$

At $T = 26\,\mathrm{meV}$ and a band gap energy of around 1 eV, silicon has $6 \times 10^{16}\,\mathrm{m}^{-3}$ intrinsic charge carriers, according to Eq. (2.1). This is significantly fewer charge carriers than a good electrical conductor, which has around $10^{28}\,\mathrm{m}^{-3}$ [Dem00].

But why is it that intrinsic silicon does not conduct electrical current as well as a *good* conductor? The band model enables us to classify the electrical properties of different materials, as seen in Fig. 2.2. Following this framework, E_G and E_F are the only properties that are

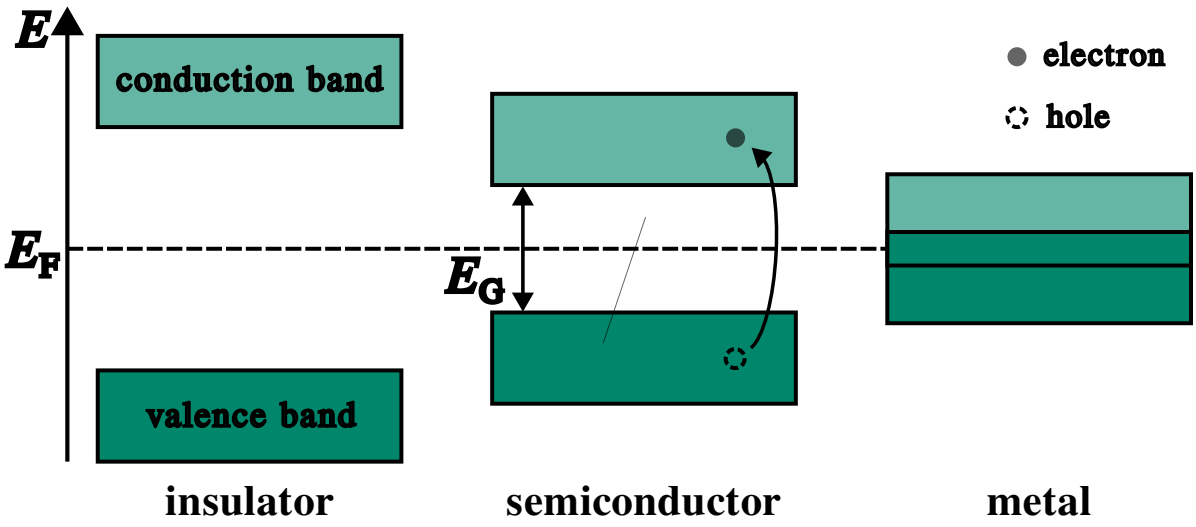

Figure 2.2.: The band model makes it possible to classify materials in terms of their electrical properties. Depending on their E_G, insulators, semiconductors and metals are distinguished.

needed to determine if a material can be classified as either an insulator, semiconductor or metal. For insulators, the band gap energy is too high to excite electrons from their fully occupied valence band into the conduction band at room temperature (RT). Since their valence bands are fully occupied and their conduction band are completely empty, there are no free charge carriers that could contribute to electrical conduction. Semiconductors have a band gap energy that is just low enough to excite charge carriers into the conduction band and a Fermi energy close to the middle of the band gap. At RT, some states are ionized and these charge carriers are free to take part in electrical conduction. Semiconductors such as silicon have band gap energies that typically lie between 1 eV and 4 eV [Dem00]. Metals are characterized by a valence band that is completely filled and a conduction band that is only partly filled. Therefore, their Fermi energy is located in the conduction band, where many states may be occupied infinitesimally higher or lower in energy. This results in the electrons being able to move freely and contribute to electrical conduction. It has to be noted that for a real, 3D crystal lattice, these idealized band structures do not hold up very well, since the period length as well as the modulation amplitude of periodic potential has a directional dependence [Dem00]. In fact, the minimum of the conduction band may not be at the same k-value as the maximum of the valence band. Such materials are called *indirect*, and silicon is such an *indirect semiconductor*. In order to excite an electron into the conduction band across its band gap energy of 1.12 eV at RT, the electron must transfer a momentum k to the lattice. The average electron-hole pair creation energy of silicon E_{eh} is 3.6 eV [Fan+19].

2.2. Doping of Silicon

Semiconductor manufacturers strive to produce crystals of impeccable purity, so much so that the industry standard for silicon crystals is 99.999 999 999% (commonly referred to as *eleven nines*), since impurities change the electrical behavior of the production material. However, if inserted in a controlled way, impurities inside of a crystal lattice are able to modify the electrical properties in a desirable way. This process is called *doping* a semiconductor. Figure 2.3a shows the lattice of an n-doped silicon crystal. In this example, the silicon lattice is doped with pentavalent phosphorus atoms, which have one electron more in their outer shell than

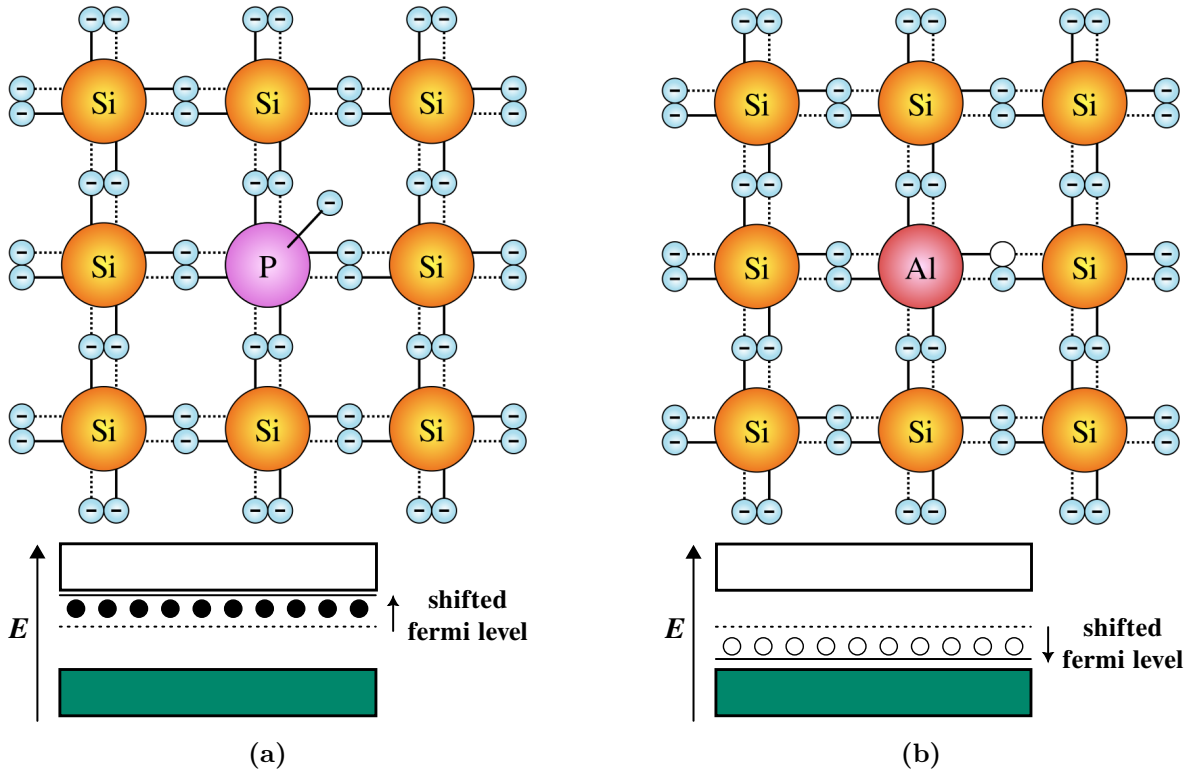

Figure 2.3.: 2D projection of an (a) n-doped or (b) p-doped silicon lattice and the shift in Fermi level caused by introduction of additional energy levels. Graphic adapted from [Hen06b; Hen06a].

silicon. This excess electron is only weakly bound to its impurity atom and may be converted into a freely moving charge carrier by a small amount of energy. As such, these pentavalent impurity atoms are called *donors* with a donor concentration n_D. The energy levels of dopant donors are located right below the conduction band. However, as opposed to the freely moving electron gas from the previous section, these states may only be occupied by a single electron. Analogous to n-doping, p-doping as shown in Fig. 2.3b uses trivalent impurity atoms inside of a silicon lattice. In this example, the lattice is doped with trivalent aluminum atoms, which have one electron less in their outer shell. This creates a lack of one electron (an additional hole) in the covalent binding scheme. The result is a positively charged lattice site that may be filled in by electrons of neighboring atoms, which is why these impurities are called *acceptors* with an acceptor concentration n_A. Dopant acceptor levels are located right above the valence band and may only be occupied by one hole at a time. Although there are excess electrons in n-type and excess holes in p-type material in terms of the covalent lattice bindings, in both cases the crystal is neutral since for every charged donor or acceptor ion there is a free electron or hole, respectively. If $n > n_\mathrm{i} > h$ electrons are called the *majority charge carriers* of this now *n-conductive* material. In this case, holes are the *minority charge carriers* in the material, vice versa for $h > n_\mathrm{i} > n$, where holes would be the majority charge carriers.

Due to the additional states introduced by the dopant atoms, the Fermi level shifts towards the conduction band for n-type silicon, and down, towards the valence band, for p-type silicon. How large the shift in Fermi level is entirely depends on n_D and n_A at a fixed temperature. In any case, doping a semiconductor increases its conductivity σ and decreases its resistivity

$$\rho = \frac{1}{\sigma} = \frac{1}{e\left(\mu_\mathrm{e} n + \mu_\mathrm{h} h\right)}, \tag{2.2}$$

where $\mu_\mathrm{e/h}$ denotes electron and hole mobilities, respectively [Dem00].

2.3. The pn-junction

The simplest device that can be created using a combination of p- and n-type silicon is the pn-junction, which is also called a *diode*. It is made by connecting n-doped and p-doped silicon on a single crystal, as shown in Fig. 2.4. Due to thermal diffusion at the interface, majority charge carriers from either material migrate to the other side of the interface. Electrons from the n-type material may either recombine with the holes on the p-side or be captured by the acceptors, while holes from the p-type silicon may recombine with electrons from the n-side. The migration of these charge carriers creates a net current called the *diffusion current*. Since the now positively charged donors and negatively charged acceptors on either side of the junction are part of the crystal and cannot move, the migration region is electrically charged since the p-side now contains more electrons than protons and vice versa for the n-side. A *space charge region* (SCR) develops due to the negative space charge density (SCD) on the p-side and positive SCD on the n-side. The SCR is also called a *depletion layer* since it is now depleted of free charge carriers. Due to the charge density gradient across the interface, an electric field opposing any further charge migration develops. Since the Fermi energy for p-type silicon is located just above the valence band due to the acceptor levels and below the conduction band for n-type silicon due to the donor levels, the bands need to bend to achieve a constant Fermi level across the device; a voltage potential is created due to this bend.

This voltage potential at thermal equilibrium can be measured as the *builtin voltage* V_bi and is given by

$$eV_\mathrm{bi} = T \log\left(\frac{n_\mathrm{D} n_\mathrm{A}}{n_i^2}\right),$$

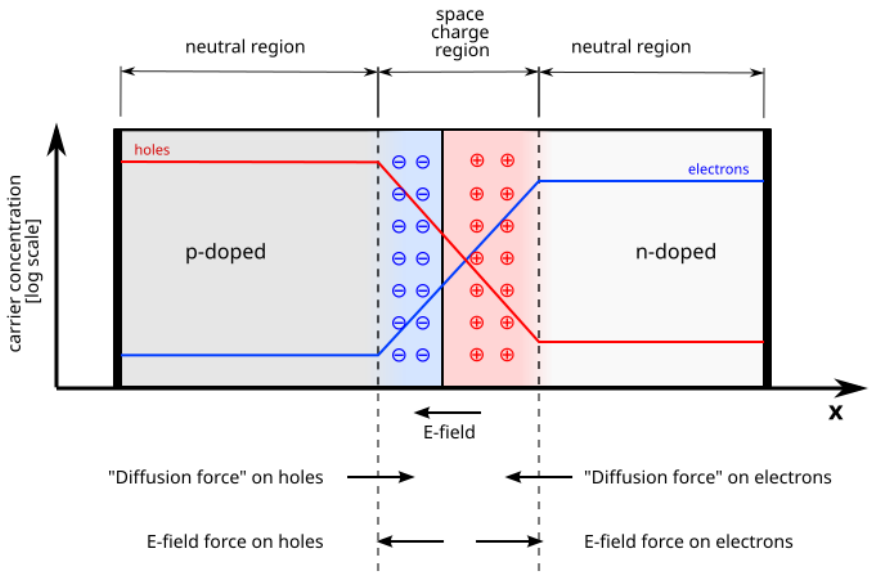

Figure 2.4.: A pn-junction in equilibrium with no external bias voltage applied. A space charge region develops at the interface with a builtin voltage potential V_{bi} preventing further carrier migration [The07].

which translates to approximately 0.7 V for the p-type devices investigated in this work, where $n_{\mathrm{D}} \approx 10^{19}\,\mathrm{cm}^{-3}$ and $n_{\mathrm{A}} \approx 5 \times 10^{12}\,\mathrm{cm}^{-3}$ [Mül21] with $n_{\mathrm{i}}(T = 26\,\mathrm{meV}) \approx 9.65 \times 10^{9}\,\mathrm{cm}^{-3}$ [Alt+03].

2.3.1. Applying an External Voltage

An external voltage V applied across the diode may now influence this opposing field. The width of the depletion layer w is either increased if the n-doped part of the diode is biased with a positive voltage or decreased vice versa. In case of an enlargement of the depletion layer the diode is operated in *reverse bias*, which is the default operation mode for silicon detectors. Then, w is determined solely by the doping concentrations n_{A} and n_{D} and is given by

$$w = \sqrt{\frac{2\epsilon_{\mathrm{Si}}}{e}\frac{n_{\mathrm{A}} + n_{\mathrm{D}}}{n_{\mathrm{A}} n_{\mathrm{D}}}\,(V_{\mathrm{bi}} + V)}, \tag{2.3}$$

where ϵ_{Si} denotes the dielectric constant of silicon. If one of the doping concentrations is much larger than the other, the depletion width can be simplified by introducing the *effective doping concentration* $N_{\mathrm{eff}} = \min(n_{\mathrm{A}}, n_{\mathrm{D}})$. For the p-type structures investigated in this work, $n_{\mathrm{D}} \gg n_{\mathrm{A}} = N_{\mathrm{eff}}$, which simplifies Eq. (2.3) to

$$w \approx \sqrt{\frac{2\epsilon_{\mathrm{Si}}}{e\,|N_{\mathrm{eff}}|}\,(V_{\mathrm{bi}} + V)}. \tag{2.4}$$

The external voltage V can be chosen such that the depletion layer encompasses the entire active thickness of the device d. This voltage is called the *full depletion voltage* V_{dep}. Since the SCR is devoid of any charge carriers, the region acts like a dielectric and has a capacitance C. Using the relation for the space charge $Q = eN_{\mathrm{eff}}Aw$ with the cross sectional area of the depletion layer A, the capacitance is given by

$$C = \frac{\mathrm{d}Q}{\mathrm{d}w}\frac{\mathrm{d}w}{\mathrm{d}V} = A\sqrt{e\frac{\epsilon_{\mathrm{Si}}\,|N_{\mathrm{eff}}|}{2\,(V_{\mathrm{bi}} + V)}}, \tag{2.5}$$

according to Eq. (2.4) [Mol99]. In full depletion, the depletion layer cannot grow any further as it is limited by the physical size of the device. At this point, the capacitance saturates at

$$C = \epsilon_{\mathrm{Si}} \frac{A}{d}. \tag{2.6}$$

In reality, the capacitance does not stay exactly constant for voltages above V_{dep}, because of the lateral growth of the depletion layer with increasing voltage. Once V_{dep} is reached, it holds

$$V_{\mathrm{dep}} = \frac{e}{2\epsilon_{\mathrm{Si}}} |N_{\mathrm{eff}}| \, d^2. \tag{2.7}$$

2.3.2. Bulk Current

In this work so far, properties of idealized silicon crystals have helped to understand the basic principles of silicon devices better. However, real silicon crystals are not made up of perfect lattice structures as shown before, but contain impurities and imperfections due to contamination or specific processing steps during manufacturing of the device. This results in additional impurity energy levels that are created within the band gap, making it easier for electrons to be excited into the conduction band. Therefore, the space charge region is never completely devoid of free charge carriers and an additional *generation current* I_{G} contributes to the total current density through the pn-junction, apart from the diffusion current I_{D} during the formation of the depletion layer mentioned earlier

$$I_{\mathrm{R}} = I_{\mathrm{D}} + I_{\mathrm{G}},$$

where I_{R} is called the *reverse current*. Not all energy levels contribute to I_{G} the same way, since their location relative to the Fermi level is different. Naturally, the rate of excitation into the conduction band strongly depends on the temperature T and the external bias voltage V, since only defects within the depletion zone contribute to the current generation mechanism. Thus, the total current flow through the pn-junction [Dem00] can be expressed like

$$I_{\mathrm{bulk}} = I_{\mathrm{R}} \left(\mathrm{e}^{eV/T} - 1 \right). \tag{2.8}$$

Operating the diode in reverse bias $V < 0$, immediately renders the exponential term in Eq. (2.8) negligibly small since at room temperature $T \approx 26\,\mathrm{meV}$, which only leaves the I_{R} term, that is controlled by the depletion width w. In summary, Eq. (2.4) and Eq. (2.8) show that the bulk current I_{bulk} is dependent on the bias voltage V like

$$I_{\mathrm{bulk}} \propto -\sqrt{|V|}. \tag{2.9}$$

However, if the bias voltage is set too high, the diode enters a regime that is called *breakdown*, where the current flowing through the device can rapidly exceed values that will permanently damage the device. Additionally, the bulk current of a silicon sensor in reverse bias is strongly dependent on the temperature T like

$$I_{\mathrm{bulk}}(T) \propto T^2 \exp\left(-\frac{E_{\mathrm{ef}}}{2T} \right), \tag{2.10}$$

with the effective band gap energy $E_{\mathrm{ef}} = 1.21\,\mathrm{eV}$ [Chi11]. Therefore, operating sensors at low temperatures is a common practice in HEP experiments to reduce the leakage current mainly after irradiation, where the generation current is higher than in unirradiated sensors (this will be discussed in the next chapter).

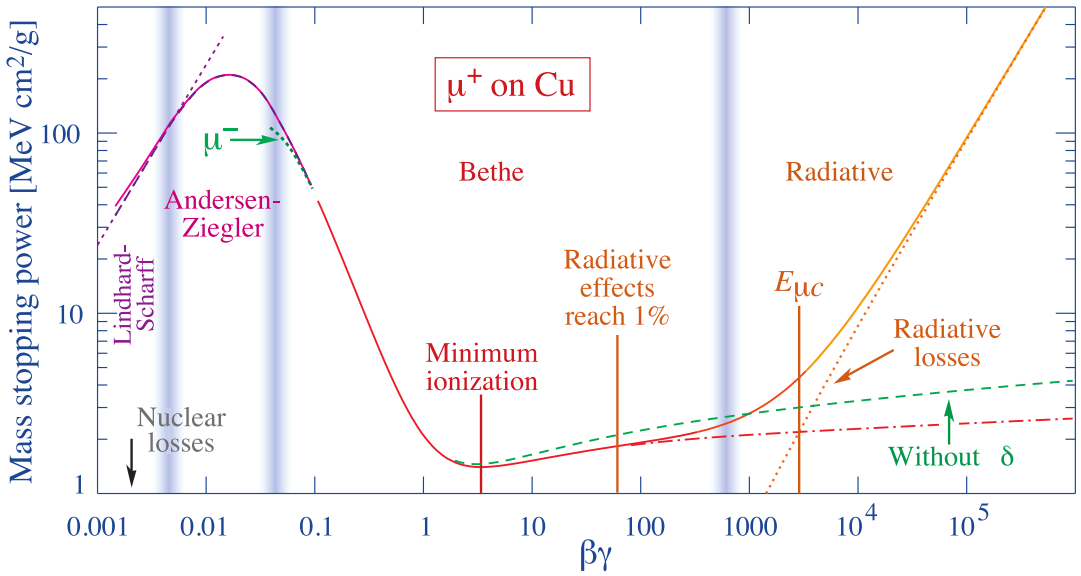

Figure 2.5.: Average energy loss of a muon projectile in a copper target. A particle with a $\beta\gamma \approx 3$ is considered a minimally ionizing particle (MIP). The regime in which the Bethe equation is valid is indicated by vertical blue bars [GK23].

2.4. Particle Interaction with Matter

Particles that traverse matter may interact with the electrons of the target atoms either by ionization or excitation, leading to an energy loss of the projectile. The following sections will go into more detail about this energy loss.

2.4.1. Energy Loss of Charged Particles

The average rate of energy loss of moderately relativistic, charged and heavy particles due to ionization is given by the *Bethe equation* [Bet30]

$$\left\langle -\frac{\mathrm{d}E}{\mathrm{d}x} \right\rangle = 4\pi N_\mathrm{A} r_\mathrm{e}^2 m_\mathrm{e} z^2 \frac{Z}{A}\frac{1}{\beta^2}\left(\frac{1}{2}\log\frac{2m_\mathrm{e}\beta^2\gamma^2 W_\mathrm{max}}{I^2} - \beta^2 - \frac{\delta\left(\beta\gamma\right)}{2}\right) \tag{2.11}$$

with all quantities described in Table A.1 [GK23]. Equation (2.11) quantifies the energy loss by ionization which results in the generation of electron-hole pairs in a semiconductor. Figure 2.5 shows the average energy loss of muons shot at a copper target. As indicated, the Bethe equation only applies within a region of around $0.1 < \beta\gamma < 1000$. Since Bethe's original theory [Bet30], various different modifications have been applied to extend the $\beta\gamma$-regime for which the equation is valid. Such modifications include the extension of the cross section to W_max using the Rutherford differential cross section σ_R, as well as using scattering theory in the Born approximation to modify σ_R. The latter modification involves introducing an effective ionization energy I that represents a weighted average of all possible energy transfers from the projectile to the electrons of the target atom [GK23]. Finding this excitation energy is a highly non-trivial task. At high energies, a correction function $\delta\left(\beta\gamma\right)$ to the density effect described by Fermi [Fer40] has to be applied, which takes into consideration a screening from interactions by polarization of the medium. At very high $\beta\gamma$, radiative effects become the dominant contribution in the energy loss mechanism, invalidating the Bethe equation in that regime. The Bethe equation does not apply to electrons because the incident electrons are indistinguishable from the target electrons and their masses are the same. Due to their small

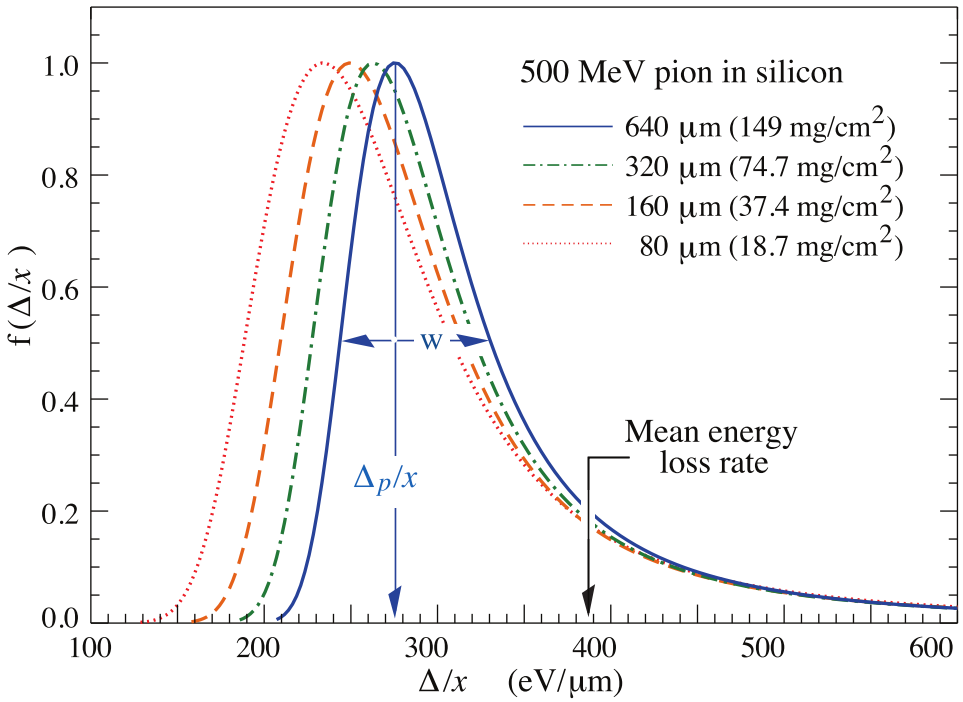

Figure 2.6.: Staggling functions of 500 MeV pions traversing silicon, normalized to unity at the most probable value Δ_p/x [GK23].

mass, Bremsstrahlung also becomes a dominant effect already at 10 MeV and the energy loss is $\propto E/m_e^2$.

Since the energy transfer from the projectile to the medium is a statistical effect, fluctuations around the mean energy loss can be observed. The number of collisions while a medium with finite thickness is traversed as well as the energy transfer per collision are subject to fluctuations. Fluctuations in energy transfer per collision are described by the *Landau-Vavilov-Bichsel straggling distribution* [Lan44; Bic88]. The straggling function for 500 MeV pions traversing a silicon target is shown in Fig. 2.6. Landau and Vavilov originally did not consider Fermi's density correction mentioned earlier, but it was added by Bichsel later on [Bic88]. Due to the large tail for high Δ/x, moments of the distribution are undefined. Therefore, the mean energy loss rate described by the Bethe equation that was discussed earlier, does not overlap with the most probable value (MPV) Δ_p/x of the straggling function. The cause of this large tail are rare incidents of high-energy transfers to electrons of the target atoms. These electrons have enough energy to travel a significant distance away from the interaction site and produce further ionization, which is why they are called *delta electrons*. With increasing target thickness, however, the straggling function approaches — but never reaches — a Gaussian distribution, due to convolution. Therefore, the mean energy loss rate by Bethe is ill-defined in an experimental sense for thin absorbers, where the MPVs are more interesting [GK23].

With an MPV of 271 eV µm^{-1} for the energy loss in silicon shown in Fig. 2.6, the number of created electron-hole pairs created in a $d = 290$ µm-thick silicon sensor is

$$N_{\mathrm{MPV}} = \left[\frac{\mathrm{d}E}{\mathrm{d}x}\right]_{\mathrm{MPV}} \frac{d}{E_{eh}} = 2.2 \times 10^4 \tag{2.12}$$

assuming a particle trajectory that is perpendicular to the sensor plane.

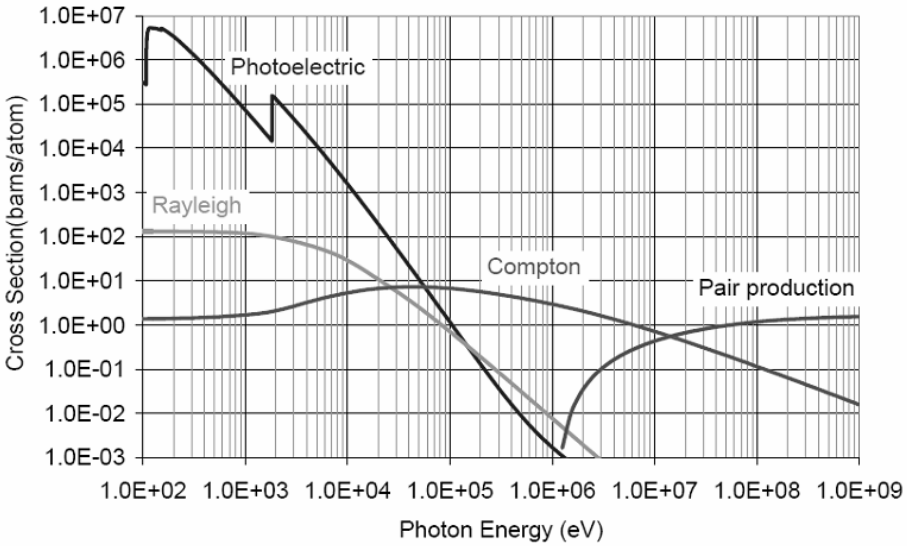

Figure 2.7.: Photonic cross sections as a function of photon energy. The photoelectric, Compton and pair production cross sections are dominant in different energy ranges [BB05].

2.4.2. Photonic Interactions

In the following, atomic interactions of photons with matter will be discussed, since parts of this work will deal with signal generation in silicon sensors using a laser source. Although the structures investigated in this work are not primarily used to detect photons, light stimulation is very useful in testing these devices.

There are four different processes that contribute to photonic interactions with matter that are dominant in different energy ranges, shown in Fig. 2.7.

- *Rayleigh scattering* [Str71] occurs when a photon scatters from target electrons without causing ionization or excitation. The photon merely grazes the atom and thus, does not impart any significant energy. Due to the negligible energy deposition, this interaction does not play an important role in detector applications.

- *The (internal) photoelectric effect* [Ein05] is the dominant effect in the low-energy regime. The photon is absorbed by the atom and, in semiconductors, an electron-hole pair is generated. Naturally, the photon must possess an energy that is greater than the band gap energy of the material for this to happen. For instance, a photon with a wavelength of $\lambda = 1055\,\mathrm{nm} \Rightarrow E_\gamma = 1.175\,\mathrm{eV}$ from a near-infrared (NIR) laser source has just enough energy to generate an electron-hole pair in silicon.

- *Compton scattering* [Com23] is an incoherent type of interaction in which the photon scatters off of an electron, transferring part of its energy to it. The photon is deflected into a different direction. In silicon, this interaction is dominant for photon energies between 100 keV and 10 MeV.

- *Pair production* dominates the total cross section for energies higher than 10 MeV and involves the conversion of the photon into a charged particle and its antiparticle. This is only possible if the photon has at least an energy equivalent to the mass of the created particle-pair, since the photon's energy is converted into particle mass and their momenta. The conservation of energy and momentum can only be satisfied in the presence of a target

atom[1], which is why pair production is only possible inside a medium. Pair production is mostly relevant for electromagnetic calorimeters, where cascades of pair production and Bremsstrahlung cause electromagnetic showers, although trackers can benefit from a low material budget to suppress pair production. Pair production is unwanted in trackers.

The interaction between target silicon atoms and photons from a NIR laser is therefore dominated by the photoelectric effect.

2.4.3. Light Absorption in Silicon

When a light beam is directed at a medium, the initial intensity I_0 of a light source as a function of penetration depth d decays exponentially

$$I(d) = I_0 \exp(-\alpha d), \tag{2.13}$$

with α denoting the *linear attenuation coefficient*. For NIR laser light with a wavelength of $\lambda = 1055\,\text{nm}$ and an energy of $E_\gamma = 1.175\,\text{eV}$ shot into silicon at 300 K, the coefficient is $\alpha_{\text{Si}} = 1.11 \times 10^{-3}\,\mu\text{m}^{-1}$ [Gre08]. Since silicon is an indirect semiconductor, as established in Section 2.1, an additional phonon interaction is necessary to jump the band gap at $E_\text{g} = 1.12\,\text{eV}$ and conserve momentum at the same time. Direct transitions would also be possible but require a higher photon energy, which is not possible with the use of NIR laser light. The need of phonons in NIR photon absorption, therefore, introduces a temperature dependence to the photon absorption probability.

2.5. Signal Generation

After having established the basic principles and interactions of semiconductors with special attention to silicon, we are now ready to look into the use of it as detector material for charged particles. The simplest detector or *sensor* that can be built with silicon is a diode. In order to deplete the sensor from free charge carriers and open up the possibility to detect a signal generated by a charged particle, the diode needs to be operated in reverse bias, as explained in Section 2.3.1. Exploiting the properties of the SCR to suppress thermally excited charge carriers rather than, for example, cooling the diode sufficiently is far easier and technically feasible. In reality, a sensor is not made from a simple diode but rather a p-doped *bulk* with many highly n-doped implants that are called *electrodes*.

When a charged particle traverses a silicon sensor, it generates electron-hole pairs along its path due to impact ionization, as explained in Section 2.4.1. Due to the bias voltage applied to the sensor, these electron-hole pairs separate and, for a p-type sensor, the electrons drift towards the electrodes. During their drift, they induce a current in the readout electronics of these electrodes, which can be calculated with the *Shockley-Ramo theorem* [Sho38; Ram39]. According to this theorem, the induced current $i_n(t)$ for a charge q drifting with velocity $\vec{v}$ is given by

$$i_n(t) = -q\vec{v} \cdot \vec{E_\text{w}}, \tag{2.14}$$

with $\vec{E_\text{w}}$ denoting the *weighting field*. This weighting field is an auxiliary quantity that exclusively depends on the geometry of the sensor. It is derived by solving the Poisson equation for the sensor configuration under question with boundary conditions of the electrode n set to 1 V while setting 0 V to all other electrodes. Figure 2.8 shows the electric potential and weighting field distributions for a p-type sensor. Solving the Poisson equation for this simple

[1]The 4-momentum of the created particle-pair is 0 in the center of mass frame. A single photon can never satisfy this requirement, which is why a second object is needed for the interaction.

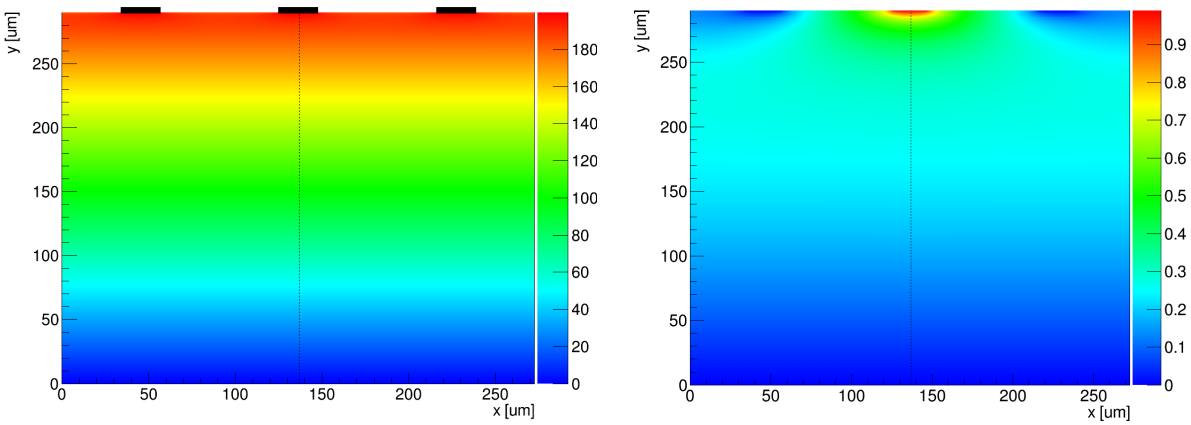

(a) Electric potential

(b) Weighting field E_{w}

Figure 2.8.: Drift potential and weighting field distributions for a 290 µm-thick, overdepleted, p-type silicon sensor with 3 n-strips spaced 90 µm apart at the top. The weighting field is calculated for the middle strip. Graphics were created using Weightfield7.1 [Cen+15].

configuration, assuming that the sensor can be approximated with a simple parallel-plate capacitor configuration, the weighting field $\left|\vec{E}_{\mathrm{w}}\right|$ is approximately constant $\approx \frac{1}{d}$. Electrons drifting towards the electrodes and holes drifting in the opposite direction thus contribute to the total electrode current i_n with the same sign, since they have opposite charge. The process of measuring the signal induced by a traversing particle is called *charge collection* with the total charge

$$Q_{\mathrm{tot}} = \int \mathrm{d}t \; i_n(t).$$

The term *charge collection* may make it seem as if the signal would only be collected upon arrival of these charge carriers. Instead, Eq. (2.14) shows that the signal is highest once all charge carriers have reached their terminal velocities inside of the silicon, during the drift towards the electrodes. Once they reach the electrodes, their velocity reaches 0, as does the induced current.

2.6. Sensors with Internal Gain

Although the signal induced in a silicon sensor does not need to be amplified in the device itself but in the readout electronics, it is still possible to increase the signal-to-noise ratio by introducing an internal gain mechanism.

2.6.1. Charge Multiplication

Internal gain is commonly achieved by introducing a *charge multiplication* mechanism. Analogous to the avalanche process in gas detectors, the charge carriers in silicon can be multiplied by traversing a region with a high electric field. When electrons traverse such a region, they produce secondary ionization, generating additional electron-hole pairs. A corrected version of Chynoweth's law [Chy58] for silicon, which describes the multiplication of charge carriers in a high electric field by an ionization rate α, is given by

$$\alpha_s(E) = \frac{a_s}{z(x)} \exp\left(-\frac{b_s}{E(x)}\right),$$

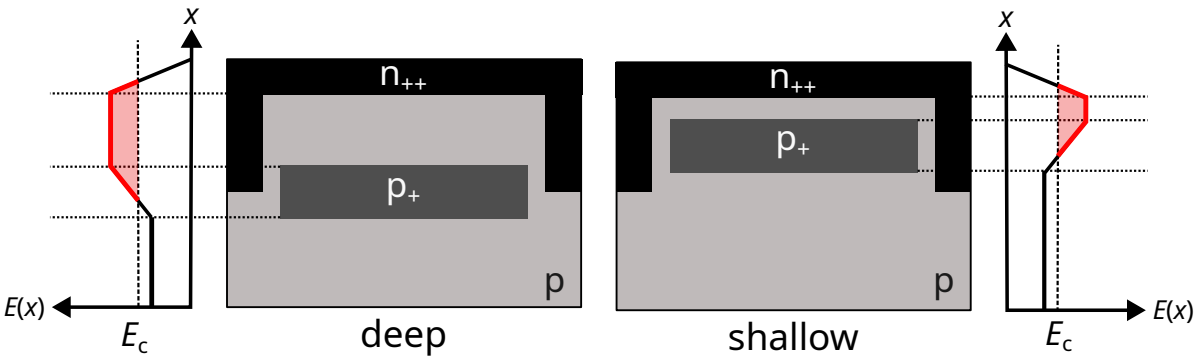

Figure 2.9.: Sketch of the impact of the depth of the gain layer on the width of the multiplication region. A shallow implant leads to a narrow multiplication region, while a deep implant leads to a wider multiplication region. The *multiplication region* is shown in red. The depicted doping concentrations and fields are not to scale and only serve as a demonstration of the concept. Details in main text.

with

$$z(x) = 1 + \sum_s \left(\frac{b_s}{E(x)} \exp\left(-\frac{b_s}{E(x)} \right) \right)$$

and

$$a_s = \frac{1}{L_s},\ b_s = \frac{U_{\mathrm{c},s}}{qL_s}, \text{where } s = \mathrm{e/h}.$$

The parameters entering this model are the threshold energies of electrons $(L_\mathrm{e}, U_{\mathrm{c},e})$ and holes $(L_\mathrm{h}, U_{\mathrm{c},h})$, respectively. This leads to ionization rates α_s as a function of the electric field $E(x)$. The model assumes the charges need to acquire a specific critical energy $U_{\mathrm{c},s}$ to initiate the multiplication process by impact ionization [Lac91]. Since the threshold parameters are temperature dependent, the multiplication process is also temperature dependent. Charge carriers reach the critical energy needed to multiply more easily at lower temperatures, due to fewer phononic interactions. Thus, the gain is higher at lower temperatures. As implied by Eq. (2.7), the local electric field strength can be controlled by modification of the doping concentration in that region. Therefore, the gain G can be controlled by the doping concentration of an additional implant that is called the *gain layer* and is given by the ratio of the number of electron-hole pairs in the absence of a gain layer $N_{0,\mathrm{eh}}$ and the number of electron-hole pairs with it N_eh

$$G = \frac{N_\mathrm{eh}}{N_{0,\mathrm{eh}}}.$$

This implant is embedded in the sensor at a certain depth and this depth is crucial in controlling the gain of the sensor. Consider Fig. 2.9, where the impact of the depth of the gain layer on the width of the multiplication region is shown. A deep implant leads to a wider multiplication region, since the region of high electric field remains above the critical field E_c for a larger distance. Typical values for E_c in silicon are at roughly $300\,\mathrm{kV\,cm^{-1}}$ [MMO90]. This specific region is called the *multiplication region*, where the charge carriers are multiplied by impact ionization.

As previously mentioned, the gain of such a device can be designed by adjusting the doping concentration of the gain layer accordingly. A device with moderate gain in the order of 10 to 30 is called a *Low-Gain Avalanche Diode* (LGAD) [Fer+21].

2.7. Signal Formation

Signal formation is the process of generation of a signal due to a particle crossing the silicon sensor. There are significant differences in the signal formation between an ordinary silicon diode and an LGAD.

2.7.1. Sensors Without Gain

Following Shockley-Ramo theory introduced in Section 2.5, the weighting field $\left|\vec{E}_{\mathrm{w}}\right|$ is mostly constant $\approx \frac{1}{d}$ in sensors without gain. Let a particle now traverse the sensor. Under the assumption that the electric field is high enough for the generated electron-hole pairs to reach the terminal velocity in silicon v_{sat}, the induced current is

$$i \approx Nq\frac{1}{d}v_{\mathrm{sat}} = q(n_{\mathrm{eh}}d)\frac{1}{d}v_{\mathrm{sat}} = qn_{\mathrm{eh}}v_{\mathrm{sat}}, \tag{2.15}$$

with n_{eh} denoting the number of electron-hole pairs created per unit length [Fer+21]. Counterintuitively, Eq. (2.15) shows that the signal induced in a sensor i does not depend on the sensor thickness d, even though the number of electron-hole pairs does. This result makes sense considering that the weighting field $\approx \frac{1}{d}$ for a thicker sensor is lower and thus, each charge contributes less to the total current, even though more charges are generated in total.

2.7.2. Low Gain Avalanche Diodes

Due to the presence of the gain mechanism in an LGAD, signal formation looks different in such devices while still building on the basic concepts of sensors without gain. In order to understand where this difference stems from, let us consider the signal formation step-by-step after a particle has crossed the sensor: First, primary electrons and holes are generated by the charged particle, which drift apart along the electric field. Holes drift to the backside of the sensor and electrons drift towards the electrodes at the top, but first, they must traverse the gain layer. An important aspect of standard LGADs is that the gain implant always is located closer to the electrodes than it is to the backside of the sensor, regardless if a deep or shallow process is chosen[2]. While the electrons traverse the multiplication region, they generate additional *multiplication* or *gain* electron-hole pairs, as established in the previous section. Since the multiplication region is near the electrodes, primary and multiplication electrons are read out almost immediately. However, the gain holes have a long way to go: They must travel along almost the entire bulk thickness to get to the backside. In fact, the difference in electron and hole mobilities $\mu_{\mathrm{e,h}}$ are so large that upon the arrival of the last primary electron, the first gain hole is still drifting [Fer+21]. Since the weighting field $\approx \frac{1}{d}$ is constant in the whole bulk, the holes — by far — contribute to the signal the most.

The individual contributions of primary and gain electrons/holes to the total signal as a function of time is shown in Fig. 2.10b. Due to the secondary holes taking so much additional time to reach the backside, the signal in LGADs are usually longer than for gainless silicon sensors of comparable size, as shown in Fig. 2.10a — though still in the $\mathcal{O}$(ns).

2.8. Noise Contributions in Silicon Sensors

After having established concepts for the signal generated in silicon sensors, the parameter that complicates measuring this signal can be discussed: noise. In addition to the electronic noise

[2]There are *inverted* LGAD designs that have their gain implant at the backside of the device. These are not considered in this thesis.

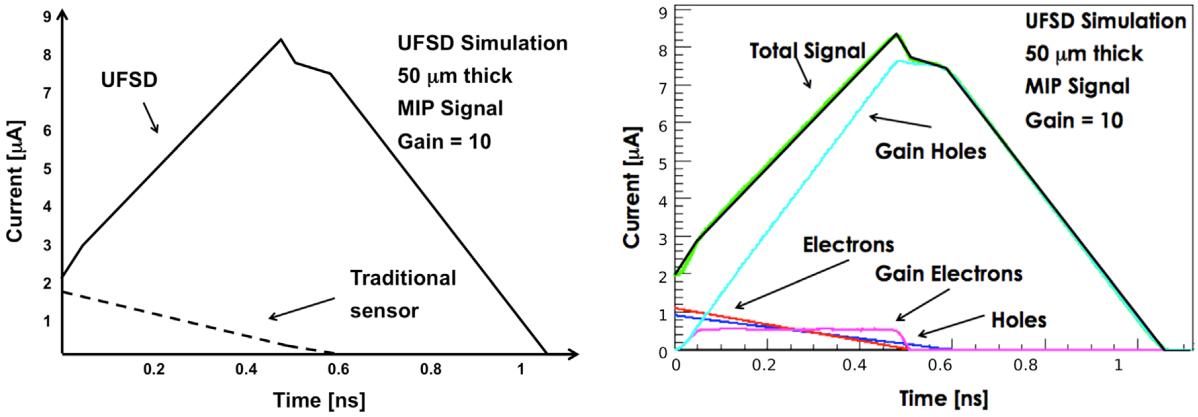

Figure 2.10.: (a) Comparison of the signals generated by a traditional silicon sensor and an LGAD/UFSD (ultra-fast silicon device) [Cen+15]. (b) Signal of an LGAD as a function of time with all contributions of the individual constituents [Cen+15].

that might be generated in the electronics reading these sensors out, the sensors, themselves, also generate noise. The following sections will briefly discuss these noise contributions. More in-depth discussions can be found in [Har24] and [Fer+21].

Since these sources of noise generate charges that compete with the charges induced by a traversing particle, noise contributions are expressed as *equivalent noise charges* (ENC), representing the number of electrons they would generate.

2.8.1. Sensors without Gain

The sources of noise are introduced as elements in the equivalent circuit of a sensor. The equivalent circuit consists of a network of a series resistance R_s, followed by a parallel resistance R_p, modelling a current source sourcing the bulk current I_bulk discussed in Section 2.3.2 leading to shot noise and a load capacitance C_d, which are connected in parallel. The noise contributions of these four sources are summed in quadrature to obtain the total noise

$$Q_\mathrm{n} = \sqrt{Q_{R_\mathrm{s}}^2 + Q_{R_\mathrm{p}}^2 + Q_{I_\mathrm{bulk}}^2 + Q_{C_\mathrm{d}}^2}.$$

While each of these noise contributions have approximate analytic forms, they will not be needed in this work and, therefore, shall only be discussed qualitatively.

Both thermal resistance terms $Q_{R_{\mathrm{s/p}}}$ as well as the shot noise term Q_{I_bulk} scale with temperature T. Thus, they can be minimized by cooling the sensors. However, for sensors that read out at high frequencies the frequency-dependent load capacitance term Q_{C_d} is dominant. Specific sensor design choices must be made to minimize the impact of sensor capacitance on the total noise, as well as optimizations of the readout chain with regard to capacitance, to increase the noise performance.

2.8.2. Low Gain Avalanche Diodes

While shot noise may not represent a dominating contribution to the total noise in devices without gain, they are very likely to become relevant for LGADs since the bulk current is multiplied with the gain value G discussed earlier. The devices investigated in this work operate at moderate gain values of around 20 [Men23]. Thus, shot noise is usually lower than the noise generated by the readout electronics. However, although G decreases after irradiation, the

total leakage current still increases due to radiation damage. This effect will be discussed in the next chapter in more detail.

In addition to the gain dependence of the shot noise term, there is also variability in the gain mechanism, since it is a statistical effect based on the charge carriers picking up enough kinetic energies to cause secondary ionization. Therefore, primary charges that enter the multiplication region might produce a number of secondary charges varying around G. This effect is called *excess noise* and is characterized by a scaling factor F to the shot noise term. It can be expressed as

$$F \approx G^x = Gk + \left(2 - \frac{1}{G}\right)(1 - k),$$

where x denotes the *excess noise index* and $k = \alpha_\mathrm{h}/\alpha_\mathrm{e}$ [Fer+21]. A way to optimize this noise term and keep F low is by using p-type LGADs. Since $\mu_\mathrm{e} > \mu_\mathrm{h}$ and electrons are read out at the electrodes, where the gain layer is located, the doping concentrations can be optimized in such a way that only electrons take part in the multiplication mechanism. This technique requires precise control over the doping concentrations.

In reality, the noise contribution from the readout electronics used for LGADs usually far outscale the noise contributions from the device itself.

3
Radiation Damage

Operating particle detectors is a love-hate relationship: On the one hand, you build them to detect particles and find out more about what the universe is made of. On the other hand, however, these very particles are sworn to destroy all you have built by damaging the detector material you so carefully thought out while they are traversing it. This is called radiation damage. The main goal of this work is to investigate the radiation damage in silicon sensors of several different designs. The following sections will, therefore, go into detail about the different types of radiation damage that can occur in silicon sensors. Discussions made here are inspired by the great work of Moll [Mol99] and sources therein. For more information on radiation damage in silicon sensors, the reader is referred to his work.

Radiation damage can generally be divided into two categories: bulk damage and surface damage. While most of this work will focus on bulk damage, surface damage is also an important aspect of radiation damage in silicon sensors and was also investigated.

3.1. Bulk Damage

Hadrons (protons, neutrons, pions, etc.) and high-energy leptons introduce radiation damage into the silicon bulk lattice by displacement of a *primary knock-on atom* (PKA) from its lattice site. This results in a pair of a vacancy, a place where an atom is missing, and an interstitial silicon atom that is not in its lattice site. The pair that is formed is called a *Frenkel pair*. In order to create a Frenkel pair, a certain amount of energy called the *displacement energy* E_d needs to be transferred to the target atom and this threshold lies at around 25 eV for silicon [Van80]. After the PKA has been knocked out of its lattice site, it can recoil and create *point defects* along its path, finally forming *cluster defects* at the end of its wake of destruction. The threshold energy for the creation of a cluster defect E_cl is higher than for a point defect and lies at around 5 keV in silicon [Van80]. While most of the Frenkel pairs will almost instantly recombine and annihilate [Mol99], leaving the silicon lattice intact, some of them remain and form point defects. Point defects are highly mobile and can migrate through the silicon lattice, forming clusters, reacting at impurity sites or annihilating with other point defects, depending on the temperature of the silicon sensor, and thus, the lattice vibrational energy. While a real silicon crystal is never perfect and always contains some defects, the introduction of radiation damage increases the number of defects in the crystal. These defects in the silicon lattice introduce new energy levels into the band gap of the silicon crystal and therefore alter the electronic properties of the silicon sensor.

The energy needed to create a Frenkel pair is different for different types of radiation. To understand why, it is helpful to look at the maximum energy transfer W_max from an incident particle to the silicon lattice that was also already used in the context of the Bethe equation in Section 2.4.1 for heavy charged particles. Since protons and neutrons have roughly the same mass, they also have roughly the same maximum energy transfer. Therefore, E_d and E_cl are also roughly the same for protons and neutrons and lies at around 187 eV and 5 keV, respectively. On the other hand, electrons need a much higher energy of $E_\mathrm{d} \approx 255\,\mathrm{keV}$ and

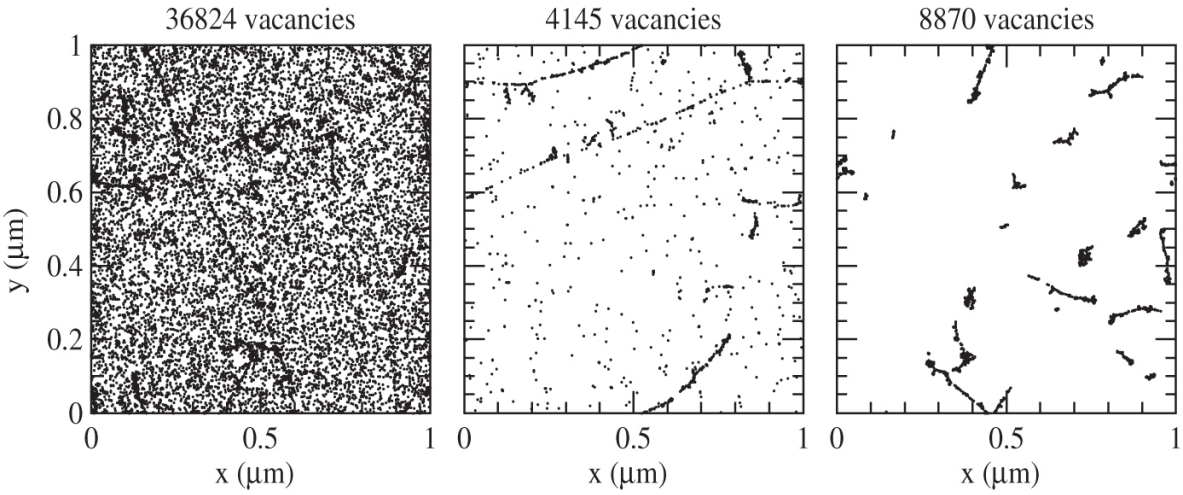

Figure 3.1.: Distribution of vacancies produced by 10 MeV protons (left), 24 GeV protons (middle) and 1 MeV neutrons [Huh02].

$E_{\mathrm{cl}} \approx 8\,\mathrm{MeV}$ [Mol99]. The naive consideration above may lead the reader to believe that neutrons and protons produce the same amount and type of radiation damage in silicon sensors due to their similar mass. However, this is not the case. Figure 3.1 shows the distribution of vacancies produced by protons and neutrons of different energies. It is clear that neutrons tend to produce cluster defects more than protons, which produce more point-like defects. This is a result of neutrons only interacting with the lattice via the strong force while charged protons may interact using the electromagnetic *and* strong forces. However, 24 GeV protons seem to blend the two types of defects, producing both point and cluster defects. To summarize, radiation damage produced in silicon sensors is dependent not only on particle type but also on particle energy.

3.1.1. The NIEL Hypothesis

Radiation damage in silicon sensors is dependent on the type and energy of the incident particle. In order to compare the radiation damage produced by different types of particles, the *non-ionizing energy loss* (NIEL) scaling hypothesis was introduced. Numerous observations have shown that (some of) the effects due to radiation damage in the bulk of any semiconductor are proportional to the *displacement damage cross section* $D(E)$. Figure 3.2 shows the normalized displacement damage cross sections as a function of particle energy for different types of particles. Following NIEL scaling, the damage inflicted to the silicon sensor by a particle of energy E may be scaled to the damage 1 MeV-neutrons would cause by the *hardness factor*

$$\kappa(E) = \frac{\int \mathrm{d}E\ D(E)\Phi(E)}{D(n)\int \mathrm{d}E\ \Phi(E)},$$

where $\Phi(E)$ is the *particle fluence*, a measure of the amount of applied radiation, and $D(n)$ is the displacement damage cross section for 1 MeV-neutrons, which is $D_{\mathrm{Si}}(n) = 95\,\mathrm{MeV\,mb}$ [VL00]. By this definition, the *equivalent fluence* Φ_{eq} is defined as

$$\Phi_{\mathrm{eq}} = \kappa\Phi.$$

Fluences expressed in terms of equivalent fluences are comparable with each other if the NIEL hypothesis holds true. However, the NIEL hypothesis is not valid for the effects of radiation damage on all properties of a silicon sensor. A very obvious reason for this is the fact that

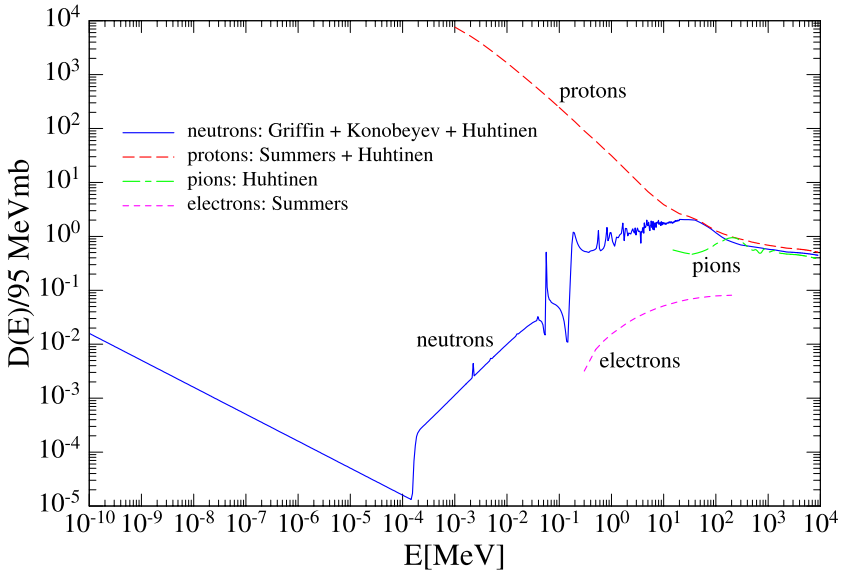

Figure 3.2.: Normalized displacement damage cross sections as a function of particle energy for different types of particles [VL00].

NIEL does not make a difference between point and cluster defects. It also does not correctly predict the difference in radiation damage between n-type and p-type silicon sensors [Arn+11]. In terms of the macroscopic effects on the silicon sensor, NIEL is a good scaling approximation for the leakage current but not at all for capacitance or charge collection efficiency (CCE). Still, it currently remains the best scaling hypothesis for the effects of radiation damage on the silicon substrate and therefore is used in this work for selected quantities.

3.1.2. Microscopic Impact of Defects on Sensor Properties

At this point, readers should naturally ask themselves how exactly radiation damage affects the properties of a silicon sensor. The answer to this question lies in the interplay between the energy levels of the defects with the Fermi level of the silicon sensor, depending on the exact type of defect. Among the endless possibilities for point defects, there are silicon self-interstitials ($(\mathrm{Si})_i$), interstitials (I), substitutions (X_S, where X is any element), vacancies (V) and divacancies (V^2). These defects may appear in the band gap of the silicon sensor as acceptor, donor or mixed (amphoteric) levels. Figure 3.3 shows the ionization state of different types of defect levels in a semiconductor. States can be occupied by electrons when they are below the Fermi level E_F in thermal equilibrium. States above the Fermi level are not likely to be occupied by electrons. Since they are not occupied by electrons, we may call them *occupied by holes*, in fact, both descriptions are equivalent. As suggested by the discussions in Section 2.2, acceptors are charged (negatively) when they are occupied by electrons and donors are charged (positively) when they are occupied by holes. Unoccupied acceptors and donors are electrically neutral. Combining these considerations, acceptor levels above the Fermi level are charged negatively in the SCR, adding to the ionized acceptor density. Donor levels below the Fermi level are charged positively and mixed levels can be either positively or negatively charged, since amphoteric defects introduce multiple energy levels into the band gap that can act as acceptor or donor levels.

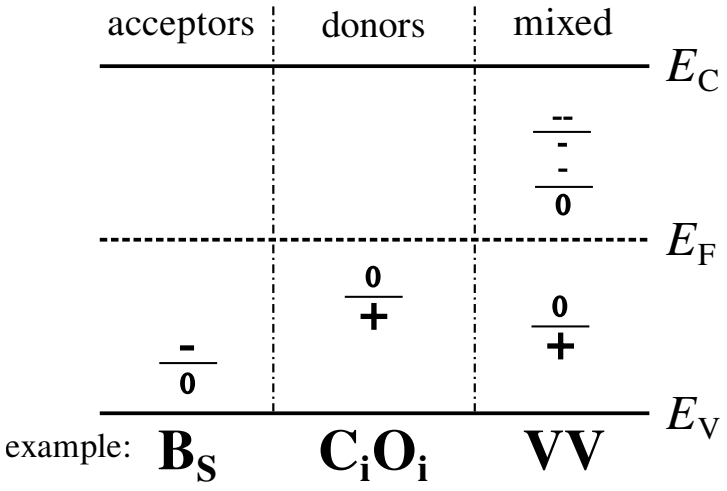

Figure 3.3.: Ionization state of different types of defect levels in a semiconductor. For each state, the sign above the bar specifies the charge of the defect above E_F and below the bar the charge below E_F. Distinguishing between acceptor, donor or mixed (amphoteric) levels, the position with respect to the Fermi level E_F decides if the state is likely to be ionized or not. Graphic adapted from [Mol99].

Depending on the distance from the band edges, the defect levels can either be classified as shallow or deep. Although the exact definition of shallow and deep levels remains subjective, shallow levels are usually close to the band edges and are ionized at room temperature, while deep levels are near the middle of the band gap. Defects or impurities that are introduced as a result of doping are usually shallow, as shown in the boron substitute B_S energy level in Fig. 3.3. To extend upon this example, the phosphorus substitute P_S is a shallow donor level. Shallow levels are usually acceptor levels above the Fermi level and donor levels below it. Therefore, they are usually ionized at room temperature and can contribute to the electrical conduction — exactly what they are designed to do in the case of doping.

3.1.3. Macroscopic Impact of Defects on Sensor Properties

Defects in the crystal lattice naturally introduce acceptor, donor or mixed states into the band structure of the silicon sensor. Thus, as established in the previous chapter, radiation damage has an influence on N_{eff}, as well as resistivity, leakage current and CCE of the silicon sensor. The following sections will give a brief overview of how these properties are affected by radiation damage.

Depletion Voltage and the Effective Doping Concentration

Ionized defects in the SCR can have an effect on the depletion voltage of the silicon sensor by changing the effective doping concentration of the sensor. As previously shown, $V_{\text{dep}} \propto |N_{\text{eff}}|$. In the previous section, it was also shown that the ionization state of defects in the band gap of the silicon sensor depends on the energy level of the defect. As shown in Fig. 3.3, this means that acceptor states above the Fermi level and donor states below it do affect the depletion voltage of a sensor. Since defects introduced by irradiation mainly create acceptor levels in the bulk and remove donor levels, the N_{eff} is increased. This leads to an increase in the depletion voltage of the sensor. Therefore, radiation damage interferes greatly with the capability of the sensor to be fully depleted and thus, to detect particles.

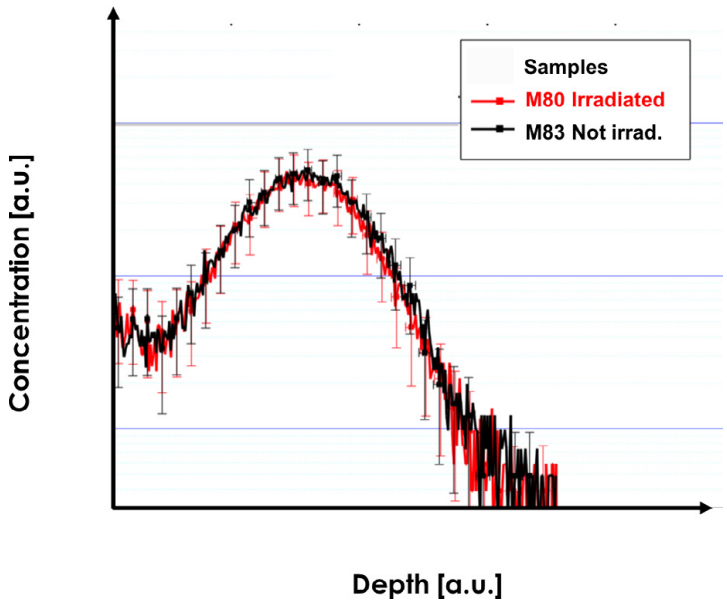

Figure 3.4.: Boron gain layer dopant concentration as a function of sensor depth for an unirradiated and heavily irradiated LGAD sensor. The boron concentration did not change after irradiation, even though the gain layer is completely inactive [Fer+19].

In total, three mechanisms are reponsible for the change in N_{eff}: *donor removal*, *acceptor removal* and *acceptor creation*. For a particle fluence Φ, it can be parameterized as [Men23]

$$N_{\text{eff}} = N_{\text{D},0} \exp\left(-c_{\text{D}}\Phi\right) - N_{\text{A},0} \exp\left(-c_{\text{A}}\Phi\right) - g_{\text{eff}}\Phi,$$

where $c_{\text{D/A}}$ are the *donor/acceptor removal constants*, $N_{\text{A/D},0}$ are the initial acceptor/donor concentrations and g_{eff} is the *effective acceptor creation rate*, which is a measure describing acceptor creation. Donor or acceptor removal work by creating mobile defects during the irradiation that can react with the dopants in the silicon sensor and form unionized defects in the SCR, effectively removing the shallow dopants from the sensor [Fer+19]. Ion-acceptor complexes are formed in this process, which are not ionized in the SCR and therefore, electrically deactivate the donors/acceptors, even though they are still present in the sensor. This is shown in Fig. 3.4, where the dopant boron gain layer concentration is plotted as a function of sensor depth for an unirradiated and heavily irradiated LGAD sensor. The dopant boron concentration did not change after irradiation, even though the gain layer is completely inactive, indicating that the boron dopants were not removed from the sensor but rather electrically deactivated.

Leakage Current

As outlined in Section 2.3.2, certain impurities and defects are generation centers for leakage current. After irradiation, the number of defects in the silicon sensor increases, leading to an increase in the leakage current. Deep levels predominantly act as generation centers for leakage current, since they can be used by electrons very effectively to jump into the conduction band. As outlined in the section about acceptor and donor removal, cluster defects often introduce deep levels into the band gap of the silicon sensor. Therefore, they predominantly are responsible for the increase in leakage current after irradiation. The increase in leakage current after irradiation ΔI normalized by the sensor volume V at an equivalent fluence Φ_{eq} follows

$$\frac{\Delta I}{V} = \alpha_{\text{eq}}\Phi_{\text{eq}}, \tag{3.1}$$

where α_{eq} is called the *(current-related) damage rate*. This parameter is a good measure to compare the quality of irradiated structures with each other, regardless of the delivered fluence. Due to the high increase in leakage current ΔI, the sensor cannot be operated at room temperature anymore and needs to be cooled down to decrease the leakage current to an acceptable level, as outlined in Section 2.3.2. For example, plugging a typical value of $\alpha_{\text{eq}} \approx 4 \times 10^{-17}\,\text{A}\,\text{cm}^{-1}$ [Mol99] into Eq. (3.1), the change in leakage current for a sensor with a volume of $V = 13\,\text{mm}^3$ would be $\approx 2\,\text{mA}$. An unirradiated sensor with the same volume would have a leakage current of $\approx 1\,\text{nA}$, emphasizing the need for cooling.

Charge Collection Efficiency

Radiation damage also increases the depletion voltage, as discussed previously. This has a direct impact on the CCE of the sensor, because it needs to be overdepleted to reach optimal CCE. Overdepletion is crucial for the CCE of the sensor because it increases the electric field in the sensor and therefore, the drift velocity of the charge carriers. According to Eq. (2.14), this means a higher signal. A careful belance between overdepleting the sensor as far as possible without breaking down the sensor and keeping the leakage current low enough to make it cost-effective is necessary.

Apart from this effect, radiation-induced defects can also act as *trapping* centers for charge carriers. Electrons or holes can be trapped at these defects for a certain amount of time that is dictated by the *trapping time* τ. The trapping time is a measure of the time it takes for a charge carrier to be released from the defect. If τ is too long, the charge carrier will not be able to contribute to the main signal of the sensor since it will be delayed in time. Therefore, this part of the signal will be lost in the noise of the sensor, as outlined in Section 2.8.

3.1.4. Protons vs. Neutrons

As discussed in Section 3.1.1, the NIEL scaling hypothesis does not distinguish between point and cluster defects and is therefore not a good scaling hypothesis for all properties of a silicon sensor. If compared to neutrons, protons tend to produce more point defects (as seen in Fig. 3.1), due to the additional Coulomb interaction between the proton and the silicon lattice with much smaller energy transfers. Neutrons may only interact with the silicon lattice via nuclear reactions with hard collisions, leading to the creation of more cluster defects.

Another shortcoming of the NIEL hypothesis is the fact that impurity-enriched materials react differently to different particle types. This is shown in Fig. 3.5, where the effective doping concentration N_{eff} is plotted as a function of fluence in different sensor processes for proton and neutron irradiation. It is clearly visible that radiation damage cannot be scaled with NIEL for non-standard sensor processes [Ruz+99]. Not only does the change in N_{eff} differ between protons and neutrons, but also between different sensor processes. Oxygen-enrichment seems to be an effective method to reduce the change in N_{eff} after irradiation for 24 GeV-protons, as well as neutrons with an energy spectrum ranging from thermal to 10 MeV [Ruz+99], effectively increasing the radiation tolerance of the material. Even though Fig. 3.5 shows measurements performed on n-type devices, the fact that NIEL does not perform well when considering these aspects still applies to p-type devices as used today.

3.2. Surface Damage

Surface damage in silicon sensors describes the damage to the SiO_2 layer that is usually grown on top of the silicon wafer. Since bare silicon is chemically very reactive, a SiO_2 layer is used to protect the silicon sensor from chemical reactions with the environment. Silicon dioxide is also a

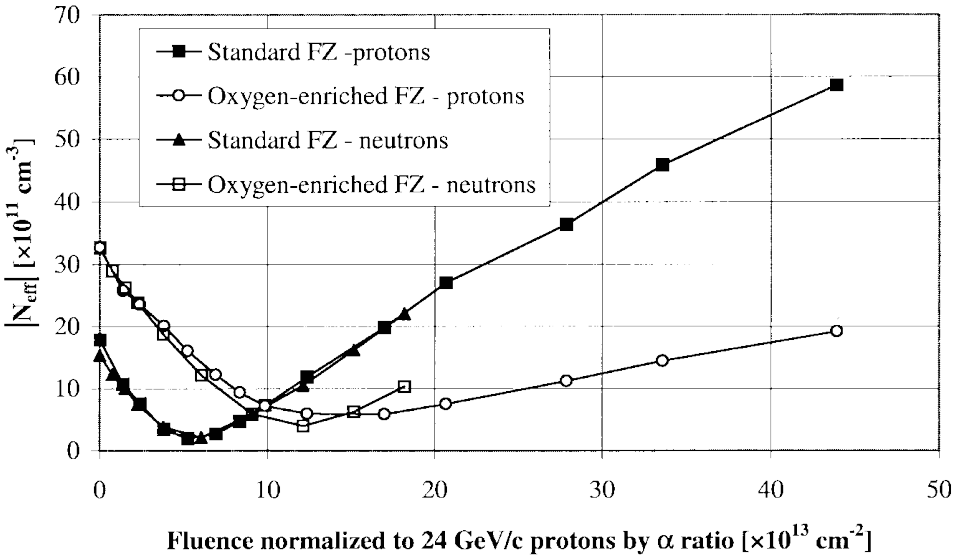

Figure 3.5.: Comparison of the effective doping concentration N_{eff} as a function of damage rate-scaled fluence in different sensor processes: standard and oxygen-enriched float-zone (FZ) silicon after proton and neutron irradiation [Ruz+99].

very good insulator due to its wide band gap. Depending on the thickness of the layer, it is used either as a passivation layer or as a dielectric layer for AC coupling of the implanted electrodes. As with the bulk of the sensor, the SiO_2 layer is also subject to radiation damage. In contrast to the bulk, the primary damage mechanism in the SiO_2 layer is ionization damage, which is why instead of NIEL, the *total ionization dose* (TID) is used to quantify the radiation damage in the SiO_2 layer. The impact that displacement damage has on the SiO_2 layer in the scope of the sensors used in this work is negligible compared to the ionization damage. Electron-hole pairs created by ionizing radiation interact with impurities and imperfections in the dioxide layer, as well as the Si-SiO_2 interface. While many different polymorphic modifications of SiO_2 exist, which all have different band gaps, the band gap of silicon dioxide used for sensors in this work is 8.9 eV, which is eight times larger than the band gap of silicon.

3.2.1. Types of Surface Defects

Due to imperfections in the SiO_2, electron-hole pairs created by ionizing radiation can be trapped at these defects. Trapping an electron would create a negative charge at the defect, while trapping a hole would create a positive charge. Charges trapped at such defects are called *oxide-trapped charges* and are spread out over the SiO_2 layer.

Since materials with different atomic structures are in contact at the Si-SiO_2 interface, naturally, the lattice is highly strained at the interface. Dangling bonds are created at the interface, which are amphoterically charged and can act as acceptor or donor levels. These levels are called *interface traps* and promote the formation of a conductive layer at the interface.

In a SiO_2 crystal, neighboring silicon atoms are connected by oxygen atoms and if this oxygen atom is missing, the silicon atoms will be weakly bound. At these oxygen vacancies, also referred to as *fixed oxide charges*, holes can be trapped. The hole mobility in the oxide layer is many orders of magnitude lower than the electron mobility. Therefore, once an electron-hole pair is created by ionizing radiation in the oxide layer, the electron will be able to move freely through the oxide layer, while the hole will move towards the interface, being trapped either at fixed oxide charges or at the Si-SiO_2 interface. Trapping of holes over time created by

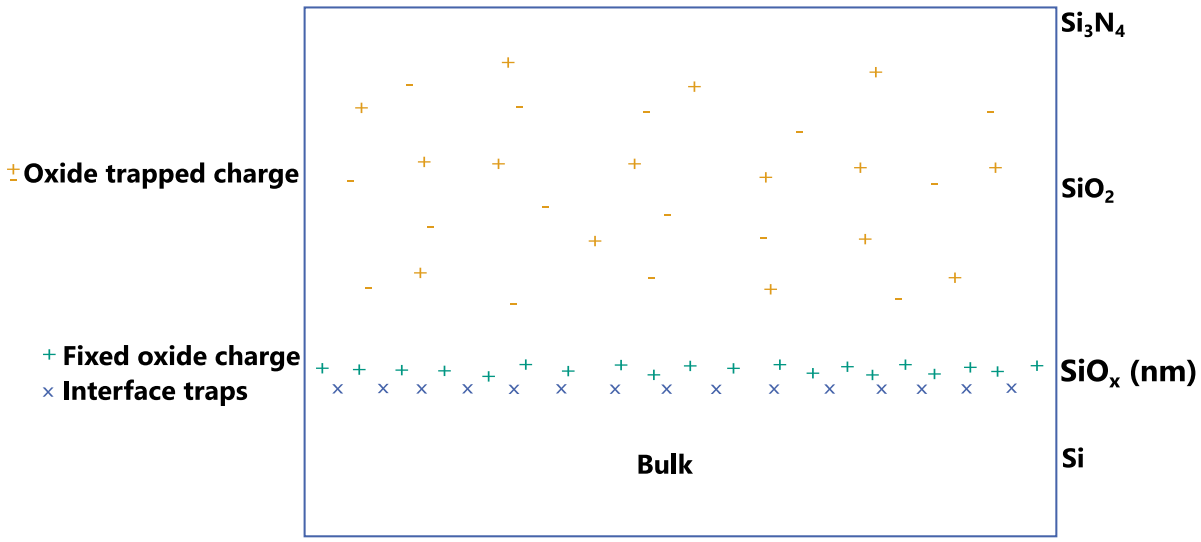

Figure 3.6.: Schematic of the different types of surface defects in a silicon sensor [Mül21].

ionizing radiation leads to positive charge build-up at the interface, promoting the formation of a conductive electron layer, called *inversion layer*, at the interface. This electron layer forges a conductive path between implanted n-electrodes in a p-type silicon sensor, leading to a short circuit between the electrodes and changed electric field lines within the substrate.

Figure 3.6 shows a schematic of the different types of surface defects that were just discussed. In summary, the interplay between the insufficient recombination of electron-hole pairs and traps at the interface lead to the formation of an inversion layer. This inversion layer results in a short circuit between the implanted electrodes and thus, deterioration of the inter-implant isolation that is necessary for optimal spatial resolution. Additionally, the inversion layer leads to a change in the electric field lines in the silicon substrate, which can lead to a change in the charge collection efficiency of the sensor.

3.3. Annealing

Depending on the temperature of the silicon sensor, lattice vibrations can provide enough energy for the defects to migrate through the lattice. Most defects and impurities become mobile with increasing temperature, promoting reactions among them. This process is called *annealing* and can be beneficial or detrimental to the sensor properties. There are two defect mechanisms that are responsible for the annealing process that are the opposite of each other: *clustering* and *dissociation*. Clustering is the process of defects migrating towards each other and forming a complex of defects, i.e. the formation of a divacancy from two vacancies $V + V \rightarrow V^2$ or the deactivation of dopant boron levels in the donor removal process discussed in Section 3.1.3. Dissociation is the process of a defect complex breaking apart to its constituents due to the energy provided by the lattice vibrations being high enough to overcome the binding energy of the complex. Annealing leads to a change in the effective doping concentration ΔN_{eff} and can be parameterized by [Mol99]

$$N_{\text{eff}}(t) = N_{\text{eff}}(\phi = 0) - \underbrace{(N_{\text{C}}(\phi) + N_{\text{A}}(t, T, \phi) + N_{\text{Y}}(t, T, \phi))}_{\Delta N_{\text{eff}}}, \tag{3.2}$$

where N_{C} represents the *stable annealing term* and $N_{\text{A/Y}}$ are the *beneficial/reverse annealing terms*, respectively. The stable annealing term is a part of the effective doping concentration

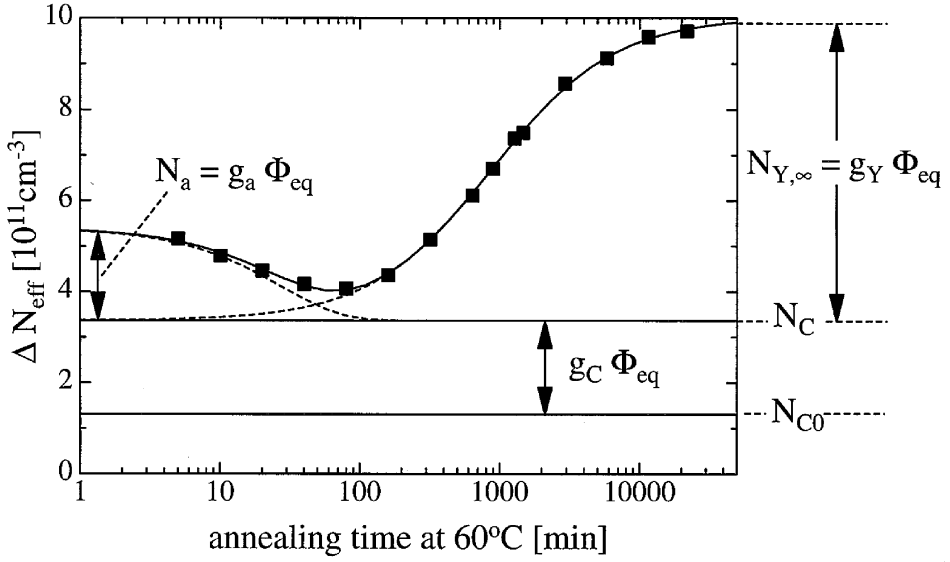

Figure 3.7.: Change in the effective doping concentration ΔN_{eff} as a function of time. Maximizing the charge collection capabilities of the sensor means aiming for the minimum of the curve [Mol99].

that does not change over time, hence, there is radiation damage that cannot be annealed. Beneficial annealing refers to a decrease of ΔN_{eff} over time, while reverse annealing refers to an increase. Beneficial annealing improves the charge collection efficiency of the sensor, while reverse annealing deteriorates it. In order to maximize the performance of the sensor, the minimum of the ΔN_{eff} as a function of time, shown in Fig. 3.7, should be aimed for when trying to anneal out the radiation damage.

As shown in Eq. (3.2), annealing has a complex impact on the effective doping concentration of the sensor since there is a minimum in the ΔN_{eff} curve. However, annealing always leads to a decrease in the leakage current of the sensor. The change in leakage current ΔI can be parameterized using a Fourier ansatz as [Mol99; Wun92]

$$\Delta I(t) = \Delta I(t=0) \sum_i b_i \exp\left(-\frac{t}{\tau_i}\right),$$

with the Fourier coefficients b_i and the time constants τ_i. Modifying this Fourier ansatz with a logarithmic time dependence, the damage rate α_{eq} can be parameterized as [Mol99]

$$\alpha_{\text{eq}}(t) = \alpha_0 + \alpha_{\text{I}} \exp\left(-\frac{t}{\tau_{\text{I}}}\right) - \beta \log\left(\frac{t}{t_0}\right), \tag{3.3}$$

with all parameters $\alpha_0, \alpha_{\text{I}}, \tau_{\text{I}}, \beta, t_0$ found by best fit to the data.

Since the annealing terms in Eq. (3.2) scale with the temperature of the sensor, the annealing process can be accelerated by increasing the temperature beyond room temperature. Equation (3.3) is used in this work with parameters found in [Mol99] to calculate an equivalent annealing time at room temperature for the sensors investigated in this work. Temperatures of 60 °C and 80 °C were used to accelerate the annealing process for the respective studies. Different annealing temperatures can be used to target specific defect levels, which is used in techniques such as thermally-stimulated current (TSC) measurements. The annealing temperatures used in this work, however, are not specific to any defect level and are only used to accelerate the annealing process.

4
The LHC and CMS

The goal of the HEP community is to understand what matter is made up of on the most fundamental level, and how these elementary building blocks interact with each other. One of the most crucial instruments to achieve this goal are particle colliders, which accelerate different kinds of particles to high energies and bring them to collision in a controlled manner. Detectors located close to the collision sites of such accelerators are used to detect the collision products of these interactions. Physicists use these data to learn more about the properties of these particles, enabling them to extend the Standard Model of Particle Physics or even discover new physics beyond the Standard Model altogether. Research in this work is centered around the Compact Muon Solenoid (CMS) experiment located at the Large Hadron Collider (LHC). The following sections will give a brief overview of these infrastructures.

4.1. CERN and the LHC

The *European Organisation for Nuclear Research* (CERN) in Geneva is the world's largest organization for particle physics research. CERN was established after World War II in an effort of hosting peaceful collaborations among nations. Nowadays, CERN celebrates its 70th anniversary and is proud to have 24 member states and ten associate member states, with 17 000 people of diverse backgrounds, representing more than 110 nationalities, collaborating together in the name of science [CER25]. It has become the largest hub for scientist all over the world to work on HEP.

The LHC currently is the largest and most powerful particle accelerator in the world, based at the CERN laboratory. It is located in a tunnel deep beneath the French-Swiss border. At a circumference of 26.7 km and sublevel height of 50 m to 175 m, the LHC forms the last stage of an accelerator chain in the CERN accelerator complex, seen in Figure 4.1. In contrast to its predecessor LEP (*Large Electron-Positron Collider*), the LHC was not designed to accelerate electrons and positrons but two counter-rotating beams of protons or heavy ions to speeds extremely close to the speed of light. So far, Pb+Pb, Xe-Xe and asymmetric p+Pb collisions have been accomplished for heavy ion runs [Jow18]. Protons need to pass four pre-accelerator links (LINAC4, BOOSTER, PS, SPS) to reach the LHC injection energy $E_{\text{min}} = 450\,\text{GeV}$. After entering the LHC, they proceed to be accelerated to a peak energy of about 7 TeV.

RF cavities operating at a frequency of $f_{\text{RF}} = 400\,\text{MHz}$ accelerate the particles along the LHC ring. Phase-focussing forces the particle beams to be split into 2808 spatially separated, equienergetic *bunches*. In order to always provide an accelerating voltage across a gap of one such RF cavity, their frequency needs to be an integer multiple h of the revolution frequency f_{rev}. $h = \frac{f_{\text{RF}}}{f_{\text{rev}}}$ is called the *harmonic number* of the accelerator and for the LHC, it is chosen to be $h_{\text{LHC}} = 35\,640$. The segments of the circumference centered around the points of the harmonic number are called *buckets*, which serve as the theoretical limit on the number of bunches of the LHC, because phase-focussing is centered around these buckets. In practice, however, not all buckets are filled with bunches. One reason for this is the aforementioned PS and SPS pre-accelerators, which deliver bunches with 25 ns spacing (which translates to a

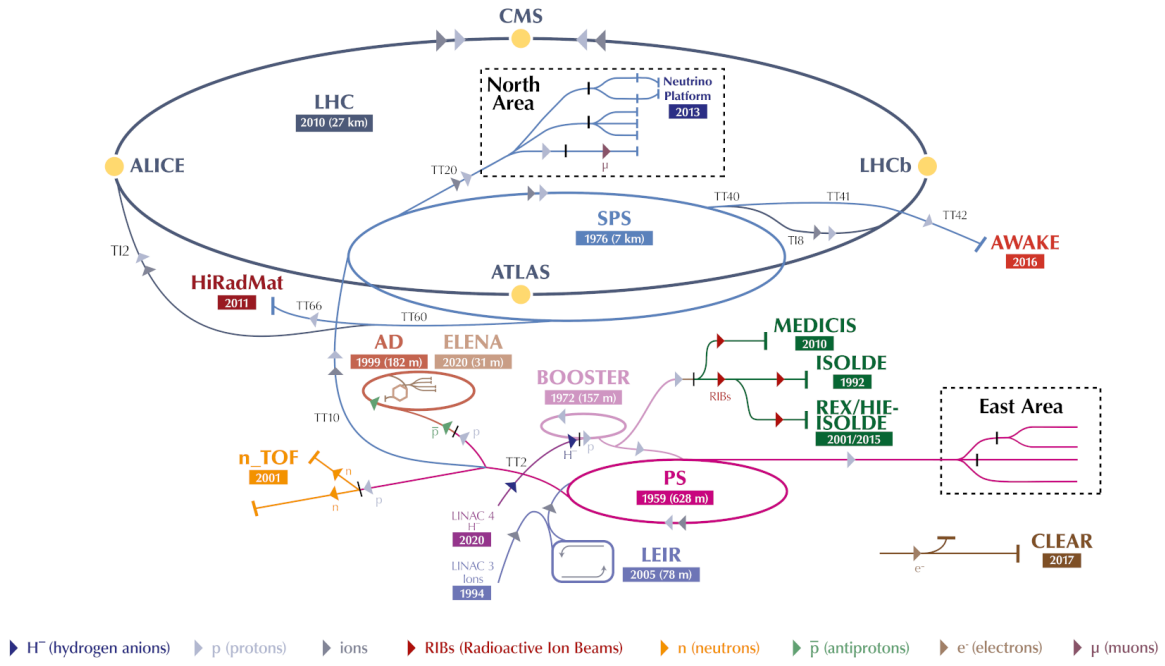

Figure 4.1.: The CERN accelerator complex. The LHC represents the last stage in this multi-stage complex, accelerating protons to $\sqrt{s} = 13\,\text{TeV}$ [Lop22].

bunch frequency of 40 MHz). The bucket configuration is also influenced by where the bunches are supposed to be brought to collision and a safety margin for the beam dump system in case of an emergency beam dump. The LHC is designed to have a maximum of 2808 bunches per beam at a bunch spacing of 25 ns. Therefore, the readout electronics in detectors observing these collisions need to be able to read data at 40 MHz.

After acceleration to the peak energy of around $E_{1,2} = E_\text{p} = 7\,\text{TeV}$, the particles are collided at a center of mass energy of up to

$$\sqrt{s} = \sqrt{4E_\text{p}^2} = 2E_\text{p} = 14\,\text{TeV},$$

immediately revealing why a collider experiment is necessary to reach such high interaction energies. Apart from the center of mass energy available for the production of new effects, the most important quantity of a particle collider is the number of useful interactions. In scattering theory, this parameter is expressed as the *instantaneous luminosity* $\mathcal{L}$ and is the proportionality factor between the interaction rate

$$R = \mathcal{L} \cdot \sigma_\text{p}$$

and the interaction cross-section σ_p of a process p. For a collider, this quantity can be obtained by considering basic beam parameters such as the beam width in x/y-direction $\sigma_{x/y}$, the number of bunches N_b, the number of particles per colliding bunch N_i and the revolution frequency of a single bunch $f = f_\text{RF}/h_\text{LHC} = 11.2\,\text{kHz}$. The instantaneous luminosity can then be expressed as

$$\mathcal{L} = f \cdot N_\text{b} \frac{N_1 N_2}{4\pi\sigma_x\sigma_y}.$$

Integrating this quantity over the duration of data taking yields the *integrated luminosity*

$$L = \int \text{d}t\ \mathcal{L},$$

which is directly proportional to the number of events N_e and is usually given in units of inverse femtobarns $\left(\text{fb}^{-1}\right)$. Thus, the integrated luminosity is a measure of how many interactions have been accumulated in the detector during data taking periods, called *runs* hereafter. In principle, particle colliders therefore try to maximize their $\mathcal{L}$ to increase the amount of data that is available for analysis. The LHC was designed to operate at an instantaneous luminosity of $1 \times 10^{34}\,\text{cm}^{-2}\,\text{s}^{-1}$. This limit was pushed even further to a maximum of $2 \times 10^{34}\,\text{cm}^{-2}\,\text{s}^{-1}$, limited by insufficient cooling of the inner triplet magnets [Abe+20]. It has reached an integrated luminosity of $196\,\text{fb}^{-1}$ during its most recent run, already surpassing the previous run's record of $160\,\text{fb}^{-1}$ [Ste].

Beams in the LHC are brought to collision at four designated interaction points (IPs). Four large experiments are located at these IPs and collect data from collisions:

- **CMS** (Compact Muon Solenoid), a general purpose particle detector that includes a special muon detection system that is particularly efficient at detecting muons [HTA24],
- **ATLAS** (A Toroidal LHC Apparatus), currently the biggest general purpose particle detector at the LHC [ATL08] with an electromagnetic calorimeter that features an outstanding energy resolution and granularity. Together with CMS, it made contributions that led to the discovery of the Higgs boson in 2012 [Cha+12; Aad+12].
- **ALICE** (A Large Ion Collider Experiment), that is designed to measure properties of quark-gluon plasma, studying the conditions that existed within the first microsecond of the Universe [ALI08],
- **LHCb** (Large Hadron Collider beauty), a general purpose forward-detector primarily designed to study b-physics effects and measure CP-violation parameters [LHC08].

In the following, only the CMS experiment will be discussed in more detail, as it is the focus of this work.

4.2. The CMS Experiment

The CMS experiment is a general purpose particle detector located in a 100 m deep cavern at the LHC. Weighing around 14 000 t, it is currently the heaviest LHC experiment [HTA24]. With a detector layout that is comprised of many different specialized subsystems, CMS is able to pursue a broad range of physics objectives. The initial physics program of CMS was centered around the study of electroweak symmetry breaking for which the Higgs mechanism was presumed to be responsible. Futhermore, the CMS collaboration aimed for consistency checks of the Standard Model above energies of 1 TeV, the contemporary limit to which the Standard Model was tested on at the time. After the discovery of the Higgs boson in 2012 [Cha+12], the focus of the collaboration shifted towards the search for new physics and precision measurements of the Standard Model.

The CMS detector layout is shown in Fig. 4.2. It is designed to be nearly hermetic around the collision point to ensure that as many collision products as possible are detected. The detector is composed of different layers of detector subsystems, each measuring different properties of the particles produced in the collision. The subsystems are, from the inside out: The silicon-based tracker, the electromagnetic calorimeter (ECAL), the hadronic calorimeter (HCAL) and the muon chambers. A strong magnetic field applied by the namesake solenoid magnet bends the trajectories of charged particles, allowing for the measurement of their momentum. This work will focus on parts of the CMS Tracker subsystem exclusively, which will be discussed in more detail in the following paragraphs.

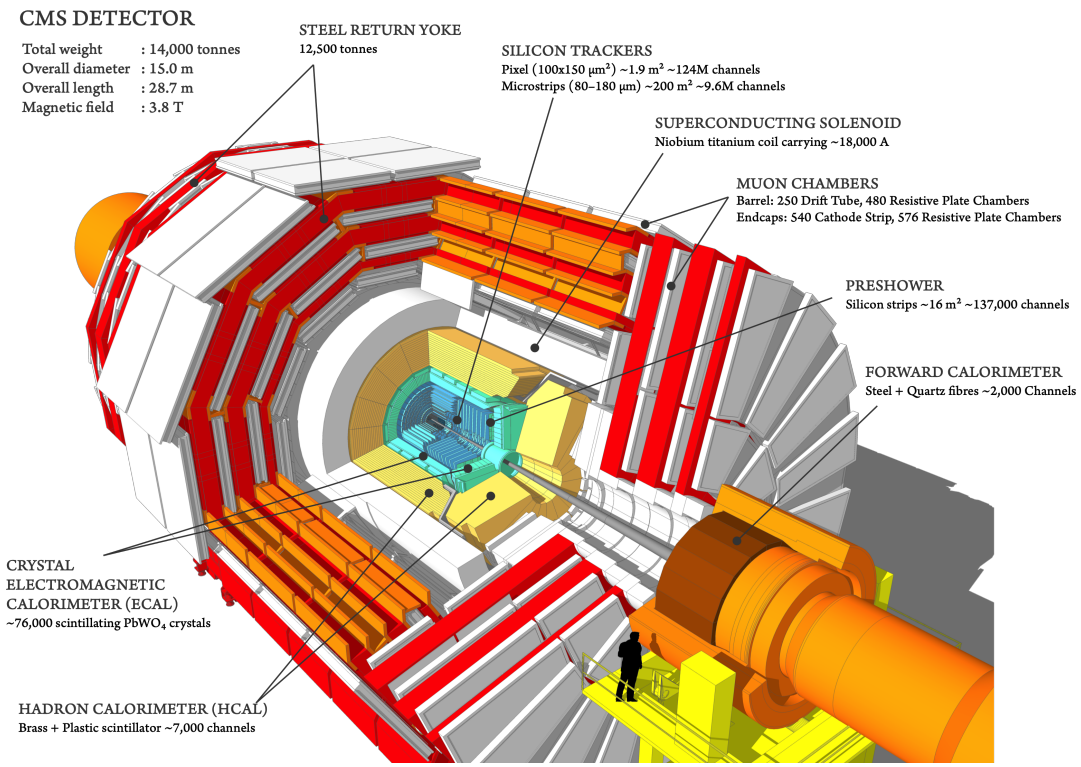

Figure 4.2.: Schematic drawing of the CMS detector. The detector is divided into the tracker, the electromagnetic and hadronic calorimeter and the muon chamber subsystems [HTA24].

The tracker is responsible for recording the spatial coordinates along the paths of charged particles interacting with its material. Based on the spatial points measured by the tracker, the trajectories of the particles can be reconstructed and their transverse momenta p_T can be determined using the relation

$$p_\mathrm{T} = qRB,$$

where q is the charge of the particle, R the trajectory radius and B the magnetic field strength applied by the solenoid magnet. Since the total transverse momentum p_T of a particle collision should be zero, measuring this quantity is of particular interest. Momentum conservation dictates that the p_T of the collision products should sum up to zero. A non-zero sum means that one or more particles could not be detected — a possible hint to neutrinos or dark matter candidates.

A layout of the current CMS Tracker is shown in Fig. 4.3. It is divided into a PIXEL detector and a Strip Tracker. The PIXEL detector is located closest to the collision point, which is why it is equipped with silicon pixel detectors that provide the best spatial resolution due to their high granularity, meaning a high density of readout channels. The original PIXEL detector has been replaced by the PIXEL Phase-1 detector in 2017, due to dynamic inefficiencies in the readout chips at high rates [CMS17]. The Strip Tracker is located further away from the collision point and is equipped with silicon strip detectors, which are less granular but cover a larger area. Tracker systems are divided into inner and outer barrel regions (TIB and TOB) and endcap (TID and TEC) regions, closing off the detector regions cylindrically in the respective detector region.

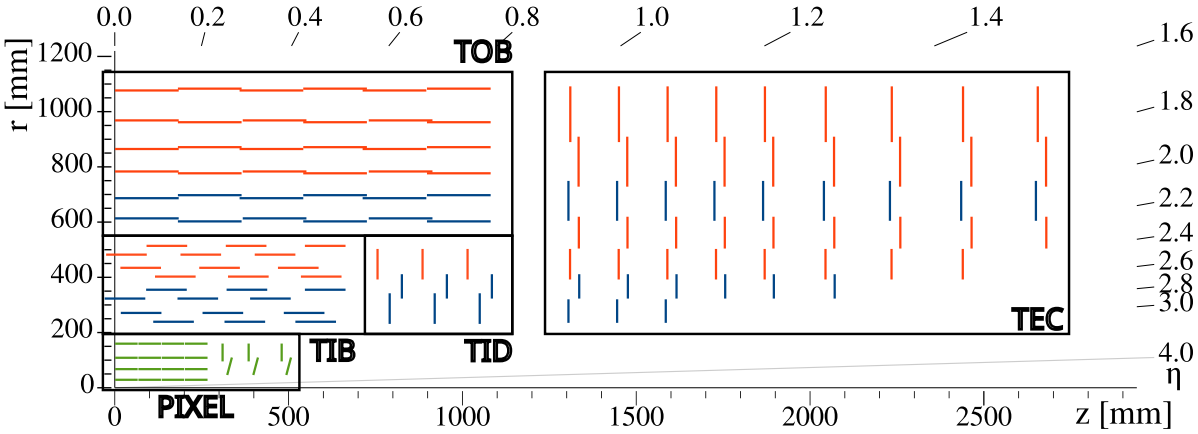

Figure 4.3.: Sketch of one quarter of the current CMS Tracker. Marked in the sketch are the PIXEL detector (green) and the Strip Tracker (TIB, TID, TOB, TEC). Single-sided modules are shown in red and double-sided modules in blue. Sketch adapted from [CMS08].

An important parameter in characterizing the kinematic parameter range within which particles are detectable is the pseudorapidity η. It is defined as

$$\eta = -\ln\left(\tan\left(\frac{\theta}{2}\right)\right),$$

where θ is the polar angle of the particle with respect to the beam axis. Moving in uniform steps of η, more or less the same number of particles are expected within each such step. However, since the pseudorapdity is a pseudorelativistic quantity, steps of high-η are more and more squished in the resting reference frame. Since more particles are squished into a smaller space, the rate as well as density of particles increases, ultimately driving the requirements on the tracker's rate capabilities and position resolution in this area of the detector. The current tracker layout allows for a maximum acceptance of $|\eta| \approx 2.5$ [CMS08].

This work focuses on the strip detectors of the future Outer Tracker, pending an upcoming upgrade, which will be introduced in the next section. Therefore, the following paragraph will give a brief overview of the strip detectors used in the current CMS Tracker.

The strip sensors used for the current Strip Tracker are single-sided p-on-n type silicon sensors, manufactured on 6-inch wafers to be as cost-efficient as possible. They vary in size and thickness, with the innermost layers having sensors with the smallest strip-to-strip distance (pitch) of 80 µm and the outermost layers having an average pitch of 184 µm. The thickness of the sensors is chosen to be (320 ± 20) µm for the inner parts of the Tracker and (500 ± 20) µm for the outer parts, while substrate resistivities vary between $\rho = 1.55\,\mathrm{k\Omega\,cm}$ to $8\,\mathrm{k\Omega\,cm}$, depending on the radial distance from the IP. The radial position with respect to the IP also leads to different sensor sizes and geometries. In total, 15 different sensor geometries across 24 244 sensors are used in the Strip Tracker. Bias voltages of up to +500 V are applied to the sensors. The sensors are built into modules, where each module contains either one sensor of 320 µm thickness in the inner parts or two sensors of 500 µm thickness in the outer parts. Depending on their position in the Tracker, 29 different module types are used, running at temperatures between $-10\,^{\circ}\mathrm{C}$ to $-25\,^{\circ}\mathrm{C}$ [CMS08].

The Tracker suffers from radiation damage over time, which degrades the performance of the sensors. At $500\,\mathrm{fb}^{-1}$, fluences of up to $\Phi_{\mathrm{eq}} = 1.8 \times 10^{14}\,\mathrm{cm}^{-2}$ for the inner parts of the Strip Tracker and $\Phi_{\mathrm{eq}} = 0.5 \times 10^{14}\,\mathrm{cm}^{-2}$ are projected for the outer parts [CMS08].

In order to process the large amount of data produced by the Tracker, a sophisticated trigger system is employed. The trigger system of the CMS experiment is divided into two parts: The Level-1 (L1) trigger and the High-Level Trigger (HLT). While the L1 trigger is hardware-based, the HLT is entirely software-based. The L1 trigger brings the throughput of detector data down from 40 MHz to 100 kHz by selecting events based on simple criteria, which can then be handled by the HLT [CMS08].

4.3. Upgrades of the LHC and CMS Outer Tracker (OT)

This section will discuss the upgrades of the LHC and CMS experiment. It should be noted that plans for the HL-LHC and the Phase-2 upgrade of the CMS experiment are still being developed and are subject to change. Since the focus of this work is on the production of silicon sensors for the Phase-2 upgrade of the CMS Outer Tracker (OT) and R&D projects for a future tracker, the following sections will only elaborate on the upgrades that are relevant to this work with the information available at the time of writing.

4.3.1. The High-Luminosity LHC (HL-LHC)

In order to increase the rate of events during runs, and thus, the likelihood of observing rare processes in a given time frame, the LHC will be upgraded to the HL-LHC [CER]. Pushing beyond the luminosity limitation of the current collider paves the way for pursuing new physics beyond the Standard Model of Particle Physics (SM) and advancing the understanding of the current SM itself, in particular flavor physics as well as precision measurements on the Higgs boson and Quantum-Chromodynamics (QCD) matter. It is foreseen to increase the nominal instantaneous luminosity of $10^{34}\,\mathrm{cm}^{-2}\,\mathrm{s}^{-1}$ to $\mathcal{L} = 7.5 \times 10^{34}\,\mathrm{cm}^{-2}\,\mathrm{s}^{-1}$. The increase in luminosity will be achieved by improvements of the low-β inner triplet magnets, cooling, and collimation systems; these improvements are described in detail in [Abe+20]. Other parts of the HL-LHC age over the time of its operation due to radiation damage and can be replaced at a later stage, giving the opportunity to increase the performance even further. The increase in luminosity will lead to a higher number of quasi-simultaneous interactions per bunch crossing, which are called *pileup* μ. After the upgrade, μ will increase from the current value of $\mu \approx 57$ to a nominal value of $\mu \approx 200$ [Abe+20].

The timeline for the entire LHC as well as HL-LHC project is shown in Figure 4.4. Runs are separated by maintenance and upgrade periods called *long shutdowns* (LS) or *technical stops*. Run 3 will continue until mid 2026, after which the LHC will enter LS3 for the HL-LHC upgrade. The HL-LHC is expected to start operation in 2030 and run until 2041, providing the LHC experiments with a total of up to $4000\,\mathrm{fb}^{-1}$ of integrated luminosity.

4.3.2. Phase-2 Upgrade of the CMS OT

At the end of Run 3, the current components of the CMS Tracker will have suffered from severe radiation damage and the tracker will need to be replaced in its entirety. With the upgrade to the HL-LHC during LS3, the CMS Tracker will therefore be upgraded to the Phase-2 Tracker to also cope with the increased requirements of the HL-LHC.

Due to the large increase in particle flux inside the detector, the Tracker will face amounts of radiation that are orders of magnitude higher than what it ever experienced before. Significantly higher radiation exposure in the Inner Tracker (IT) compared to the OT requires the IT to be fully accessible during regular maintenance periods. The OT, on the other hand, will not be accessible for maintenance during the HL-LHC operation. Therefore, the OT design needs to be

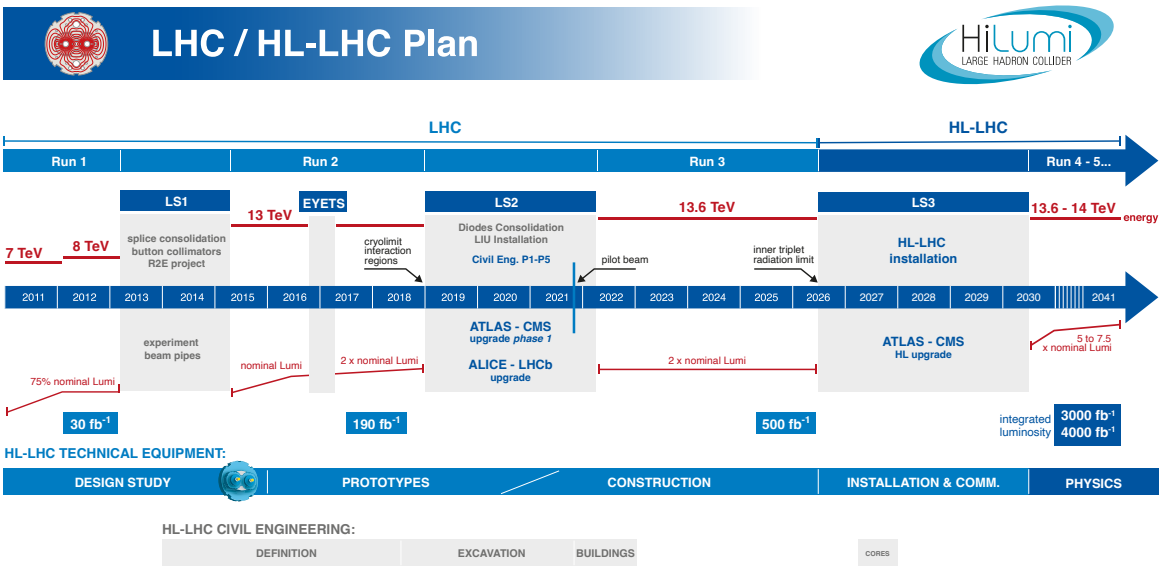

Figure 4.4.: The (HL)-LHC project timeline. The LHC is currently in its third run phase (Run 3) until mid 2026, pending the High-Luminosity LHC upgrade (HL-LHC) after Run 3 [CER].

radiation tolerant in order to prevail in the harsh radition environment of the HL-LHC [CMS17]. This aspect will be discussed in more detail in Section 4.3.3.

Furthermore, operation of the current CMS detector has shown that the material budget is too high and needs to be reduced to lower the impact of multiple scattering processes on global track reconstruction. This goal will be achieved in the Phase-2 Tracker even though the acceptance of the Tracker will be extended to $|\eta| \approx 4$ [CMS17].

With pileup rates of $\mu \approx 200$ during nominal operation, the Phase-2 Tracker will need to be more granular to maintain hit efficiency. Increasing the granularity will also effectively mitigate some effects of pileup, as the tracker will be able to resolve individual tracks more accurately. Other measures of pileup mitigation include the addition of timing layers to the Tracker, which will be discussed in Section 4.4.

Operating the Tracker at such high pileup rates will also render the L1 trigger system inefficient, since — at its current state — it will not be able to handle the increased data rates. The following section will discuss a sophisticated solution to this problem.

Tracker Design and the OT Module Concept

In Fig. 4.5, the layout of the upcoming Phase-2 Tracker is shown. The acceptance of the full Tracker will be extended to $|\eta| \approx 4$, as illustrated in the sketch. In great contrast to the current Tracker layout, the Phase-2 Outer Tracker will only use two types of sensor modules: *2S* and *PS* modules. An exploded view of both module types is shown in Fig. 4.6. Both module types use two back-to-back sensors, mounted on a single carrier. The sensors are spaced apart with spacer elements that are varying between 1.6 mm and 4 mm in thickness, to be used at different r from the beam line. While the 2S modules are composed of two silicon strip sensors with two banks of 1016 strips at a strip length of 4.8 cm, the PS modules consist of a *PS-s* strip

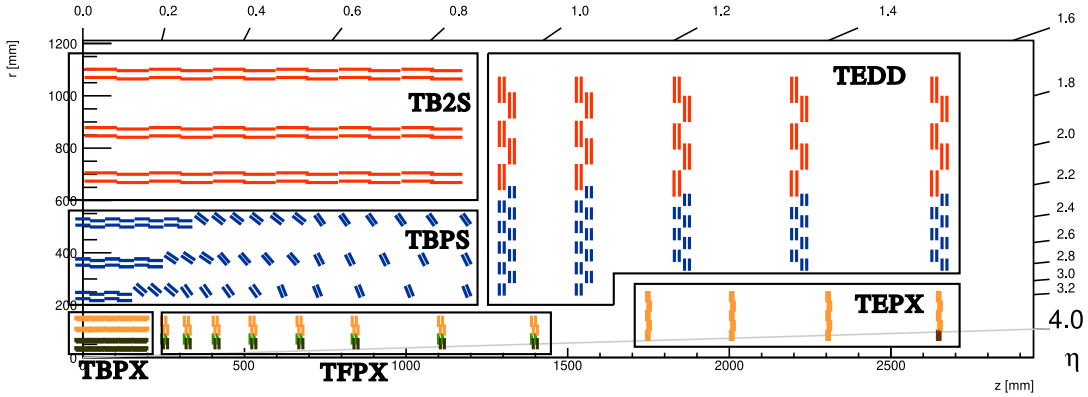

Figure 4.5.: $r\phi$-view of a quadrant of the Phase-2 Tracker. The IT is made up of the TBPX, TFPX and TEPX sections, while the OT consists of the TB2S, TBPS and TEDD sections. Details in main text. Sketch adapted from [CMS23b].

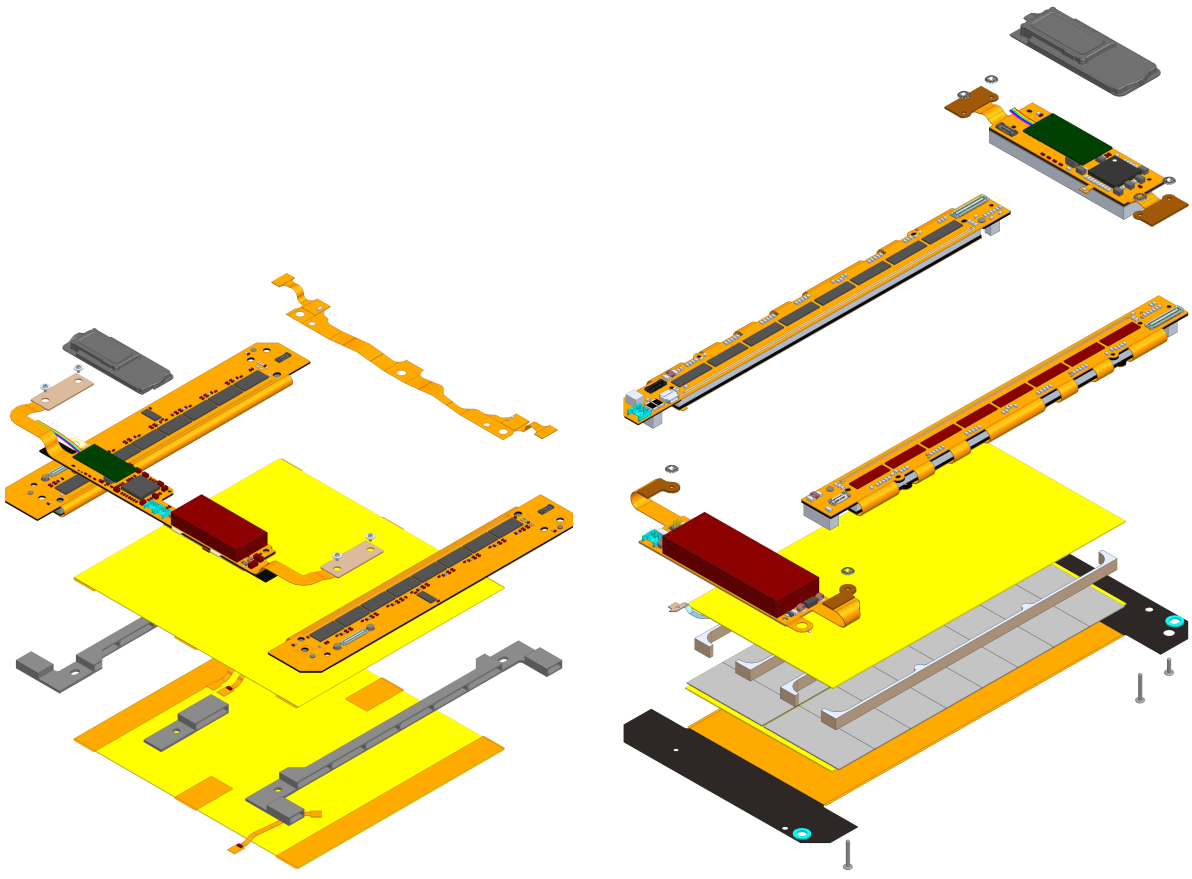

(a) 2S module **(b)** PS module

Figure 4.6.: The two module types used in the Phase-2 Tracker. In both, two sensors are closely spaced apart by spacer elements. Sketches modified from [CMS17].

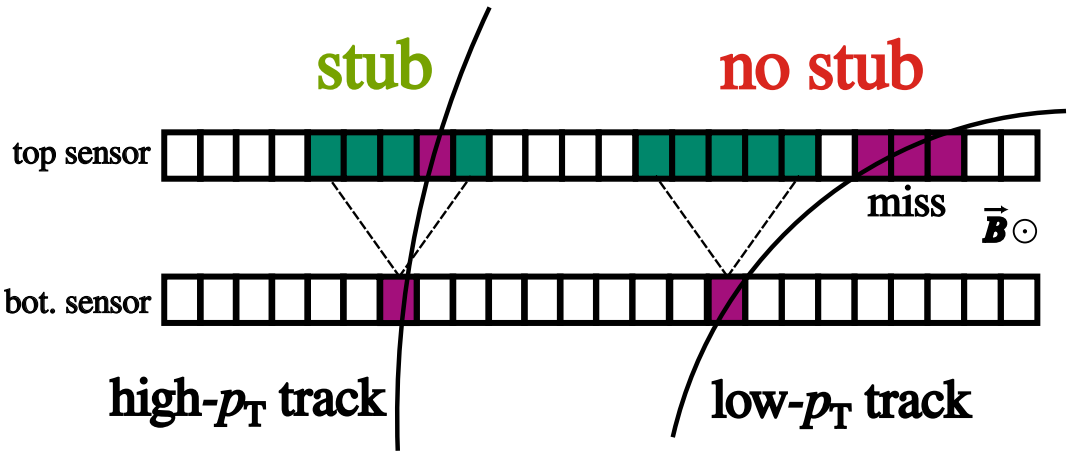

Figure 4.7.: Stub logic used in the p_T-module. The correlation of hits in the two sensor layers enables rejection of tracks with low p_T.

sensor and a *PS-p* macro-pixel sensor. The PS-s sensors, like 2S sensors, are segmented into two banks of 960 strips down the middle of the sensor and have a strip length of 2.3 cm.

Three sub-detectors are distinguished in the OT: the Tracker Barrel equipped with PS modules (TBPS), the Tracker Barrel equipped with 2S modules (TB2S), and the Tracker Endcap Double Discs (TEDD) equipped with both PS and 2S modules, depending on the radial distance from the luminous region. Almost all particles emerging from there must pass through at least six module layers up to $|\eta| = 2.4$ [CMS17].

Since the use of tracking information in the L1 Trigger system implies that self-selected data is sent out at every bunch crossing, the p_T-module concept has been developed [CMS17]. Both sensors in a module are connected to the same readout electronics performing a module-level algorithm called *stub finding*. It allows to pre-select data based on the transverse momentum of the particles and provide an input to the L1 trigger system directly, drastically reducing the data rate the trigger needs to handle and the module has to send out. This stub finding logic is illustrated in Fig. 4.7 and is based on the correlation of hits in the two sensor layers of a module. For the future physics event selection of the CMS experiment, only high p_T tracks are of interest. The stub logic rejects tracks with low p_T, by checking if the hit in the second sensor layer is within the expected stub window of the hit in the first sensor layer. If the hit is not within this window, the track very likely belonged to a particle with low p_T and is stored for readout at L1 acceptance. The stub window will be selected such that only particles with $p_T > 2$ GeV are accepted. This will result in a data volume reduction of one order of magnitude, which is sufficient for L1 Trigger handling [Con+15]. Inefficiencies in the stub finding logic are reduced by having a fraction of the PS modules in the TBPS be tilted towards the luminous region. Tilting the modules like this also saves on material, reducing the material budget of the Tracker. This clever arrangement ensures that particles with a shallow incident angle are less likely to traverse the gap between strip segmentations, a location where loss of stub efficiency would otherwise not be recoverable [CMS17].

Implementing this stub logic is only possible due to the high granularity of the Phase-2 Tracker, which is achieved by the use of smaller pitch sensors and a lower material budget, suppressing multiple scattering effects. With strip pitches of 90 µm for 2S sensors and strip/pixel pitches of 100 µm for PS-s/p sensors, the sensor pitch in the Phase-2 Tracker is smaller than in the current Tracker on average. The sensors are n-on-p type silicon sensors, shifting in technology from the current n-type sensors. As with the current Tracker, they are manufactured on 6-inch wafers, but compatibility with 8-inch wafers is maintained to remain flexible. They

have a resistivity exceeding 3 kΩ cm, ensuring that the full-depletion voltage remains below 300 V. Typical values for V_{dep} for the OT sensors lie between 230 and 250 V [Wit23]. In order to operate the sensors well over depletion, the operation voltage of the Phase-2 Tracker modules will be 600 V with a possibility to boost the operation voltage to 800 V should the charge collection performance suffer too severely due to radiation damage. Thanks to CO_2 cooling, module temperatures in the OT will be in the range of −20 °C to −35 °C, reducing the bulk leakage current and effectively preventing a thermal runaway. A deep-diffused float-zone process is used in sensor manufacturing that limits the physical thickness of 320 µm to an active thickness of 290 µm, limiting the active volume of the sensor while at the same time maintaining a thickness that is mechanically stable enough for handling and assembly. A number of 7680 2S modules (7256 with 1.8 mm-spacing, 424 with 4 mm-spacing) and 5616 PS modules (826 with 1.6 mm-spacing, 1462 with 2.6 mm-spacing, 3328 with 4 mm-spacing), amounting to 13 296 modules in total, will be used in the Phase-2 OT [CMS17]. The total material budget will be reduced to $x/X_0 \approx 0.8$ in the OT and $x/X_0 \approx 0.3$ in the IT[1], improving by a factor of two compared to the current Tracker [La 19].

The 2S modules are read out by two times eight CMS Binary Chips (CBCs) with data of each eight CBCs being merged by a Concentrator Integrated Circuit [CMS17]. The PS modules are read out by a Short-Strip ASIC, reading out the PS-s sensors and a Macro-Pixel ASIC reading out the PS-p sensors [CMS17]. Simulations for the p_{T}-module readout electronics including the whole readout chain, considering also the strip capacitances, show that the average noise levels of these readout chains are expected at ENCs of

$$\sigma_{\text{2S}} = 1000\,\text{electrons and } \sigma_{\text{PS-s}} = 800\,\text{electrons}, \tag{4.1}$$

for both module types, respectively [CMS17]. This will be an important quantity to determine the necessary signal height for the readout electronics to be able to distinguish between signal and noise later on in this work.

4.3.3. The Radiation Environment in Phase-2

As mentioned in the previous chapter, with the increase in luminosity, the CMS Experiment will be exposed to significantly higher radiation levels than ever before. The radiation environment that is expected during operation of the Phase-2 Tracker can be estimated in simulations with the FLUKA software framework [Fer+05; CMS23a]. Simulated radiation fluence and ionizing dose distributions in the Phase-2 Tracker at 4000 fb^{-1} are shown in Fig. 4.8 and Fig. 4.9, respectively. For each module in the Tracker, the FLUKA simulation code simulates the NIEL fluence as well as TID at all four corners of the module [CMS23a]. The radiation environment at a proton-proton machine such as the LHC is largely dominated by neutrons, protons and charged pions. At low r, the NIEL fluence is dominated by charged pions and protons, while at high r, the fluence is dominated by neutrons. Additionally, neutrons are scattered back from the calorimeters, contributing to the fluence at high r. As visible in the fluence distributions, the maximum fluences seen in the OT exceed the fluences seen in the current Tracker by several orders of magnitude, which is why CMS needs sensors that are highly radiation-tolerant. This is especially important for the OT due to its inaccessibility during the 10-year HL-LHC operation period. As outlined in Section 4.3.1, maintenance periods are foreseen at the end of every year over the 10-year operation duration of the Phase-2 OT. These maintenance periods would approximately take two weeks, which amounts to 20 weeks over the whole tracker lifetime. There is a good chance that the OT could be annealed at room temperature for these periods. As explained in Section 3.3, the amount that a silicon detector is annealed needs to be closely

[1] This, of course, also depends on the exact η of a track.

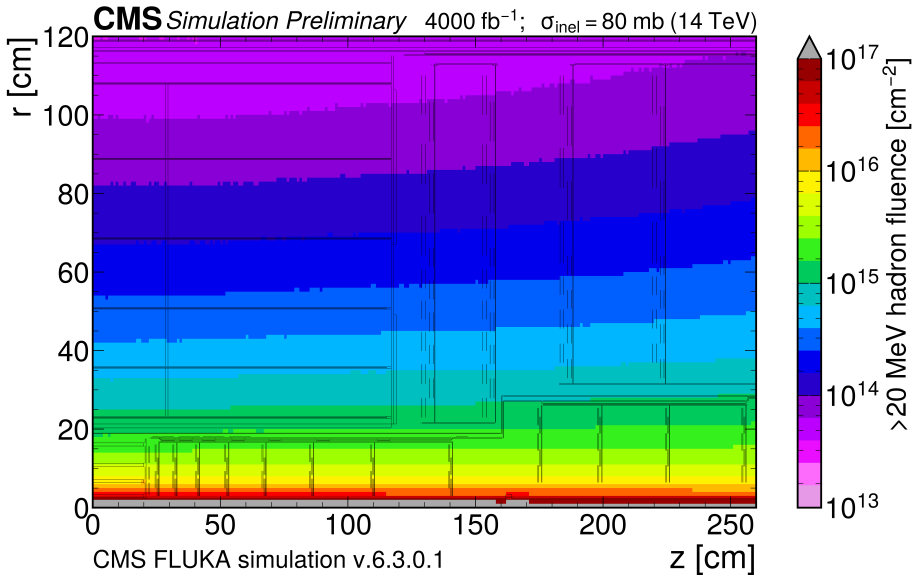

Figure 4.8.: Expected radiation fluence distribution in the CMS Phase-2 Tracker at 4000 fb^{-1} [FLU].

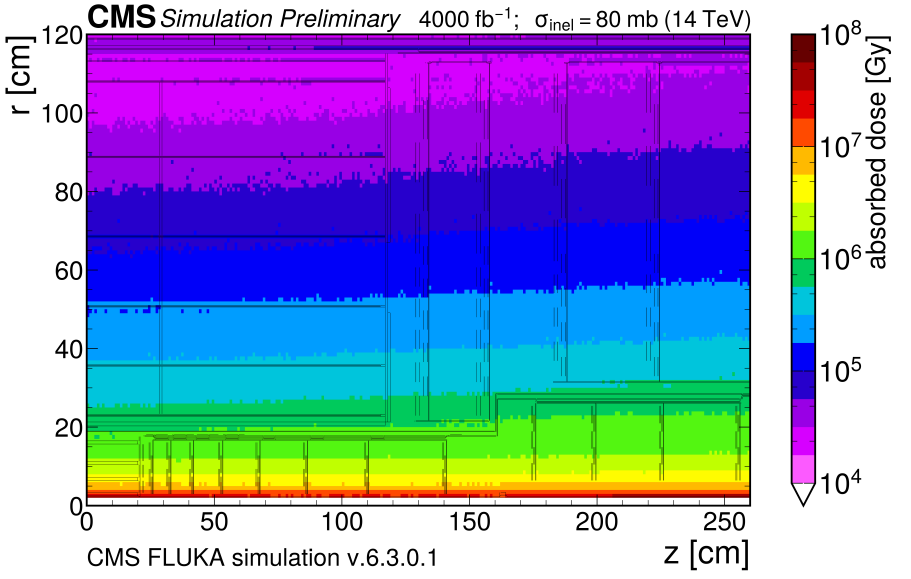

Figure 4.9.: Expected ionizing dose distribution in the CMS Phase-2 Tracker at 4000 fb^{-1} [FLU].

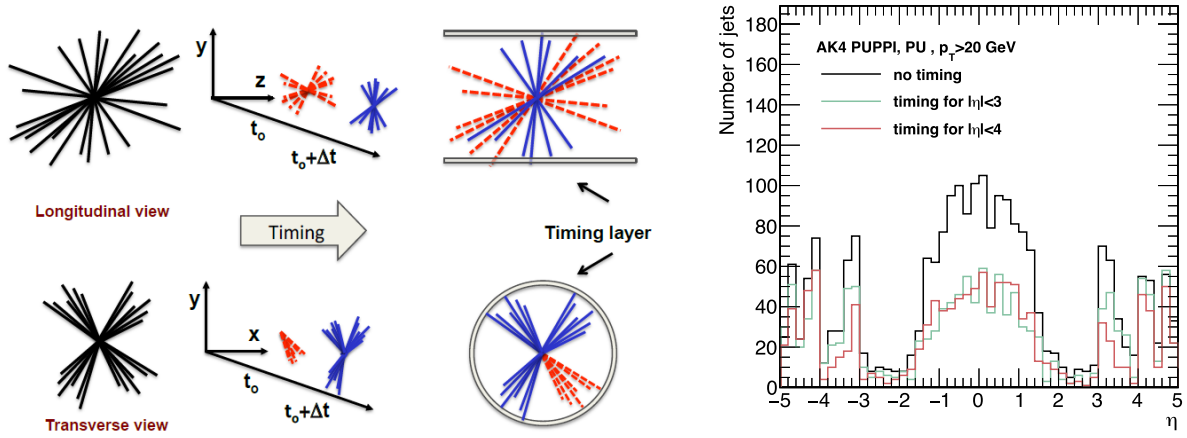

(a) (b)

Figure 4.10.: (a): Concept of how a timing detector in the CMS experiment would help in mitigation of pileup [Men23]. (b): Simulation of pileup jet suppression with timing detectors up to $|\eta| \approx 4$ [Alb22].

monitored since the charge collection efficiency is highly dependent on this effect. Annealing sensor radiation damage within the regime of beneficial annealing could, indeed, boost the charge collection efficiency but in the case that the sensors anneal for too long, reverse annealing effects could be detrimental to sensor performance. Therefore, understanding the annealing behavior is a topic of utmost importance for the operation of sensors in the Tracker.

4.4. Timing Detectors for Future Applications

As previously mentioned, the CMS experiment will face unprecented pileup rates during the HL-LHC era. While the current proposal for the Phase-2 detector maintains the current performance and even improves upon it in efficiency, resolution and background rejection by implementing concepts such as the p_T-module concept and the particle-flow reconstruction method [Sir+17], the pileup rates will still be a challenge for the experiment. While increasing the granularity of the Tracker will certainly be able to mitigate some of the effects of pileup, it will not be able to resolve all of them. However, implementing a sensor layer that is able to measure the time of arrival of particles would be a valuable addition to the CMS experiment in that regard. Figure 4.10a illustrates how a timing detector would aid in mitigation of pileup effects. By measuring the time of arrival of particles in the timing layer witha resolution of about 30 ps, it would be possible to assign a time stamp to each particle track [The17]. Slicing the pileup contributions into time slices of this resolution would drop the pileup vertices of the HL-LHC down to pileup levels of the current LHC [The17]. Therefore, the detector mostly would be able to assign particles to the correct pileup vertex. Figure 4.10b shows a simulation of the number of pileup jets as a function of pseudorapidity. Implementation of one timing layer in the CMS Tracker would greatly suppress the number of pileup jets, especially at low $|\eta|$, as shown in the simulation. The MIP Timing Detector (MTD) [The17] will be included as a timing layer in the CMS detector during the Phase-2 era [CMS19]. The MTD will be placed in the endcap and barrel regions between the Tracker and calorimeters.

While this new subdetector will be able to assign a time stamp to most of the tracks after track finding has been executed, CMS would still greatly benefit from including timing information in the Tracker itself. Like this, a time stamp for each hit in the Tracker would be available,

which would allow for a more accurate track reconstruction and pileup mitigation even on a track-finder level. This would greatly reduce the number of possible track combinatorics, fast-tracking reconstruction. Using this method would enable 4D tracking capabilities, giving an input to the HLT on a track-finding level. In order to use these detectors in future 4D tracking applications, they would need to comply with the same requirements as the other components in the Tracker, such as radiation tolerance, low material budget and high granularity/hit resolution to be able to distinguish between primary and secondary vertices of short-lived particles. For excellent timing capabilities, these detectors also need to have a high time resolution, which is a challenging task for silicon sensors due to many sources of noise. 4D tracking is a topic of high interest for future colliders such as FCC-ee for time-of-flight measurements or a future hadron machine with even more pileup. This topic will be disscussed in Part Two of this work, where the R&D on cutting edge silicon sensors for future applications will be presented.

5
Facilities and Software

During the course of this work, many different setups and facilities were used, to either measure or irradiate the investigated silicon sensors. While some of these setups worked well for small campaigns with a limited number of samples, scalability and reliability became a serious issue for larger and more complex projects like the ones presented in this work. Some of the setups described in the following sections were developed from scratch or rebuilt from existing setups to improve them regarding the aforementioned aspects.

5.1. Measurement Setups

In the following sections, the measurement setups located at the Institute of Experimental Particle Physics (ETP) of the Karlsruhe Institute of Technology (KIT) that were used in this work are described. Three measurement setups were used in total: the probe station, the ALiBaVa setup, and the TCT setup. An existing ALiBaVa setup was already available at the beginning of this work, but needed to be refurbished due to unreliable temperature measurements and controls. The TCT setup was built as part of this thesis from scratch for the R&D work that will be presented later on, as no TCT setup was available at ETP at the beginning of this work.

5.1.1. The Probe Station

The probe station is a setup that is used for electrical characterizations of silicon sensors. Out of the two probe stations available at ETP, one was used, exclusively, for the measurements presented in this work, to exclude any setup-related uncertainties. Figure 5.1 shows the custom-made probe station and its components. Measurements in the probe station are performed by contacting the device under test (DUT) with a set of needles. The probe station is equipped with a microscope camera that is used to view the contact pads of the sensor and the needles. At the heart of the station a flat aluminum sensor chuck is located on which the DUT is placed. Vacuum holes in the chuck secure the sensor in place. The sensor chuck is mounted on a stepper motor stage on three axes that allows for precise positioning of the DUT. The station has a two-stage cooling concept. Primary cooling or heating is achieved by four thermoelectric elements that are located right underneath the sensor chuck. By adjusting the electric power supplied to the primary cooling elements, the temperature of the sensor chuck can be controlled. A liquid pre-cooling system on the other side of these elements removes the excess heat from them. The chuck temperature at two points as well as the pre-cooling inlet and outlet temperature are monitored. By averaging the two chuck temperatures, the temperature of the sensor is determined and primary cooling power is controlled by a PID[1] controller that uses this temperature as a setpoint.

[1] short for: **P**roportional, **I**ntegral, **D**erivative, referring to coefficients used in the feedback-based control loop algorithm

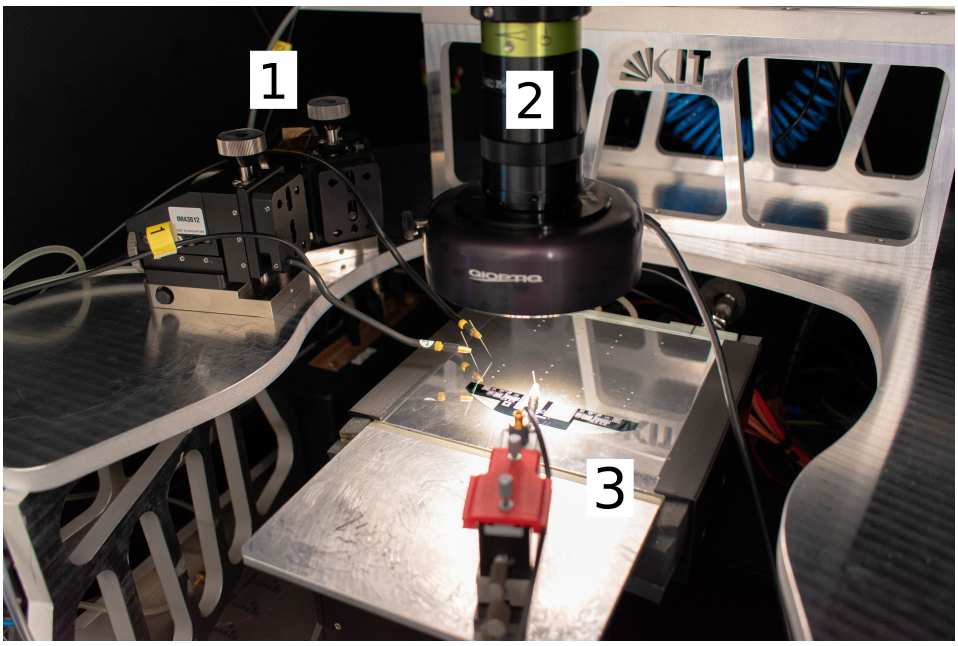

Figure 5.1.: The Probe Station used for the measurements in this work with (1) strip needle holders, (2) microscope camera and (3) the bias needle holder.

Measurements in this work were performed with three needles at most. All needles are connected to a switching matrix that is responsible for the connection of the needles to different measurement devices. Depending on the measurement programmed by the user, the switching matrix connects the DUT to all necessary devices. In order to apply a bias voltage to the DUT, a *bias needle* is used as a grounding contact that is placed on a ledge galvanically isolated from the chuck but moving with it. The aluminum chuck itself provides high voltage to the sensor from its backside. Needles can be used in scans across the sensor pads by placing them on a separate ledge that is stationary. The movable sensor chuck then moves the sensor under these *strip needles* at a safe distance, which entails that the needles are not in contact with the sensor when the chuck is moving.

The whole setup is enclosed by a light-tight aluminum box, shielding the setup from electromagnetic interference, that is flushed with dry air to prevent condensation. The box is placed on a vibration-isolated table to prevent external vibrations from affecting the measurements. In order to control the measurement devices, cooling, and the stepper motor stage, the MeasurementControl software is used, which will be described in Section 5.3.1.

5.1.2. The ALiBaVa Setup

The ALiBaVa (**A Li**verpool, **Ba**rcelona and **Va**lencia) setup is a setup that is used to characterize the charge collection properties of silicon strip sensors. The full setup is based on the ALiBaVa system [ALi] that is built around the LHCb Beetle chip [LS06] as its critical component.

The Full Setup

The full ALiBaVa setup at KIT houses an ALiBaVa board, shown in Fig. 5.2, that the DUT with the readout board is mounted on. The ALiBaVa board is screwed onto a copper cooling bridge that uses a two-stage cooling concept like the probe station from the previous section, only with two instead of four thermoelectric elements for primary cooling. Temperature sensors

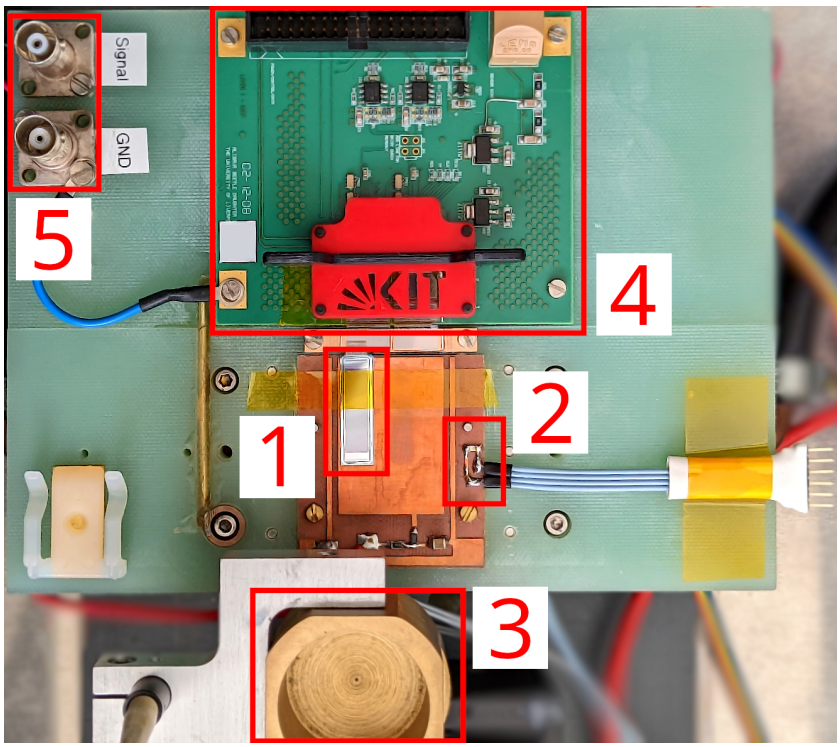

Figure 5.2.: The ALiBaVa board with (1) DUT, (2) temperature sensor, (3) movable source collimator, (4) daughter board (5) HV and ground connectors.

are located nearby the sensor, on the upper side of the cooling bridge and at the in- and outlet of the liquid pre-cooling stage. A PID controller is employed for temperature regulation that gets the first temperature sensor reading as an input and controls the primary cooling power. The DUT on the ALiBaVa board is mounted on a copper sheet that also contains an RC-filter for powerline noise suppression. polyimide tape secures the sensor in place. Wire bonds are used to connect the sensor to ground and to connect the strips via fan-outs with the channels of the readout chip. Biasing is done from the backside of the sensor with the copper jig and grounding from the front side with a wire bond.

In order to measure the charge collection properties of the sensor, test MIPs (minimally ionizing particles) are shot into the sensor and the charge collected by the strips is measured. For this setup, test particles are provided by a Sr-90 source that is placed inside a movable source collimator with an opening of 0.5 mm aligned with the sensor. This isotope decays into Y-90 with a half-life of 28.8 years, emitting beta particles with a maximum energy of 546 keV. The daughter isotope Y-90 decays into stable Zr-90 with a half-life of 64 hours, emitting beta particles with a maximum energy of 2.3 MeV, which are the MIPs used in this setup. Low energetic beta particles from the Sr-90 decay are absorbed by the DUT and the copper jig, so that only the Y-90 MIPs are detected with a scintillation counter underneath the copper jig that is used to trigger the readout chip.

The whole setup is placed in a light-tight box that is flushed with dry air to prevent condensation. Placement in this metal box shields the setup from electromagnetic interference at the same time.

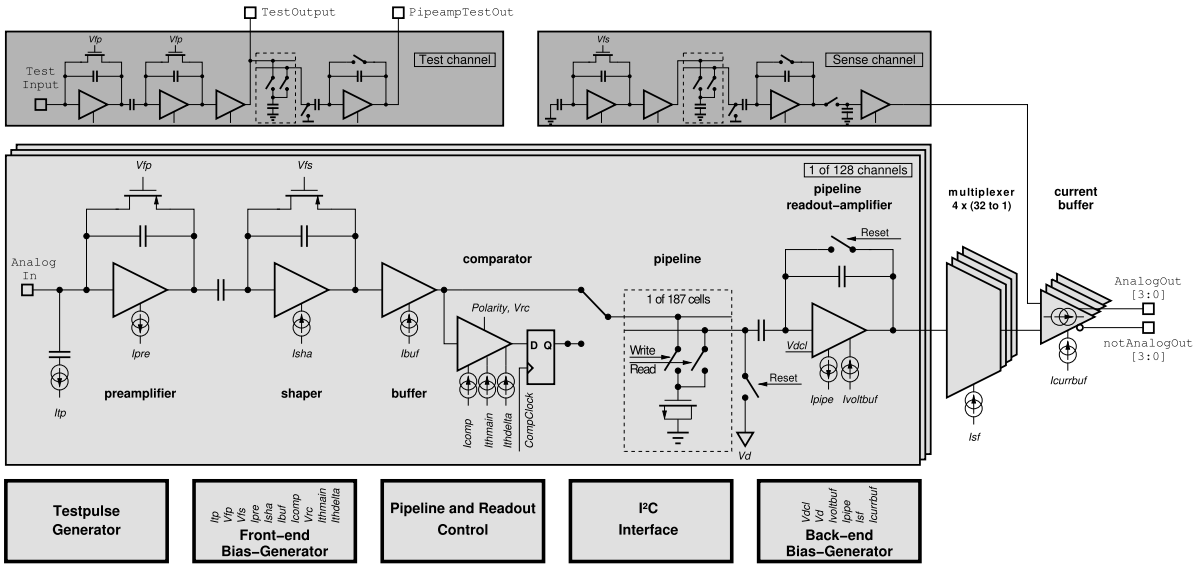

Figure 5.3.: Schematic diagram of the main parts of the Beetle readout front-end. Schematic adapted from [LS06].

The Beetle Chip

The readout front-end of the ALiBaVa system is the Beetle chip that was originally developed for the LHCb experiment at CERN. In order to understand how to ALiBaVa system operates, a deeper look at the inner workings of the Beetle chip is necessary. Part of its schematic diagram is shown in Fig. 5.3. The chip implements 128 bipolar channels, each integrating a low-noise charge-sensitive amplifier, shaper and buffer. The shaper output is sampled at 40 MHz into an analog ring buffer with 160 sampling intervals of programmable 25 ns-latency steps. For all measurements in this work, the latency was set to the same value that was obtained by reference measurements conducted prior to data-taking. Each channel has its own charge injector circuit with adjustable amplitude for calibration and testing purposes. A dummy channel is used to account for common-mode noise and to provide a reference signal for the pedestal correction (explained in Section 5.3.5), internally [LS06].

While the chip can be operated in analog or binary mode, only the analog mode was used in this work and ADC values were converted to electron counts for each channel using the charge injection capabilities (discussed later). Internal test pulses are injected into the channels alternating the polarity for each neighboring channel to account for polarity-dependent effects. The Beetle chip uses triple-redundant logic to ensure data integrity against single-event upsets [LS06].

The ALiBaVa System

The ALiBaVa system is a multi-purpose system that can be used to characterize silicon strip sensors. The system is based on the LHCb Beetle chip that was described in the previous section and consists of two parts: the mother board and the daughter board. The daughter board is screwed on the KIT-ALiBaVa board as shown in Fig. 5.2 and contains the biasing and filtering circuitry and, of course, the Beetle chip. The mother board is connected to the daughter board via a flat ribbon cable and digitizes the analog data from the daughter board. It also processes the trigger signals and programs the daughter board. The mother board is connected to a PC via USB and controlled with proprietary software provided by the ALiBaVa

collaboration. The software allows for the configuration of the Beetle chip, the mother board and the daughter board.

The ALiBaVa system was designed to operate in two measurement modes: laser and source mode, but only the source mode was used in this work. Three run modes are relevant for the source mode measurements: *pedestal*, *calibration* and *radioactive source* (RS) mode.

- In **pedestal mode**, random triggers generated internally by the mother board are sent to the daughter board and (mostly) noise events are recorded. This produces events with values varying around the baseline of each channel to obtain the noise N as well as the baseline ADC value P, which is called *pedestal*.

- In **calibration mode**, the internal charge injection circuitry of the Beetle chip is used to inject a certain known charge into each channel. The ADC values of each channel are recorded and the conversion factor from ADC to electrons is calculated, which is called the *gain* G. Calibration runs can be performed either as charge scans or delay scans. While a charge scan injects a variable charge into the channels, a delay scan injects a fixed charge into the channels with a variable readout delay after the charge injection. This yields the ADC value as a function of the injected charge or the readout delay, respectively. In a charge scan, the gain is calculated as the slope of the linear fit of the ADC values as a function of the injected charge. In a delay scan, the ADC value peaks at a certain delay ($\rightarrow \mathrm{ADC}_{\mathrm{max}}$), which is the optimal readout delay and at the same time yields the gain value for this channel by

  $$G(i) = \frac{15\,000 \text{ electrons}}{\mathrm{ADC}_{\mathrm{max}}}.$$

  For all measurements in this work, delay scans were used.

- In **radioactive source mode**, the source collimator is placed on top of the sensor and the source generates MIPs that traverse the sensor, creating the signal, and are detected by the trigger scintillator underneath, sending a trigger signal to the mother board. A latency that takes into account the geometrical distance between the trigger and the sensor, as well as the trigger signal propagation time, is set in the mother board, as established in the previous section. For all measurements in this work, 100 000 events were recorded in radioactive source mode.

Analysis of the ALiBaVa data is done with the ALiBaVa analysis software that will be described in Section 5.3.5.

5.1.3. The TCT Setup

In the following sections, a setup will be described that uses the transient current technique (TCT) to measure the charge collection properties of LGAD devices. The setup needed to be built from scratch, as no TCT setup was available at ETP at the beginning of this work. Therefore, extended calibration and commissioning procedures were necessary to ensure the reliability of the setup, which will also be described.

The Setup

The setup was built in the same box as the ALiBaVa setup described in the previous section while utmost care was taken to keep both setups operable at the same time with only minor adjustments. The idea behind the TCT setup is to inject a short laser pulse into the sensor at a specific location and measure the time-resolved voltage signal that is generated by the charge

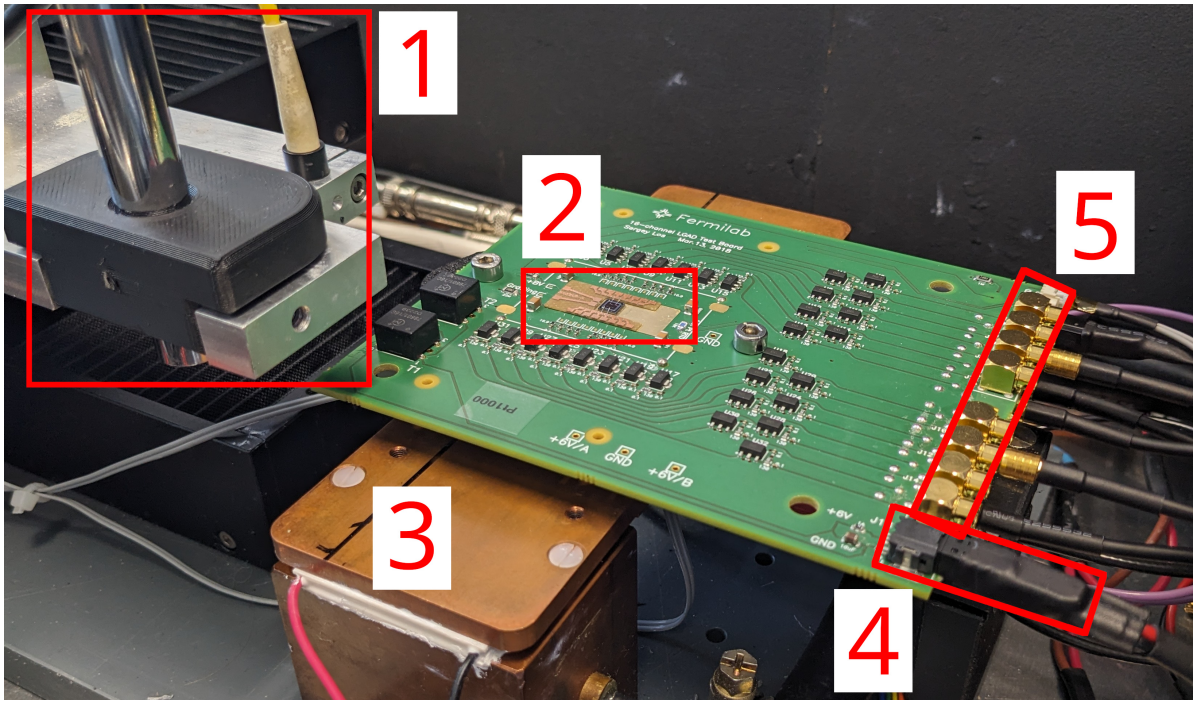

Figure 5.4.: The TCT setup at ETP with (1) movable camera and laser, (2) bonding adapter with DUT, (3) cooling bridge, (4) FNAL board LV and (5) 16 channel outputs. Underneath the FNAL board, the custom-made cooling adaptation is mounted on the cooling bridge, out of view in this picture.

carriers that are created by the laser pulse. The analog voltage signal is amplified with an amplifier board, outputting to a digitizer that samples the signal at a high rate. The digitized signal is then analyzed to extract the charge collection properties of the sensor. Figure 5.4 shows the setup in the ALiBaVa box.

For the laser signal, a laser system consisting of a laser pulse generator, a laser head and focusing optics is used. This system is capable of generating laser pulses with a pulse width of 40 ps at a wavelength of 1055 nm. The pulse frequency of the generator is adjustable up to 1 MHz but for all measurements in this work, a frequency of 100 kHz was used since that is the minimum frequency required to exhaust the speed of the digitizer. Since the samples investigated with the TCT setup in this work are 350 µm in physical thickness, as explained in Section 2.4.3, a laser at this wavelength penetrates the sample entirely and creates a uniform charge distribution in the sensor. The laser is focused onto the sensor with a lens that is mounted on the movable stage. A laser attenuator is used along the glass fiber path from the generator to the focusing optics to adjust the laser intensity. A microscope camera is mounted next to the laser optics with a line-of-sight that is offset by a known distance (measured with a vernier caliper) from the laser beam. Both the laser and the camera look down onto the sensor in a perpendicular fashion. The camera is used to align the sensor with the laser beam. Both the camera and the laser are mounted on a movable, three-axis stepper motor stage that is used to move the laser spot across the sensor, also used at the ALiBaVa setup. Laser focus is adjusted by moving the sensor up and down with the stepper motor stage. This focussing procedure will be described in Section 5.1.3.

The readout board used in this setup is a 16-channel amplifier board made by Fermilab (FNAL) and was originally built for general LGAD R&D purposes, called *FNAL board* in the following. The bias voltage at the LV input of the board providing necessary power to the

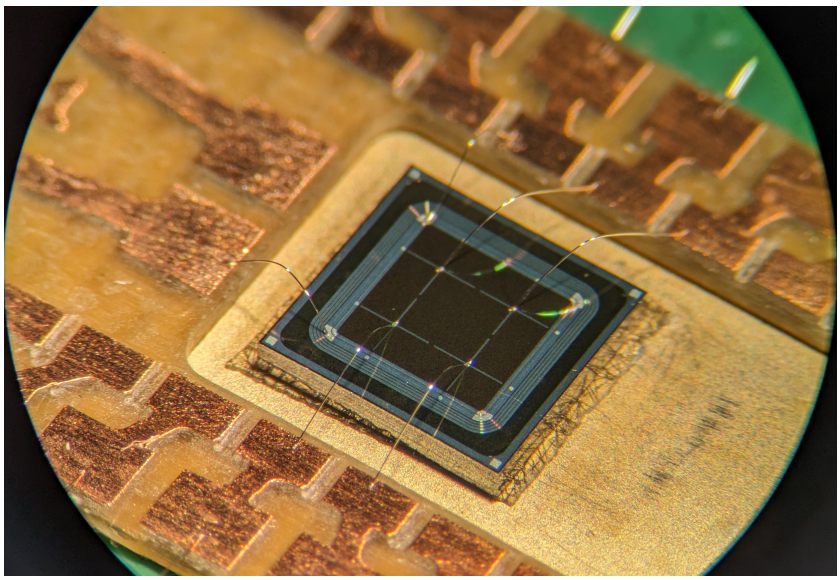

Figure 5.5.: LGAD sensor wire-bonded to the copper pads of the bonding adaptation as seen through a microscope.

amplifier circuitry was adjusted such that the board drew a current of 540 mA at all times. This ensured that the board was always in the same operating state and amplified the signal with the same gain. The board has an HV input with an on-board RC filter that is used to bias the sensor, filtering out noise from the powerline. The sensor is placed on the gold-plated sensor area of the board using double-sided conductive tape and wire bonds are used to connect the sensor to the board. Sensor bias is provided from the backside through the tape and grounding is done with a wire bond from the front side. Due to the small size of the samples investigated in this work, a custom-made bonding adapter was used to bond the sensor to the FNAL board, which is shown in Fig. 5.5. This bonding adapter serves as a mechanical interface between the sensor and the FNAL board bonding pads, bridging part of the distance between the sensor and the board pads and, thus, reducing the wire length of each individual bond. This made bonding possible with the semiautomatic wire bonder available at ETP. The digitizer that was used is a CAEN DT5742 with 16 channels and a sampling rate of 5 GHz [CAE].

Since irradiated samples were investigated using this setup, the sensors needed to be cooled to avoid annealing. By using the same experiment box as the ALiBaVa setup, the cooling bridge was already in place and could be reused for the TCT setup. However, a custom-made adapter connecting the cooling bridge to the FNAL board was necessary to cool the sensor and hold the board in place. Four temperature sensors were used, three of which were already present on the cooling bridge. The fourth temperature sensor was placed on the FNAL board to monitor the temperature of the board and provide a proxy for the sensor temperature. A dedicated calibration procedure was necessary to correlate the temperature sensor readings to the actual temperature of the sensor and will be presented in the following section.

Temperature Calibration

Since the gain of an LGAD as well as the leakage current are strongly temperature-dependent, it is crucial to know the temperature of the sensor during measurements. As outlined previously, four temperature sensors were used to monitor the temperatures of the setup: one on the liquid pre-cooling inlet, one on the outlet, one on the top side of the copper cooling bridge and one on the FNAL board. Since the on-board temperature sensor on the FNAL board is

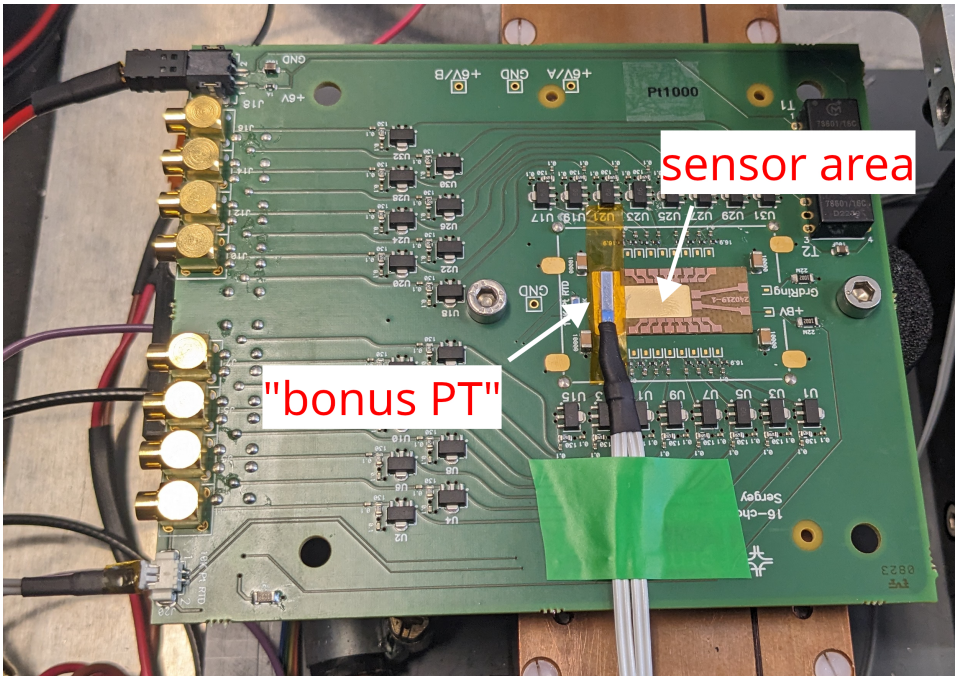

Figure 5.6.: Measurement setup for the temperature calibration. The *bonus PT* is glued on a piece of polyimide tape, which is taped to the sensor area to avoid remnants when removing the bonus PT while, at the same time, providing a good contact.

surrounded by PCB material which has bad thermal conductivity, it is not suited to measure the temperature of the DUT that is mounted on the gold-plated sensor area of the board accurately. However, if the difference ΔT between the on-board temperature sensor and the sensor area temperature is known, the on-board temperature sensor can be used as a proxy for the sensor area temperature. In order to determine this difference, a different temperature sensor was used to measure the temperature of the sensor area directly and read the on-board temperature sensor at the same time while the setup was put into various configurations that have an influence on the temperature. This additional temperature sensor will be called *bonus PT* for the remainder of this section. The measurement setup is shown in Fig. 5.6. The normal operation point of the setup while measuring irradiated samples was chosen as the reference point and the preferred measurement temperature on the sensor was $-20\,°\mathrm{C}$, initially. Possible sources that generate heat in the setup are the dissipated power of the FNAL board and the dry air that is flushed into the box, while heat is removed from the setup by means of cooling. Therefore, different configurations for these sources of influence were tested during the procedure. The setup temperature is controlled by setting a temperature T_{bridge} on the cooling bridge, which the software PID controller uses as a control point. A set temperature T_{bridge} was set and the temperatures of the bonus PT, T_{bonus}, and the on-board temperature sensor, T_{board}, were recorded. Table 5.1 shows the results obtained with this procedure. As expected, both setting the dry air inflow to the maximum level as well as biasing the FNAL board increased the temperature in the system. To combat the temperature increase from the dry air inflow, the flow rate was adjusted to a setting that would keep the dew point just low enough (with a margin) to carry out measurements without condensation. During the procedure, the minimum temperature that could be adjusted with the cooling system was $-19.9\,°\mathrm{C}$ on the bonus PT and, thus, the sensor area. However, operating the thermoelectric elements at their maximum power for a longer time is not recommended, as it might damage the elements and accelerate the aging of the setup, tremendously. Therefore, a measurement

Table 5.1.: Results of the temperature calibration procedure for different configurations of the dry air flow c_{flow}, set temperature on the cooling bridge T_{bridge} and power state of the FNAL board c_{FNAL}. The lower row setup was used for all measurements.

c_{flow}	c_{FNAL}	T_{bridge}	T_{board} (°C)	T_{bonus} (°C)	ΔT
OFF	OFF	-	11.6	9.2	2.4
HIGH	OFF	-	12.2	10.4	1.8
LOW	OFF	−19.7	−9.2	−16.3	7.1
LOW	ON	−26.4	−7.6	−19.9	12.3
LOW	ON	−22.9	−5.2	−16.7	11.5

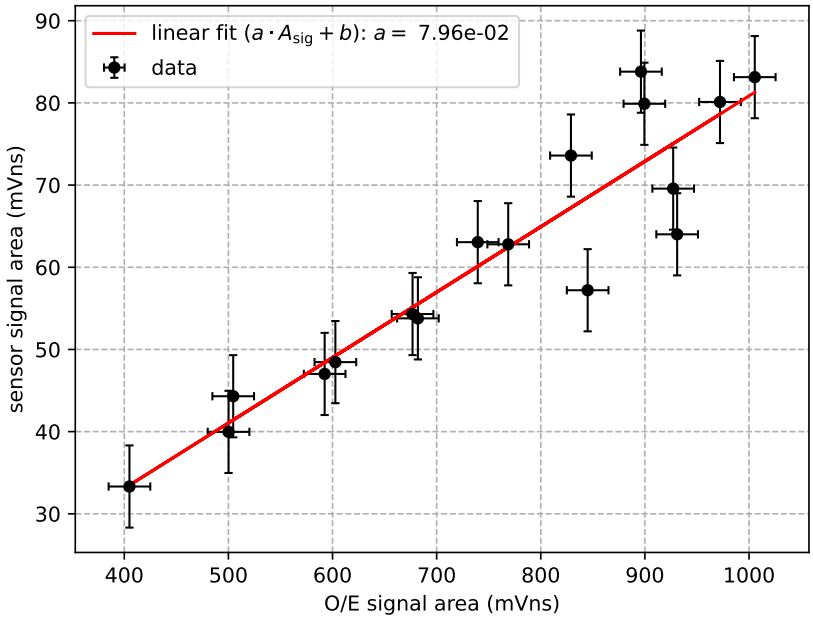

Figure 5.7.: LGAD sensor signal as a function of the O/E converter diode signal. An operation point of 850 mV ns was chosen for all measurements in this thesis.

temperature of $\approx -16.7\,^{\circ}\text{C}$ was chosen for the TCT measurements presented in this work. The difference of the on-board temperature sensor and the bonus PT lies at 11.5 °C for this configuration and was used to correct the on-board temperature sensor readings to the sensor area temperature. Empirical evidence gathered during the measurements showed that the breakdown voltage of the irradiated samples indeed was sensitive to even small temperature changes of one to two centigrade around this value. Although a lower temperature would have been preferred to push the breakdown voltage of the irradiated samples towards higher values, the chosen temperature was a compromise between the desired temperature and the maximum power that the thermoelectric elements should be operated at. Annealing effects should be mostly frozen out at this temperature.

Intensity Calibration

Gain quenching in LGADs is a phenomenon that occurs for large charge densities created by high energy deposition in the sensor. The generated charges produce an electric field that opposes the field in the multiplication region, effectively reducing the gain of the sensor. This

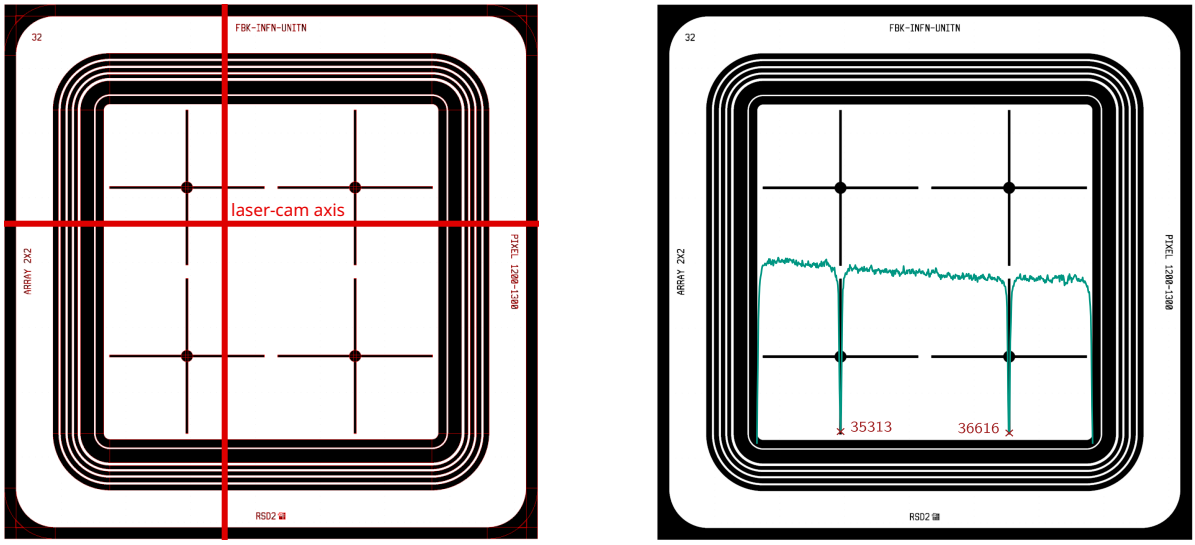

(a) **(b)**

Figure 5.8.: Concept of the position calibration. (a) The laser spot is moved across each direction over the sensor indicated by red lines, crossing aluminum pads along its way and producing dips in the signal. The axis on which both the camera and laser optics are mounted is marked as *laser-cam axis* and (b) the signal along this laser-cam axis is overlayed with the sensor layout. Dips in the signal are marked with crosses and the dip positions are annotated with the corresponding position with respect to the motor stage coordinate system.

effect leads to a gain saturation that is dependent on the charge density [Car24]. To reduce the influence of LGAD gain quenching by selecting a laser intensity that is too high, a calibration procedure was necessary to determine the optimal laser intensity for the measurements. Since the electric field for an unirradiated LGAD device is higher than for an irradiated one, the calibration was done with an unirradiated sensor to ensure that the laser intensity is not too high for the irradiated samples. The procedure was carried out by adjusting a value on the attenuator, and measuring the signal both using the LGAD as well as a separate optical-to-electrical (O/E) converter (InGaAs diode with a transimpedance amplifier stage) [Ter]. For both devices, the area under the signal pulse was calculated and the whole attenuator range was scanned. The results are shown in Fig. 5.7. The data indicate that the signal of the LGAD sensor shows no quenching effects in the recorded attenuation range. Therefore, an arbitrary operation point of $A_{\text{sig}} = 850\,\text{mV ns}$ on the O/E converter was chosen for all measurements in this work. This specific attenuation setting has not been changed for the measurements presented in this work but monitored periodically during the data-taking period to account for possible changes in the laser intensity over time which did not occur. As recommended by the manufacturer of the laser pulse generator, a warm-up period of at least 2 hours was used prior to any measurements to ensure a stable laser intensity.

Position Calibration

In order to determine the offset between the laser spot and the camera line-of-sight mentioned previously, a position calibration was necessary. The calibration was performed by approximately aligning the laser spot along a line on the sensor that crosses two of its cross-shaped aluminum pads, shown in Fig. 5.8a. The idea behind the calibration is to move the laser spot in steps of 5 µm across the sensor and record the signal as well as the position of the laser spot at

each injection point. As seen in the figure, the sensor layout of the measurement samples includes cross-shaped aluminum pads. Whenever the laser spot crosses such an aluminum pad, a dip in the signal is expected since the aluminum reflects the laser light away from the active sensor area. This is shown in Fig. 5.8b, where the signal recorded along the line is overlayed with the design layout of the sensor. The dips in the signal are marked with crosses and the corresponding positions are annotated with the motor stage coordinate system. After this measurement, the camera line-of-sight was aligned with each of these cross-shaped aluminum pads that were crossed along the calibration line, the motor position was recorded and the offset between the camera line-of-sight and the laser spot was determined by taking the average of the distances between the dip positions (as seen with the laser) and pad positions (as seen with the camera). Possible uncertainties of this procedure are the motor stage precision as well as how parallel the sensor is aligned with the laser-cam axis while taping it to the readout board, since the pad positions as seen with the camera and the dip positions as seen with the laser need to align. Since the offset is naturally not known beforehand, the calibration relies on the assumption that the sensor is aligned parallel to the laser-cam axis. This could, in principle, be solved by performing this calibration iteratively. However, none of the measurements presented in this work need perfect offset alignment, therefore, one iteration was deemed sufficient.

Laser Focus

The laser spot needs to be focused onto the sensor to ensure that the charge carriers are created in a small volume and an optimal resolution is achieved for spatial sensor scans. The focus of the laser spot is adjusted by moving the sensor up and down with the stepper motor stage. Since the laser has a cone-shaped beam, the spot size is smallest at the focal length but the intensity is not necessarily the highest. To find the optimal focus height, two regions of interest are defined: an area which yields no signal even when hit with a laser and an area which yields a signal. With the sensors investigated in this work, the sides of the active sensor area were chosen as the interface between these two regions. Outside of the active sensor area, the signal is expected to be zero, while the signal is expected to be high inside the active sensor area.

The focus procedure is performed by scanning a line across this interface and recording the signal. This is done for different heights of the motor stage and a set of S-curves is obtained. Error functions are fitted to these S-curves and the focus height is determined by the minimum FWHM of the error functions

$$\mathrm{FWHM} = 2\sqrt{2\ln 2}\sigma,$$

where σ is the standard deviation of the error function.

The results of this procedure are shown in Fig. 5.9. A small offset between two sets of curves is visible in Fig. 5.9a which is due to performing the focus procedure during the warm-up period of the laser system. While this is not optimal, the offset should only influence the absolute signal amplitude and not the beam spot size. Using this procedure, the optimally focused beam spot size was determined to be 18 µm in diameter. The laser focus procedure was performed at the beginning of each TCT study (gain deterioration, charge spreading, discussed in Section 13.1) to ensure consistency in the measurements.

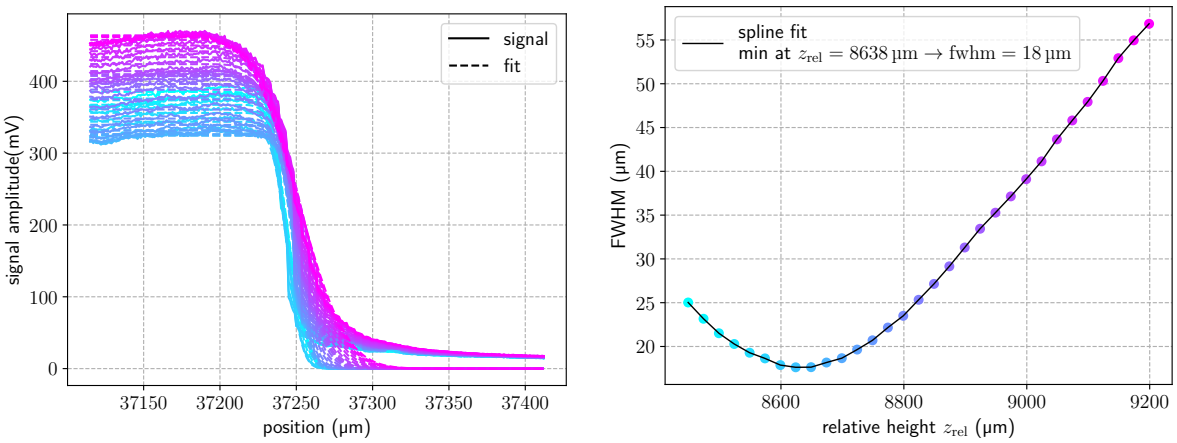

(a) **(b)**

Figure 5.9.: Results of the laser focus calibration. (a) The signal amplitude as a function of the position across the active sensor area interface for different heights. Error functions are fitted to the S-curves. (b) The FWHM is extracted for all error functions and plotted as a function of height. The minimum marks the optimal focus height.

5.2. Irradiation Facilities

In the following, facilities that were used to irradiate the sensors investigated in this work are described.

5.2.1. Proton Irradiation Facility

Proton irradiations were performed at the KAZ cyclotron operated by the Zyklotron AG (ZAG) [Zyk] in Karlsruhe, Germany. The proton beam energy is 23 MeV with a hardness factor of $\kappa = 2$ and a beam current of 2 µA. The target fluences were reached within a margin of error of ±15% due to fluctuations in beam current. Irradiations took a maximum of two hours and the sample temperature was kept below 0 °C during the irradiation to reduce annealing effects. The samples were placed in a custom-made irradiation box mounted on a motorized stage that was used to scan the samples across the beam in a snake-like pattern. After the irradiation procedure, the samples were stored in a freezer at −20 °C as quickly as possible to prevent annealing effects. Fluences were determined by measuring the activity of nickel foils that were irradiated together with the samples. Gamma ray spectroscopy of the nickel foils was used to determine the fluence within an uncertainty of 10.3% [Mül21].

5.2.2. Neutron Irradiation Facility

Neutron irradiations were performed at the TRIGA[2] Mark II spallation reactor [SŽT12] at the Jožef Stefan Institute (JSI) in Ljubljana, Slovenia. The 250 kW light water pool type reactor is cooled by natural convection and allows for irradiation of samples with a flux uncertainty of 10% [Žon+99]. Inelastic neutron collisions also produce gamma rays that can contribute to the TID of the samples. During the irradiation process, the samples placed in the reactor heat up to around 40 °C but are cooled down right after the irradiation and for the travel back to ETP to prevent any more annealing effects. Taking the spectroscopy at RT subsequent to the irradiation into account, a conservative short-term annealing duration of 1 h was assumed.

5.2.3. X-Ray Irradiation Facility

Irradiations with x-rays were carried out with the tungsten x-ray tube setup at ETP.

The X-Ray Tube

The tube is located in a lead-aluminum interleaved housing to shield the environment from radiation with a kill switch at the housing lid to prevent accidental exposure. For all irradiations, the tube was operated at a tube voltage of 60 kV and 30 mA of tube current with a vanadium filter to harden the x-ray spectrum. A collimator with a diameter of 7 mm was used to limit the beam on the samples and the distance between the tube and the samples was fixed at 100 mm. This yields a spectrum with a cutoff energy at 60 keV shown in Fig. 5.10a and a spectrum modified for soft x-rays due to the vanadium filter. A PiN diode yielding a current that scales with the x-ray intensity was used to measure the x-ray beam profile. The diode current was converted to a dose rate using a calibration factor obtained from a Monte Carlo simulation of the setup [Gut+12]. The diode was covered with a Pb-mask with a 1 mm-opening. Recording the diode current while moving it across the beam in 1 mm-steps, subtracting the dark current at each point by closing the tube shutter temporarily, yielded the beam profile shown in Fig. 5.10b. The beam profile is highly inhomogeneous. This needs to be compensated

[2]short for: **T**raining, **R**esearch, **I**sotopes, **G**eneral **A**tomic

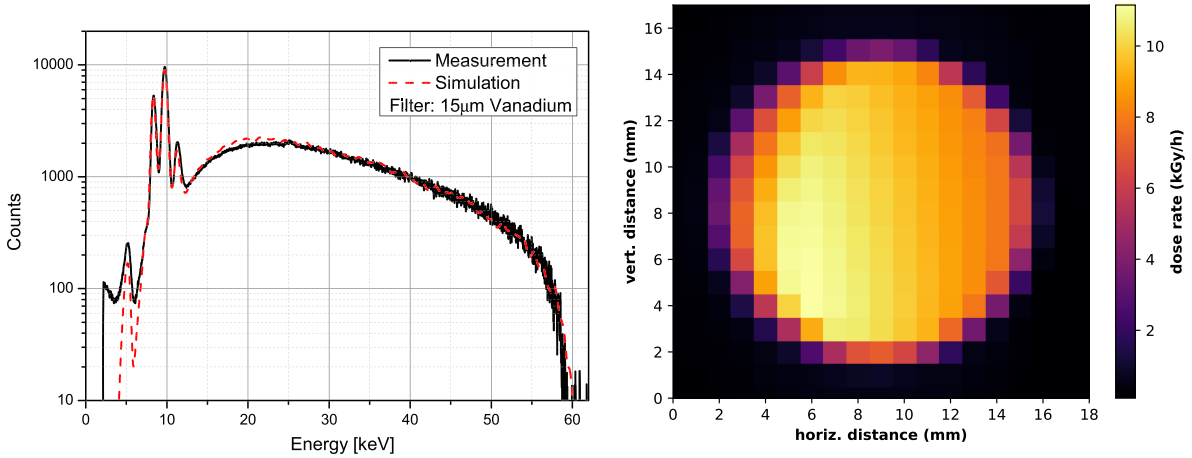

(a) (b)

Figure 5.10.: (a) Simulated and measured x-ray spectra of the tungsten x-ray tube setup at ETP using a vanadium filter [Gut+12]. (b) Inhomogenous x-ray beam profile at a distance of 100 mm from the tube.

for during the irradiation procedure to ensure a homogeneous dose distribution across the samples.

The Irradiation Procedure

The samples were placed in a custom-made irradiation box, shown in Fig. 5.11a with a plastic window at the top used as an entrance window for the x-rays. The box is mounted on a motorized stage that is used to scan the samples across the beam in a snake-like pattern to account for the inhomogeneous beam profile. By scanning the samples back and forth with this snake-like pattern, the dose homogeneity across the samples is improved not only with respect to the beam profile but also with respect to possible fluctuations in beam intensity over time. Inside the box, the samples are placed on an aluminum chuck on top of a single suction hole holding them in place, shown in Fig. 5.11b. During the time of this work, the setup was extended to allow for the measurement of the humidity inside the box as well as at the x-ray generator on the outside. For this, humidity sensors were mounted to the inside of the box and the outside of the generator. During the irradiation procedure, the temperature and humidity inside the box were monitored constantly and the samples were irradiated at a temperature of $-20\,^{\circ}\mathrm{C}$ while the dew point was kept below $-30\,^{\circ}\mathrm{C}$ to prevent condensation on the samples.

Distance vs. Beam Diameter

Even though the beam width w as a function of the distance z from the tube was not needed to be known for the sake of the irradiations presented in this work, the operation of the tube for external visitors to the facility was improved by the author by measuring $w(z)$. Assuming the beam had a width w_0 at the collimator, the increase in beam width Δw over distance due to beam divergence is

$$\Delta w = 2z \tan\theta,$$

with the divergence angle θ, which is assumed to be constant with respect to z. Therefore, the beam width at a distance z from the tube is linear in z and given by

$$w(z) = w_0 + \Delta w = w_0 + 2z \tan\theta.$$

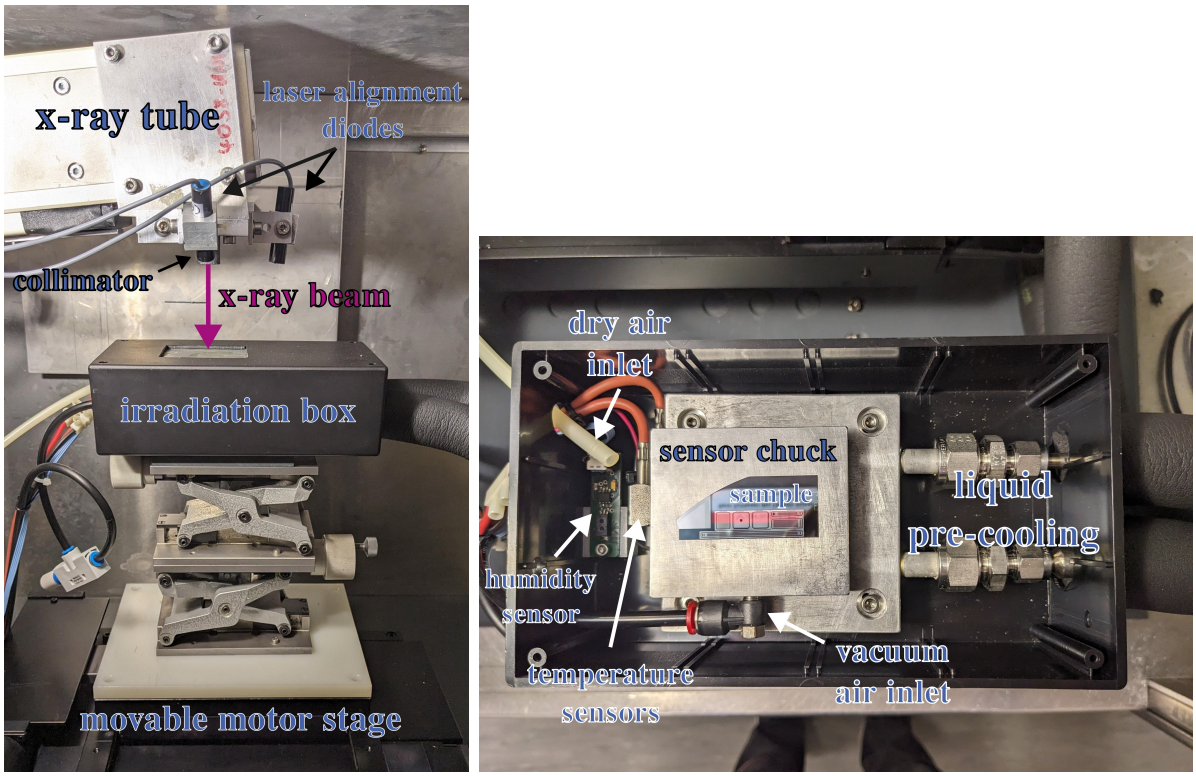

(a) **(b)**

Figure 5.11.: (a) The x-ray irradiation setup at ETP. (b) Detail of the inside of the irradiation box. All critical components are annotated.

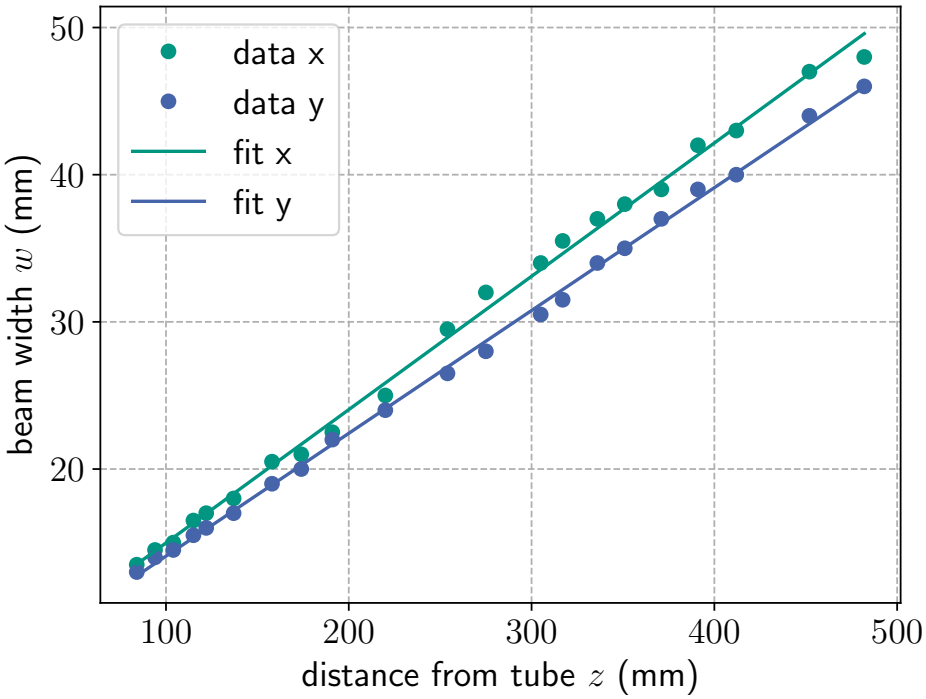

Figure 5.12.: Beam diameter in x and y direction as a function of the distance from the x-ray tube.

Figure 5.12 shows the measured beam diameter in x and y direction as a function of the distance from the tube. Following the previous argument, the beam diameter is linear in z as expected.

The fit functions may be used to calculate the beam diameter at any distance from the tube, which is useful to determine the appropriate distance for the irradiation of samples with a certain size. Therefore, the fit functions are implemented in the control software of the x-ray tube setup that will be presented in Section 5.3.4.

5.3. Software (Upgrades) and Technology Stacks

As was the case for the hardware, the software used for the measurements and analysis of the samples was also upgraded and developed during the course of this work. While some of the software was already in place before the start of this work, the sheer throughput of measurements in this work required the development of new software or the upgrade of existing software. The goals of these software upgrades and developments were

- **User-friendliness:** The software that was already in place did its job for the very specialized use case of the facility, but was not user-friendly. Science disciplines thrive on ever-changing personnel such as students and post-docs, many of whom are not experts in the field out of the box and need to be trained in the use of the software. The software architecture and usage should be as user-friendly as possible while retaining software solutions that have been proven to work in the past.
- **Scalability:** The software should be able to scale with the number of samples, the number of measurements and the number of measurement operators.
- **Maintainability and documentation:** Software should be maintainable and well-documented. This is especially true for the software used in a facility that is used by many different people over time. While developing all software in Python may not be the best solution for all use cases — especially in the case of real-time data acquisition — most of the people using the software are familiar with Python since it is taught in many universities and is the de-facto standard for data analysis in many fields of science.

The following sections will give an overview of the software used in this work and the technology stacks used to implement it.

5.3.1. The MeasurementControl

Based on the prior work of Daniel Schell, Andreas Nürnberg, Roland Koppenhöfer and others, the MeasurementControl (MC) is a Python-based extensible software framework that allows for the control of laboratory equipment, maintenance of measurement data and the analysis of the data. It is modular in design and allows for the integration of new hardware and software components. MC is software that is based on the Flask [Pal] web application framework and is used as a backend application that exposes a REST API to the user and exchanges data between the client and MC server via `json`. A REST API is a web service that allows for the interaction with the MC via HTTP requests by specifying endpoints in the form of URLs, which are then called by the user or client application. For example, sending an HTTP-GET request to `localhost:1234/status`, will return the current temperature status of the station in JSON format by calling the `status` endpoint of the temperature monitoring module. In this example `localhost` is the address of the MC server and `1234` is the network port of the module that handles the temperature monitoring. In reality, the MC handles REST API requests via a specialized module, called `gateway`, that is responsible for routing the requests to the appropriate module. This way, only one port is needed to access the MC, while the individual modules can be accessed via their own endpoints. The MC usually runs on a local server at the various different measurement setups, entirely configurable via YAML files. Usually, these endpoints are requested by a client frontend application but can also be requested by other applications, such as the measurement scheduler discussed in Section 5.3.2.

Over the years of usage, the MC has been extended various times, adding new features and modules with every new version — at the expense of readability, proper documentation and, often times, functionality. The author of this work, together with the help of Roland Koppenhöfer,

refactored the MC code base entirely, which meant removing unused code and modules, simplifying the code and improving the documentation. Ensuring backwards-compatibility with the existing code base was a major concern, since setups rely heavily on the existing code base. During the refactoring process, the CI/CD (continuous integration/continuous deployment) pipeline was also improved. CI/CD pipelines are predefined processes that automatically build, test and deploy the software. The pipelines have been improved by

- introducing a recommended development workflow, which means that developers should work with the same development setup and use the same tools to simplify the development process,
- adding a pre-commit hook, which runs a set of checks before committing code to the repository. This ensures code quality and cleanliness locally before any code is pushed to the repository, keeping it clean, reducing the need for code reviews and manual checks,
- replacing the current tool used to check for code errors and style issues (this tool is called a *linter*) during the CI/CD process. The `PyLint` [pyl] linter was replaced with `Flake8` [Cor] and `Black` [Pyt] for code formatting. `Flake8` and `Black` offer the same functionality as `PyLint` but are less particular about code quality. While it is possible to configure `pylint` to be less specific about code quality, `Flake8`'s default configuration is perfect to catch code errors and enforce a code style that follows the PEP8 recommendations [RWC25] of Python, while still being extensible via plugins. Moreover, the `Flake8` and `Black` tools are more widely used in open-source projects nowadays, making is easier to find help and documentation for them,
- dockerizing the MC to allow for easy deployment on any machine. Dockerization is the method of defining an application together with its dependencies in a file, which can be used to build an image of the application that can be run on any machine that has Docker [Doc25] installed. Dockerization offers the advantage of being able to run the application in a container that is isolated from the host system, which eliminates the need to install dependencies on the host system, saves time and guarantees that the application is run in a clean environment.

A hands-on quick introduction to the MC was also given to any new user who was also interested in developing for it.

In order to do the work presented in this thesis, code to control three new devices had to be added to the MC: the CAEN DT5742 digitizer (`caen.py`) [CAE], the iseg SHR high-voltage power supply (`iseg.py`) [ise] and the ALiBaVa readout software, based on the existing command-line utility provided by the ALiBaVa team (`alibava.py`) [ALi]. Two new controller modules were also added: the TCT-controller (`tct-controller.py`) and the stepping motor controller for the x-ray setup (`motor-controller.py`).

5.3.2. The MC Measurement Scheduler

The MC software stack was originally designed to program one measurement at a time. For the work presented in this thesis, the author has added a measurement scheduler to the MC that allows for the scheduling of multiple measurements at once, monitoring their progress and notifying the user of status changes via a Mattermost and Telegram bot. While it would have been possible to implement this functionality directly into the MC, implementing it as a separate piece of software that communicates with the MC via its REST API seemed like a more sensible approach, due to the fact that such a change would have broken compatibility with setups critical for day-to-day operation. The measurement scheduler is implemented in

Python and is a modular framework that allows for the scheduling of any type of measurement. The following modules were implemented:

- **The Controller**: The Controller communicates with the MC and can RESTfully access and modify MC objects such as adding measurements, starting a measurement run, etc.
- **The Observer**: The Observer performs read-only operations on MC-relevant data. Even though the SOLID[3] principles of object-oriented programming suggest that due to high coupling between the Controller and the Observer, they should be implemented in one module, a segregated approach was chosen to allow users the use of the measurement scheduler as an observer-only tool.
- **The Scheduler**: The Scheduler exposes a data structure, the *entry list*, that can be interacted with by the user. Entries are objects that define which actions to take, such as starting a measurement, running a script, etc. Modification of the entry list means changing the course of the schedule.
- **The Communicator**: The communicator handles communication with the group-internal measurement database and instant messaging services such as Mattermost and Telegram. Arbitrary, further services can be added to the Communicator easily.

A measurement schedule is a list of entries that can be added by means of configuration and template files. The Scheduler reads measurement definitions from templates and entry lists from `json` files. Templates have the general `json` structure but contain placeholders enclosed in double curly braces. The template variables are looked up in the parameters of the entry defined in the entry list file. A sample of an entry list file containing three entries would look like this:

```
{"entry_type": "measurement", "meas_type": "iv", "params": null},
{"entry_type": "measurement", "meas_type": "alibava", "params": null},
{"entry_type": "measurement", "meas_type": "annealing",
    "params": {"temp": 60, "duration": 20}}
```

The first two entries do not require any parameters, while the third entry contains two parameters that are passed to the template. As a safety feature, an additional key `wait_time` can be added to an entry to specify the minimum and maximum time the measurement is allowed to take `notshorterthan` and `notlongerthan`:

```
{
    "entry_type": "measurement",
    "meas_type": "alibava",
    "params": null,
    "wait_time": {"notshorterthan": 420, "notlongerthan": "1:30"}
}
```

If the measurement takes shorter or longer than the specified times, the measurement is paused awaiting input and the user is notified via the instant messaging service.

The introduction of the measurement scheduler revolutionized the way long-running measurements were conducted on the overwhelming number of samples in this work. Prior to its implementation, nighttime measurements were practically impossible, since the MC lacked the capability to schedule multiple measurements at once. Even if it could, an operator would still need to be physically present to monitor and manage the process. With the scheduler in place,

[3] **S**ingle responsibility, **O**pen-closed, **L**iskov substitution, **I**nterface segregation and **D**ependency inversion

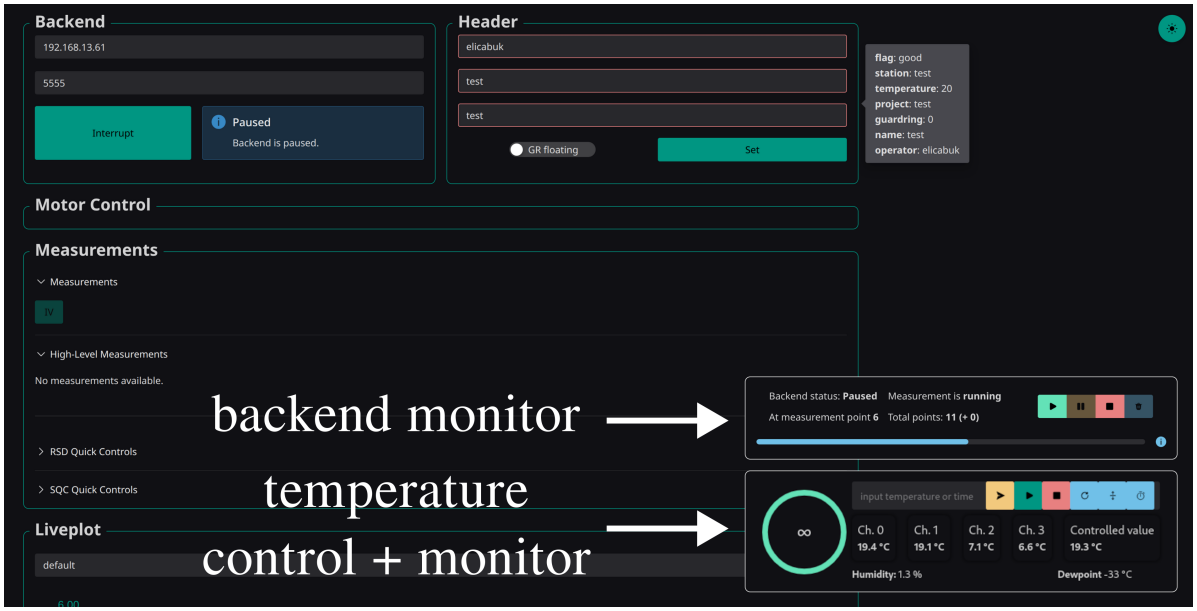

Figure 5.13.: Screenshot of the MC-GUI's main components with annotated modules.

measurements could now run seamlessly around the clock, maximizing efficiency. Moreover, the scheduler's user-friendly design and flexibility were validated when it was successfully integrated into workflows at stations not directly managed by the author. This demonstrated its adaptability and ease of use for a broader audience. The measurement scheduler, along with comprehensive documentation and many examples, is available in a team-internal GitLab repository.

5.3.3. The MC-GUI

In order to interface with the endpoints of the MC, a graphical user interface (GUI) was developed by Andreas Nürnberg. This elementary but very useful GUI allowed users to program measurements, monitor their progress and visualize the data, as well as control various hardware such as the temperature controlling unit. The GUI was rewritten by the author from scratch, calling it the *MC-GUI*, which improves upon the previous version in different ways. The MC-GUI is a dockerized, single-page application that is based on the frontend framework `Vue 3` and uses the `naive-ui` [TuS] GUI component library for the user interface. `Vue 3` is a modern JavaScript framework for building user interfaces, while `naive-ui` provides a set of pre-built components that can be used to build user interfaces quickly and easily, also considering that new developers should have it easy to get started with the project. Both projects have been chosen because they are widely used in the open-source community and have a large user base, making it easier to find help and documentation. CI/CD pipelines were also added to the GitLab repository to handle code quality and deployment to a centralized server part of a Docker Swarm [Doc25] cluster. In contrast to its predecessor, the MC-GUI does not implement all of its functionality in one monolithic file, but instead uses a modular approach, where each component is implemented in its own file. A screenshot of the MC-GUI is shown in Fig. 5.13. The design of the GUI is very simplistic and modular, partly retaining the look and feel of the old GUI. Going with a design that is similar to the old GUI was a conscious decision, to avoid any errors in the workflow of the users during handling of important measurement samples. Therefore, the design of the GUI was chosen as simple as possible, while still allowing for a modern look and feel. While retaining basic elements of the old GUI, the new GUI features

two floating monitors and controls at the bottom right corner of the screen, allowing for easy access to the most important functions of the GUI such as starting and stopping measurements, monitoring the progress of measurements and controlling the temperature of the sample.

The introduction of the new GUI has greatly improved the user experience in production scenarios[4] and at other stations. The GUI is now much more user-friendly and responsive, not only by the intuitive UI/UX design specifically forged for its target audience but also due to its increased performance. The GUI is available in a team-internal GitLab repository and is also used at stations such as probe stations, the TCT setup and several other setups.

5.3.4. The X-Ray Irradiation Interface

Irradiation of samples with x-rays at the x-ray setup as it was used prior to this work was a cumbersome process for several reasons. First, the setup lacked any way of monitoring the humidity of the sample during the irradiation process which was added with the help of a new humidity sensor discussed previously. Second, the setup was controlled using very basic Python scripts that were not user-friendly, lacked any form of documentation and required a lot of trial and error to get the setup running. To provide functionality during the sensor mass production of the CMS Phase-2 Outer Tracker sensors, a GUI and documentation for the x-ray setup were implemented. The GUI is a `Vue 2` [You] application that is based on the `vuetify` [Vue] GUI component library. Again, both projects are widely used in the open-source community, providing ample documentation and help. It is a single-page application that features five views:

- a **motor control view** that allows for the control of the stepping motors and alignment of the sample,
- a **temperature control view** that allows for the control of the temperature and humidity of the sample,
- an **offline dose calculator** that allows for the calculation of the dose delivered to the sample based on parameters input by the user. It is used for dose calculations prior to the irradiation of the sample to get an estimate of the irradiation time. The distance-beam size relation found in Section 5.2.3 was implemented in this module,
- An **x-ray control view** that allows for the manual control of the x-ray source and shutters and
- the **irradiation view** that allows for the control of the scanning irradiation process of the samples irradiated for this work.

Figure 5.14 shows a screenshot of the irradiation view of the x-ray irradiation interface. The user needs to input parameters that are used to calculate the irradiation path of the sample. Based on the input parameters, the irradiation path is calculated by the MC and displayed to the user in a visual representation of the sample. The user can then start the irradiation process, which will move the x-ray beam across the sample along the calculated meander path.

Apart from the GUI, documentation for the x-ray setup was also created, including a step-by-step guide on how to use the setup. The x-ray irradiation interface was used to irradiate all samples with x-rays in this work. So, it has proven to perform well in a production environment and has been used by other users at the x-ray setup, including external users. The project code base is available in a team-internal GitLab repository.

[4] *Production* environments are defined by situations where deployed software is used by actual users and not just during prototyping or development testing.

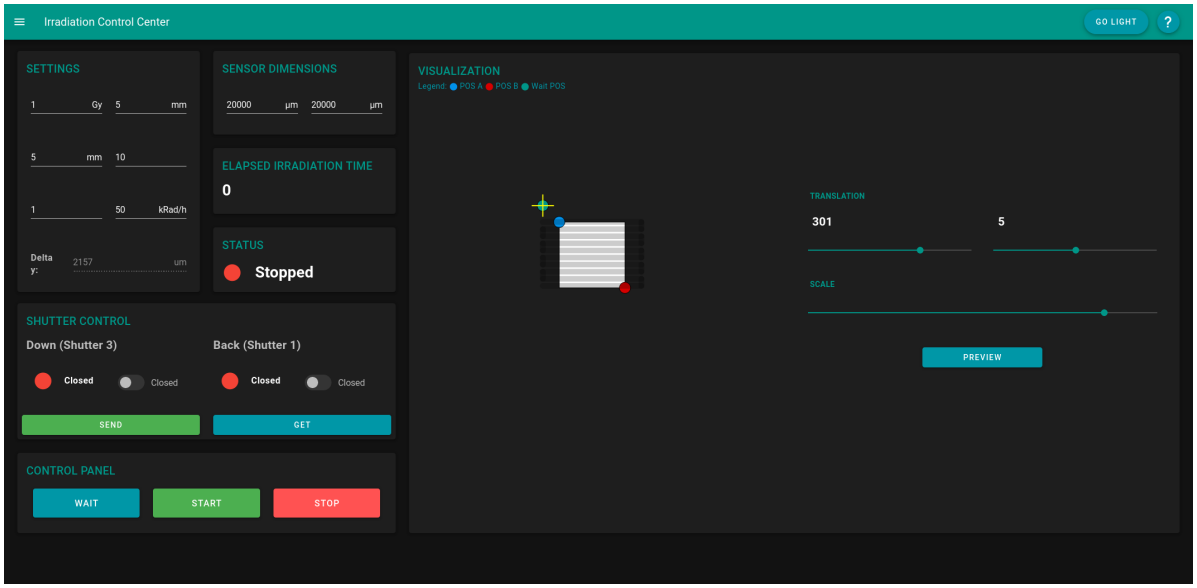

Figure 5.14.: Screenshot of the irradiation view of the x-ray irradiation interface. User settings are shown on the left, while a visual representation of the sample and the calculated irradiation path is shown in the center. The settings shown in the screenshot are not realistic and were used for demonstration purposes.

5.3.5. The ALiBaVa Analysis

Analysis of the data acquired with the ALiBaVa setup was done using a Python-based analysis framework that was developed by the author of this work in cooperation with Andreas Nürnberg. A modular approach was chosen as for most of the software in this work, allowing for easy integration of new analysis modules by new developers. The framework is divided into the following modules:

- `clustering.py`: This is the heart of the analysis framework and contains algorithms that convert ADC signals of channels in an event into clusters of signals.
- `plotting.py`: The plotting module contains all plotting functions used to visualize the data.
- `fitting.py`: The fitting module contains all fitting procedures as well as automatic intial parameter estimation for each implemented fit function.
- `signal.py`: The signal module is a representation of the data structure produced in the radioactive source run mode of the ALiBaVa setup. It contains all the information about the signal and exclusion of certain unwanted strips (masking) by the user.
- `pedestal.py`: This module is a representation of the pedestal run mode of the ALiBaVa setup. It contains all the information about the pedestal and noise calculations. Automatic masking procedures based on the noise are also implemented in this module.
- `gain.py`: The gain module is a representation of the calibration run mode of the ALiBaVa setup. It contains all the information about the calibration and gain calculations for every strip.

Apart from these modules, there are also several helper modules like `db.py` that is used to upload the results of the analysis to the internal ETP database.

The analysis itself works in the following way: Three files are produced by the ALiBaVa setup as described in Section 5.1.2:

- a file containing pedestal data that has been recorded in pedestal run mode,
- a file containing calibration data that has been recorded in calibration run mode and
- a file containing radioactive source data that has been recorded in radioactive source run mode.

Quantities extracted from the file containing pedestal data

The pedestal data containing the raw ADC signal $\mathrm{ADC}_{\mathrm{ped}}(i,k)$ of channels i in events k in the absence of the Sr-90 radioactive source using random triggers is used to calculate

- the pedestal value $P(i)$ of each channel,
- the noise $N(i)$ of each channel,
- the common-mode noise $D(k)$ of each event and
- the common-mode subtracted noise $N_{\mathrm{sub}}(i)$ of each channel.

The pedestal noise $P(i,k)$ is a source of noise that causes the signal to fluctuate around the pedestal value $P(i)$. In other words, $P(i,k)$ follows a normal distribution with a mean value of $P(i)$ and a standard deviation of $N(i)$, the noise of channel i. In the analysis, it is calculated as the mean over all events k of the pedestal data and the noise $N(i)$ is calculated as the standard deviation over all events k, respectively. The common-mode noise $D(k)$ is a source of noise that affects all channels in the same way and changes from event to event. Therefore, it is calculated as the mean over all channels i of the pedestal data. Additionally, the common-mode subtracted noise N_{sub} is calculated using $D(k)$ and $P(i)$

$$N_{\mathrm{sub}}(i) = \sqrt{\frac{1}{N}\sum_{k}\left(\mathrm{ADC}_{\mathrm{ped}}(i,k) - P(i) - D(k)\right)^2}.$$

N_{sub} is used to calculate the noise per channel and is used in the clustering algorithm. If a channel containing a noise higher than a certain threshold is found, the channel is masked and not used in the analysis of aforementioned quantities. User-defined masking is also taken into account.

Quantities extracted from the remaining files

Next, the calibration data is used to calculate the gain of the channels, thus, conversion of ADC counts to electrons. Then, the radioactive source data is used to process the total ADC signal, which is composed of

$$\mathrm{ADC}_{\mathrm{rad}}(i,k) = P(i,k) + D(k) + \mathrm{Signal}(i,k), \tag{5.1}$$

where $\mathrm{Signal}(i,k)$ is the signal of interest, induced by the radioactive source, and $\mathrm{ADC}_{\mathrm{rad}}(i,k)$ is the raw ADC signal contained in the radioactive source data file. Following Eq. (5.1), subtracting $P(i,k)$ and $D(k)$ from the total ADC signal $\mathrm{ADC}(i,k)$ gives the $\mathrm{Signal}(i,k)$. In this calculation, $P(i,k)$ is approximated by the pedestal value $P(i)$ calculated from the pedestal data. This signal is then used in the event-based clustering algorithm to find clusters of signals in each event.

The clustering algorithm works by defining two *cuts* or thresholds: the *seed* and *neighbor* cut, which are defined as multiples of the noise $N_{\mathrm{sub}}(i)$ of that channel i. In this work, a seed cut of 5 and a neighbor cut of 2 were used. Seed strips are defined as strips with a signal above the seed cut, while neighbor strips are defined as strips with a signal above the neighbor cut. Seeds and neighbors are then used to form clusters of signals with a cluster size equal to the number of strips making up the cluster and a cluster (charge) signal equal to the sum of the signals of all strips in the cluster. The clustering algorithm discards clusters that overlap with the user-defined or automatic mask, even if the masked strip happens to be a seed strip. Seed signals are also calculated for every cluster, which is defined as the signal of the seed strips in the cluster.

The ALiBaVa analysis was used to analyze all samples in this work that were measured with the ALiBaVa setup and is available in a team-internal GitLab repository, along with extensive documentation. Deployment of the analysis framework is done dockerized as part of a message-queue-based analysis pipeline. The concept of message-queuing is based on a *message broker*, processing instructions of certain actions to be performed. These instructions are called *messages* and contain the necessary information that needs to be provided to the *workers* doing the actual work. In this instance, the RabbitMQ [Bro] software is used as the message broker and Python applications implementing the Celery [Sol] interface are the worker processes, allowing for queuing of analysis jobs and scaling of the analysis framework to handle multiple jobs at once. A Flower dashboard [Mov] providing a graphical user interface of the currently running, completed or failed analysis jobs is used to monitor the progress of the analyses and the status of the workers. A worker number of two was used for the analysis of this work, but the framework allows for scaling to any number of workers. This pipeline has proved operational in a production environment.

Part I.

Irradiation Testing of Silicon Sensors for the CMS Phase-2 Upgrade

6 Introduction

This chapter introduces the quality control (QC) strategy for the Phase-2 Outer Tracker of the CMS experiment and the samples that were used in the irradiation tests (ITs).

6.1. The Phase-2 Outer Tracker Quality Control Strategy

During the sensor mass production for the Phase-2 Outer Tracker, a comprehensive quality control (QC) strategy was put into place by the Outer Tracker Sensor Experts Production Panel (OTSEPP), which is a subgroup of the Sensor Group of the CMS Tracker Collaboration. The QC strategy is designed to monitor the quality of the sensors during the (pre)-production phase.

The following terminology is used in this thesis: a *batch* refers to a group of silicon wafers that are manufactured under identical conditions but could originate from different silicon ingots. Each batch can only contain sensors of a specific kind, e.g. only 2S or only PS-s/p sensors (introduced in Section 4.3.2). Batches are uniquely identified by a *batch number*, which is a five-digit number. The batch numbers represent sequential production runs and sensors with a higher batch number were produced later in time.

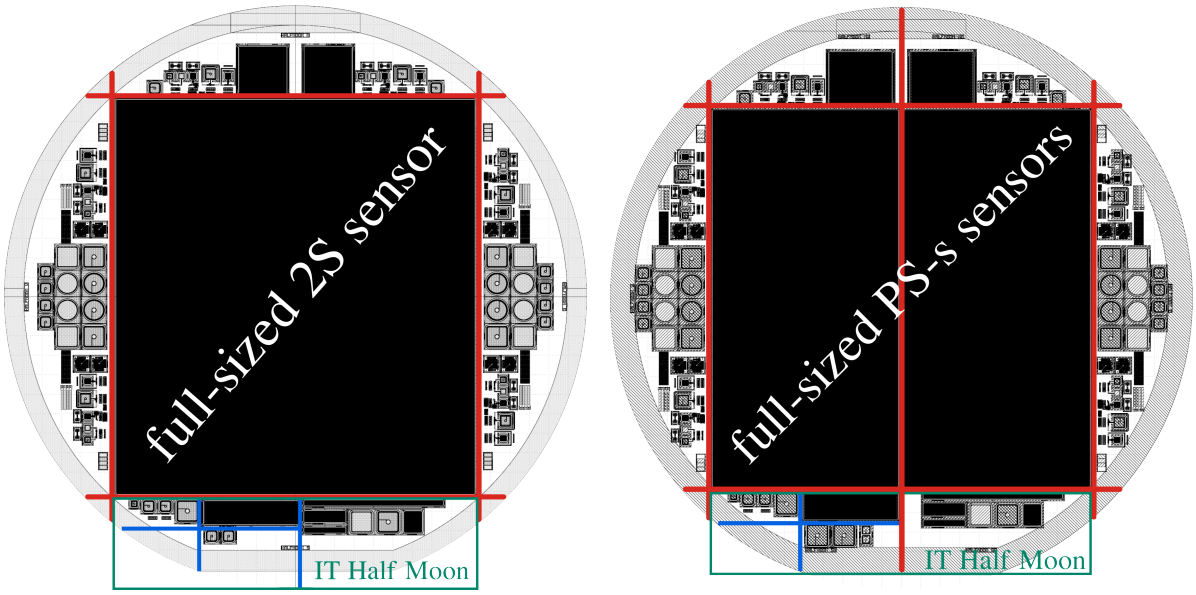

(a) (b)

Figure 6.1.: The (a) 2S and (b) PS-s wafers with the full-sized sensors in the middle. The *half moons* are located to the four sides of the sensors with the IT half moon located to the south, marked in green. Cuts performed by the vendor are indicated by red lines, custom dicing lines are marked in blue.

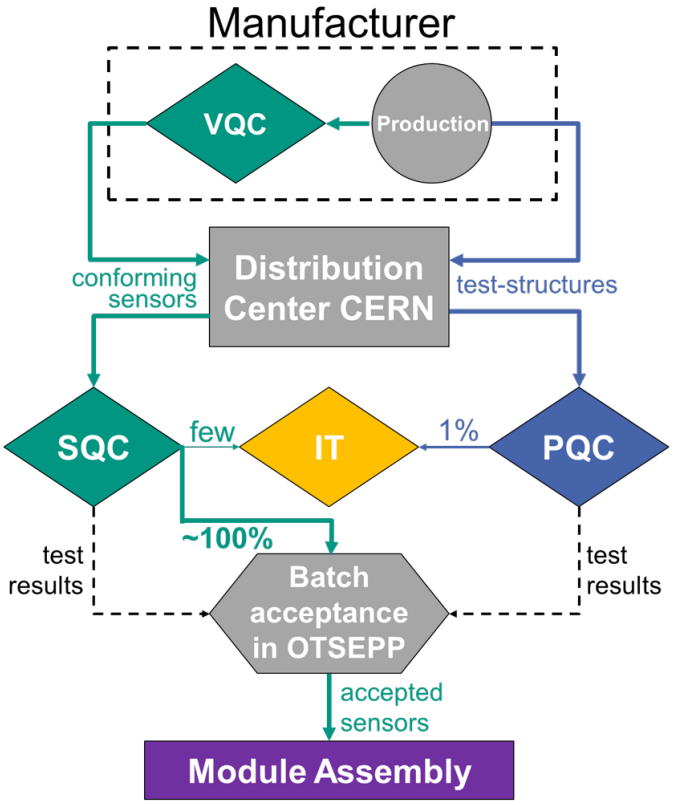

Figure 6.2.: Flowchart of the Phase-2 Outer Tracker quality control (QC) strategy. Details in main text.

The layouts of the 2S and PS-s wafers are shown in Fig. 6.1. In the middle of both wafers, the *full-sized sensors* are located. These are the sensors that will be used in the Phase-2 Outer Tracker later on. Since the full-sized sensors are rectangular in shape and the silicon wafers are round, spare silicon is left in the north, east, south, and west of the sensor (directions are defined as seen in Fig. 6.1). These four parts are called *half moons*. In order to utilize as much of the silicon wafer as possible, test structures are placed on the half moons that allow for the monitoring of different wafer/sensor/processing parameters. The half moon that is relevant for this work is the *irradiation test (IT) half moon*, which is located to the south of the sensor. The full-sized sensors are cut out of the wafer by the vendor using a process called *dicing*. The cuts performed by the vendor are marked in red. In addition to the vendor dicing lines, custom dicing lines had to be performed to separate different parts of the south IT half moon and test them individually.

All sensors in the Phase-2 Outer Tracker production are manufactured by the same vendor: Hamamatsu Photonics K.K. (HPK) [Ham23] in Japan. HPK has a long-standing history in the fabrication of silicon sensors for HEP experiments. Thus, the CMS Collaboration can benefit from the expertise of HPK in the production of silicon sensors, while HPK can benefit by further refining processing steps during the mass production for the CMS Phase-2 Upgrade.

The heart of the QC strategy that is shown in Fig. 6.2 consists of four parts:

- **Vendor Quality Control (VQC)**: After being manufactured at HPK, all sensors directly undergo a set of measurements qualifying the electrical characteristics (IV/CV tests and tests of strip implants) of the sensors. After VQC, all sensors that pass the tests are shipped to CERN along with their corresponding half moons. Two envelopes

per wafer are shipped: one containing the pre-diced sensors and one its half moons. PS-p sensors are subjected to a reduced set of tests compared to 2S/PS-s sensors since testing the pixel implants would be too time-consuming.

- **Sensor Quality Control (SQC)**: After distribution to the six SQC centers, the sensors are tested at each site to ensure that they meet the CMS specifications, visually and electrically. A fraction of the sensors is subjected to a full set of measurements, consisting of a visual inspection, electrical tests, and long-term leakage current measurements, while the majority of tested sensors undergo a quick test only containing IV/CV measurements. Sensors that showed anomalies during VQC are preferred for SQC.
- **Process Quality Control (PQC)**: Since some process parameters are not directly accessible on the sensors, or would require the destruction of the sensors, test structures are used to monitor these parameters. These test structures are located on the east and west half moons of the wafers and are measured after the sensors have been diced out. Tests in the PQC include but are not limited to the measurement of the p-stop (will be discussed in Section 6.2.2) sheet resistance, flat-band voltage (will be discussed in Section 6.2.4), and the breakdown voltage.
- **Irradiation Tests (ITs)**: The main focus of this work are ITs which involve measuring properties of the sensors before and after irradiation with different types of particles. Since irradiating the full-sized sensors would render them unusable for the Phase-2 Outer Tracker, test structures are used instead that are located on the south half moon of the wafers. Irradiation tests use a similar set of measurements as SQC but with some additional parameters, with the charge collection being of particular interest. Very few samples from SQC are also tested in IT but are not discussed in this work. Batches that showed anomalies during the PQC phase are preferred for ITs.

For each tested batch, a decision is made whether the sensors are accepted or rejected, based on the results of the QC measurements. Irradiation tests are the most time-consuming part of the QC strategy and are usually performed after the sensors have been accepted or rejected based on the results of the other tests. However, if deviations or non-conformities are found during the ITs, showing that the radiation hardness is inconsistent with results from the prototyping phase, the batch can be rejected after the fact. Since the results from the PQC phase are usually readily available, IT centers can have a look at the PQC results and decide which batches are interesting for further irradiation testing. Half moons from interesting batches are then requested by the IT centers and shipped to them, tracking the location of the half moons at all times in the central CMS construction database. The results from each part of QC are presented in a weekly to biweekly meeting of the OTSEPP, where the acceptance or rejection of batches is decided. Two IT centers performed the irradiation tests: KIT in Germany performing ITs with proton and x-ray radiation and Brown University in the USA, performing neutron irradiation tests. This work will only discuss the results from KIT.

6.2. Samples

In the following, all samples that were used in the ITs are described in detail. All of these structures are located on the south half moon of the wafers.

6.2.1. Bulk Material

Since all structures are part of the same wafer, they have their physical thickness of 320 µm and active thickness of 290 µm in common. This is achieved by a process that is called *deep*

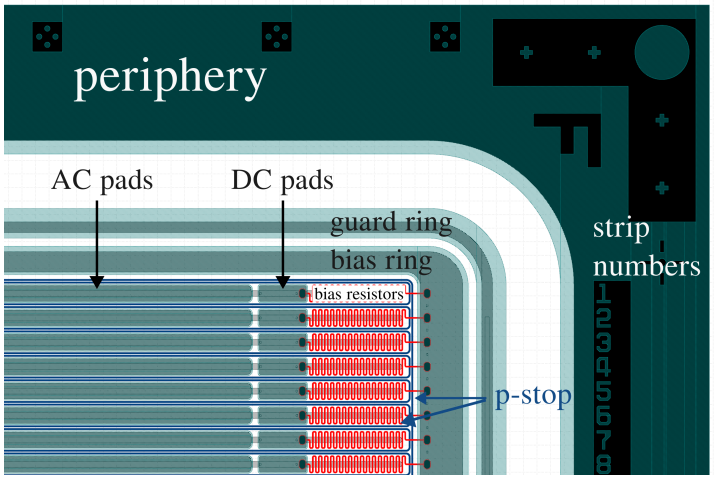

(a)

parameter	value	
	2S	PS-s
width (mm)	25.8 (24.2)	
height (mm)	7.4 (5.8)	8 (6.2)
doping	n-in-p	
p (µm)	90	100
w_{imp} (µm)	22.5	25
no. of strips	60	

(b)

Figure 6.3.: (a) Top-left corner of the sensor layout of a babysensor. All relevant parts are annotated. (b) Layout specifications of babysensors. Widths and heights in parentheses specify the area measured from the middle of the bias ring (active area when the guard ring is grounded). The guard ring needs to be left floating for optimal electric strength.

diffusion which involves heating the material to a high temperature to diffuse the dopants into the silicon bulk[1]. The bulk material is p-doped with n-implants, has a resistivity higher than $3\,\text{k}\Omega\,\text{cm}$ and an oxygen concentration in the range of $0.5 \times 10^{16}\,\text{cm}^{-3}$ to $1 \times 10^{16}\,\text{cm}^{-3}$ [Ada+20] (referenced to as *ddFZ 300/320 P* therein) and thus can profit from the radiation hardness of oxygen-vacancy complexes, as discussed in Section 3.1.4. The doping concentations are $n_{\text{D}} \approx 10^{19}\,\text{cm}^{-3}$ and $n_{\text{A}} \approx 5 \times 10^{12}\,\text{cm}^{-3}$ [Mül21] for the n-implants and the substrate, respectively.

6.2.2. The Babysensor

The *Babysensor* is a miniature version of the respective full-sized sensors, trying to replicate their characteristics as closely as possible.

Design

The sensor design of the babysensor is identical to the design of the full-sized sensors, with the exception of fewer and shorter strip implants. So, all of the following descriptions also apply to the full-sized sensors unless stated otherwise. Figure 6.3a shows the top-left corner of the babysensor layout. The sensor is enclosed by a bias ring that is enclosed by a guard ring. The strip implants can be interfaced either capacitively over the *AC pads* or with the *DC pads* that have a short-circuit impedance connection to the strip implants over via holes. All AC pads and aluminum strips are separated from the strip implants by a 250-300 nm thick oxide layer as a dielectric. Depending on if the sensor is a 2S or PS-s sensor, the strip implants have different pitches p and implant widths w_{imp} but for both, the ratio $w_{\text{imp}}/p = 0.25$ holds. Detailed data on the babysensors can be found in Fig. 6.3b. The bias ring shown in Fig. 6.3a is used to ground the 60 strip implants of the sensor over *polysilicon (bias) resistors* connecting the bias ring with the DC pads. These polysilicon resistors are fabricated in a snake-like shape

[1] How exactly this is achieved is only known to the vendor of the wafers.

to increase the resistance to values in the $\mathcal{O}(\mathrm{M}\Omega)$-range. Negative high voltage is applied to the metallized backside of the p-type sensor to bias it. In order to ensure good ohmic contact, a highly p-doped layer is added in-between the bulk and the backside contact. Every strip is enclosed by a p-doped implant called *p-stop* that prevents the formation of a conductive layer between the strips due to oxide charges, which were discussed in Section 3.2. Since the dicing process introduces mechanical stress along the cutting lines, high electric fields could occur in this region and need to be avoided to keep the sensor from drawing a high current. This is achieved by a wide, highly p-doped implant called *periphery* that is added around the sensor.

The babysensor is used for the following purposes:

- Electrical tests (IV/CV, strip tests)
- Charge collection studies.

IV/CV Measurements

As explained in Section 2.3.1, measurements of the current-voltage (IV) and capacitance-voltage (CV) characteristics of the sensor are essential to understand the electrical properties of the sensor. The IV measurements are performed by applying a negative high voltage to the backside of the sensor and grounding the bias ring, while measuring the current flowing on this line. The voltage is increased gradually to predefined levels and at each voltage step, the current is measured. The leakage current scales with the depleted bulk volume, which is why, regardless if the sensor is of type 2S or PS-s, the IV curves should look similar. Technically speaking, PS-s babysensors should draw a marginally higher current because they are slightly larger than 2S babysensors, which is mostly negligible. Mechanical defects in the sensor can lead to either a higher leakage current or a breakdown of the sensor, entirely, and sometimes, theses defects cannot even be seen by visual inspection.

The CV measurements are performed by measuring the capacitance of the sensor with an LCR meter and gradually increasing the bias voltage, measuring the capacitance at each step. As shown in Section 2.3.1, CV curves can be used to extract the full depletion voltage of a sensor. However, doing this for CV measurements after irradiation is a highly non-trivial task, as will be discussed in Chapter 10, making it impossible to extract the full depletion voltage from the CV curves. Since ITs are performed by comparing sensor characteristics before and after irradiation, as there would be no added benefit, CV measurements as a part of regualar ITs will not be discused in this work.

Strip Tests

Damage to individual strips of the babysensor can impact the electrical properties of the sensor while not necessarily being visible in the global[2] IV/CV measurements. Radiation damage also leads to changes in the electrical properties of the individual strips, such as the resistance between individual strips. Changes in these parameters can affect readout, strip noise, and the occupancy of the readout channels. Thus, testing the individual strips of the babysensors is crucial in the qualification process. The following sections will explain the strip parameters that are of interest for ITs.

Strip tests are performed by applying a bias voltage to the sensor and placing strip needles on either the DC or AC pads of the sensor using the probe station described in Section 5.1.1. In order to define the positions of each strip, an alignment procedure is performed for every sensor with the measurement software by recording the position of the first (y_{first} with strip no. a)

[2]Global parameters are parameters of the sensor in total, in contrast to strip parameters, which only affect individual strips.

and last (y_{last} with strip no. b) strip. The pitch is then calculated as $p = (y_{\text{last}} - y_{\text{first}})/(b-a)$. The measurement software then automatically calculates the positions of the strips in-between the first and last strip and places the needles accordingly. To avoid short-circuiting the strip needles, the needles are placed in a steep angle with respect to each other. For every strip, the following parameters are measured:

The strip leakage current i_{leak} is the part of the leakage current that flows through a single strip when a bias voltage is applied to the sensor. In an ideal sensor, the sum of all i_{leak} should be equal to I_{bulk}. In reality, however, stray currents can contribute to the measured current from the periphery, the sensor surface or mechanical damage. Measuring i_{leak} is performed by placing a strip needle on the DC pad of the strip and measuring the current flowing through it with a picoammeter.

The polysilicon resistance R_{poly} is the resistance of the polysilicon resistor connecting the bias ring with the DC pads. Ideally, the resistance of all polysilicon resistors should be equal to ensure that the bias voltage is distributed equally among all strips, yielding a uniform drift field across the sensor. A uniform field distribution is paramount for optimal sensor performance because only then, charges that are created by ionizing radiation induce a signal that is the same everywhere, regardless of its hit position. Moreover, R_{poly} has an impact on the AC signal amplitude by RC filtering the AC signal and thus, should be equal for all strips. For the full-sized sensors, a maximum spread of 5% is allowed for the polysilicon resistances. The polysilicon resistance is measured by applying a low voltage between the DC pad of the strip and the bias ring and calculating the resistance with Ohm's law. To correct for the additional strip leakage current, a voltage ramp is applied rather than a constant voltage, regression analysis yields the resistance per

$$R_{\text{poly}} = \frac{\Delta V}{\Delta I},$$

with ΔV the voltage ramp, and ΔI the change in current.

Since the noise of a resistance is $\propto \sqrt{\frac{T}{R}}$ at a temperature T, the resistances R_{poly} are designed to be in the $\mathcal{O}(\text{M}\Omega)$-range to minimize the noise.

The coupling capacitance C_{c} of a strip is the capacitance between the AC pad and the strip implant that is formed by the oxide layer dielectric. As for the polysilicon resistances, the coupling capacitances should be equal for all strips to ensure a uniform signal readout, since it is directly proportional to the signal amplitude and its noise. In order to achieve a constant C_{c} across the sensor, a good amount of control over the oxide thickness is required. Drifts in the oxide thickness lead to drifts in the coupling capacitance, which are inacceptable for proper sensor operation if they are too large. The coupling capacitance is measured by placing a needle on the DC pad and AC pad of a strip and measuring the capacitance with an LCR meter. Due to their different implant widths, the coupling capacitance of 2S sensors is smaller than that of PS-s sensors, according to $C \propto A/d$.

The current through the dielectric i_{diel} is the current that flows through the oxide layer between the AC pad and the strip implant. Ideally, this quantity should be exactly zero. However, damage in the oxide layer can result in a conductive path between the AC pad and the strip implant, leading to a current flow which is called a *pinhole*. Pinholes could compromise signal integrity in the affected sensor channel and can also damage the readout electronics by drawing a high current. The current through the dielectric is measured by placing a needle on the DC pad and AC pad of a strip, applying a voltage of 10 V between the needles and measuring the current with a picoammeter.

The interstrip resistance R_{int} is the resistance between two neighboring strips. This value should be as high as possible to avoid crosstalk between neighboring strips which can be detrimental to the single-hit resolution. It should be high with respect to the polysilicon

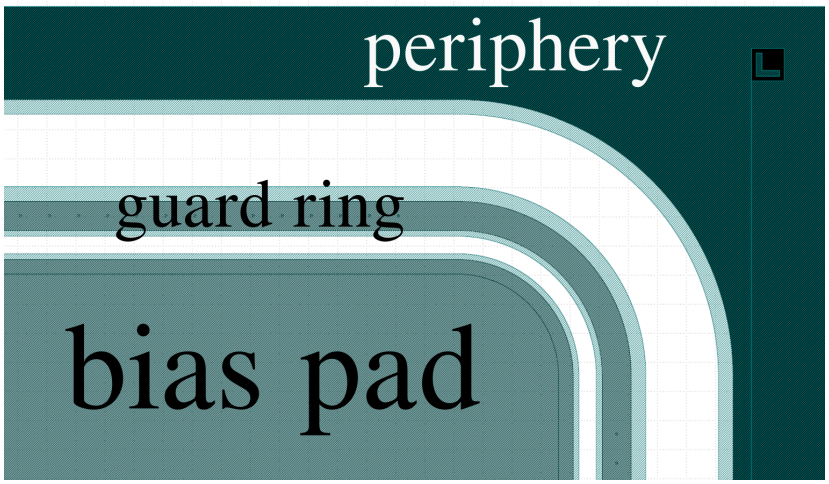

(a)

parameter	value
width (mm)	6.7 (5.3)
height (mm)	6.7 (5.3)

(b)

Figure 6.4.: (a) Top-right corner of the sensor layout of a diode test structure. The hole without a metallization is not shown in this picture because it was irrelevant for this work. All relevant parts are annotated. (b) Layout specifications of diodes. Widths and heights in parentheses specify the area measured from the middle of the bias ring (active area when the guard ring is grounded).

resistance. The interstrip resistance is not only probing defects between any two strips but also the quality of the p-stop implant. Since the p-stop is supposed to isolate the strips from each other, a low interstrip resistance can indicate a low p-stop doping concentration, which is quantified by the *p-stop sheet resistance* being high. The interstrip resistance is measured by placing needles on the DC pads of two neighboring strips and measuring the resistance with a voltage ramp and regression analysis.

The interstrip capacitance C_{int} is the capacitance between two neighboring strips. The interstrip capacitance contributes to capacitive crosstalk between neighboring strips, which is beneficial for the single-hit resolution due to charge sharing to some extent. However, C_{int} should be small compared to the coupling capacitance to avoid a significant signal loss. The interstrip capacitance is measured by placing needles on the DC pads of two neighboring strips and measuring the capacitance with an LCR meter. Due to the ideally low value of C_{int}, an offset compensation of the measurement lines is necessary to avoid a systematic error.

6.2.3. The Diode

The *diode* test structure is a simple pad diode manufactured in a planar process with a hole in the center of the pad with no metallization to allow for laser applications, which was not used in this work. Since the diode lacks any segmentation into strips, it is best suited for studying the bare silicon properties without the influence of strip segmentation. The diode structure comes in three sizes on the IT half moon, with the largest one being used in this work. Figure 6.4a shows the top-right corner of the very simplistic diode layout. A bias voltage is applied from the backside while grounding the bias pad of the structure. The diode has a single guard ring that was grounded for measurements after irradiation to allow for a comparison with the work in [Mol99]. Detailed data on the diodes can be found in Fig. 6.4b. In this work, the diode is solely used to extract the current-related damage rate α_{eq}.

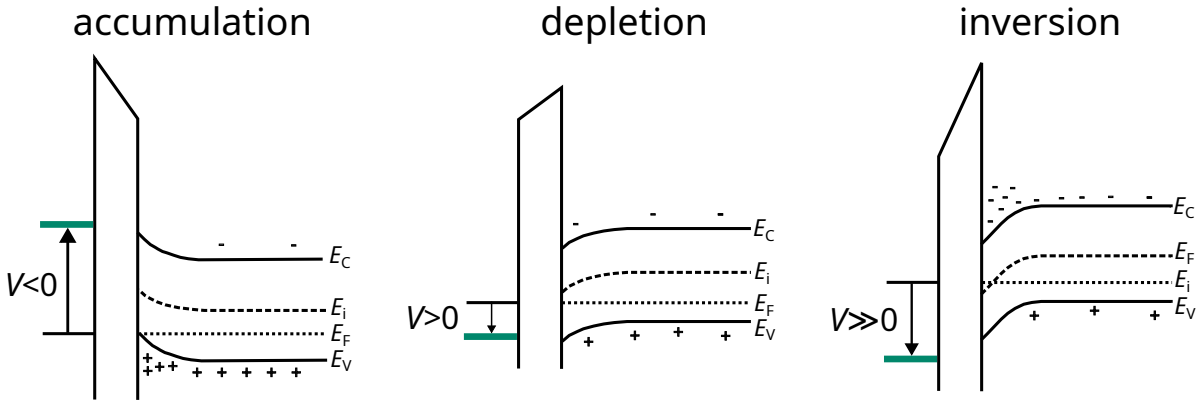

Figure 6.5.: Different states of a MOS capacitor. The external bias voltage (visualized in green) dictates how the bands bend. The flat-band state is the state between accumulation and depletion/inversion, where the bands are flat and the surface charge is zero.

6.2.4. The Metal-Oxide-Semiconductor (MOS) Capacitor

A MOS capacitor is a simple structure that consists of a metal pad, an oxide layer, and a silicon substrate. While many different applications exist for MOS capacitors with the most prominent one being field effect transistors (FET), one very practical example in the context of this work would be an AC pad of a babysensor that was presented in Section 6.2.2. In the scope of the Phase-2 OT QA program, dedicated MOS test structures were used to extract the flat-band voltage of the sensors. In the following section, the reason why the flat-band voltage is of interest will be explained.

States of a MOS Capacitor

In order to understand the flat-band voltage, it is necessary to understand the different states a MOS capacitor can be in. The states of a MOS capacitor can be changed by applying an external bias voltage between the metal pad on top and the semiconductor substrate below. For the sake of the following discussion, let us assume that the device has a p-type substrate, as is the case for all Phase-2 OT sensors and test structures.

Grounding the backside of the device and starting by applying a negative bias voltage to the metal pad, the bands bend upwards. This is shown in Fig. 6.5 on the left. The surface charge is negative and therefore, holes from the p-type substrate are attracted to the surface and accumulate under the Si-SiO_2 interface. Since holes are the majority charge carriers in the p-type substrate this state is called *accumulation*. In this state, the total capacitance of the device is given by the oxide capacitance $C = C_{\text{ox}}$. This state is bad for sensor operation because neighboring strips are shorted. Increasing the bias voltage until only a small positive voltage is applied, the bands bend downwards. This is shown in the middle of Fig. 6.5. The gentle downward bend drives the majority charge carriers away from the surface into the bulk and the region near the surface starts to deplete. Once a thin SCR develops, the state is called *(surface) depletion*. In this state, the total capacitance of the device is given by the series connection of the oxide capacitance and the depletion capacitance

$$C = C_{\text{ox}} C_{\text{dep}} / \left(C_{\text{ox}} + C_{\text{dep}} \right),$$

with C_{dep} the capacitance of the developing SCR. This state is ideal for sensor operation since in the SCR, the sensor is depleted of free carriers and strip-to-strip isolation is guaranteed.

(a)

Parameter	Value
Width	6.8 mm
Height	6.8 mm
Active thickness	290 µm
Oxide capacitance	1.2 nF

(b)

Figure 6.6.: (a) Sensor layout of a MOS test structure. All relevant parts are annotated. (b) Layout specifications of MOS capacitors.

Increasing the bias voltage even more, the now strong bend downwards leads to a strong positive surface charge. This is shown on the right of Fig. 6.5. The repelling mechanism becomes so strong that minority charge carriers are attracted to the surface and an *inversion layer* is formed. This state is called *inversion*. In this state, the total capacitance of the device is given by the series connection of the oxide capacitance and the bulk capacitance

$$C = C_{\text{ox}} C_{\text{bulk}} / \left(C_{\text{ox}} + C_{\text{bulk}} \right) , \tag{6.1}$$

with C_{bulk} the bulk capacitance. The fact that this equation holds is highly non-trivial. A static capacitance measurement would just yield $C = C_{\text{ox}}$ in this state. However, the measurements in this work were performed in resonance using an LCR meter, applying a small AC signal to the device. In a real device, interface states, which were discussed in Section 3.2, can be present at the Si-SiO_2 interface, which show a frequency dependence. Some of these states have trapping times that are much longer than the measurement frequency, which makes them invisible to the measurement, yielding the capacitance in Eq. (6.1). Since the capacitance changes depending on the state of the device, a CV measurement is perfectly suited to characterize its properties.

Adjusting the bias voltage to a specific value between accumulation and depletion, the bands are flat and the surface charge is zero. This state is called the *flat-band* state at a *flat-band voltage* V_{fb}. In an ideal MOS capacitor, V_{fb} is equal to zero. But why is the flat-band voltage of interest for sensor operation? Moving away from our initial assumption of a perfect oxide layer, a real oxide layer has positive charges at the Si-SiO_2 interface, as discussed in Section 3.2. This leads to a shift of the flat-band voltage towards a negative value, when applying the bias voltage from the top metal pad. So, the flat-band voltage is a direct measure of the oxide quality. For this work, the voltages need to be inverted, as the bias voltage is applied from the backside of the sensor. Therefore, all reported flat-band voltages are positive.

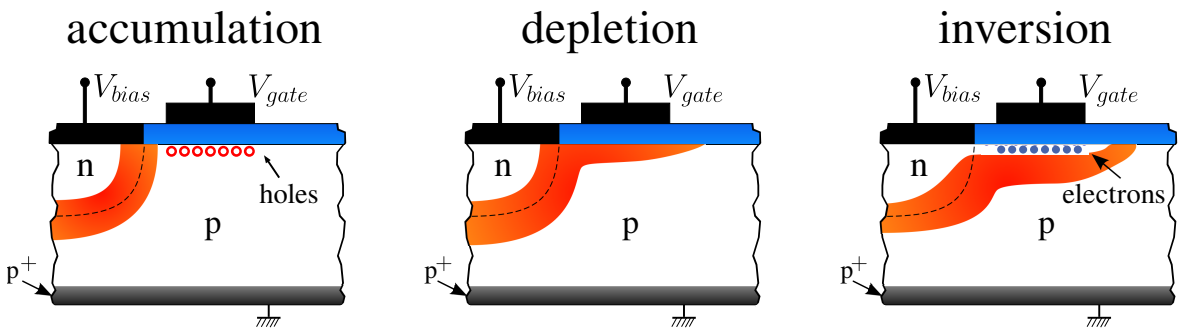

Figure 6.7.: Different states of a GCD. The external bias voltage V_{gate} dictates how the bands bend in the MOS. The SCR of the diode part and the MOS part are connected in the depletion state. Graphic adapted from [Per11].

The MOS Test Structure

The MOS test structure is shown in Fig. 6.6a. Much like the diode structure, when viewed from the top, the MOS test structure consists of a single pad with a guard ring around it that was left floating. The bias voltage is applied from the backside of the sensor while the pad is grounded. Detailed data on the MOS test structures can be found in Fig. 6.6b. The MOS test structure is used to extract the flat-band voltage V_{fb}. After irradiation with ionizing radiation, the flat-band voltage is expected to increase due to surface damage. The irradiation tests performed in this work are not intended to measure absolute values for the increased flat-band voltage after irradiation, but rather to monitor the flat-band voltage over the production period of the sensors. Constant V_{fb}-values over production time after irradiation mean that the oxide quality is stable over the production period.

6.2.5. The Gate-Controlled Diode (GCD)

A GCD structure is the next step in complexity after the MOS capacitor. It consists of a diode next to a MOS capacitor. In the context of this work, this dedicated test structure has the purpose of extracting the *surface generation velocity* s_0, a rate of electron-hole pair generation at the Si-SiO_2 interface with units of a velocity. In the following section, the GCD structure along with why s_0 is of interest will be discussed.

States of a GCD

The states a GCD can be in are essentially exactly the same as those of a MOS capacitor, with the only difference being that the GCD has a diode contact that is kept at a constant voltage V_{diode}. Varying the MOS voltage, the bands bend upwards or downwards and the three states of accumulation, depletion, and inversion can be achieved. As established in the previous section, applying a voltage V_{gate} to the MOS gate contact that is smaller than the flat-band voltage V_{fb} leads to a hole accumulation layer at the Si-SiO_2 interface. This is the same as the accumulation state of a MOS capacitor. Increasing the gate voltage to a value larger than $V_{\text{fb}} + V_{\text{diode}}$, the near-surface region begins to deplete and an SCR develops, putting the device in the depletion state. Increasing the voltage even further, an inversion layer is formed at the Si-SiO_2 interface, which is the inversion state. The difference between the GCD and MOS structure is revealed by inspecting the current flowing through the diode contact while the MOS gate voltage is varied. In the accumulation and inversion states, the diode's SCR is the only current source contributing to the total diode current, as shown in in Fig. 6.7 on the left and right. However, something interesting happens in the depletion state: The SCR of the

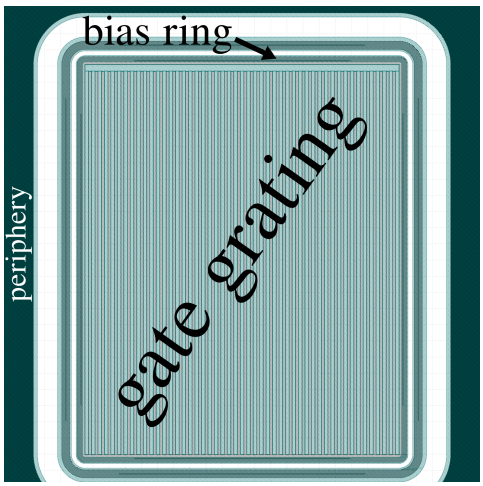

(a)

Parameter	Value
Width	5.9 mm
Height	6.8 mm

(b)

Figure 6.8.: (a) Sensor layout of a GCD test structure. All relevant parts are annotated. (b) Layout specifications of GCD capacitors.

diode and the near-surface SCR of the MOS capacitor are connected, shown in Fig. 6.7 in the middle. This directly exposes the diode part to the interface traps of the MOS capacitor that were discussed in Section 3.2. Interface traps are mainly the reason for the surface current i_{surf} that is generated in the SCR of the MOS capacitor. Therefore, the total current measured at the diode contact is the sum of the current generated in the SCR of the diode and i_{surf}. Since the current in the depletion state is the sum of the two currents, i_{surf} can be recovered by subtracting the diode current in the inversion state i_{inv} from the total current in the depletion state i_{dep}

$$i_{\mathrm{surf}} = i_{\mathrm{inv}} - i_{\mathrm{dep}}.$$

From i_{surf}, the surface generation velocity s_0 can be calculated using

$$s_0 = \frac{i_{\mathrm{surf}}}{e n_i A_{\mathrm{gate}}}, \tag{6.2}$$

with e, the elementary charge, n_i, the intrinsic carrier concentration, and A_{gate}, the area of the gate contact. Since interface traps are the primary surface current generation centers, s_0 relates to the interface trap concentration N_{it} at the Si-SiO_2 interface

$$s_0 \propto N_{\mathrm{it}}.$$

Therefore, measurements of the surface generation velocity can be used to quantify the number of interface traps at the Si-SiO_2 interface. When irradiated with ionzing radiation, the number of interface traps increases, leading to an increase in s_0. The important aspect in this work is that the s_0-level should be constant from batch to batch throughout the entire sensor production period to ensure a constant oxide quality.

The GCD Test Structure

The GCD test structure is shown in Fig. 6.8a. It has two contacts: one for the gate which is processed as a grating and one for the diode which is processed as a (bias) ring around the gate grating. The guard ring was left floating for all measurements in this work. The diode bias voltage is applied from the backside while the bias ring is grounded. The gate voltage is applied

to the gate contact with an additional needle that is placed on the gate grating. Detailed data on the MOS test structures can be found in Fig. 6.6b. Width and height parameters were used to calculate the area of the gate contact A_{gate}. The GCD test structure is used to extract the surface generation velocity s_0.

7

Procedures and Analyses for Irradiation Testing of Silicon Sensors

This chapter will go into detail about all procedures that were performed on the samples introduced in the previous chapter. In addition, the analysis methods used to evaluate the results will be described.

Babysensors and diodes were used to qualify the radiation hardness of the sensor material with respect to electrical performance prior to and after irradiation. MOS and GCD structures were used to qualify the quality of the oxide with respect to the radiation hardness. Additionally, the babysensors were used to qualify the charge collection after irradiation for different annealing durations. The full qualification procedure is summarized in Table 7.1. In the following sections, the individual steps will be described in detail. In order to characterize the babysensors and diodes separately, custom dicing was performed at ETP. There is no physics-related reason to separate these structures, since the planar, highly p-doped periphery would isolate the two structures from each other. However, there are two logistical reasons for this separation: On the one hand, for the charge collection studies with the babysensors the sensors must be bonded to the ALiBaVa board. There is not enough space on the board to accommodate both structures. On the other hand, diodes were used to extract damage rates and a comparison to literature values was made. The amount of annealing that was needed to replicate the annealing state from the literature would be too high to obtain meaningful results for the babysensors. However, these problems are not relevant for MOS and GCD structures, which is why they were not diced apart and passed the same stations during characterization.

Babysensors	**Diodes**	**MOS/GCD**
Dicing	Dicing	Dicing
Electrical Tests	Electrical Tests	Electrical Tests
Proton Irradiation		X-Ray Irradiation
Reception Annealing	**Specific Annealing**	**Specific Treatment**
Electrical Tests	Electrical Tests	Electrical Tests
Bonding to ALiBaVa Board	—	—
Annealing Study	—	—
Storage	Storage	Storage

Table 7.1.: Full characterization procedure for babysensors and diodes and MOS/GCD structures in chronological order (top to bottom). The MOS and GCDs passed the same stations during characterization. The *specific treatment* will be described in Section 7.3.2.

The proton irradiations presented in this work are separated into multiple irradiation *campaigns* that are performed at different times. Sensor batches were selected randomly over a period of 20 production months, which represents 50% of all production batches. As mentioned in Section 6.1, batches with a higher batch number were produced later in time. In order to rule out any systematic effects between campaigns, a conscious effort was made to include batches from a later production date in earlier campaigns. In total, five campaigns spanning 32 batches were performed. Table A.2 shows exactly how many samples from which batch were measured in each campaign. Per batch, five south half moons were requested from the respective PQC centers for IT at KIT. Out of these five sets, usually three babysensors, two diodes and three MOS/GCD structures were measured per batch before irradiation. Out of these three, at least two babysensors, one diode and two MOS/GCD structures were measured after irradiation. Deviations from these numbers can either be attributed to mechanical damage during handling, electrical faults of the devices or the need to measure more structures to obtain more statistics for batches that showed anomalies. Even though MOS and GCD structures can technically be assigned to a campaign by their batch number, the notion of campaigns is not relevant for these structures since they were irradiated in the x-ray setup in a highly reproducible manner. As such, the x-ray irradiations were not separated into campaigns.

7.1. Irradiations

In this work, protons are used to approximate the large amount of charged pions that are expected during physics runs of the CMS experiment. Protons of 23 MeV, that were used in this work, damage the sensor substrate by NIEL and inflict ionization damage in the oxide layer at once. Meanwhile, x-rays with a cutoff energy of 60 keV used in this work do not inflict any displacement damage in the sensor substrate but only ionization damage in the oxide layer. Therefore, protons are used to qualify the radiation hardness of the sensor substrate and x-rays are used to qualify the oxide quality. As described, MOS and GCD structures are best suited to qualify the oxide quality and the babysensors and diodes are used to qualify the radiation hardness of the sensor bulk material. This is why babysensors and diodes were irradiated with protons, while MOS and GCD structures were irradiated with x-rays. After proton irradiation of the babysensors and diodes, two out of the three babysensors and one out of the two diodes were selected for the measurement program after irradiation. If, for some reason, one structure should be damaged during the measurements after irradiation, the other structure could be used as a backup.

7.1.1. Fluences and Doses

The target fluences and doses for the irradiation tests were derived from FLUKA simulations (version 7.20.0) [CMS23a].

Protons

Figure 7.1a shows the simulated NIEL fluences for the OT p_{T}-modules at the end of HL-LHC operation at 4000 fb^{-1}. The fluences for the ITs were selected from these simulations such that 95% of the sensors in the OT of the respective type will receive less than this value. Since the fluence is dependent on the radial distance from the interaction point, naturally, 2S modules receive a smaller fluence than PS modules on average. Therefore, the target fluences used for 2S structures are different than for PS-s structures. Table 7.2 shows the target and measured equivalent fluences for the proton irradiations. Campaigns one and two were performed with lower target fluences than subsequent campaigns. This is due to different scenarios for the

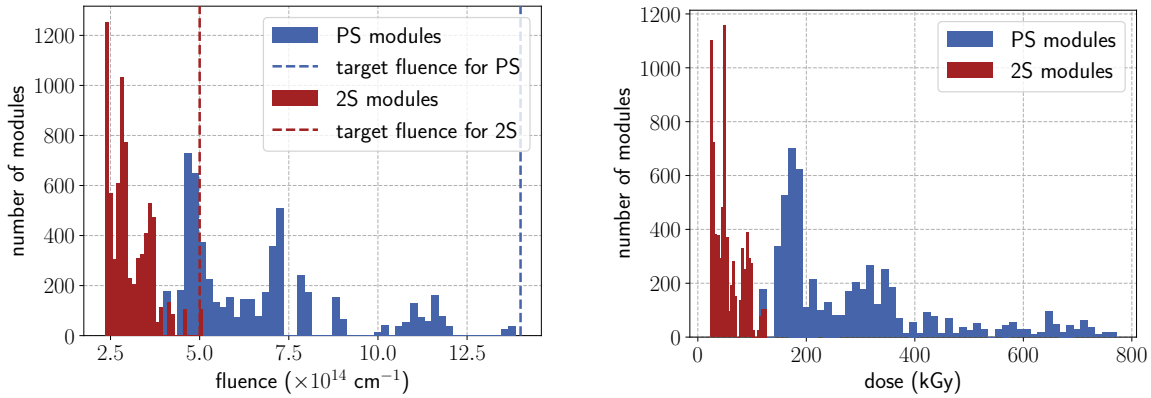

(a) **(b)**

Figure 7.1.: Simulated mean (a) NIEL fluences and (b) TID for the OT p_{T}-modules at end of life at 4000 fb^{-1}. Plots created using the data from the FLUKA simulations in [CMS23a] as input.

Table 7.2.: Target and measured equivalent fluences for the proton irradiations. Values are quoted in units of $10^{14}\,\mathrm{cm}^{-2}$.

Campaign	target 2S fluence	meas. 2S fluence	target PS fluence	meas. PS fluence
1	4	4.3	11	11
2	4	4.1	11	11
3	5	4.7	14	13
4	5	4.0	14	13
5	5	4.1	14	14

Table 7.3.: Measurement settings for (a) IV curves for babysensors and diodes and (b) strip scans for babysensors, before irradiation.

(a)

Parameter	Setting
backplane bias	0 – 1000 V, 10 V steps
current compliance	3 µA
temperature	20 °C

(b)

Parameter	Pads	Setting
i_{leak}	DC	—
R_{poly}	DC	0 – 5 V, 5 V steps
C_{c}	AC,DC	1 V at 1 kHz
i_{diel}	AC,DC	10 V
R_{int}	DC,DC	0 – 5 V, 3 V steps
C_{int}	DC,DC	1 V at 1 MHz
temperature	–	20 °C

expected integrated luminosity for the CMS experiment at the HL-LHC. At the beginning of the IT project, the nominal scenario of 3000 fb^{-1} was more likely to happen than the ultimate scenario of 4000 fb^{-1}. This changed over time, so the target fluences for campaigns three, four and five were set to the ultimate scenario.

X-Rays

Figure 7.1b shows the simulated TID for the OT p_{T}-modules at the end of HL-LHC operation at 4000 fb^{-1}. The target dose for the x-ray irradiations was set to 40 kGy for all structures. As can be seen in the histogram, this is one order of magnitude below the maximum dose expected in the OT. Previous studies [Mül21; MDN21] showed that the effects of ionizing radiation on the oxide layer saturate after around 20 kGy. This means that the target dose of 40 kGy is well above the saturation dose and represents a worst-case scenario in terms of surface damage.

7.2. Electrical Characterization of Diodes and Babysensors

7.2.1. Before Irradiation

After dicing, the babysensors and diodes were electrically characterized to have a reference measurement before irradiation. For babysensors, IV curves and strip scans were performed with the measurement settings listed in Table 7.3. For diodes, only IV curves were measured with the same settings as for the babysensors. Strip scans before irradiation are performed to assess if strips with properties that are out of specification were the result of irradiation damage or if they were already present before irradiation. As shown in the table, the bias voltage for the strip scans was set to 600V. This is the operating voltage for the babysensors in the experiment and was chosen to be the same for the measurements. All full-sized sensors need to meet the requirements that are listed in Table A.3 in the scope of SQC and did so, generally. During IT, the same requirements before irradiation should be met, but the tolerances are relaxed or the requirements for specific samples was discarded altogether to investigate anomalies. The goal of ITs is to characterize the radiation hardness of the sensors and not to pass or fail them based on their performance before irradiation. Thus, a more experimental approach was taken.

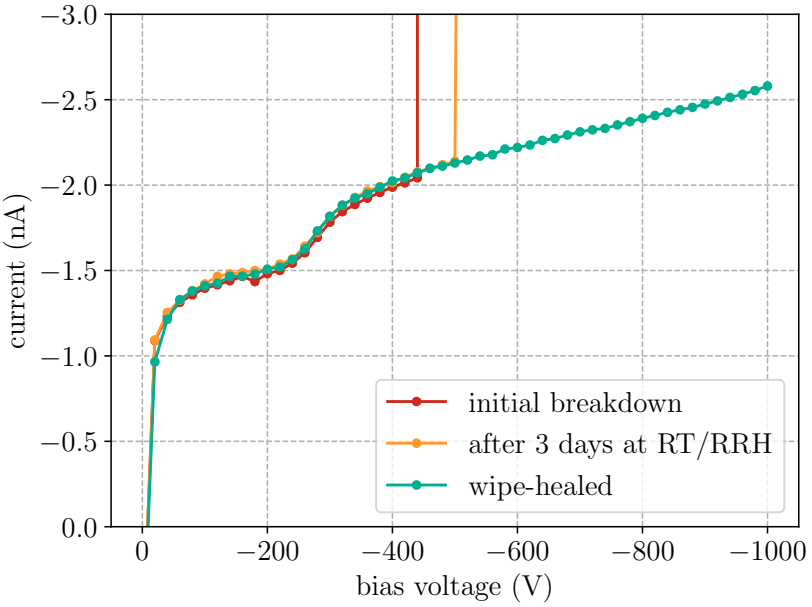

Figure 7.2.: Example IV curves to demonstrate the effect of the *wipe healing* method measured with a test structure before application and immediately after application *in situ*. Measurement performed at 20 °C. The early breakdown vanished (RT = room temperature, RRH = relative humidity in room temperature laboratory).

7.2.2. Wipe Healing

Due to early breakdowns observed for some test structures prior to irradiation, a breakdown mitigation method has been developed which is called *wipe healing*. The method involves wetting a clean room towel with isopropyl alcohol and subsequently wiping the surface of the sensor, covering the whole sensor area. Afterwards, the sensor is dried off with a compressed dry air blower. The effect of the wipe healing method is demonstrated in Fig. 7.2. Early breakdown vanished after application of the method. The exact cause of early breakdowns mitigated with the method are yet unknown but is most likely related to charge-up of the test structures. At the time of authoring this work, it is assumed that wipe healing removes static charges on the surface of the sensor under test since the usage of an ionizer fan accomplished the same effect for the full-sized sensors in SQC. Application of an ion blower for IT structures proved to yield inconsistent early-breakdown mitigation. Static charges on the surface of the sensor are hypothesized to change the local electric field configuration in the sensor and thus, cause early breakdowns if located near the edge of the sensor or localized changes in strip parameters if located near the strips. Following the empirically determined success of wipe healing, it has become the de facto standard for electrical characterizations prior to irradiation at ETP and is applied to every diode and every babysensor.

7.2.3. Irradiation and Annealing

After irradiation with protons at the KAZ cyclotron facility, all babysensors and diodes were stored at −20 °C to prevent annealing. The time for removing them from the irradiation setup and subsequent handling introduces uncontrolled annealing that was estimated to be around two hours. Since the exact amount of annealing is unknown, all structures were subjected to a reception annealing. Reception annealing is a procedure that is meant to equalize the annealing states of all measurement samples by subjecting them to a controlled and significant

amount of annealing, effectively rendering the unknown annealing negligible when compared to this reception annealing. To accomplish this, babysensors were annealed in a hot air oven for 20 minutes at 60 °C which amounts to approximately four days at room temperature, using Eq. (3.3) for the conversion. Diodes were subjected to a special annealing procedure [Mül21], heating them to 60 °C for 80 minutes, which corresponds to approximately two weeks at room temperature. This specific annealing time was chosen to compare the results with values from a reference work in [Mol99]. Annealings performed in the hot air oven were performed by pre-heating the oven to the desired temperature with a aluminum chuck inside. After pre-heating, the aluminum chuck was at the desired temperature and the structures were placed on the chuck, starting a timer. After the time has elapsed, the structures were removed from the chuck in the order they were put on it, to ensure that all structures were subjected to the same annealing time. Insertion and removal of the structures was done by hand and never lasted longer than a few seconds, making the uncertainty in the annealing time negligible. Temperature loss by opening the oven was minimized by leveraging the thermal mass of the aluminum chuck.

7.2.4. After Irradiation

After irradiation and annealing, the babysensors and diodes were electrically characterized again to obtain a measurement after irradiation. The same measurement settings as before irradiation were used for the babysensors with the only exception of the temperature, which was set to −20 °C and the current compliance (the maximum allowed current flowing through the sensor), which was set to 300 µA. Diodes, on the other hand, were measured at room temperature and with a current compliance of 1 mA. This is done because, as shown in Eq. (2.10), the bulk current is exponentially temperature dependent. This means that at room temperature, the uncertainty in the bulk current is significantly smaller than at −20 °C. The uncertainty in the sample temperature at the probe stations was estimated as $\sigma_T = 1\,°\mathrm{C}$, based on the temperature sensor specifications and the temperature inhomogeneity of the setup [Mül21]. Since the results obtained with diodes are used to extract damage rates that largely depend on the precision of the current measurement, the measurement temperature was set to room temperature. Moll [Mol99] extracted the damage rates from the IV curves of similar pad diodes with the same special annealing state used in this study. Equation (3.1) was used to calculate damage rates from the IV curves of the diodes and toy Monte-Carlo uncertainty propagation was performed to estimate the uncertainties in the damage rates. The change in leakage current after irradiation ΔI was approximated with just the leakage current after irradiation, since the leakage current before irradiation is negligible. Two sources of uncertainty were considered: the temperature uncertainty σ_T and the uncertainty in measured equivalent fluences σ_ϕ.

For the temperature uncertainty, a normal distribution D_T with a standard deviation of σ_T was assumed, 1×10^6 samples were drawn. Using Eq. (2.10), a distribution of 1×10^6 scaled currents D_I was calculated, getting D_T as input. The samples from D_I yield the mean scaled current I and the standard deviation σ_I.

For the fluence uncertainty, the specified uncertainty from the fluence spectrometry was used, which is $\sigma_\phi = 10.3\% \cdot \Phi_{\mathrm{eq}}$. Finally, damage rate uncertainties were calculated with Gaussian uncertainty propagation

$$\sigma_\alpha = \frac{1}{V}\sqrt{\left(\frac{\sigma_I}{\Phi_{\mathrm{eq}}}\right)^2 + \left(\frac{I\sigma_\phi}{\Phi_{\mathrm{eq}}^2}\right)^2}. \tag{7.1}$$

Table 7.4.: Annealing steps for the charge collection studies with the cumulative equivalent annealing times at each step (excluding reception annealing). Details in main text.

Step	time (min)	T (°C)	cum. eq. time (days)
1	20	60	4
2	40	60	10
3	60	60	20
4	60	60	32
5	15	80	88
6	15	80	153
7	30	80	267
8	30	80	372

7.2.5. Charge Collection

After the babysensors have been electrically qualified in the probe station, they are prepared for charge collection studies. For this, they are bonded to the ALiBaVa board that was described in Section 5.1.2. During bonding and subsequent handling of the structures, the babysensors are subjected to an additional annealing time that was measured to be negligibly small. After bonding all 60 strips of the babysensor, the board is placed in the setup and the MIP source is placed in the movable source holder. The MIP source is aligned with the middle of the babysensor by eye, the lid of the box is closed and the setup is cooled down to $-20\,°C$ after being flushed with dry air. The babysensor is then characterized in an annealing study. The annealing study is performed for different annealing times and temperatures, which are listed in Table 7.4. Each annealing step consists of three parts:

1. **IV curve**: The babysensor is measured with the same settings for the IV curves as in the electrical characterizations but in the ALiBaVa setup. These IV curves do not serve to be precise but to check the functionality of the babysensor.

2. **ALiBaVa measurement**: The charge collection of the sample is measured with the ALiBaVa system, using the MIP source to generate the signal.

3. **Annealing**: The babysensor is annealed for a certain amount of time at a certain temperature. The measurement software also tracks temperature ramps at the start and end of the annealing periods and takes them into account in the calculation of the equivalent annealing time at room temperature. The annealing is done in situ, using the thermoelectric elements of the ALiBaVa setup.

A single ALiBaVa measurement consists of a calibration, a pedestal run and a source run. The analyses for each annealing study are queued with the alibava analysis pipeline (introduced in Section 5.3.5) and each step is performed automatically with the help of the MC measurement scheduler (introduced in Section 5.3.2). The measurement temperature for IV and ALiBaVa measurements was set to $-20\,°C$. Two bias voltages were used: 600 V, being the operation voltage in the future Phase-2 Tracker, and 800 V, being an optional value to boost the bias voltage to in the experiment if the charge collection is not sufficiently high at 600 V due to radiation damage. For each annealing step, a cluster and seed signal is extracted from the ALiBaVa measurement.

To normalize all charge measurements, the number of electrons generated by a MIP traversing an unirradiated babysensor n_{theo} calculated in Eq. (2.12) is used. At the begin of each campaign, a randomly selected, unirradiated babysensor is used to account for any potential drift in

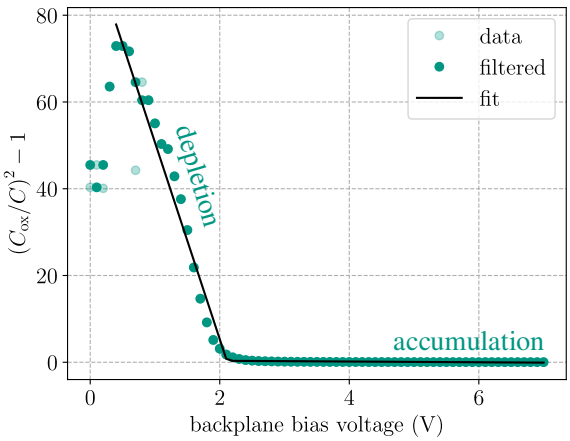

(a)

Parameter	Value
backplane bias	−2 V to 5 V, 0.1 V steps
curr. compliance	300 µA
AC signal	250 mV at 10 kHz
temperature	20 °C

(b)

Figure 7.3.: (a) Sample CV curve of a MOS structure before irradiation. The states introduced in Section 6.2.4 are annotated. (b) Measurement settings for the CV curves of MOS structures before irradiation.

charge collection over time. Every number of charges n_{meas} obtained during a charge collection measurement was scaled by campaign according to

$$n_{\text{calib}} = \frac{n_{\text{theo}}}{n_0} n_{\text{meas}},$$

with n_0 denoting the cluster charge measured for the reference sensor. The thresholds of the readout chips introduced in Section 4.3.2 are established at four times their noise level, shown in Eq. (4.1). The limits for seed charges is defined as three times their corresponding readout threshold levels. In other words, the charge limits for the sensor types are defined as twelve times their noise level

$$\text{limit(2S)} = 12\,000 \text{ electrons} \qquad \textit{and} \qquad \text{limit(PS-s)} = 9600 \text{ electrons}$$

which defines limits for the seed charges presented in this work.

7.3. Electrical Characterization of MOS and GCD Structures

7.3.1. Before Irradiation

The following sections will discuss the electrical characterization of MOS and GCD structures before irradiation and the analysis methods used to evaluate the results.

MOS

The MOS structures were electrically characterized in the probe station prior to irradiation with x-rays. For MOS structures, CV curves were recorded with the measurement settings listed in Fig. 7.3b. A sample CV curve with the corresponding MOS states introduced in Section 6.2.4 is shown in Fig. 7.3a. In order to remain consistent with the analysis procedure presented in [Mül21], the capacitance C was normalized to the oxide capacitance under the aluminum gate C_{ox}, transforming the capacitance into a dimensionless quantity $(C_{\text{ox}}/C)^2 - 1$. The oxide capacitance C_{ox} is the same for all MOS structures since it is defined by geometry.

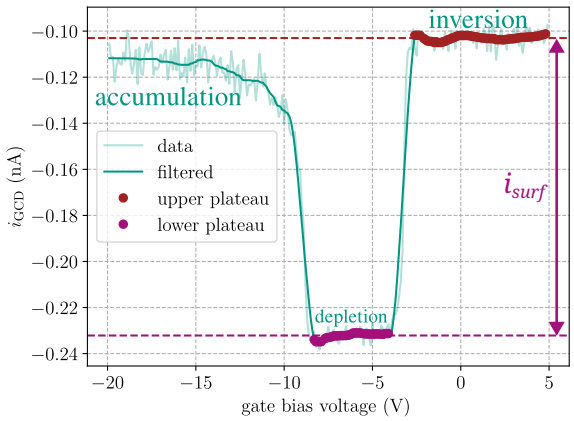

(a)

Parameter	Value
diode bias	constant −5 V
gate bias	−20 V to 5 V, 0.1 V steps
curr. compliance	30 µA
temperature	20 °C

(b)

Figure 7.4.: (a) Sample i_{GCD} curve of a GCD structure before irradiation. The states introduced in Section 6.2.5 are annotated. (b) Measurement settings for the i_{GCD} curves of GCD structures before irradiation.

To extract the flat-band voltage V_{fb} from the $C(V)$ measurement, first, a piece-wise defined function of form

$$f(V) = \begin{cases} m_1 \cdot V + b_1, & V \leq V_i \\ m_2 \cdot (V - V_i) + m_1 \cdot i + b_1, & V > V_i \end{cases}$$

is fitted to the data points of the CV curve. The first part of the function is a linear function with slope m_1 and intercept b_1 that describes the depletion region of the MOS characteristic. The second part with slope m_2 describes the accumulation region. The transition voltage V_i is the point where the two functions meet. Not all points of the depletion region are used for the fit. Points that are too far away from the linear region are excluded from the fit by repetitively fitting the function to the data points in the linear region, including more points from the left side and using the χ^2-metric for a goodness of fit test At most, ten points from the left side are excluded from the fit. The fit with the best χ^2 is used as the final fit to extract the flat-band voltage with

$$V_{\mathrm{fb}} = -\frac{b_1}{m_1}.$$

Theoretically, only the fit in the depletion region is needed to extract the flat-band voltage. However, the total piece-wise function is needed for the fit since the transition voltage V_i is not known a priori. The uncertainty in the flat-band voltage is determined from the diagonal of the covariance matrix of the fit. The fit uncertainties $\sigma_{b_1}, \sigma_{m_1}$ are propagated to the flat-band voltage using Gaussian uncertainty propagation, making

$$\sigma_{V_{\mathrm{fb}}} = \sqrt{\left(\frac{\sigma_{b_1}}{m_1}\right)^2 + \left(\frac{b_1 \sigma_{m_1}}{m_1^2}\right)^2}.$$

GCD

The GCD structures were electrically characterized in the probe station prior to irradiation with x-rays. For GCD structures, the current flowing through the GCD diode i_{GCD} as a function of the backplane bias voltage was recorded with the measurement settings listed in Fig. 7.4b. A sample i_{GCD} curve with the corresponding states introduced in Section 6.2.5 is shown in Fig. 7.4a.

Table 7.5.: *Specific treatment* for MOS capacitors [Mül21]. MOS and GCD structures passed the same stations during characterization. The *specific treatment* was performed on all MOS and GCD structures.

Process	Info
irradiation	40 kGy at −20 °C
annealing	30 min at 60 °C
relaxation	2 h at RT in laboratory
measurement × 2	V_{fb} and i_{GCD}
relaxation	30 min at RT in probe station
final measurement	V_{fb} and i_{GCD}

Extraction of the surface generation velocity works by identification of plateaus in the i_{GCD} curve. The lower plateau corresponds the depletion region of the GCD device, while the upper plateau corresponds to the inversion region. As described in Section 6.2.5, the difference between the two plateaus is used to extract the surface current i_{surf}. Before irradiation, the current in the plateau regions are not exactly constant but vary due to electronic noise. Therefore, the average current in the plateau regions is used to extract the surface current. Equation (6.2) is used to convert the surface current to the surface generation velocity s_0. The uncertainty in the surface generation velocity is calculated by adding the standard errors of the two plateaus in quadrature and propagating the uncertainty to the surface generation velocity using Eq. (6.2).

7.3.2. *Specific Treatment*

For every MOS and GCD structure, a *specific treatment* [Mül21] was performed. The steps of the *specific treatment* are listed in Table 7.5. The treatment consists of a series of electrical measurements and a special annealing procedure and is meant to make the results obtained for the flat-band voltage of MOS structures reproducible. It is based on oberservations made during the qualification of the pre-production MOS structures for the Phase-2 Tracker. A drift of the flat-band voltage was observed after irradiating them to the target dose, even when stored in a freezer. This makes it difficult to obtain a meaningful value for the flat-band voltage of a MOS structure. In order to mitigate this effect, the *specific treatment* was developed. The surface current i_{GCD} measured in the GCD structures did not show any significant drift after irradiation. Thus, the *specific treatment* would not have been necessary for these structures. However, since the MOS and GCD structures were not diced apart, the *specific treatment* was performed on MOS and GCD structures alike. The only steps affecting i_{GCD} after irradiation are annealing and relaxation. However, as long as these steps are performed on all structures, the effects on i_{GCD} are of systematic nature and thus, the results are still comparable. The risk of breakage during an additional MOS/GCD dicing process was deemed too high, so the *specific treatment* was performed on all structures.

7.3.3. After Irradiation

The following sections will discuss the electrical characterization of MOS and GCD structures after irradiation. After irradiation with x-rays, the MOS/GCD structures were stored at −20 °C.

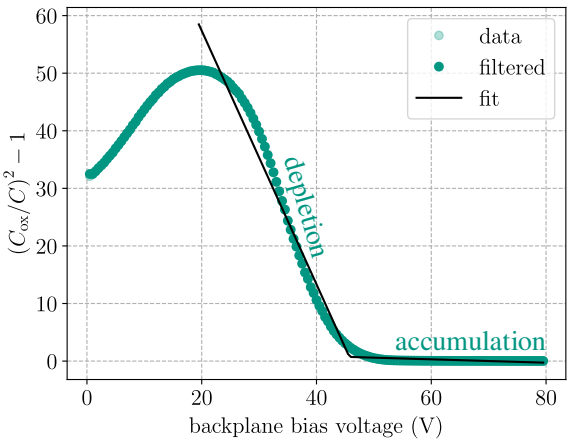

(a)

Parameter	Value
backplane bias	0 V to 80 V, 0.5 V steps
curr. compliance	300 µA
AC signal	250 mV at 10 kHz
temperature	20 °C

(b)

Figure 7.5.: (a) Sample CV curve of a MOS structure after irradiation. The states introduced in Section 6.2.4 are annotated. (b) Measurement settings for the CV curves of MOS structures after irradiation.

MOS

The MOS structures were electrically characterized in the probe station after irradiation with x-rays during the execution of the *specific treatment*. A sample CV curve normalized to C_{ox} after irradiation is shown in Fig. 7.5a. The same algorithm as for the pre-irradiation measurements was used to extract the flat-band voltage. Figure 7.5b shows the measurement settings for the MOS structures after irradiation. Results in this work only include the final measurement of the flat-band voltage after the *specific treatment*.

GCD

The GCD structures were electrically characterized in the probe station after irradiation with x-rays during the execution of the *specific treatment*. Figure 7.6b shows the measurement settings for the GCD structures after irradiation. A sample i_{GCD} curve after irradiation is shown in Fig. 7.6a. Due to the higher absolute current after irradiation, the noise in the plateau regions is significantly lower in the plateau regions. Therefore, instead of using the average current in the plateau regions, the minimum current of the lower plateau and the maximum current of the upper plateau were used to extract the surface current.

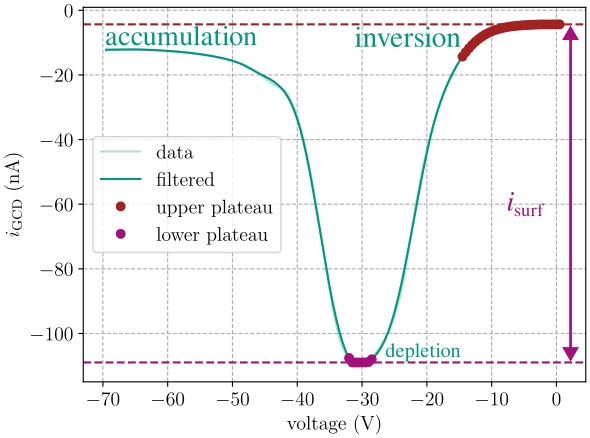

(a)

Parameter	Value
diode bias	constant −10 V
gate bias	−70 V to 5 V, 0.5 V steps
curr. compliance	300 µA
temperature	20 °C

(b)

Figure 7.6.: (a) Sample i_{GCD} curve of a GCD structure after irradiation. The states introduced in Section 6.2.5 are annotated. (b) Measurement settings for the i_{GCD} curves of GCD structures after irradiation.

8 Results

The following sections will discuss the results obtained during the ITs for the CMS Phase-2 Outer Tracker sensor production. The results that will be presented in this chapter were used during the production phase of the sensors to ensure that the sensors produced by HPK are of sufficient quality regarding radiation hardness. The results are divided into proton-irradiated and x-ray-irradiated samples. Measurement settings and extraction procedures of all relevant parameters are described in the previous Chapter 7. As previously explained, the batch numbers represent sequential production runs. Therefore, if the batch number is chosen as the x-axis of a plot, it can be interpreted as a proxy for production time.

The results that are presented in this chapter are mostly shown in the form of a fusion of box-whisker [Tuk77] and violin plots [Ha98]. Box-whisker and violin plots are a standardized way of reporting on the distribution of a set of data points based on particular quantiles, while violin plots additionally convey information about the density of the data points. Box-whisker plots show the median of the data set as a line in the box, while the box itself represents the interquartile range (IQR) of the data. The IQR is the range between the first and third quartile of the data set, which contains 50% of the data points. The whiskers extend to extremal data points of the data set that are not considered outliers. In this work, a variation of the original Tukey box-whisker plot is used, where the whiskers extend to the last data points that are smaller than three times the IQR instead of the usual 1.5 times the IQR. Following this definition, the whiskers can be different in length. While a different definition of the whiskers is not common, it is used in this work to avoid the appearance of outliers in the plots, while still showing the full range of the data to make for clearer plots. Violin plots also show the local

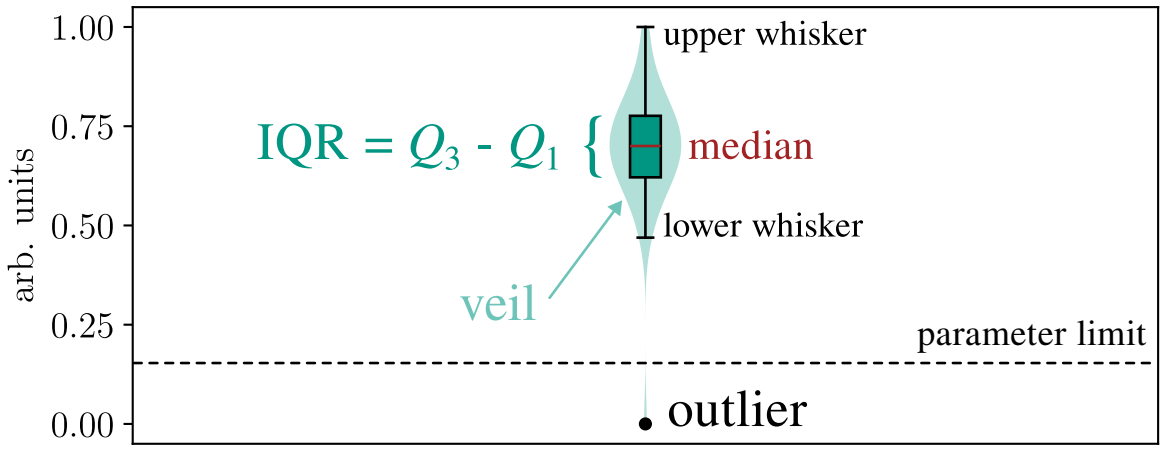

Figure 8.1.: Sample *veiled box-whisker plot*. The box-whisker plot shows the median and IQR of the data set, while the veil shows the local density of the data points. The whiskers extend to the last data points that are smaller than three times the IQR. Limits on parameters will be displayed as dashed lines.

Table 8.1.: Requirements for babysensor and diode test structures before and after irradiation. These values represent limits on the parameters. All bulk current-related specifications do not apply after irradiation due to the leakage current scaling with fluence. After irradiation, R_{int} is loosely defined by the requirement of R_{poly}. No breakdowns are allowed under a bias voltage of 800 V.

Parameter	Before Irradiation		After Irradiation
	Lower Limit	Upper Limit	Limit
$I_{\text{bulk,baby}}(600\,\text{V})$	—	96 nA	—
$I_{\text{bulk,diode}}(600\,\text{V})$	—	20 nA	—
$I_{\text{bulk}}(800\,\text{V})$	—	$2.5 \times I_{\text{bulk}}(600\,\text{V})$	—
i_{leak}	—	23.5 nA	—
R_{poly}	1 MΩ	2 MΩ	unchanged
$C_{\text{c,2S}}$	62 pF	—	unchanged
$C_{\text{c,PS-s}}$	70.5 pF	—	unchanged
i_{diel}	—	10 nA	unchanged
R_{int}	4.26 GΩ	—	$> 10^2 \times \mathcal{O}(R_{\text{poly}})$
C_{int}	—	1.175 pF	unchanged

density of the data points, obtained by kernel density estimation. In this work, this density feature is displayed as a veil around the box-whisker plot. Figure 8.1 shows an example of such a *veiled box-whisker plot*.

8.1. Proton-Irradiated Samples

This section deals with results obtained for the proton irradiations performed on babysensors and diode test structures. Sensors from batches of the same campaign were measured within a short time frame of about three weeks. Table 8.1 summarizes the requirements on the parameters of babysensor and diode test structures before and after irradiation. These requirements are based on the specifications on CMS Phase-2 OT sensors listed in Table A.3. No requirements on properties related to the bulk current (I_{bulk} and i_{leak}) are defined after irradiation, since the leakage current scales with the fluence of the irradiation. However, the Phase-2 OT Group specified that no new dysfunctional strips should be created after irradiation, which means that the remaining strip parameter specifications still apply — except for the interstrip resistance R_{int}, which is loosely defined by the requirement of R_{poly}. In order to ensure sufficient hit efficiency, the interstrip resistance R_{int} must be at least two orders of magnitude larger than the bias resistor resistance R_{poly}, regardless of the radiation damage that has been inflicted on the sensor. Furthermore, the breakdown voltage of the sensors must remain above 800 V after irradiation. Limits will be included as dashed lines in the plots of the results, as shown in Fig. 8.1. Each box will represent a batch containing the data of all sensors that were measured from that batch. The number of sensors measured for each batch is listed in Table A.2. A consistent color scheme will be used for all plots in this chapter. Green boxes and veils represent 2S type structures, while Blue boxes and veils represent PS-s type structures. Additionally, each campaign is colored as follows: Blue for campaign 1, Red for campaign 2, Green for campaign 3, Yellow for campaign 4, and Black for campaign 5. The background in all veiled box plots will be colored according to the campaign of the data set. The colors might appear less saturated when they are used as background colors.

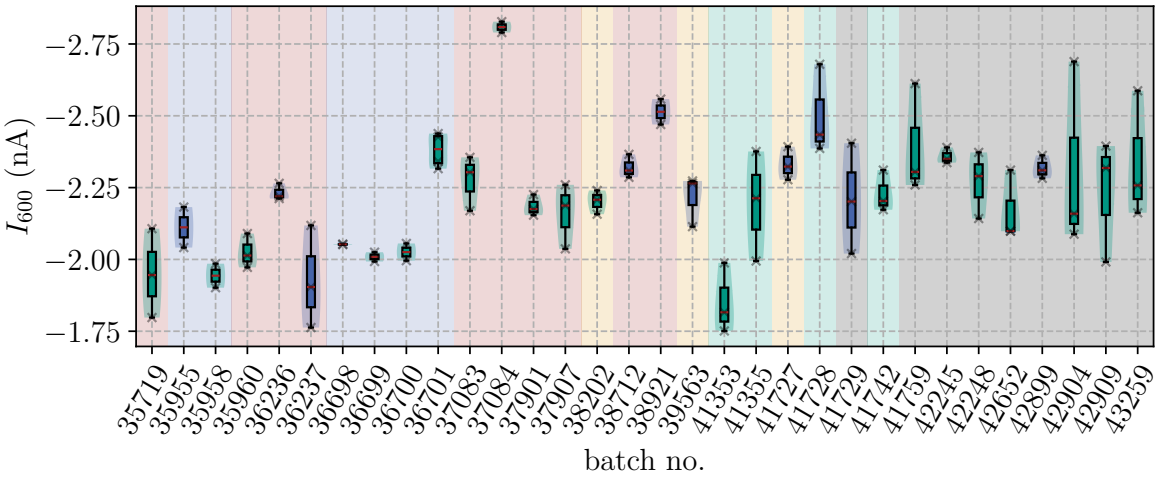

Figure 8.2.: Bulk leakage currents of babysensors before irradiation. Individual data points for each batch are shown as crosses. The color code used here is described on Page 94.

8.1.1. Electrical Qualification Before Irradiation

Bulk Current

IV curves were measured for all babysensors and diodes before irradiation. From these IV curves, the bulk leakage current at a bias voltage of 600 V was extracted. Therefore, the number of data points in each box is equal to the number of sensors measured. Since usually three babysensors and two diodes were measured from each batch, the number of data points in each box is usually three or two, which means that, for this metric, few data points contribute to each box. Therefore, the individual data points are shown as crosses here. Figure 8.2 shows the bulk leakage current of all measured babysensors at a bias voltage of 600 V before irradiation. All recorded values are well below the upper limits and thus, they fulfill the requirements. Sensors from batches until including 36 237 consistently show about 250 pA less leakage current than sensors from later batches. However, all of the sensors showed leakage currents that are well below the upper limit and therefore, all tested sensors are usable for further irradiation testing. Figure 8.3 shows the bulk leakage current of all measured diodes at a bias voltage of 600 V before irradiation. All recorded values are well below the upper limits and thus, they fulfill the requirements and are usable for further irradiation testing. As expected, diodes generally draw less current than babysensors, due to their lower active volume. The diodes from batches until including 36 237 show a lower leakage current than the diodes from later batches with the difference being about 100 pA. The same trend was observed for full-sized sensors of early (pre-)production dates, as well, comparing with data from [Wit23]. This combined with the fact that the same behavior was observed for both babysensors and diodes, suggests that the difference in leakage current is due to a change in the production process of the sensors.

Babysensors from batch 37 084 systematically show a significantly higher leakage current than other sensors. PQC centers also observed anomalies with respect to the p-stop sheet resistance and flat-band voltage for this batch. Diodes of this batch did not show a high leakage current, which means that this effect is most likely exclusive to structures that contain a p-stop implantation. The microscopic reason for this behavior is not yet known. Babysensors and diodes that showed breakdown voltages lower than 1000 V or increased current towards the end of the IV curve were excluded from further measurements since they are not representative of

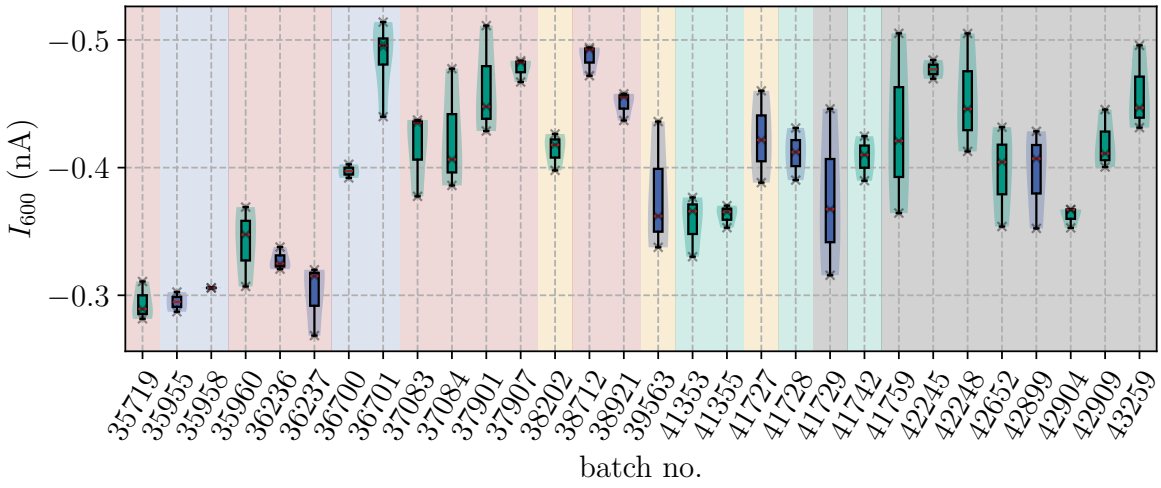

Figure 8.3.: Bulk leakage currents of diodes before irradiation. Individual data points for each batch are shown as crosses. The color code used here is described on Page 94.

the statistical majority of the structures. Additionally, since the irradiation of these structures is a cost-intensive process, structures were favored for further testing that are definitively operable. An early breakdown most likely indicates a defect in the structure, whose effects on sensor performance are unpredictable.

Strip Leakage Current

The following sections will discuss results obtained with the strip scan measurements before irradiation with protons. All quantities that will be discussed are explained in Section 6.2.2. In contrast to the bulk current measurements, per sensor, 60 strips were measured, which means that the number of data points in each box is equal to the number of sensors multiplied by 60, making for a much larger data set. In total, about 5500 strips were tested for the strip scans of the babysensors. Figure 8.4 shows the strip leakage current of all babysensors before irradiation. All measured values are well below the upper limit for i_{leak} and thus, all tested sensors fulfill the requirements. Occasionally, strips were found that drew a significantly higher current than the average of the batch. Such strips are called *leaky strips* and are most likely caused by mechanical defects in the sensor or contamination of the sensor surface and, thus, are not representative of the general production quality of the sensors. Therefore, sensors with leaky strips were excluded from further irradiation testing to increase the yield of tests after irradiation.

Bias Resistor Resistance

In Fig. 8.5, the bias resistor resistances of all babysensors before irradiation are shown. The data show very little spread and all resistances remain well within the limits of $(1.5 \pm 0.5)\,\text{M}\Omega$. The low spread not only within a batch but also between batches suggests a very high amount of control over the production of the bias resistors by HPK. This result is especially promising for subsequent charge collection measurements after irradiation with regard to a uniform potential distribution across the sensor, provided that the uniformity of the bias resistors is preserved after irradiation.

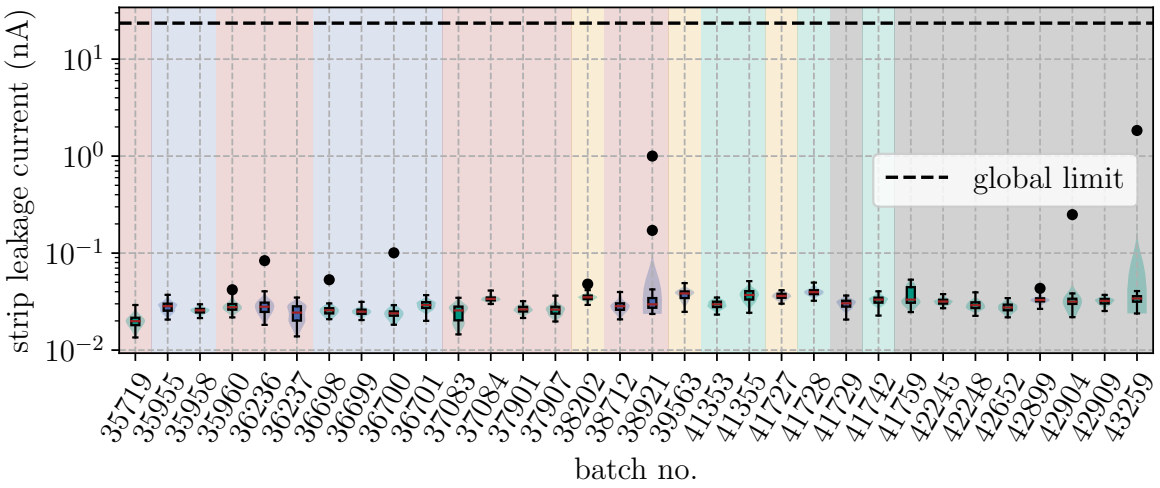

Figure 8.4.: Strip leakage currents of babysensors before irradiation. Each box includes data from 60 strips per babysensor, times the number of babysensors measured in that batch. The color code used here is described on Page 94.

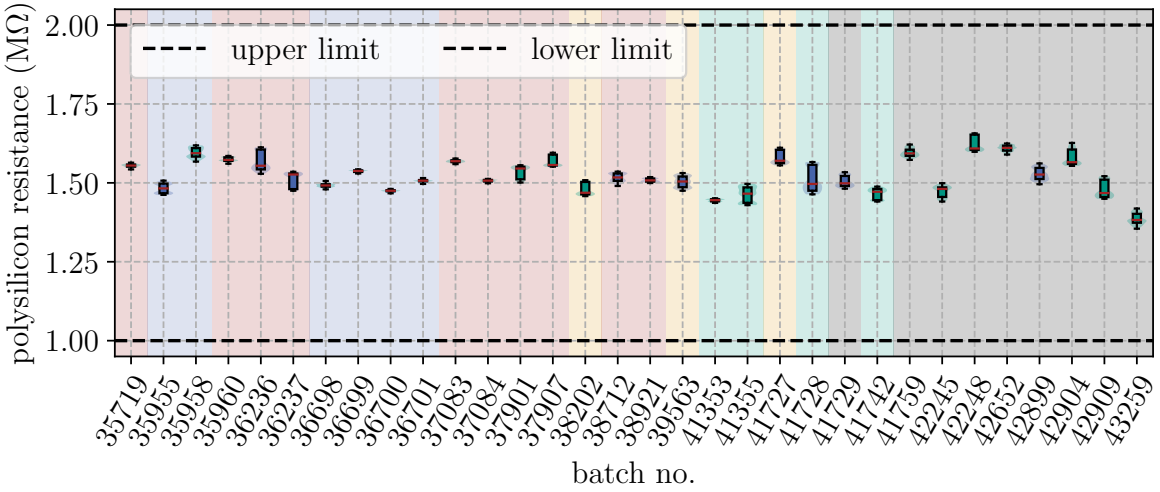

Figure 8.5.: Bias resistor resistances of babysensors before irradiation. Each box includes data from 60 strips per babysensor, times the number of babysensors measured in that batch. The color code used here is described on Page 94.

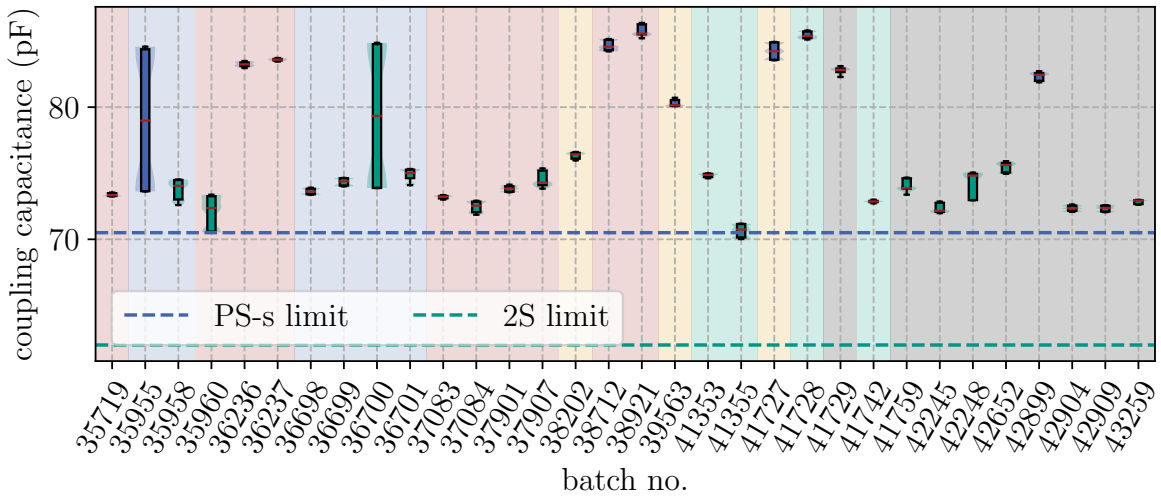

Figure 8.6.: Coupling capacitances of babysensors before irradiation. Each box includes data from 60 strips per babysensor, times the number of babysensors measured in that batch. The color code used here is described on Page 94.

Coupling Capacitance

Figure 8.6 shows the coupling capacitance of all babysensors before irradiation. Due to different implant widths, the lower limit for the coupling capacitance is different for 2S and PS-s sensors. All measured capacitances are above the lower limit and thus, all sensors fulfill the requirements. PS-s sensors systematically show a higher capacitance than 2S sensors, as expected due to the larger implant width. Generally, the capacitance values show a very low spread, which is a good indicator for a uniform coupling strength of the analog charge signal across the sensor. However, batches 35 955 and 36 700 show a significantly higher spread than the other batches. Examining the veils for these boxes reveals that the value distribution is bimodal. Two sensors were measured for both of these batches with all of their respective capacitance values at either end of the boxes. In other words, two sensors from each of these batches showed capacitance values that are not equal. Remeasuring these particular sensors yielded the same results even after a few months of storage, indicating that this effect is stable over time. The reason for this behavior is not yet known but can only be attributed to either a different oxide thickness or a different implant width for these sensors. Looking at how either ends of the IQRs are located at the 2S and PS-s levels, respectively, it seems as if 2S and PS-s sensors were mixed up for these batches during handling in the lab. However, measuring the strip pitches for both affected sensors showed that the sensors were, indeed, not mixed up and belong to the correct respective batch. In order to investigate the effect of irradiation on this bimodal behavior, both sensors were chosen for further irradiation testing.

Dielectric Current

Figure 8.7 shows the dielectric current of all babysensors before irradiation obtained from pinhole testing of the babysensors. Due to the very low currents for this measurement and the logarithmic scale, the data points are cut off from below. Out of the 5500 strips measured, only a single pinhole was found in batch 36 698 with a dielectric current in the order of $\mathcal{O}(100\,\mathrm{nA})$. In order to investigate the effect of irradiation on this pinhole, this sensor was chosen for further irradiation testing.

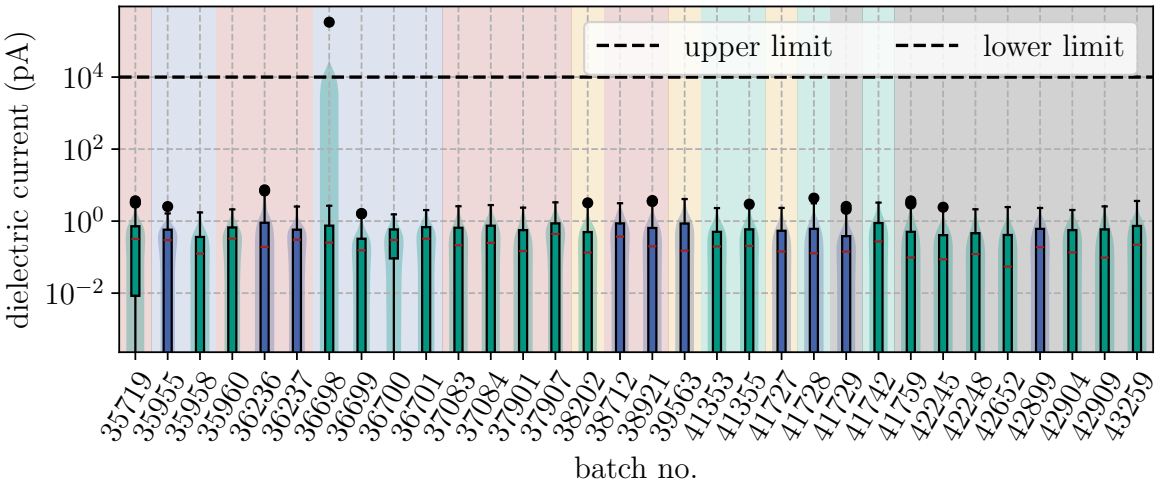

Figure 8.7.: Dielectric currents of babysensors before irradiation. Each box includes data from 60 strips per babysensor, times the number of babysensors measured in that batch. The color code used here is described on Page 94.

Interstrip Resistance

Figure 8.8 shows the interstrip resistance of all babysensors before irradiation. The interstrip resistance remains well above the lower limit for all measured sensors, although large spreads are observed, which is due to the method used to measure R_{int}. Before irradiation, the interstrip resistance is very high, which leads to a miniscule current flowing between the strips during the measurement. This current is usually in the order of the resolution limit of the picoammeter, which leads to a large spread in the measured values. Additionally, a poor needle contact would lead to a higher resistance value, which would not be immediately obvious among the already high resistance values. Therefore, the data distribution is expected to be skewed towards higher values, additionally. However, a strip defect resulting in low R_{int} for that strip would be detected easily due to the higher current drawn, which would exclude the sensor from further testing. This was not the case for any of the sensors measured and even though the currents were close to the resolution limit, meaningful data could be obtained. However, especially high spread is observed for measurements performed during campaign two (shown with a red background). Batches from campaign one (shown with a blue background) with an earlier production date do not show this behavior. Therefore, anomalies stemming from the production process are not expected to be the cause of this behavior. The spread being lower for all other campaigns suggests that this was an effect related to the measurement setup that was only present during the time of campaign two.

Interstrip Capacitance

Figure 8.9 shows the interstrip capacitance of all babysensors before irradiation. All recorded values are well within the limit, although the high number of outliers might be surprising at first. However, these outliers are expected when measuring C_{int} of a babysensor with a finite number of strips. The observed outliers correspond to the interstrip capacitance of strips that are located close to the edge of the sensor. Generally, C_{int} remains constant in the middle of the sensor but decreases towards the last four strips on each side of the sensor. The exact origin of this behavior is not yet known but two hypotheses seem plausible:

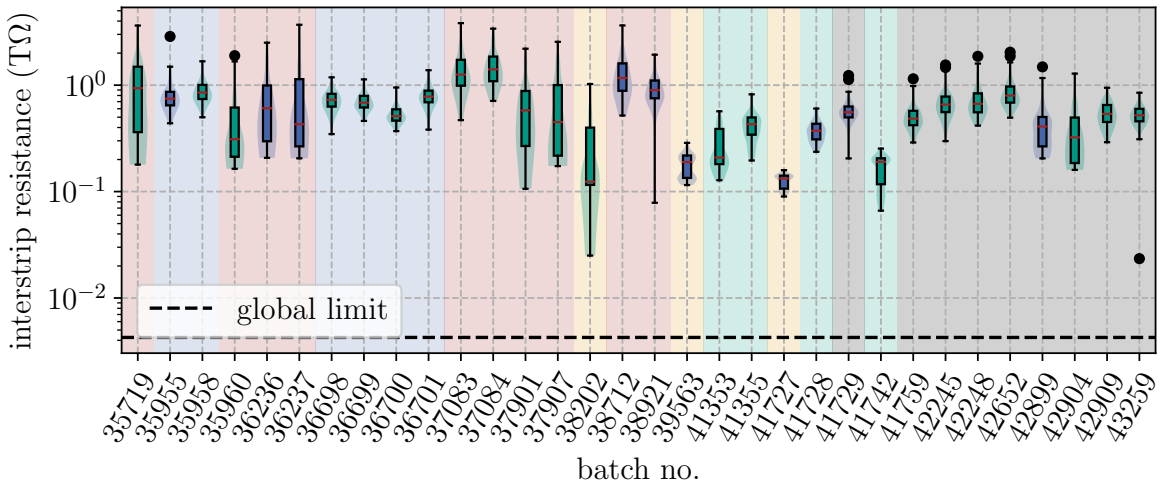

Figure 8.8.: Interstrip resistances of babysensors before irradiation. Each box includes data from 60 strips per babysensor, times the number of babysensors measured in that batch. The color code used here is described on Page 94.

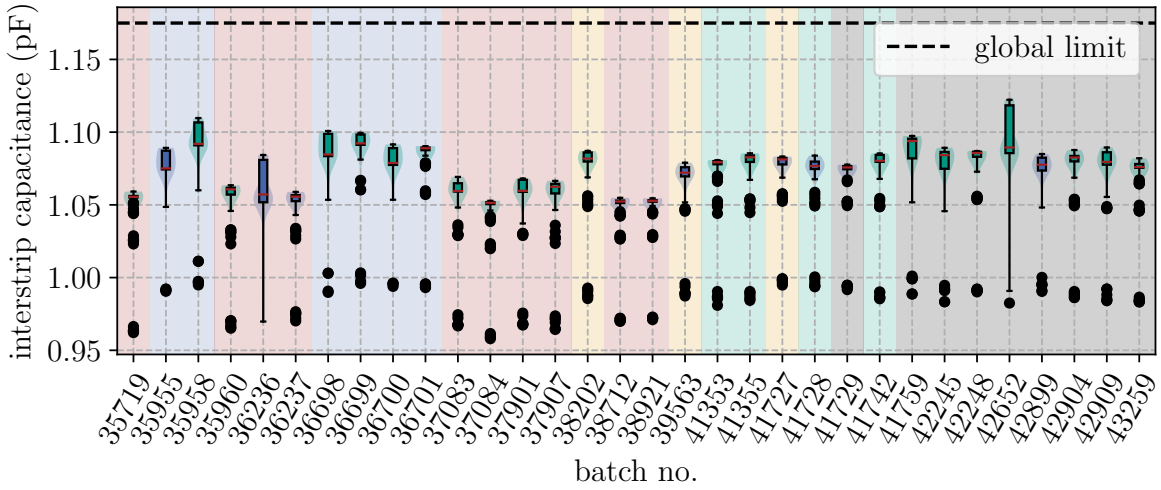

Figure 8.9.: Interstrip capacitances of babysensors before irradiation. Each box includes data from 60 strips per babysensor, times the number of babysensors measured in that batch. The color code used here is described on Page 94.

1. The measured capacitance value of a strip in the middle of the sensor is screened by the capacitance of the neighboring strips.
2. The inhomogeneous electric field at the edge of the sensor leads to a different capacitance value. This would mean that grounding the guard ring of the sensor — which was not done for the measurements in this work — would lead to a different behavior.

Although this issue was not investigated further during SQC [Wit23], it certainly warrants further investigation in the future, even if it is only for academic interest. In any case, neither edge nor middle strips showed values that were out of specification and, thus, all sensors are usable for further irradiation testing in the scope of this work.

Summary

To summarize the results of the electrical characterization of test structures located on 2S and PS-s wafers before irradiation, almost all babysensors and diodes measured before irradiation showed values that are well within the limits, demonstrating the excellent quality of the sensors produced by HPK. The only exception to this is one babysensor from batch 37 084, which showed a significantly higher leakage current than the other sensors. The sensors from batches 35 955 and 36 700 showed a bimodal distribution of the coupling capacitance, which was not observed for any other batch. Only one pinhole was found in batch 36 698. All of the sensors showing such anomalies were chosen for further irradiation testing.

8.1.2. Electrical Characterization After Irradiation

The following sections will discuss results obtained with the electrical characterization after irradiation. As explained, the characterizations after irradiation with protons were performed on a subset of the sensors that were irradiated with protons and characterized before irradiation.

Bulk Current

Figure 8.10 shows the IV curves of all babysensors after irradiation, grouped by measured fluence and campaign. IV curves were obtained by calculating a median curve for each campaign, aggregating the IV curves of all sensors from that campaign that received the same fluence. In other words, since all 2S sensors received the 2S fluence and all PS-s sensors received the PS-s fluence, the IV curves of all 2S sensors were averaged and the same was done for the PS-s sensors for each campaign. A band is shown for each curve, representing the minimum and maximum of the data points used to calculate each median curve. Minima and maxima are shown instead of standard deviations or confidence intervals to show possible breakdowns following radiation exposure or handling. Due to careful handling, irradiation and storage of the sensors, no breakdowns were observed for any of the sensors. The IV curves of the sensors after irradiation show a significant increase in leakage current compared to the IV curves before irradiation, as expected. Two groups of curves can be distinguished, belonging to the two different target fluences for 2S and PS-s sensors. As expected, the PS-s sensors show a higher leakage current than the 2S sensors, due to their higher fluence. The form of the IV curves follows the expected square-root behavior of a pn-junction, while before, the leakage current had a strong influence from the lateral growth of the SCR. An example of this behavior is shown in Fig. A.1 in the appendix for a babysensor from batch 41 355 before irradiation. This influence has decreased after irradiation, as expected, and thus, the curves are more similar to the expected behavior of a pn-junction even though full depletion is not necessarily reached, even for high bias voltages. This effect had already been observed in previous measurements of the IV curves of irradiated sensors [Eli19].

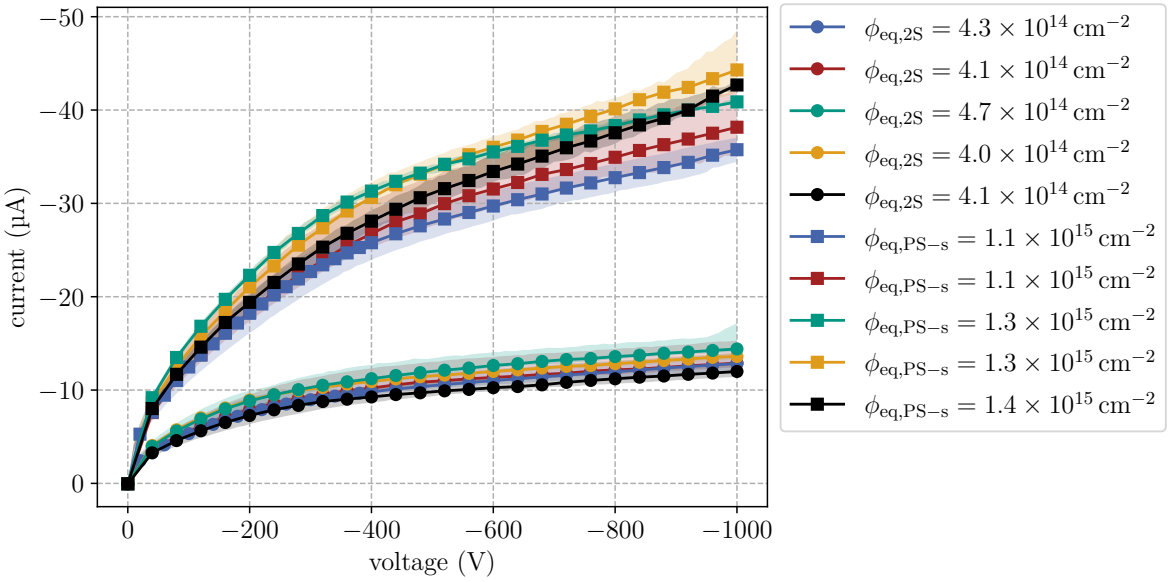

Figure 8.10.: Bulk leakage currents of babysensors after irradiation. Bands around each median curve represent the minimum and maximum of the data points used to calculate each curve. Circle markers denote data from 2S babysensors, square markers show data from PS-s sensors. The color code used here is described on Page 94.

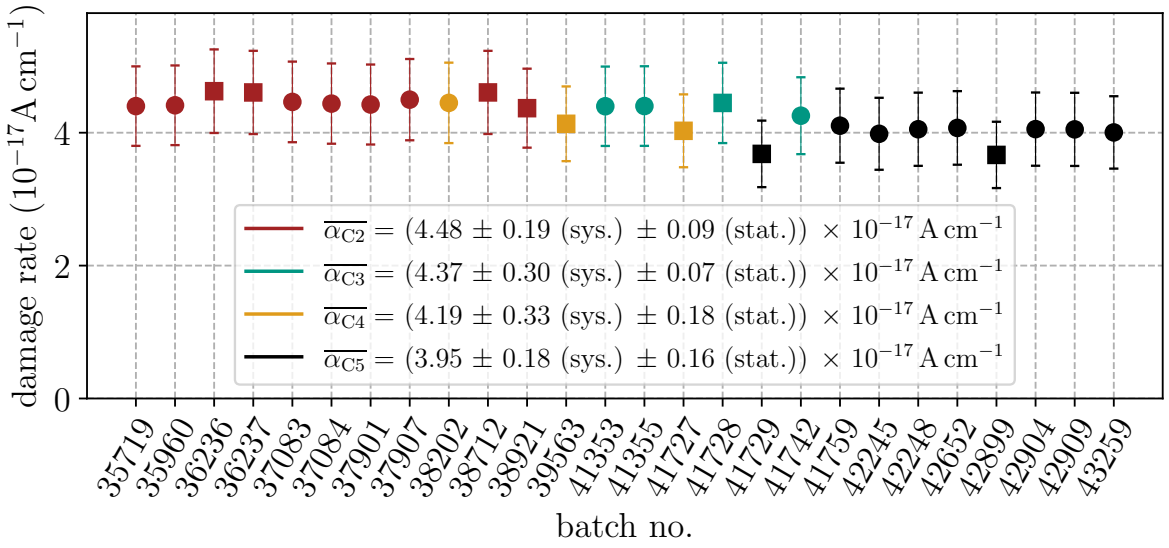

Figure 8.11.: Damage rates of diodes after irradiation with Monte-Carlo-simulated uncertainties obtained from temperature and irradiation fluence uncertainties. Weighted means with both statistical and systematic uncertainties are shows per campaign. Square markers are PS-s sensors, 2S sensors are shown as circles. The color code used here is described on Page 94.

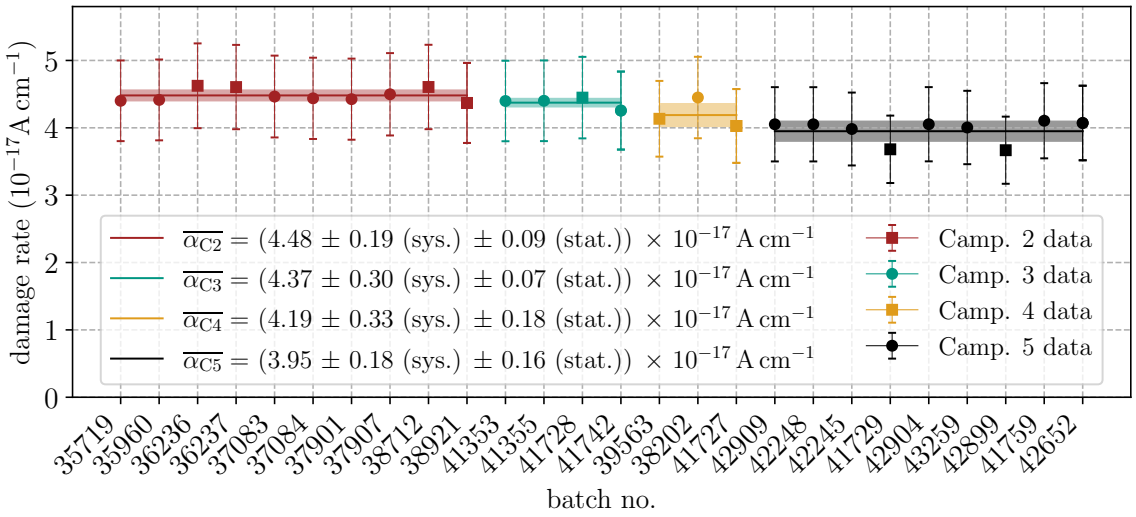

Figure 8.12.: Damage rates of diodes after irradiation with protons, sorted by irradiation campaign. A slight downwards trend is visible from campaign to campaign. The color code used here is described on Page 94.

Figure 8.11 shows the current-related damage rates α_{eq} of all characterized diodes after irradiation and the special annealing procedure. As already explained in the previous chapter, damage rates were extracted from the IV curves of diodes with a grounded guard ring to explicitly confine the electric field to the pad area of the diode. Equation (3.1) was used to extract the diode leakage current ΔI at a bias voltage of 600 V from the IV curves. The wafer design of the diodes yields a value of 7.366 mm^3 for the active volume V. Using these values and calculating the uncertainty in the measurement from Eq. (7.1), the α_{eq}-values for each batch is calculated. This specific method of measuring diodes was not introduced to the common measurement procedure until campaign two, which means that damage rate data is not available for campaign one. For each campaign, weighted means are calculated to obtain the final damage rates per campaign α_{Cn}, where n is the campaign number. The weighted uncertainties got the Monte-Carlo-simulated uncertainty from Eq. (7.1) as input and were taken as the systematic uncertainties for each weighted mean. The standard deviation from calculating the mean represents the statistical uncertainty. The results suggest a mostly constant damage rate throughout 50% of the production phase. Furthermore, results obtained in this work are compatible with the damage rate found in [Mol99], the literature source mentioned in the previous chapter. The study in this literature that investigated pad diodes similar to the ones tested in this work found $\alpha_{\text{lit}} = (3.99 \pm 0.03) \times 10^{-17}\,\text{A cm}^{-1}$. The compatibility of the results is especially surprising since the IV characteristics of the diodes in [Mol99] had a voltage region in which the current clearly saturated while diodes examined in this work do not saturate even at 600 V. This can either be attributed to a significant portion of the SCR extending in the lateral direction with increasing voltage compared with the diodes in [Mol99] or a stronger impact of surface effects in the diodes examined in this work. In any case, since the operation voltage in the future Phase-2 Tracker will be 600 V, the damage rates were extracted at this voltage to allow for extrapolations of sensor currents during operation. Despite the uncertainty in measurement temperature and especially in the irradiation fluence, meaningful values could be extracted. Although the damage rates remain mostly stable in time, a slight downwards trend in α is visible. This effect becomes more apparent when sorting the values by campaign,

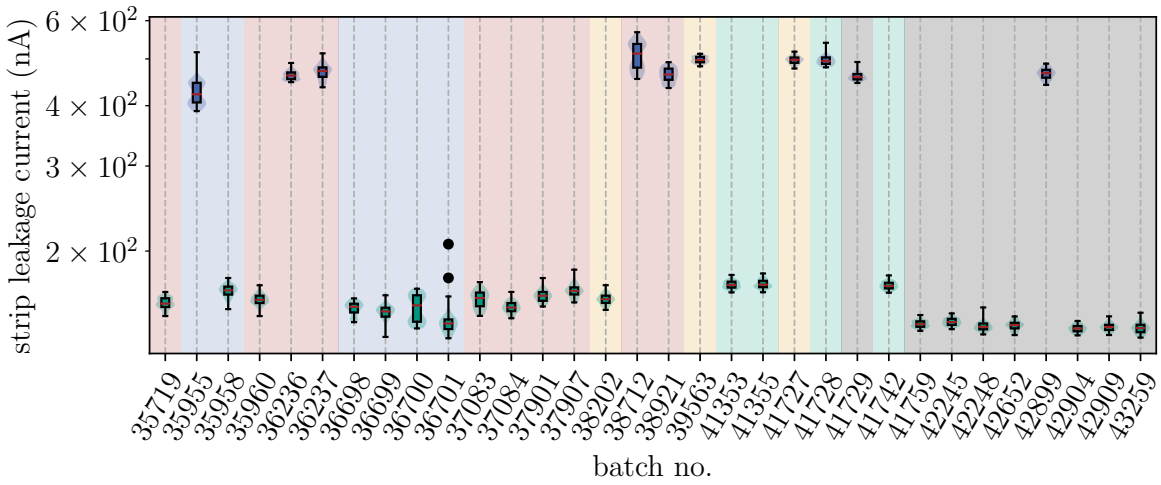

Figure 8.13.: Strip leakage currents of babysensors after irradiation. Each box includes data from 60 strips per babysensor, times the number of babysensors measured in that batch. The color code used here is described on Page 94.

as shown in Fig. 8.12. The trend appears to develop from campaign to campaign rather than with increasing batch number. Were this trend more significant, it would suggest a drift in either radiation delivery, current measurement or annealing procedure. However, due to the large window of uncertainty no such claim can be made at this point in time. The number of campaigns would have to be increased to make a more statistically sound statement about this alleged drift. However, if this trend is not related to any of the aforementioned sources of error, it would suggest an increasing radiation hardness of the structures, nonetheless. So, as far as ITs in the scope of quality control is concerned, these results are at least satisfactory.

Strip Leakage Current

In the following sections, results obtained with the strip scan measurements after irradiation with protons will be discussed. In total, about 3800 strips were tested for the strip scans of the babysensors after irradiation, which is less than the number of strips tested before irradiation due to the fact that only a subset of the sensors was chosen for further testing.

Figure 8.13 shows the strip leakage current of all babysensors after irradiation. As was the case for the bulk leakage current, the strip leakage current is also divided into 2S and PS-s sensors, which is the expected behavior since the strip leakage current is linearly related to the total bulk leakage current. Apart from some minor outliers observed for sensors from batch 36 701, nothing out of the ordinary can be reported.

Bias Resistor Resistance

Figure 8.14 shows the bias resistor resistance of all babysensors after irradiation. Compared to the measurements before irradiation, the resistances of the bias resistors have increased significantly. However, this is not the result of radiation damage acting on the resistors but rather an effect of the measurement conditions attributed to the lower temperature of −20 °C for measurements after irradiation compared to +20 °C before irradiation. The aforementioned effect has already been observed in [Fis20]. This offset is observed for every sensor, regardless of the applied fluence, which already suggests that the increase in resistance is not due to radiation damage. Figure 8.15a shows the scaling of the bias resistor resistance with temperature as

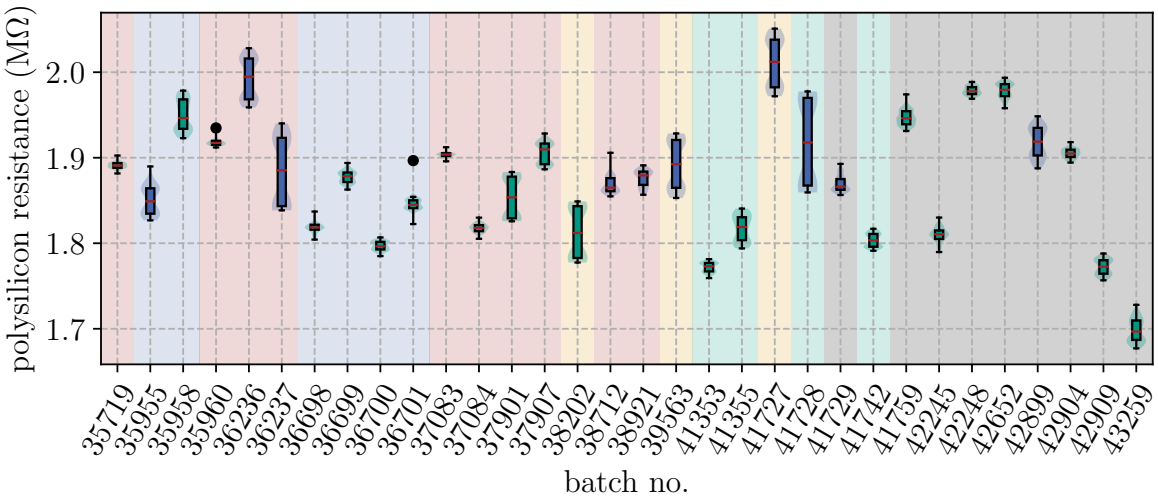

Figure 8.14.: Bias resistor resistances of babysensors after irradiation. Each box includes data from 60 strips per babysensor, times the number of babysensors measured in that batch. The color code used here is described on Page 94.

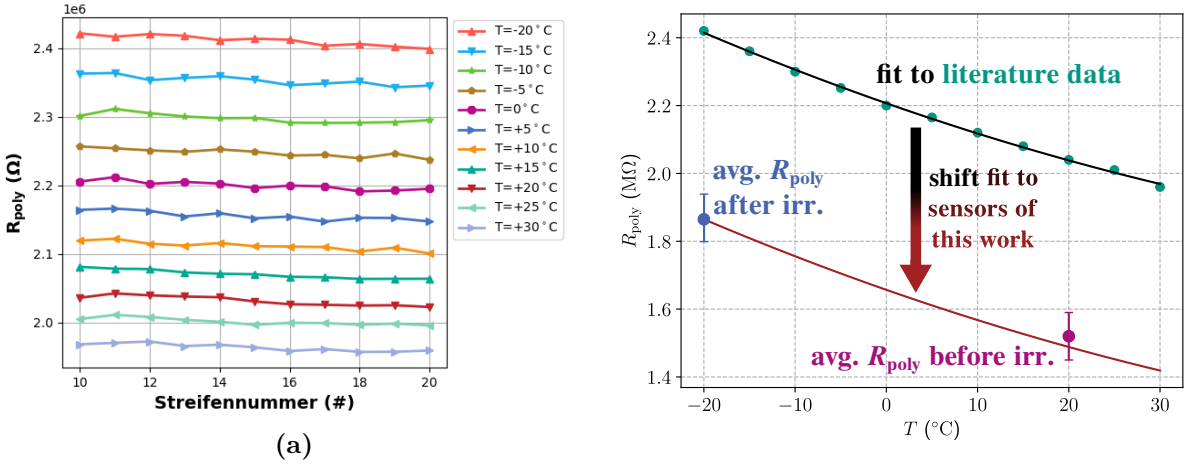

(a) (b)

Figure 8.15.: (a) Data for scaling of R_{poly} with temperature according to the reference work in [Fis20]. (b) Fit to the literature data and subsequent offset correction to sensors measured in this work. Details in main text.

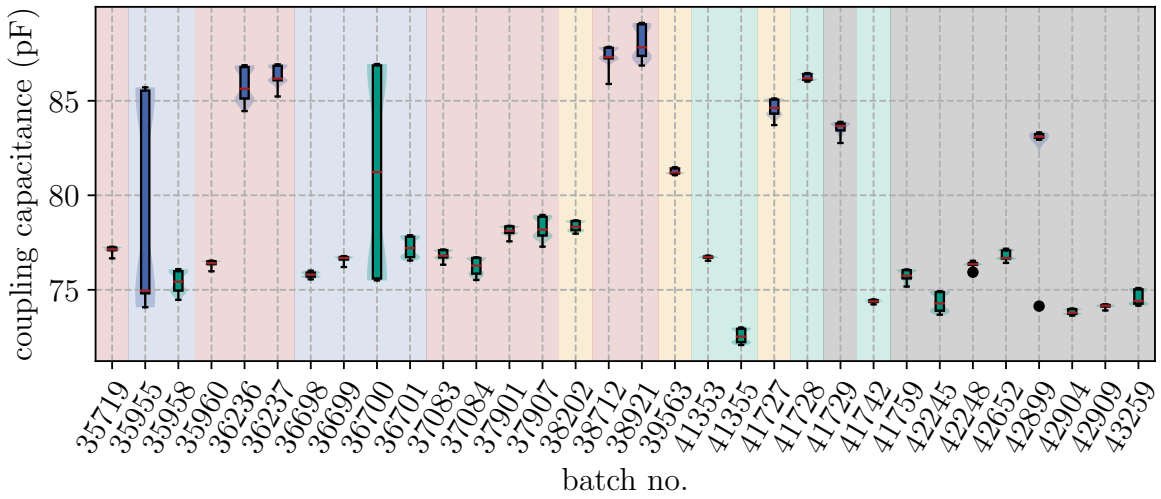

Figure 8.16.: Coupling capacitances of babysensors after irradiation. Each box includes data from 60 strips per babysensor, times the number of babysensors measured in that batch. The color code used here is described on Page 94.

measured in [Fis20]. In order to further underline that the increase in resistance is not due to radiation damage but rather to temperature, the literature data was fitted with a second order polynomial, shown as a black line in Fig. 8.15b. Since sensors with different (higher) R_{poly} resistances from the sensor R&D phase were measured in the literature [Fis20], the fit needed to be corrected for the offset in bias resistance. This offset, shown as a black to red gradient in the plot, is calculated by subtracting the average of the bias resistances measured in this work after irradiation from the fit values, yielding the red line in Fig. 8.15b. Plotting the average value for R_{poly} before irradiation (shown in purple) with the standard deviation as error bars shows that this value is well within the range of the fit, ultimately confirming the initial assumption. In conclusion, when the bias resistances measured after irradiation are corrected for the temperature offset, no significant change in resistance is observed after irradiation.

Coupling Capacitance

Figure 8.16 shows the coupling capacitance of all babysensors after irradiation. As expected, the irradiation did not have an impact on the coupling capacitance of the sensors, which means that the requirements for the pre-irradiation state are still met. The recorded values are almost identical to the values measured before irradiation. Due to the unchanged magnitude of the capacitance values after irradiation, both absolutely and with respect to each other, equivalent signal coupling as to before irradiation can be expected. The effect of batches 35 955 and 36 700 having sensors with different capacitance levels observed before irradiation is still present after irradiation. This not only means that irradiation did not have an impact on the capacitance values but also that the effect is stable over time. This emphasizes yet again that it is not due to a measurement artifact but a real effect that is present in the sensors.

Dielectric Current

Figure 8.17 shows the dielectric current of all babysensors after irradiation obtained from pinhole testing. Surprisingly, the sensor selected for closer investigation due to a pinhole, did

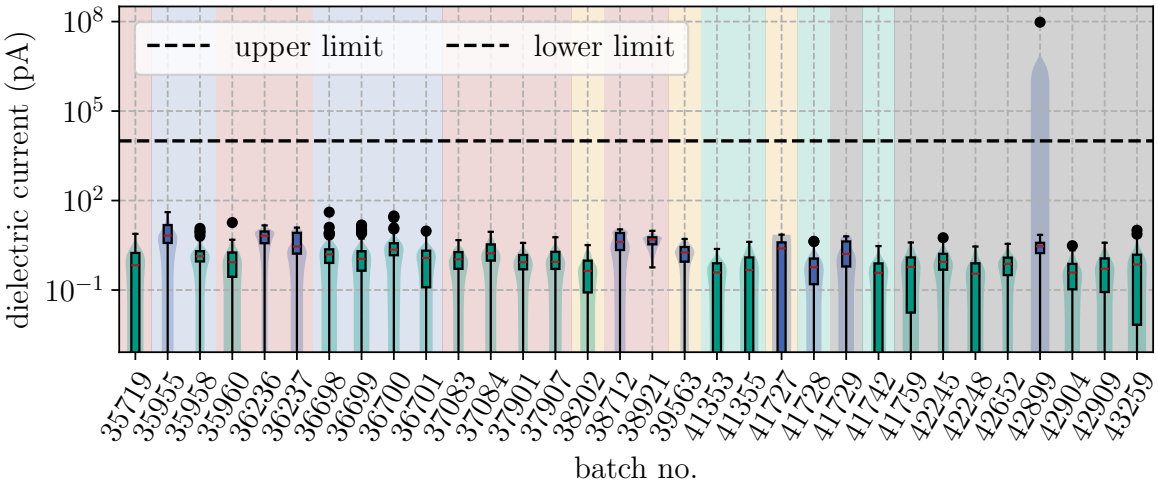

Figure 8.17.: Dielectric currents of babysensors after irradiation. Each box includes data from 60 strips per babysensor, times the number of babysensors measured in that batch. The color code used here is described on Page 94.

not show this pinhole after irradiation. But instead, a different sensor from batch 42 899 showed a pinhole. There are two possibilities for this behavior:

1. The pinhole observed initially was a measurement artifact or
2. the pinhole vanished after irradiation and subsequent annealing.

Since the sensor with the initial pinhole has already been put through the irradiation and annealing procedure, the measurement before irradiation cannot be repeated, which means that option one cannot be ruled out, although it seems unlikely that such a high current could be an artifact. The sensor has been remeasured several times after irradiation to definitively rule out a measurement artifact. However, the pinhole was not observed again. Option two also seems unlikely since the pinhole channel in the oxide layer is expected to be affected by neither the ionizing radiation nor the subsequent annealing. At this point in time, a definitive conclusion cannot be drawn, although the same effect of vanishing pinholes following radiation exposure has been observed for pre-production test structures in [Mül21]. The occurance of the additional pinhole in batch 42 899 is not optimal but also not unexpected. The dielectric current discovered on this pinhole is much higher than the dielectric current of the pinhole discovered before irradiation, which is expected since the leakage current after irradiation is significantly higher than before. In any case, radiation damage is not shown to affect the number of pinholes in a negative way, which is a good sign for the reliability of the sensors. Since the behavior observed with the pinhole of batch 36 698 is not statistically significant, no definitive claim that the irradiation has a positive effect on the number of pinholes can be made, either.

Interstrip Resistance

Figure 8.18 shows the interstrip resistance of babysensors after irradiation. After irradiation with protons, the interstrip resistance has decreased significantly, which is expected due to the radiation damage. This is also the reason why PS-s sensors consistently showed a lower interstrip resistance than 2S sensors as a result of the higher fluence. The variation in the observed R_{int} values within each batch is also much lower than before irradiation, which is

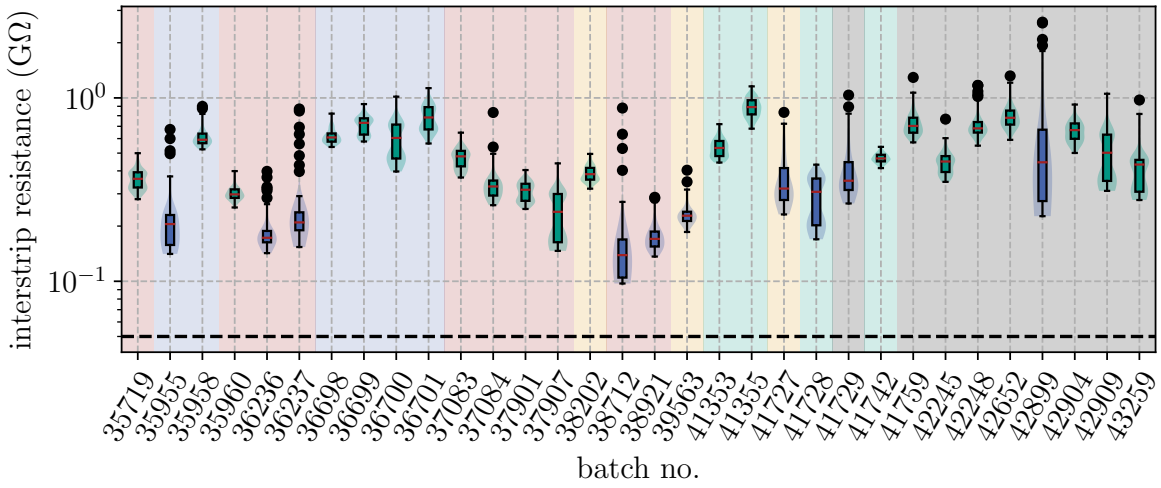

Figure 8.18.: Interstrip resistances of babysensors after irradiation. Each box includes data from 60 strips per babysensor, times the number of babysensors measured in that batch. The color code used here is described on Page 94.

the result of the overall lower interstrip resistance and thus, higher currents flowing between the strips during the measurement, leading to a better measurement resolution. Thus, the significantly higher data spread observed for campaign two before irradiation is not present after irradiation. In addition, all values remain at least two orders of magnitude above their respective bias resistances, indicating a sufficiently high interstrip isolation.

Interstrip Capacitance

Figure 8.19 shows the interstrip capacitance of babysensors after irradiation. The interstrip capacitance was not expected to significantly change after irradiation and indeed, the capacitance values are almost identical to the values measured before irradiation. The interstrip capacitance values are still well within the limits and due to their unchanged magnitude, capacitive charge sharing between neighboring strips is still expected to be the same as before irradiation. The systematic decrease in capacitance towards the edges of the sensor is still present after irradiation.

Summary

To summarize the results of the electrical characterization after irradiation, all babysensors and diodes measured after irradiation showed values that are well within the limits, demonstrating the excellent quality of the sensors produced by HPK. The only exception to this is the babysensor from batch 42 899, which showed a pinhole after irradiation. Unexpectedly, the pinhole that was observed before irradiation was not present after irradiation. The reason for this behavior is not yet known but it is most likely not related to the irradiation, although a definitive conclusion cannot be drawn at this point in time. The consistently higher polysilicon resistances after irradiation can be attributed to the lower measurement temperature of $-20\,°C$ and not due to radiation damage. Two sensors showing different coupling capacitance values observed before irradiation for batches 35 955 and 36 700 each is still the case after irradiation and is stable over time. The interstrip resistance and capacitance values are still well within the limits and the interstrip resistance is at least two orders of magnitude larger than the bias

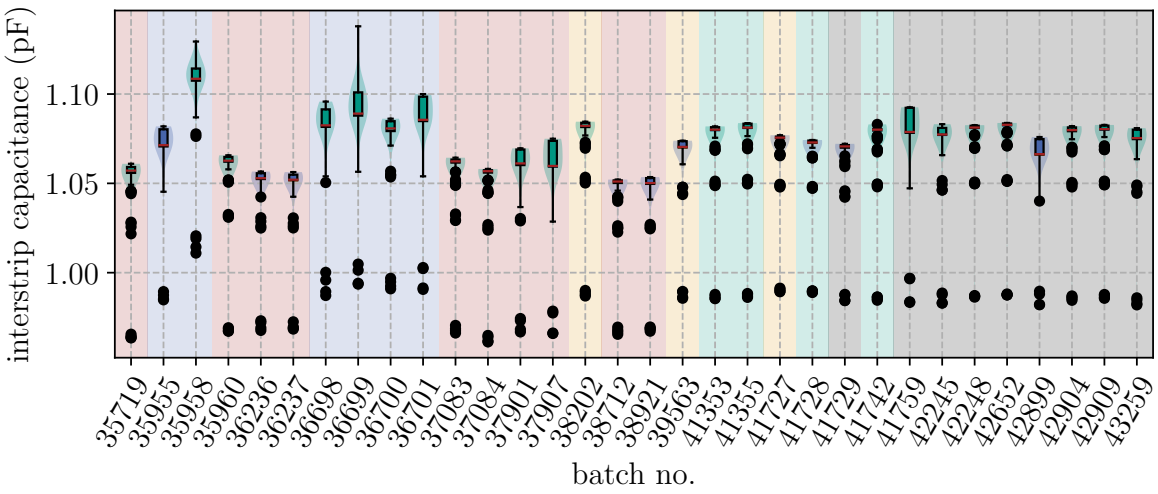

Figure 8.19.: Interstrip capacitances of babysensors after irradiation. Each box includes data from 60 strips per babysensor, times the number of babysensors measured in that batch. The color code used here is described on Page 94.

resistor resistance, indicating a sufficiently high interstrip isolation. Otherwise, no significant changes in the electrical properties of the sensors were observed after irradiation.

8.1.3. Charge Collection After Irradiation

This section will discuss the charge collection of babysensors after irradiation with protons. The comparability between all campaigns is ensured by scaling all charge values to a common reference using the technique described in Section 7.2.5. As expected, no significant drift in charge collection was observed in babysensors for the first half of the production phase before irradiation. Since the charge collection parameters are expected to be the same for all sensors before irradiation, which is also confirmed by these occasional samples per campaign, only the results of babysensors after irradiation will be discussed in the following sections. In the following plots, the intial reception annealing duration was subtracted from the total annealing duration to place the first step of the annealing study at 0 h. The same color code as introduced on Page 94 is used to distinguish between campaigns as in the previous sections. Circle markers are used for 2S sensors and square markers are used for PS-s sensors.

Cluster Signal

Figures 8.20a and 8.20b show the cluster signals of 2S and PS-s sensors, respectively, after irradiation with protons at a bias voltage of 600 V. No dashed limit line is shown in these plots since a signal limit is only defined on the seed signal. The results are separated by sensor type to present the data more clearly over the entire range of the annealing study. Cluster signals of 2S sensors are clearly higher than those of PS-s sensors, which is expected due to the higher fluence received by the PS-s sensors, which results in a higher trapping probability and lower amount of depletion. Not all PS-s sensors show the same annealing characteristic, though. Reverse annealing effects are increased for sensors that received a significantly higher fluence, e.g. 2S sensors from campaigns three and five and PS-s sensors from campaigns three to five, suggesting that the reverse annealing effect is fluence dependent, as expected. Both sensor types, however, show similar behavior with respect to the annealing duration. Clear beneficial annealing is visible for short annealing durations and reverse annealing is observed

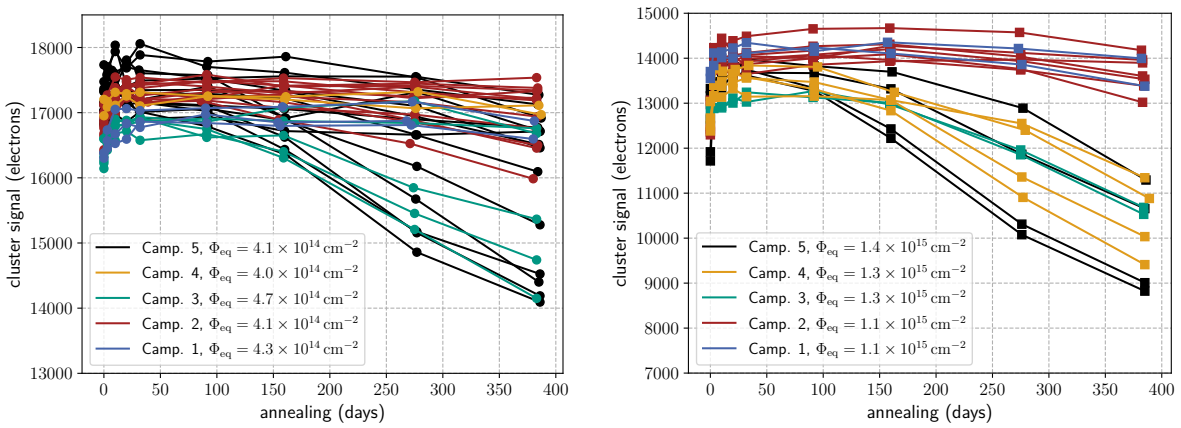

Figure 8.20.: Cluster signal as a function of equivalent room temperature (RT) annealing duration at 600 V for (a) 2S sensors and (b) PS-s sensors. The charge values are scaled to a common reference. The color code used here is described on Page 94.

for longer annealing durations. A separation of cluster charge curves is visible between most of the campaigns, although campaigns three and five show a significantly higher variation for the reverse annealing region. Batch-to-batch dependencies are visible especially for PS-s sensors. Pairs of two sensors emerged, belonging to one batch each, that showed virtually the same signal over annealing characteristic. A good example of this are PS sensors in Fig. 8.20b with signals at the lower end of the plot. At the same fluence, the pair-to-pair variation can amount to up to 1500 electrons. The variation within each campaign is on the same level, mostly owing to batch-to-batch spread rather than individual spread between sensors, meaning that sensors of the same batch tend to behave similarly, as expected. The specified uncertainty of the Beetle readout chip is comparable at 1000 electrons, which means that the results obtained in this study are indicative of a reliable measurement procedure.

Figures 8.21a and 8.21b show the cluster signals of 2S and PS-s sensors, respectively, after irradiation with protons at a bias voltage of 800 V. Again, no dashed limit line is shown in these plots since a signal limit is only defined on the seed signal. A clearer campaign separation is visible for the cluster signals at 800 V than at 600 V. The cluster signals of 2S sensors are still clearly higher than those of PS-s sensors, as expected. The pair-to-pair variation is still present and more pronounced than at 600 V, again especially apparent for PS-s sensors at the lower end of Fig. 8.21b. However, the reverse annealing region is significantly less pronounced than at 600 V; so much so that it is not even visible for 2S sensors. PS-s sensors still show reverse annealing effects, although less pronounced. Not only is less reverse annealing observed at this bias voltage, but also the beneficial annealing has increased. A possible explanation for this behavior could be that the higher bias voltage leads to a lower trapping probability of charge carriers due to higher drift velocities. Moreover, point defects are more easily untrappable at higher electric fields than cluster defects, which are the dominant defect type in the reverse annealing regime. In the beneficial annealing regime, point defects are dominant which leads to a higher charge collection efficiency at a higher bias voltage due to the higher probability of point defects being untrapped. Compared to the cluster charge at 600 V, the total signal is increased by about 1000 electrons for 2S sensors and 1500 electrons for PS-s sensors. The overall increase in charge collection is expected due to the higher electric field and more depletion. All in all, the results obtained for 800 V are consistent with the expectations and very promising

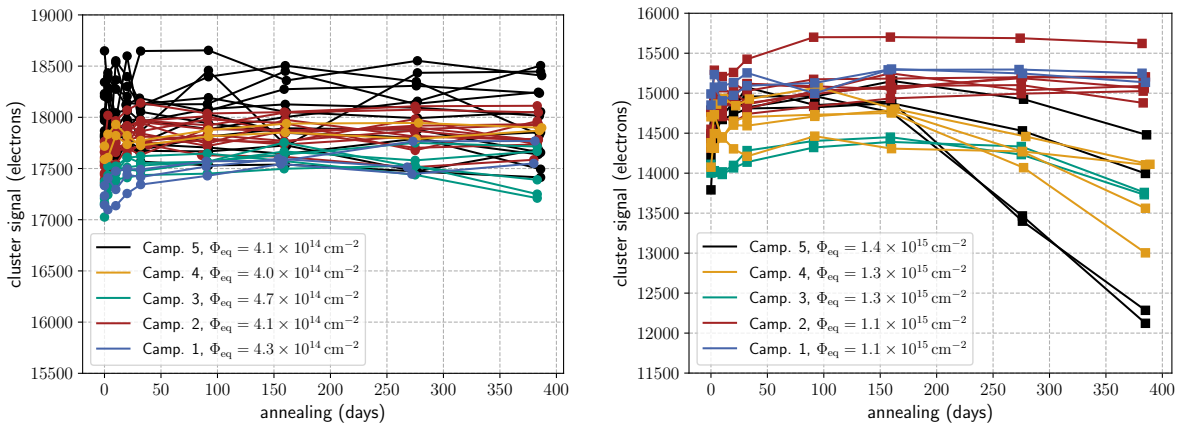

(a) **(b)**

Figure 8.21.: Cluster signal as a function of equivalent RT annealing duration at 800 V for (a) 2S sensors and (b) PS-s sensors. The charge values are scaled to a common reference. The color code used here is described on Page 94.

for the future Phase-2 Tracker. Not only can charge collection capabilities be increased by increasing the bias voltage, but also reverse annealing effects can partly be compensated for if deemed necessary. Although an increase in bias voltage would lead to significantly higher power consumption, the results show that this option is available and adds flexibility to the operation of the future Tracker. In order to isolate a specific bias voltage that maximizes the charge collection while minimizing the power consumption, a more detailed study of the bias voltage dependence of the charge collection would be necessary.

Seed Signal

Figures 8.22a and 8.22b show the seed signals of 2S and PS-s sensors, respectively, after irradiation with protons at a bias voltage of 600 V. All recorded signal values are mostly above their respective limits, indicating that single-hit capabilities will be satisfactory even at the projected end of lifetime for the Phase-2 Tracker. The recorded seed charges are systematically lower than the cluster charges, as expected, owing to the fact that the seed signal is only a subset of the cluster signal that contains the total charge collected by the sensor. The seed signal seems to be more prone to fluctuations than the cluster charges, which makes it impossible to observe the same clear separation between the campaigns as for the cluster signals. Additionally, sensors from the same batch could not be observed to behave similarly as was the case for the cluster signals, which is also a result of the higher spread in the seed signal. This spread can be attributed to the way the seed signal is extracted. Depending on the method of extraction — either fitting a Landau-Gauss distribution or using a cubic spline interpolation — the spread of the seed signal can vary significantly. While the spread for fitting a Landau-Gauss distribution to the data is a bit lower, the fit is not as robust as the cubic spline method, which is why the cubic spline method was used for the analysis in this work. Occasional data points dip slightly below the signal limits but could either be attributed to the aforementioned spread or the inherent uncertainty in the measurement. As was the case for the cluster signals, the PS-s sensors show a higher reverse annealing effect than the 2S sensors, owing to the higher fluence. Beneficial annealing was observed for both sensor types until about 150 days of equivalent RT annealing. The seed signal is still well above the limits at the benchmark annealing duration of 20 weeks, which means that beneficial annealing can

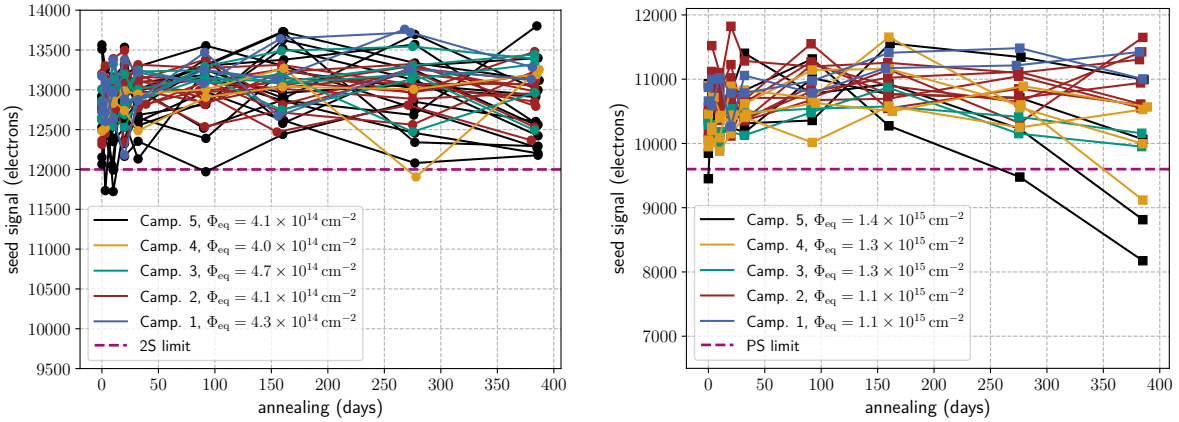

(a) **(b)**

Figure 8.22.: Seed signal as a function of equivalent RT annealing duration at 600 V for (a) 2S sensors and (b) PS-s sensors. The charge values are scaled to a common reference. The color code used here is described on Page 94.

be leveraged to increase the charge collection efficiency during the operation of the Phase-2 Tracker. However, annealing effects in general seem to be less pronounced for the seed signal than for the cluster signal.

Figures 8.23a and 8.23b show the seed signals of 2S and PS-s sensors, respectively, after irradiation with protons at a bias voltage of 800 V. The same spread as in the case of a bias voltage of 600 V is visible, although the campaign-to-campaign separation is slightly more pronounced, especially for campaign 2. As was the case for the cluster signal at the same bias voltage, the reverse annealing effect is less pronounced than at 600 V. However, in the case of the seed signal, no reverse annealing is observed at all. The seed signal rises over the entirety of the annealing study, which is a very unexpected but also promising result. All recorded seed charges are well above their respective limits, which was to be expected due to the higher bias voltage. Once again, this result demonstrates the possibility of increasing the bias voltage during operation of the Phase-2 Tracker to increase charge collection efficiency. Looking back at the history of the CMS experiment, projected end-of-lifetime luminosities have always been exceeded to some extent. Even if this would be the case during the Phase-2 era, the results suggest that additional margin is available in terms of charge collection efficiency by increasing the bias voltage.

Summary

To summarize the results of the charge collection measurements after irradiation, all babysensors measured after irradiation showed values that are well within the limits, demonstrating the excellent quality of the sensors produced by HPK. The sensors showed expected fluence dependencies, with the 2S sensors showing a higher charge collection than the PS-s sensors. The charge collection measurements were performed at two different bias voltages, 600 V and 800 V, to investigate the influence of the bias voltage on the charge collection efficiency. The results show that the charge collection efficiency can be increased by increasing the bias voltage, which is a promising result for the future Phase-2 Tracker. Depending on the bias voltage, reverse annealing effects were less pronounced than expected.

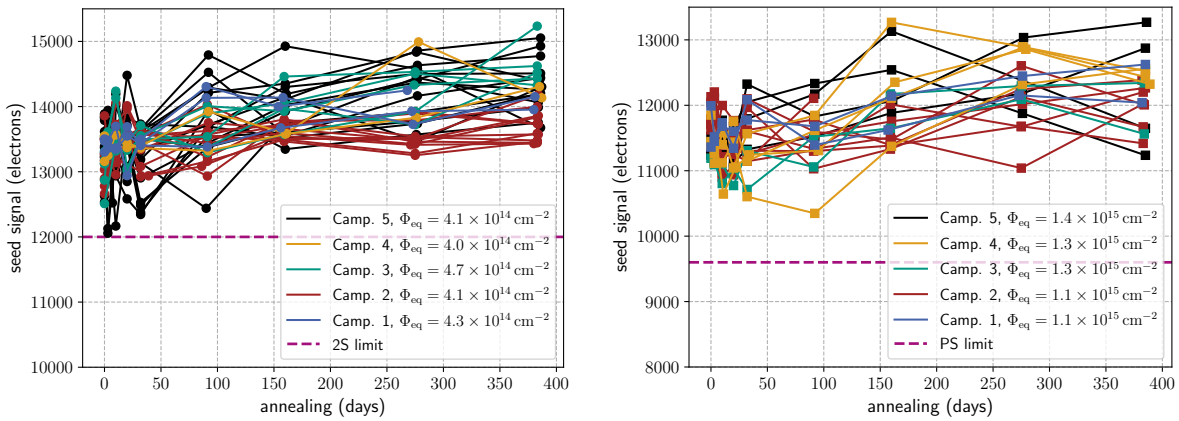

(a) **(b)**

Figure 8.23.: Seed signal as a function of equivalent RT annealing duration at 800 V for (a) 2S sensors and (b) PS-s sensors. The charge values are scaled to a common reference. The color code used here is described on Page 94.

8.2. X-Ray-Irradiated Samples

The following sections will discuss the results obtained for the MOS/GCD structures that were irradiated with x-rays. Structures that were selected for irradiation have all been subjected to the *specific treatment* described in Section 7.3.2. As explained previously, the notion of campaigns is not applicable to the x-ray irradiation, which is why the background of the veiled box plots are not colored. The only requirement defined for theses structures are a flat-band voltage that is less than 5 V before irradiation.

The flat-band voltage is determined from the CV curves of the MOS capacitors by fitting a piecewise function to the data. The uncertainty for each flat-band voltage is derived from the fit parameters. Median values across all measured structures are reported, with uncertainties calculated using a bootstrap method [Hor19], similar to the method used to evaluate the damage rates of the proton-irradiated diodes. This involves resampling the data set 10 000 times, assuming a normal distribution based on the original uncertainties. The median and standard deviation of the resampled data provide the median value and its uncertainty. Using this method, the statistical uncertainty was found to dominate over measurement uncertainty, so only the standard deviation is reported. For the surface generation velocity, no significant measurement uncertainties were identified, so no bootstrap method was applied in this case and just the standard deviation was used.

8.2.1. Properties of MOS and GCD Structures Before Irradiation

The following paragraphs discuss the results obtained with the MOS/GCD samples before irradiation with x-rays.

Flat-band Voltage

Figure 8.24 shows the flat-band voltage of all measured MOS capacitors before irradiation. All examined structures met the requirement of a flat-band voltage of less than 5 V before irradiation. A median value of (2.2 ± 0.3) V can be reported for the flat-band voltage of all structures examined over the course of 50% of the production era. This value is comparable to values reported by PQC, despite different methods of extracting the flat-band voltage from the

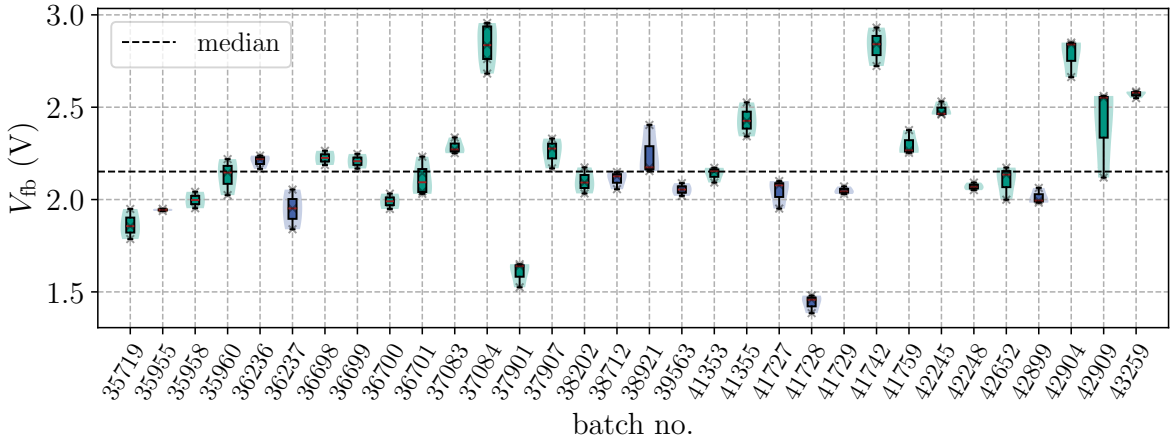

Figure 8.24.: Flat-band voltage of MOS structures before irradiation. Green and blue boxes show values obtained from 2S and PS-s structures, respectively.

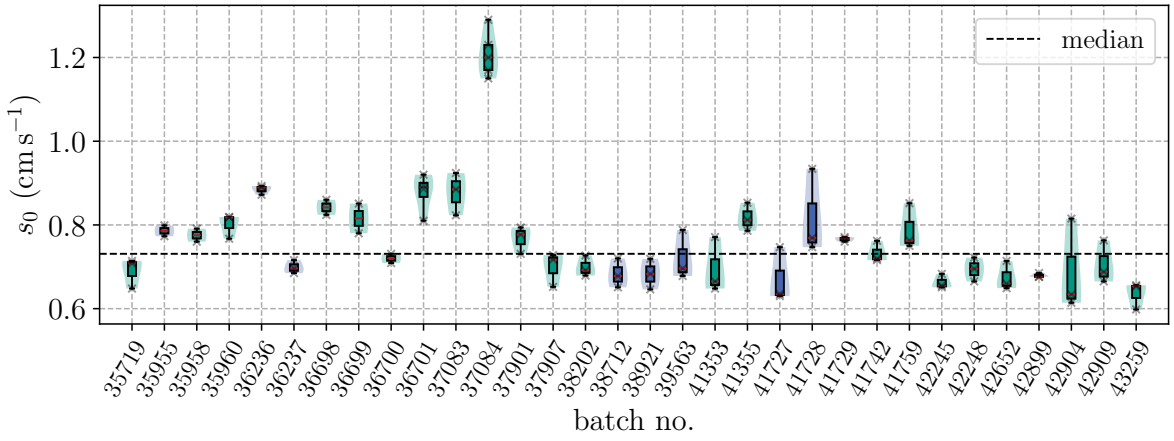

Figure 8.25.: Surface generation velocity of GCD structures before irradiation. Green and blue boxes show values obtained from 2S and PS-s structures, respectively.

CV curves. The values remain stable over time and the spread is very small, which confirms the excellent quality of the structures produced by HPK and suggests reproducibility of the measurement. Occasional high outliers are visible, e.g. batches 37 084 and 41 742, which are both production batches that showed anomalies in p-stop concentration. This matter will be discussed in more detail in Chapter 9. In order to increase the statistical significance of these outlier batches and as a form of sanity check, all five structures of each batch were measured, in contrast to the usual two to three structures per batch. The severity of these outliers in terms of the flat-band voltage is not high enough to be considered a problem. However, an interesting finding is that outliers within the context of all batches appear to be linked to specific production batches, which suggests that variations in V_{fb} are likely to be a batch-related phenomenon. This strongly suggests this effect to be due to a variation in the production process.

Surface Generation Velocity

Figure 8.25 shows the surface generation velocity of all measured GCD structures before irradiation. A median value of $(0.73 \pm 0.13)\,\mathrm{cm\,s^{-1}}$ is observed for the surface generation

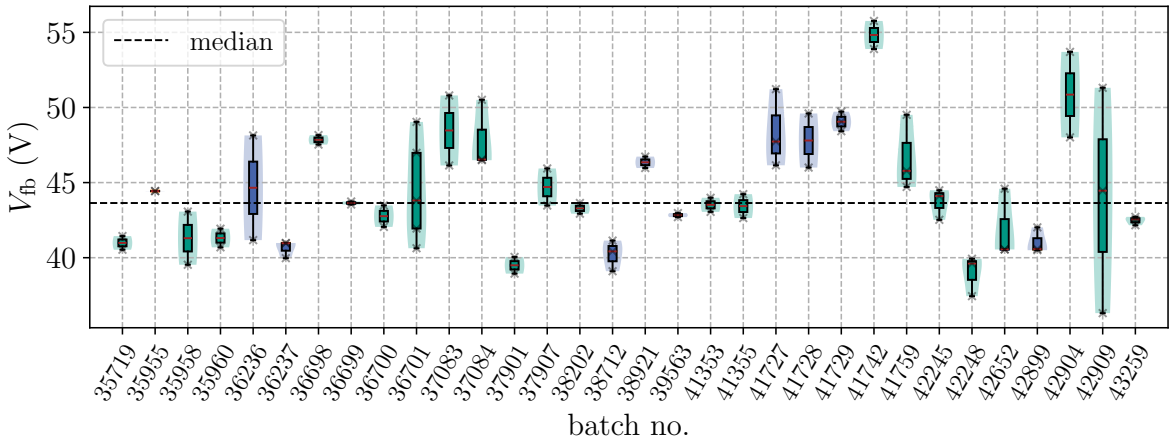

Figure 8.26.: Flat-band voltage of MOS structures after irradiation with x-rays. Green and blue boxes show values obtained from 2S and PS-s structures, respectively.

velocity of all structures. Like the flat-band voltage, s_0 remains very stable over time and the spread per batch is very small, indicating that the structures are of excellent quality. An especially high outlier batch 37 084 emerged with an s_0 that is almost twice as high as the median value. This batch is also the one that showed the highest flat-band voltage before irradiation, which is an expected effect since the surface generation velocity is related to the oxide charge density. As was the case for the flat-band voltage, all five structures of this batch were measured to increase the statistical significance of the outlier. Surprisingly, some batches that were outliers in terms of V_{fb} showed no outliers in s_0, e.g. batch 41 742, which was unexpected and currently unexplained. As was the case for the flat-band voltage, outliers are likely to be batch-related and due to variations in the production process.

8.2.2. Properties of MOS and GCD Structures After Irradiation

The following paragraphs will present the results obtained with the x-ray-irradiated MOS/GCD samples.

Flat-band Voltage

Figure 8.26 shows the flat-band voltage of all measured MOS capacitors after irradiation with x-rays up to 40 kGy. As expected, the flat-band voltage of all structures increased after irradiation due to the radiation-induced oxide charge and the resulting higher voltage needed to achieve flat-band conditions. A median value of (44 ± 4) V can be reported for the flat-band voltage of all structures examined over the course of 50% of the production era. No significant trends could be made out over time, indicating a stable irradiation procedure and good radiation hardness of the oxide layer. The outlier batch 37 084 did not show a significant increase in flat-band voltage after irradiation, which is unexpected, while the outlier batch 41 742 showed a slightly increased flat-band voltage after irradiation. Something that is worth noting is that the outlier batch 37 084 had shown an outlier in V_{fb} and not in s_0 before irradiation, while the outlier batch 41 742 had shown an outlier in both quantities before irradiation. While no obvious explanation for this behavior can be given at this point in time, future studies could pay more attention to this pattern to investigate whether this is a random effect or if there is a correlation.

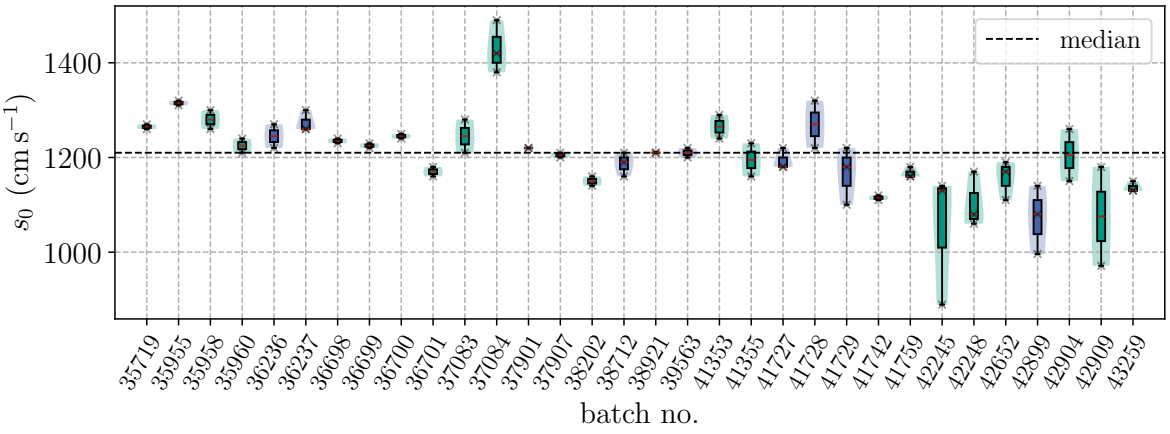

Figure 8.27.: Surface generation velocity of GCD structures after irradiation with x-rays. Green and blue boxes show values obtained from 2S and PS-s structures, respectively.

Surface Generation Velocity

Figure 8.27 shows the surface generation velocity of all measured GCD structures after irradiation with x-rays. Again, as expected, the surface generation velocity of all structures increased after irradiation due to the radiation-induced oxide charge. A median value of $(1210 \pm 90)\,\mathrm{cm\,s^{-1}}$ can be reported for the surface generation velocity of all structures examined over the course of 50% of the production era. A slight downwards trend is visible for the surface generation velocity over time, which is unexpected. This effect could arise due to a drift in the irradiation procedure, measurement method or be a real effect present in the oxide layer itself. Considering that the flat-band voltage did not show a similar trend, this effect could likely be attributed to a real effect in the oxide layer. While this is not an expected effect, it would indicate that the quality of the oxide layer is improving over time, which is a very good sign. As explained previously, interface traps are the main reason for surface generation current. A declining s_0 over time would specifically mean that the interface trap concentration is decreasing over production time. Batch 37 084 is again the outlier batch with a surface generation velocity just above $1400\,\mathrm{cm\,s^{-1}}$. While the relative difference to the median value is not as pronounced as before irradiation, it is still a significant outlier. This batch was therefore selected, among others, for further investigation of the p-stop concentration that will be discussed in Chapter 9.

8.2.3. Summary

All MOS/GCD structures showed values that are well within the limits before irradiation that remain stable over time, demonstrating the excellent quality of the structures produced by HPK. The flat-band voltage and surface generation velocity of all structures increased after irradiation with x-rays, as expected. The surface generation velocity showed a slight downwards trend over time, which is unexpected and could indicate a decline in the interface trap concentration over time. Flat-band voltages remained on a steady level over time. Outliers in both quantities were observed for specific batches, which could indicate a batch-related phenomenon. In combination with anomalous findings from PQC, this suggests that the production process is not as stable as it could be. A closer investigation of this phenomenon will be presented in Chapter 9.

9 P-Stop Inhomogeneity Study

As previously outlined in Section 6.1, the wafers produced by HPK need to undergo a series of QC tests before they can be accepted for the Phase-2 Outer Tracker. PQC is responsible for monitoring the process parameters that are not directly accessible on the sensors by using dedicated test structures. In particular, the electrical resistance of the p-stop implantation layer, also called p-stop sheet resistance R_{sheet}, using special Van-der-Pauw structures and the threshold voltage V_{FET} of field-effect transistors (FETs) are monitored. The p-stop sheet resistance is a measure of the resistivity of the p-stop implant and is expected to be uniform across the wafer. However, during the PQC measurements, some wafers showed an untypical variation in the p-stop sheet resistance and the threshold voltage of the FETs. For such wafers, p-stop sheet resistances varied across the four corners of the wafer that were probed by the PQC team and threshold voltages that are usually positive were negative. This is an indication of non-uniform properties of the p-stop isolation structures in the sensors. In the case of an anomalous p-stop implantation, sensor performance can suffer severely, as the p-stop implant is responsible for the interstrip isolation of the sensors. These fluctuations have been duely reported during the weekly meetings of the OTSEPP and discussed with HPK. The PQC team flagged these wafers as anomalies and recommended further investigation. A large topic of interest is the response of wafers that were affected by this issue to radiation. As part of this thesis, this issue was further investigated and a dedicated study was performed in communication with the OTSEPP and the vendor HPK. The following sections will go into more detail about this p-stop inhomogeneity study.

9.1. Measurement Program

Babysensors are the only test structures that are sensitive to the p-stop inhomogeneity and were therefore used for the study. Even though the effect discussed here is called an inhomogeneity, it is highly unlikely to manifest itself as such in a single babysensor, since the non-uniformity usually spans the whole wafer. Therefore, distinguishing between low and high p-stop sheet resistance R_{sheet} is the figure of merit in terms of these small sensors used to test this effect within the scope of this study. The previously discussed IT results obtained for babysensors showed that the p-stop inhomogeneity is not a problem for either the electrical parameters or the charge collection efficiency of the sensors when irradiated with protons. This is shown by anomalous batches performing well within the specifications, as shown in the previous section. In fact, almost all tested sensors showed good interstrip isolation, as seen in Fig. 8.18, and charge collection efficiency, as shown in Figs. 8.20 to 8.23, and discussed in the respective sections. However, the interstrip isolation is particularly sensitive to the formation of an inversion layer between the strips and the p-stop concentration. X-ray irradiation with a cutoff energy of 60 keV as used in this work is expected to promote the formation of an inversion layer and to effectively reduce the interstrip resistance between neighboring strips. X-Ray irradiation is therefore a good candidate to investigate the p-stop inhomogeneity. Proton irradiation introduces radiation damage in both the substrate and oxide layer. The effects

Table 9.1.: Auxiliary data for the p-stop inhomogeneity study. Parameters ΔR_{sheet} and $V_{\text{FET,min}}$ were measured by PQC and extracted from the CMS Phase-2 construction database as part of this work. The last column indicates whether the sensor was flagged as an anomaly by the PQC. Details in main text.

Batch	Samples	ΔR_{sheet} ($\text{k}\Omega\,\square^{-1}$)	$V_{\text{FET,min}}$ (V)	Anomaly?
36236	1	0.6	3.66	no
37083	1	0.7	3.54	no
38921	2	17.7	−0.58	yes
41353	2	3.8	2.89	no
41355	1	0.6	4.07	no
41742	3	17.1	−0.67	yes

of positive oxide charge are counteracted by positive donor levels in the substrate, which is probably why the p-stop inhomogeneity did not show up in the proton irradiation tests as an either low interstrip resistance or low cluster charge signal due to increased charge sharing. The connection between charge sharing and signal height is not immediately obvious and will be discussed in more detail in Section 9.3. X-ray irradiation represents a worst-case scenario for the p-stop inhomogeneity due to the lack of radiation damage in the substrate. A reference study in [MDN21] showed that the effect ionizing radiation has on the R_{int} saturates after a dose of about 20 kGy. In order to investigate the effect well beyond the saturation point, a dose of 40 kGy like in regular ITs was chosen.

In the following sections, three different parameters will be discussed:

1. **The interstrip resistance** R_{int} of the babysensors to investigate the electrical interstrip isolation,
2. **the cluster signal** to investigate if x-ray-irradiated babysensors show a different charge collection behavior than reference sensors and
3. **the average cluster size** to investigate charge sharing properties which are expected to be affected by variations in R_{int}.

For each batch that showed anomalies in PQC, two reference batches were chosen at random that were not flagged as anomalies that went through the same measurement program. After the irradiation, the babysensors were tested for R_{int} at the probe station and charge collection parameters were measured as part of an annealing study in the ALiBaVa setup with seed and neighbor cuts as described in Section 5.3.5. Table 9.1 shows a summary of the batches that were used for the p-stop inhomogeneity study. For each batch, the range of the p-stop sheet resistance ΔR_{sheet} over the whole wafer as well as the minimum threshold voltage $V_{\text{FET,min}}$ of the FETs on that wafer are shown. ΔR_{sheet} is used as a measure of the p-stop inhomogeneity, with larger values indicating a larger variation in the p-stop sheet resistance across the wafer, while $V_{\text{FET,min}}$ is a measure that was shown to correlate with p-stop non-uniformities by PQC centers. Batches that were flagged as anomalies by the PQC team are marked. Anomalous batches showed a significantly larger variation in the p-stop sheet resistance than the other batches and featured negative threshold voltages.

9.2. Interstrip Resistance

The babysensors that were irradiated with x-rays and the interstrip resistance R_{int} was measured in the probe station. All samples were placed into the probe station in the same orientation,

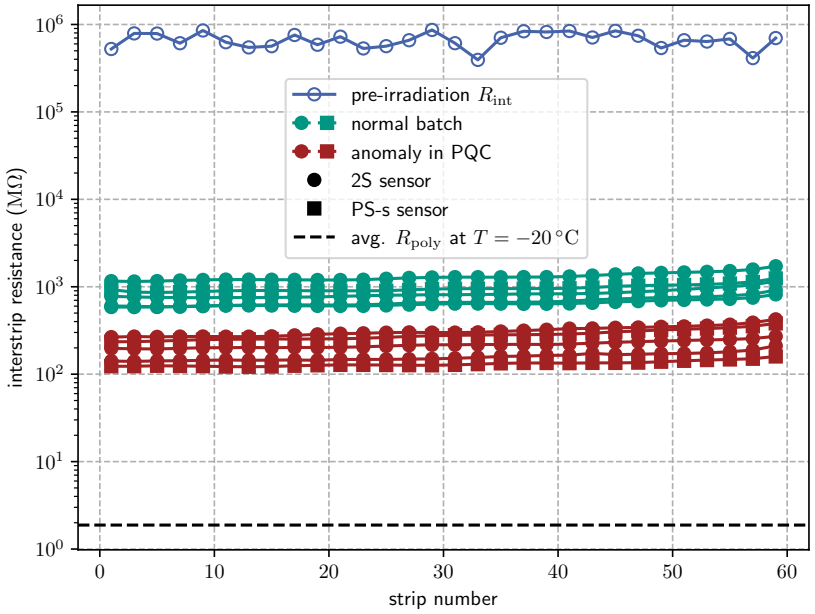

Figure 9.1.: The interstrip resistance of x-ray-irradiated babysensors as a function of the strip number measured at $T = -20\,°\mathrm{C}$. Babysensors without anomalies are marked in green, while sensors with anomalies during PQC are marked in red. For reference, the average R_{poly}-value at the same measurement temperature is indicated by a dashed line and a sample R_{int}-curve of a randomly selected sensor *before* irradiation is shown.

the polysilicon resistors facing the probe needles. The measurements were performed at a temperature of $-20\,°\mathrm{C}$ and a finer low voltage ramp compared to the common IT measurement was used to gather more data points for the R_{int}-fit (0 to 5 V in 1 V-steps).

Figure 9.1 shows the interstrip resistance R_{int} of the babysensors as a function of the strip number. A clear separation between the anomalous and non-anomalous batches can be seen. The anomalous batches show a significantly lower interstrip resistance after exposure to radiation than the non-anomalous batches. However, the interstrip resistance is still larger than the corresponding average R_{poly}-value of the babysensors by at least two orders of magnitude at the same measurement temperature. This is a clear indication that the babysensors are still in a good state and that the impact of the higher p-stop resistivity is not too severe. However, the results clearly show that the anomalous batches are affected by the p-stop resistivity for worse interstrip isolation compared to reference batches. Since a clear separation between anomalous and non-anomalous batches can be seen, one might infer that the p-stop inhomogeneity is a batch-related issue. However, PQC showed that this is not the case and the p-stop inhomogeneity is a wafer-related effect. The results are presented here on a batch level for better readability. However, no conscious selection of wafers from batches with anomalies was made. Batches 38 921 and 41 742 were chosen because they featured an especially high number of wafers with anomalies. Surprisingly, the interstrip resistance shows a clear trend with the strip number that was not present in the proton-irradiated samples. R_{int} increases towards higher strip numbers. With the placement of the babysensors on the south half moon, the strip number increases from the edge of the wafer to the middle. So, increasing strip numbers correspond to increasing distances from the edge of the wafer. This means that the interstrip resistance is higher in the middle of the wafer, where the full-sized sensors reside, than at the edge. Assuming that the increase in R_{int} towards the middle of the wafer does not

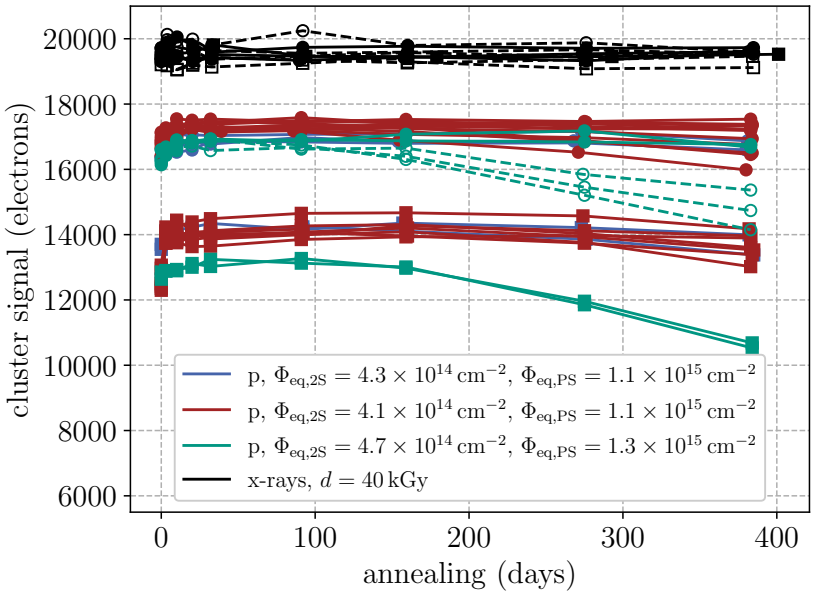

Figure 9.2.: Cluster signal of irradiated babysensors as a function of the equivalent annealing duration at RT. Samples irradiated with x-rays as part of this study are shown in black. For reference, the first three campaigns from regular proton ITs are shown in their respective colors. Curves belonging to sensors with p-stop anomalies are marked with dashed lines. Details in main text.

only apply to the babysensors, this would mean that the interstrip resistance of the full-sized sensors is higher than measured for the babysensors in this study. Keeping in mind that this is a worst-case scenario for the p-stop inhomogeneity, this would mean that the interstrip isolation of the full-sized sensors is even better than measured for the babysensors.

9.3. Cluster Signal

After the interstrip resistance was measured, CC and annealing behavior were studied using the ALiBaVa setup. All parameters were measured at a temperature of $-20\,^{\circ}\mathrm{C}$ and the sensors underwent the same annealing steps as the sensors in the proton ITs.

Figure 9.2 shows the cluster signal of the babysensors as a function of the equivalent annealing duration at room temperature. For reference, the results from three proton irradiation campaigns are shown in their respective colors. The cluster signal of the x-ray-irradiated babysensors is shown in black. Cluster signals that were measured for sensors coming from batches with anomalies are marked with dashed lines. The cluster signal of all x-ray-irradiated babysensors is significantly higher than proton-irradiated sensors. This is expected, as the x-ray irradiation does not introduce displacement damage in the bulk and only introduces ionization damage in the oxide layer, leading to a higher charge collection efficiency. The more interesting finding, however, is that the anomalous batches irradiated with x-rays show the same behavior as the non-anomalous batches. This result suggests that the p-stop inhomogeneity does not affect the charge collection efficiency of the babysensors for x-ray irradiation.

Looking at the results from the proton irradiation campaigns, however, curves belonging to sensors with p-stop anomalies show a different long-term annealing behavior than the other proton-irradiated sensors. Sensors from anomalous batches exhibited a cluster signal for long annealing durations that was up to about 3000 electrons lower than reference sensors from

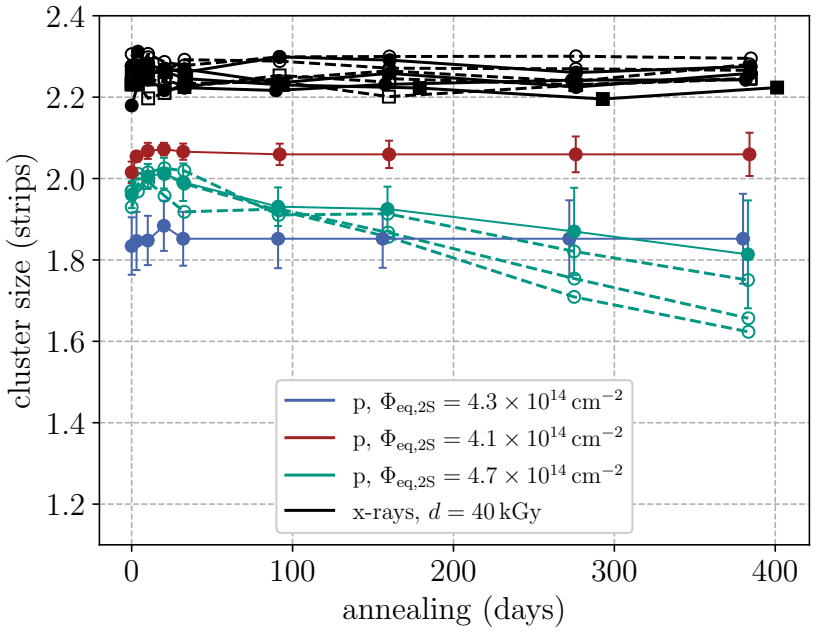

Figure 9.3.: Median cluster sizes for irradiated babysensors as a function of the equivalent annealing duration at RT. Samples irradiated with x-rays in this study are in black. For reference, medians of the first three campaigns from regular proton ITs are shown in their respective colors (only 2S sensors). Curves belonging to sensors with p-stop anomalies are marked with dashed lines. Details in main text.

the same campaign. This result is particularly surprising, since it was not visible in the x-ray-irradiated babysensors. A possible explanation for this behavior might be that the p-stop inhomogeneity leads to a lower interstrip isolation, as seen in the previous section. Over time, radiation defects in the substrate might anneal but oxide defects remain and may lead to a lower R_{int} for the anomalous sensors in the long-term annealing phase. A lower R_{int} can result in increased charge sharing between neighboring strips, causing the collected charge from a particle to be distributed over more strips. As a consequence, the signal on each individual strip would decrease. Since the clustering algorithm requires strips to exceed specific seed and neighbor cuts to be included in a cluster, some strips that would otherwise be counted as neighbors may now fall below the neighbor cut due to the reduced signal per strip, excluding them from the cluster. This would lead to clusters with lower total signal and smaller cluster sizes. Naively, one might expect that charge sharing leads to larger clusters but due to cut-based clustering, this is not necessarily the case. Thus, in the next section, the average cluster size will be examined to investigate the charge sharing properties of the sensors.

9.4. Average Cluster Size

Figure 9.3 shows the average cluster size of the babysensors as a function of the equivalent annealing duration at room temperature. As previously, the results from the x-ray-irradiated babysensors are shown in black. For reference, the results from the first three proton irradiation campaigns are shown in their respective colors. In contrast to the previous plot, the median aggregate cluster size for each of the three first campaigns is shown here. Only results from 2S sensors are shown in order to exclude the influence of high PS fluence sensors from the

median calculation. Additionally, the average cluster size of sensors from anomalous batches are indicated by dashed lines, including the three sensors from campaign three in green. Presented this way, these three 2S sensors that belong to anomalous batches can be compared to the 2S-level median of campaign three.

As expected, the average cluster size of the x-ray-irradiated babysensors is significantly larger than for the proton-irradiated sensors due to promotion of charge sharing as a result of the lower R_{int} following x-ray irradiation. X-ray-irradiated babysensors with anomalies show the same behavior as the non-anomalous batches, as expected from the previous section. However, comparing the average cluster size of the three anomalous sensors from campaign three with the median of the other 2S sensors from the same campaign, it can be seen that the average cluster size of the anomalous sensors is consistently lower, albeit only slightly. This results suggests that the p-stop inhomogeneity has a small effect on the charge sharing properties of proton-irradiated sensors.

9.5. Conclusion

A study investigating p-stop inhomogeneity was performed to research the effect of the p-stop inhomogeneity on the electrical parameters and charge collection efficiency of babysensors. Parameters extracted from the PQC data sets were used to select batches that were affected by the p-stop inhomogeneity and quantify how much that was the case. Interstrip resistances of babysensors were measured after x-ray irradiation and the charge collection efficiency was measured as part of an annealing study in the ALiBaVa setup. The interstrip resistances of anomalous batches were significantly lower than those of typical batches, indicating that the p-stop inhomogeneity has a negative effect on the interstrip isolation. However, the interstrip resistance was still significantly higher than the average R_{poly}-value of the babysensors at the same measurement temperature. The charge collection efficiency of the x-ray-irradiated babysensors was not affected by the p-stop inhomogeneity, as both anomalous and non-anomalous batches showed the same behavior. The average cluster size of the x-ray-irradiated babysensors was also not affected by the p-stop inhomogeneity. However, the average cluster size and cluster signals of the anomalous sensors from the third proton irradiation campaign were consistently lower than the median of the other 2S sensors from the same campaign. This suggests that the p-stop inhomogeneity has a small effect on the charge sharing properties of proton-irradiated sensors. Summarizing the results, the p-stop inhomogeneity does not seem to impact the performance of the sensors significantly and the sensors are still in a good state, maintaining a good interstrip isolation and charge collection parameters that are well within the specifications.

10

Temperature, Frequency and Fluence Dependence of CV Measurements

In contrast to various other works, no CV measurements were discussed in this work. This was due to the fact that CV measurements performed on the IT samples were not conclusive because of a dependence on both measurement frequency and temperature of the CV characteristics of heavily irradiated sensors [CCS02]. While the topology of the SCR in an ideal and unirradiated sensor is well understood, the situation in irradiated sensors is much more complex [Mol18]. Not only does the presence of defects in the silicon lattice change the electric field distribution, but also the presence of charge carriers in the oxide and at the Si/SiO_2 interface can lead to a significant change in the CV characteristics and defining a clear depletion voltage is next to impossible. Trapping and detrapping of charge carriers at various lattice defects also distort the CV characteristics, with temperature and measurement frequency playing a significant role in this process. A study was performed to test if this complex behavior could be disentangled by means of an empirical model. Therefore, a series of CV measurements scanning a reasonable phase space were performed.

10.1. Measurement Program

The ultimate tool of when the sensor is depleted in an optimal way is the charge collection measurement. At a given fluence and temperature, the maximum of the charge collection efficiency is expected to be reached at the depletion voltage. This way of determining the depletion voltage is not only more precise but also more relevant to the application of the sensor. However, CV measurements are a quick and easy way to determine the depletion voltage, given that the sensor is not too heavily irradiated. So, in order to verify if the CV measurement correctly predicts the depletion voltage, the CV measurements are compared to charge collection measurements. As previously explained, the diode test structure of the IT half moon is suited for extraction of properties related to the bare sensor material. This means that, ideally, the CV measurements should be performed on them. Regular charge collection measurements at the ALiBaVa setup are performed with babysensors. Therefore, this study used

- **diodes for CV measurements** at measurement frequencies between 500 Hz and 1 MHz and temperatures between $-20\,°C$ and $+20\,°C$ and
- **babysensors for charge collection measurements** at the ALiBaVa setup at a temperature of $-20\,°C$.

Diodes instead of babysensors were used for the CV measurements because the diodes are more suitable to characterize the bare sensor material due to a more uniform electric field distribution. The measurement temperature of the ALiBaVa measurements was chosen as $-20\,°C$ as this is the temperature at which the sensors are expected to be used in the CMS Tracker, and because the IT measurements were performed at the same temperature in order

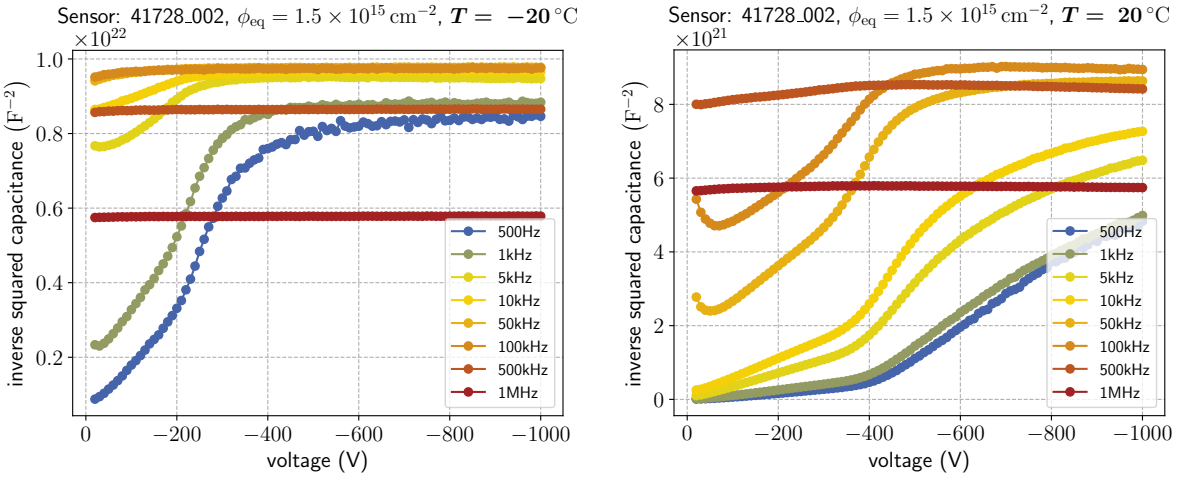

(a) **(b)**

Figure 10.1.: Sample CV curves of the PS-s diode showing the frequency dependence of the measurement at a temperature of (a) −20 °C and (b) +20 °C.

to lower the bulk current of irradiated samples. One diode and one babysensor from batches 41 353 (2S) and 41 728 (PS-s) each — with no p-stop anomalies — were selected for this study. The 2S batch structures were irradiated to $5 \times 10^{14}\,cm^{-2}$ and the PS-s batch structures were irradiated to $13 \times 10^{14}\,cm^{-2}$. The babysensors were chosen from the same wafer as the diodes to ensure that the same material was used.

10.2. Frequency Dependence

Figure 10.1 shows the CV curves of the PS-s diode at −20 °C and +20 °C for different measurement frequencies. At a fixed temperature, the CV curves show a clear frequency dependence; so much so that the usual CV behavior of a sensor is not visible anymore. For example, at −20 °C starting from 50 kHz, the CV curves do not even resemble the expected behavior and stay flat. Additionally, different capacitance values were measured at the plateaus of the CV curves that did resemble the expected behavior. In total, the range of capacitance values varied between about 40%. This behavior is also dependent on the temperature. At +20 °C, more CV curves show the expected behavior, but the capacitance values were still vastly different. Informally speaking, the CV curves are *squished* into the upper left corner of the plot with decreasing temperature and increasing frequency. Calculating the median capacitance values of the plateaus of the CV curves yields about 11 pF at −20 °C and 13 pF at +20 °C. As expected, these values deviate from the unirradiated capacitance value of 16 pF for these diodes due to defects introduced by the irradiation, which is somewhat qualitatively reasonable, though the exact value that is expected after irradiation is not known. Thus, no quantitative conclusions could be drawn from the CV curves alone. However, the results clearly show that the CV characteristics of the sensors are strongly frequency-dependent.

10.3. Temperature Dependence

Figure 10.2 shows the CV curves of the PS-s diode at 500 Hz and 500 kHz for different temperatures. At a fixed frequency, the CV curves show a clear temperature dependence and the capacitance values were significantly different. At a measurement frequency of 500 Hz, most

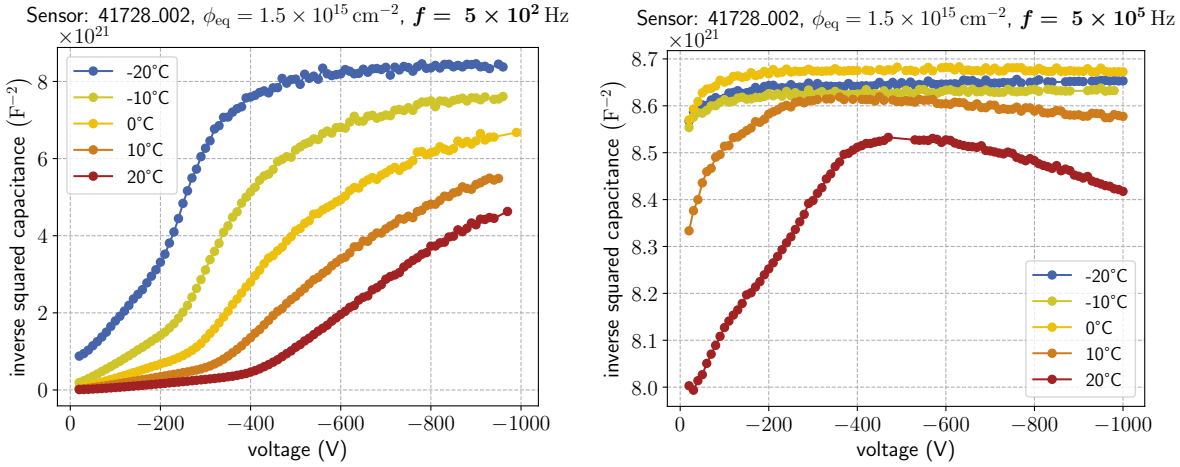

(a) (b)

Figure 10.2.: Sample CV curves of the PS-s diode showing the temperature dependence of the measurement at a measurement frequency of (a) 500 Hz and (b) 500 kHz.

of the CV curves show the expected behavior, however, due to the squishing mentioned in the previous section, a plateau was not reached for all characteristics in the recorded range. At high frequencies, the CV curves even show a decrease in capacitance for high voltages, which is not expected and certainly not of physical origin. This behavior is also dependent on the temperature. The capacitance values are clearly lower the higher the temperature is.

10.4. Fluence Dependence

Figure 10.3 shows the maximum inverse squared capacitances as a function of measurement frequency at different temperatures for the 2S and PS-s diodes. For this study, the assumption was made that the maximum capacitance is the most meaningful value of a CV curve in terms of representing the capacitance of the sensor in highest possible depletion. In theory, a median capacitance value of the plateau (or perhaps the few last points of the CV curve) should be used, but this is not possible due to the squishing and capacitance drop of the CV curves that was observed. A resonance-like behavior was observed for both samples, regardless of their fluence. However, the peak of this resonance is shifted towards higher frequencies with increasing fluence, although not in a way that is completely independent of the temperature. The peaks of curves belonging to lower temperatures are shifted more than those of higher temperatures. Capacitance values tend to be lower for higher fluences, which is expected and thus confirms the validity of the measurement.

10.5. Comparison to Charge Collection Measurements

As a final step, the CV measurements were compared to charge collection measurements that were performed on babysensors in the ALiBaVa setup. The charge collection measurements were performed at the usual temperature of −20 °C and the bias voltage was varied. All CV curves that were measured in this study were fitted to the cluster signal ramps of the babysensors and a χ^2-value was calculated. The CV curves that achieved the best fit were selected and are shown in Fig. 10.4. For the lower fluence 2S samples, the CV curve at 20 °C and 500 Hz achieved the highest χ^2-value, while for the higher fluence PS-s samples, the CV curve at 0 °C

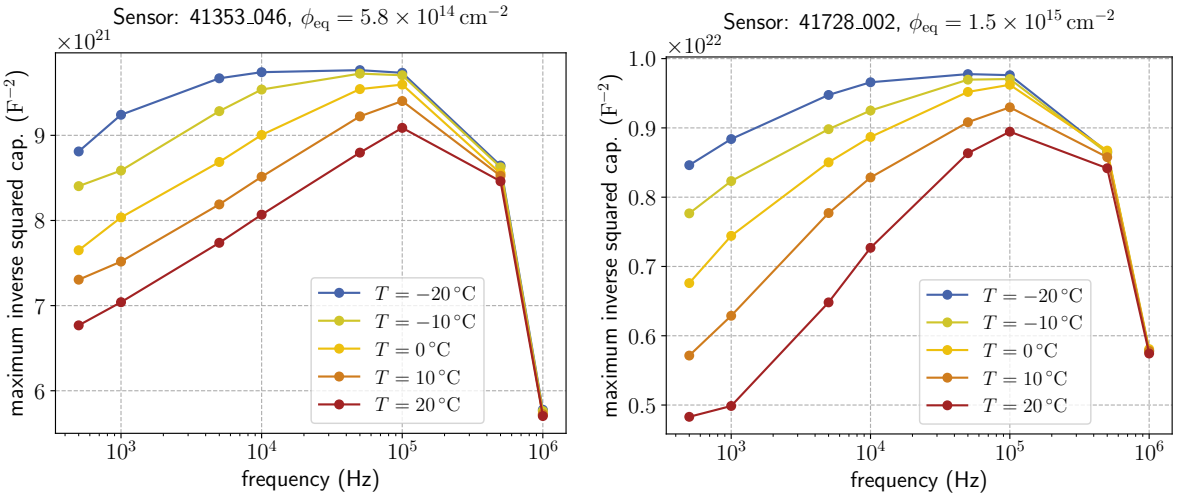

(a) **(b)**

Figure 10.3.: Maximum inverse squared capacitances as a function of measurement frequency at different temperatures of the (a) 2S (low fluence) and (b) PS-s (high fluence) diode.

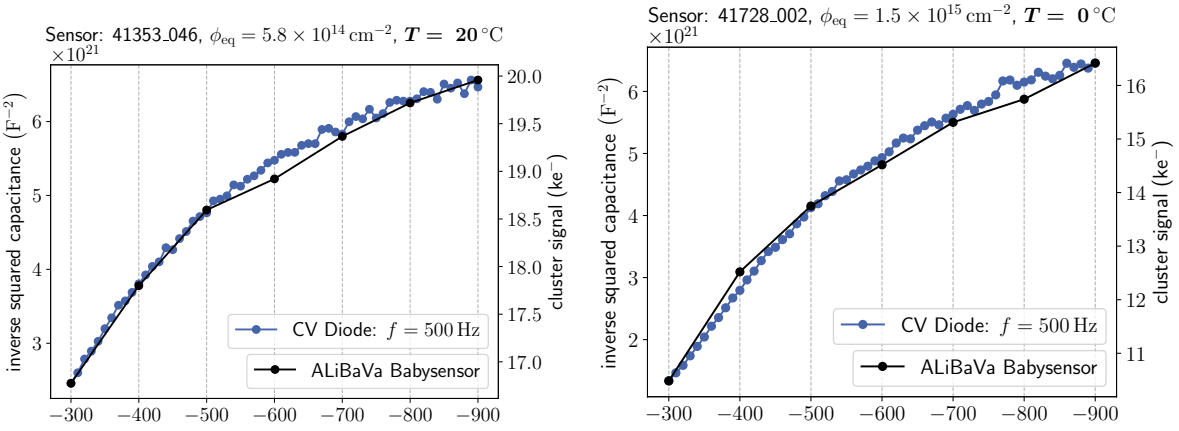

(a) **(b)**

Figure 10.4.: Comparison of the cluster signal obtained for the babysensors with the CV curves that achieved the highest χ^2-probability for (a) the 2S samples at $f = 500\,Hz$, $T = 20\,°C$ and (b) the PS-s samples at $f = 500\,Hz$, $T = 0\,°C$.

and 500 Hz achieved the highest χ^2-value. Surprisingly, both best fits were achieved at the same measurement frequency and only differed in temperature. Making the already bold assumption that the 500 Hz measurement frequency is optimal for the CV measurements performed on these specific diodes, the temperature would have to be fine-tuned every time the fluence changes, or vice versa. This is not only impractical, but also impossible in a real-world application, where the temperature of one setup might not be the same as the temperature of another setup. These results perfectly demonstrate the difficulty of using CV measurements to determine the depletion behavior of heavily irradiated sensors such as the ones used in this work.

10.6. Conclusion

The CV measurements performed in this work show a strong dependence on the measurement frequency, temperature and on the fluence of the sensor. The capacitance values of the CV curves were significantly different and the typical form of the CV curves was not visible anymore for some measurement configurations. The capacitance values of the CV curves were lower for higher fluences, which is expected and thus confirms the validity of the measurement. The CV curves were compared to charge collection measurements performed on babysensors and the best fits were achieved at the same measurement frequency, but different temperatures. This demonstrates the difficulty of using CV measurements to determine the depletion behavior of heavily irradiated sensors such as the ones used in this work. Therefore, the author of this work does not recommend using CV measurements to determine the depletion behavior of irradiated sensors neither qualitatively nor quantitatively and instead suggests using charge collection measurements even though they are more time-consuming. The results obtained in this work are very nuanced and a limited sample size was used. Therefore, usage of the measurement frequency and temperature that yielded the best results in this work for other samples is not recommended.

The results obtained in this work are mostly in alignment with the findings in [CCS02], where the authors also found a strong dependence of the CV characteristics on the measurement frequency and temperature after heavy irradiation. However, the cited work performed measurements on n-type detectors that have undergone space-charge sign inversion after irradiation, while this work focused on p-type detectors that were not inverted but also oxygenated as some of the samples used in the cited work. Therefore, the work presented in this chapter is not directly comparable to the cited work but shows that the same effects can be observed in contemporary p-type detectors as well.

11

Summary and Outlook: Irradiation Testing for the Phase-2 Upgrade

In order to cope with the new challenges the upgrade of the Large Hadron Collider (LHC) to the High-Luminosity LHC brings, the entire Outer Tracker of the current CMS experiment has to be replaced as part of the CMS Phase-2 Upgrade. A comprehensive quality control (QC) strategy was implemented by the CMS Tracker Group to ensure and verify the quality of the sensors produced for the Phase-2 Outer Tracker, with the Irradiation Testing (IT) program being a key component of this strategy. KIT contributed to the IT program as one of the two irradiation test centers. The results from the IT program gathered during 50% of the sensor mass production for the Phase-2 Outer Tracker were presented in this work, along with additional studies on p-stop inhomogeneity and the temperature and frequency dependence of capacitance-voltage (CV) measurements. Test structures located on the same silicon wafers as the full-sized sensors to be used in the Phase-2 Outer Tracker were irradiated with protons and x-rays to assess the radiation hardness and electrical performance of the sensors. Babysensors, diodes, MOS, and GCD structures from the alotted IT test structures were used to monitor both bulk and surface properties before and after irradiation as part of this work. In detail, comprehensive electrical and charge collection characterization on these test structures was performed.

All test structures met the specifications set by the CMS Tracker Group prior to irradiation, confirming the excellent quality of the sensors produced by HPK for the Phase-2 Outer Tracker. After proton-irradiation, most parameters remained within specification, with expected increases in leakage current and decreases in interstrip resistance while still maintaing sufficient interstrip resistance. Charge collection measurements showed that the sensors meet the requirements for the Phase-2 Outer Tracker up to the maximum tested equivalent fluence of $1.4 \times 10^{15}\,\mathrm{cm}^{-2}$. Additionally, charge collection could be increased by raising the bias voltage from the nominal voltage of 600 V to 800 V, also decreasing reverse annealing effects. This finding in particular showed that increasing the bias voltage is a viable option to maintain charge collection performance should the sensors be exposed to higher radiation levels than expected.

A dedicated study was conducted to investigate the impact of p-stop resistivity inhomogeneity, which was observed in a subset of production wafers, reported by the process quality control team of the Outer Tracker Sensor Experts Production Panel. Babysensors from affected and reference batches were subjected to both proton and x-ray irradiation. The study focused on the interstrip resistance, cluster signal, and charge sharing properties, as these are most sensitive to p-stop variations. The results showed that, even in wafers with pronounced p-stop inhomogeneity, the interstrip resistance remained sufficiently high and the charge collection properties were sufficient for the requirements of the Phase-2 Outer Tracker. X-ray irradiation, representing a worst-case scenario for surface effects, did not lead to a significant reduction in interstrip resistance or cluster signal. However, a slightly adverse impact on interstrip isolation was observed in the affected batches, as well as a slightly more pronounced long-term annealing effect in terms of collected cluster signal. These findings indicate that the observed p-stop

inhomogeneity does not compromise the operational performance of the sensors, and affected batches can be safely used in the tracker.

An additional study was performed to assess the reliability of capacitance-voltage (CV) measurements for irradiated sensors. CV measurements were carried out on diodes at various temperatures and measurement frequencies, and compared to charge collection measurements performed on babysensors from the same wafers. The study revealed a strong dependence of the CV characteristics on both temperature and frequency after irradiation. In many cases, the CV curves deviated significantly from the expected behavior, making it difficult or impossible to extract a meaningful depletion voltage. These results highlight the limitations of CV measurements for irradiated sensors and support the use of charge collection as the primary method for sensor qualification in the IT program. A comparable study [CCS02] performed on heavily-irradiated, n-type sensors showed similar results. This thesis confirms the findings of that study even for contemporary p-type sensors as they are used in the Phase-2 Outer Tracker.

The results of the IT program and the additional studies confirm that the sensors produced for the CMS Phase-2 Outer Tracker meet the requirements for radiation hardness and electrical performance. The production process is robust, and even batches with process-induced inhomogeneities perform within specifications. The findings from the CV study provide important guidance for future sensor qualification, emphasizing the need for charge collection measurements in the presence of high radiation damage.

Overall, the comprehensive IT program has ensured the quality and reliability of the sensors for the CMS Phase-2 Upgrade in the harsh radiation environment encountered at the Phase-2 CMS experiment, contributing to the long-term success of the experiment.

Part II.

Irradiation Studies on Ultrafast Silicon Devices for Timing Applications

12
The Resistive Silicon Device (RSD)

The evolution of particle accelerators, detectors and the need for high energy physics experiments make clear demands: speed and accuracy. As outlined in Section 4.4, the future of HEP detectors is in the development of fast timing detectors. Naturally, among tackling other challenges, R&D in the last decade has focused on the development of such detectors, namely in the field of radiation-hard LGADs.

12.1. The Standard LGAD Design

But why are LGADs so important for achieving timing resolutions that are required for the next generation of HEP detectors? A description of signal formation in silicon sensors is given in Section 2.5 and a description of the basic principles of using a gain layer for charge multiplication is given in Section 2.6. Building fast timing detectors builds on these principles, reducing the readout time by reducing the active thickness of the sensor. However, reducing the active thickness also reduces the number of electron-hole pairs that are generated by a charged particle traversing the sensor, diminishing the signal amplitude. To compensate for this, a gain layer is introduced in the sensor design that increases the signal strength, which makes the importance of LGADs in the field of fast timing detectors clear. In the last years, LGADs have been optimized in many ways and were able to achieve timing resolutions of 30 ps while still being able to operate in a high radiation environment. Due to the high temporal resolutions that can be achieved with these devices, recently the term *ultra-fast silicon detector* (UFSD) has been coined to describe them. However, introducing a gain layer in the sensor design comes with its own challenges, such as the need for a *junction termination extension* (JTE) around each sensor channel to prevent edge breakdown between the implants. Figure 12.1 shows a schematic of such a standard LGAD design with these JTEs. The layout also includes p-stop implants to prevent conductive layer build-up at the surface of the sensor. In order to use a UFSD in 4D tracking, apart from the high timing resolution and radiation hardness, high

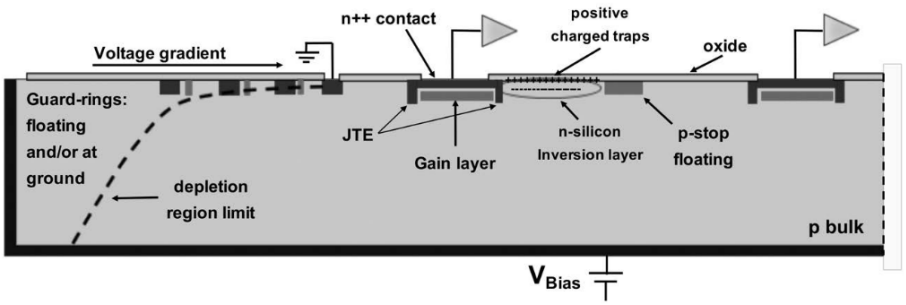

Figure 12.1.: Schematic of a standard LGAD design. For each readout pad, *junction termination extensions* are included to shape the high electric fields created by the gain layer and prevent edge breakdown between the implants [Men23].

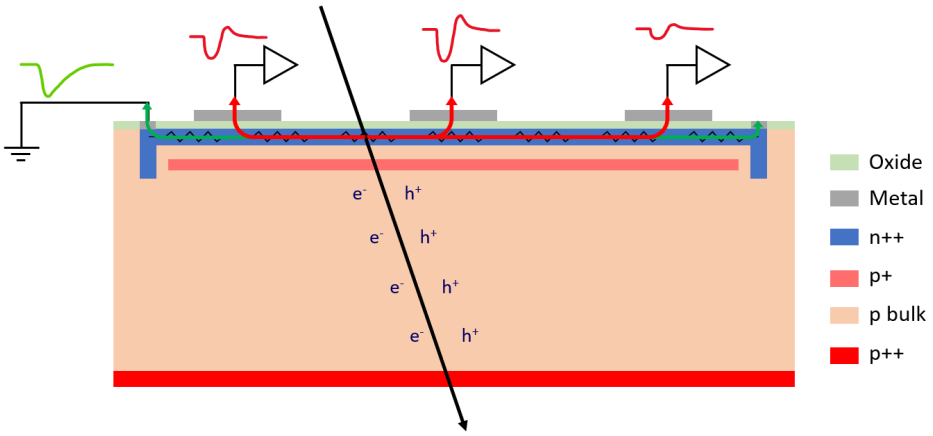

Figure 12.2.: Schematic of the AC-RSD design. The resistive n++ layer is placed on top of the p-type substrate containing the gain layer. The metal readout electrodes are located on the resistive layer with an AC-coupling oxide inbetween [Men23].

spatial resolution is also required. The usage of a JTE limits the intrinsic fill factor of the sensor, which is defined as the ratio of the active area to the total area of the sensor. P-stop implants further diminish the fill factor, since they are not active and do not contribute the the active area. While solutions like trench-isolated LGADs (TI-LGADs) [Sen+22] exist, the intrinsic fill factor is still limited to about 80–90% while featuring a high number of readout channels. Naively, one could think that the latter is not a problem, but implementing a high number of readout channels in such a device introduces many new challenges, such as the need for a high number of readout electronics channels. Not only would this make the readout electronics exponentially more complex, it would also increase the power consumption not only on the side of electronics but also cooling, making the device vastly more expensive. Innovative solutions are needed to achieve the required timing resolution and radiation hardness but one thing is clear: conventional LGADs are not the solution when it comes to 4D tracking, especially in the high radiation environment of the HL-LHC. Enter, the Resistive Silicon Device (RSD), a novel silicon sensor concept that is based on the idea of a resistive layer on top of a silicon substrate with a single gain layer. RSDs are a potential new candidate to be used in the next generation of high energy physics detectors with the objective of achieving 4D tracking — a concept that will find its way into future colliders and beyond if tracking is needed.

12.2. The AC-RSD

The AC-coupled RSD (AC-RSD) is based on the LGAD concept and instead of segmentation of the readout implants, metal electrodes are placed on the resistive layer, eliminating the need for JTEs around each readout implant. JTEs are still required at the edges of the sensor to prevent edge breakdown, but the intrinsic fill factor is not limited by the JTEs anymore. Thanks to this concept, the AC-RSD achieves a fill factor of 100% intrinsically, which is a significant improvement over traditional LGADs. Instead of strictly forbidding crosstalk between the readout electrodes, the AC-RSD design opts for charge sharing between them. This makes it possible to reduce the number of readout channels while still achieving a high spatial resolution, simplifying the previously mentioned problem of the complexity of the readout electronics. An internal gain mechanism is implemented by a highly doped p-type layer embedded in the substrate, underneath the resistive layer, enabling good timing performance. Figure 12.2 shows a schematic of the AC-RSD design. When a charged particle traverses the sensor, electron-hole

pairs drift from the impact point towards the ground contact located at the edge of the sensor. This ground contact is called *DC ring*. The induced current flows through the resistive layer, under the readout electrodes, which induces a bipolar signal on the AC electrodes, as shown in the figure. The decay time of the positive lobe of the signal is determined by the RC-constant formed by the impedance of the resistive layer and the capacitance of the readout electrodes. Ideally, this time constant should be low to achieve a fast signal rise time but high enough to be longer than the signal formation time, which is typically in the order of 1 ns [Men23]. The interesting negative signal lobe has an amplitude that is dependent on the signal splitting due to charge sharing. Depending on many factors, such as the electrode pitch, geometry and size, relative signal splitting is influenced. The gain value achieved by the multiplicaiton region is also especially important due to this signal splitting, since the signal in each electrode is a fraction of the total signal; a high-enough signal-to-noise ratio (SNR) is crucial for the readout electronics, especially in the case of a high radiation environment. The gain also plays a role in the timing performance of the sensor. As in the case of traditional planar silicon sensors as used in the CMS Phase-2 OT, the backplane is made up of a highly p-doped layer to provide a good ohmic contact to the substrate. Fondazione Bruno Kessler (FBK) has produced three runs of RSD sensors, with the first two runs being AC-RSDs and the third run being a prototype of a DC-coupled RSD (DC-RSD, more information on the current status of the project can be found in [Men25]). This work focuses only on production run two [Man+22], kindly provided by FBK and INFN Torino for radiation hardness studies.

The devices manufactured in these AC-RSD productions have undergone extensive simulation campaigns [Man17; Man+20], beam tests [Men+24] and laboratory measurements [Men23]. However, the effects of radiation damage on the sensor performance are not yet fully studied. Since 4D tracking devices need to be able to operate in a high radiation environment, it is crucial to understand the effects of radiation damage on the sensor performance. Therefore, the objective of this work is to study the radiation hardness of the AC-RSD, specifically acceptor and donor removal, as well as the effects of the radiation damage on the charge sharing capability of the sensor.

12.3. Measurement Samples

Two types of AC-RSDs were used in this work, both produced by FBK. Both sensor types are segmented with cross-shaped readout electrodes. Four such electrodes in a square configuration are defined as a *pixel* with the four electrodes representing the four corners of the pixel. The first sensor type, shown in Fig. 12.3a, is a 2×2 AC-RSD with a pitch of 1.3 mm and the second sensor type, shown in Fig. 12.3b, is a 6×6 AC-RSD with a pitch of 450 µm. The crosses of the 450 µm-pitch sensor vary in size, which is best seen when comparing the lower left pixel with the lower right pixel. Although the cross-shaped electrodes are not identical in size, the pitch remains the same.

The first production run focused on the demonstration of the charge sharing concept by exploring different manufacturing and crystal growth processes such as float-zone (FZ) and epitaxial growth, gain layer and resistive layer doping, as well as electrode geometry and pitch [Men23]. Optimization of these design parameters led to the second production run, including both float-zone and epitaxial substrates, with 55 µm and 45 µm thicknesses, respectively. The wafers used in this work do not include carbon doping, which means that all irradiation testing performed in this work is done on sensors without any radiation hardening procedures. Wafers three, four, six and 14 were used in this work. All of these wafers operate at moderate gains of about 20, depending on the gain layer doping [Men23]. Of course, the gain increases for high bias voltages due to higher electric fields in the multiplication region, but this value can

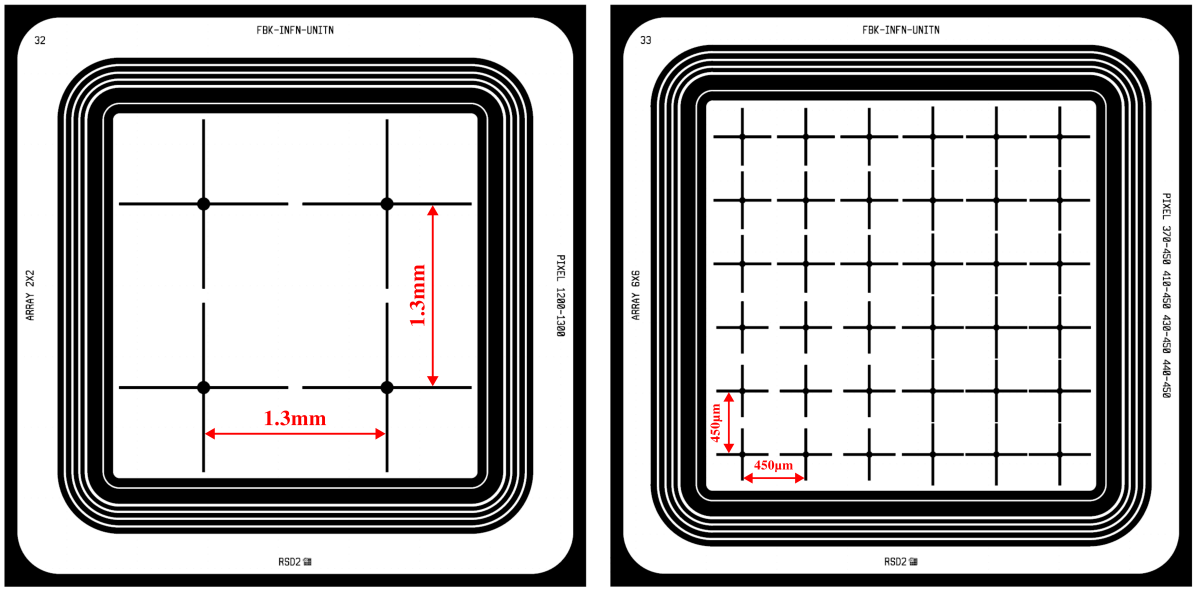

(a) **(b)**

Figure 12.3.: The (a) 2×2 and (b) 6×6 AC-RSD sensors used in this work. The sensors are segmented with cross-shaped readout electrodes. Four such electrodes are defined as a *pixel*.

Table 12.1.: Overview of the wafers from production run two used in this work. Epitaxial (epi) wafers are 45 µm thick, float-zone (FZ) wafers are 55 µm thick. No wafers include carbon dopants in the gain layer. The dose of the n+ resistive layer is denoted as A < B < C, A being the most resistive dose. Exact n+ doses have not yet been disclosed at the time of writing. Table adapted from [Men23].

wafer no.	type	n+ dose	p-gain dose
3	FZ	A	0.98
4	FZ	A	1
6	epi	B	1
14	epi	C	0.98

be reported in a region where the sensors are fully depleted but not yet close to the breakdown regime. The wafers used in this work are summarized in Table 12.1. The selection of the wafers was based on covering a large enough parameter space of the design parameters such as resistive layer doping, gain layer doping and substrate type. Wafers three and four are float-zone wafers that virtually have the same parameters, except for a slightly different p-gain dose. Therefore, the results obtained for these wafers were combined as ”3+4” instead of treating them separately. Before irradiation, all sensors that were received from the Torino group were characterized electrically, totalling 72 sensors. From these 72 sensors, 24 were selected for irradiation and subsequent characterization, picking a proton- and neutron-irradiated sensor from each wafer, fluence and pitch. The measurement samples that were used in this work after irradiation are listed in Table A.4. In total, 24 sensors were characterized after irradiation, six of which were characterized within the the scope of their resistive layer doping. Measurements dealing with the resistive layer doping were carried out on wafer 14, exclusively, since it is the wafer with the highest resistive layer doping. Wafer 14 only contained 2×2 AC-RSDs, wafer

3+4 contained 6×6 AC-RSDs with a pitch of 450 µm and wafer six contained six 6×6 AC-RSDs and six 2×2 AC-RSDs. Thus, wafer six was used to study the influence of the pitch on the sensor performance.

13
Procedures and Methods for the RSD Irradiation Studies

This chapter will describe the methods used to irradiate and characterize the RSDs, and the techniques used to analyze the data.

13.1. Measurement Program

All measurement samples listed in Table A.4 were characterized electrically before and after irradiation. They were irradiated with protons at the KAZ facility and with neutrons at the TRIGA reactor in Ljubljana. Three different fluence levels were used for the irradiation per particle type. The exact particle fluences are listed in the same table. All fluences were chosen based on the expected fluences in the outer pixel layers of the Phase-2 Tracker. The gain layer was expected to vanish after an equivalent fluence of about $\Phi_{\text{eq}} = 1 \times 10^{15}\,\text{cm}^{-2}$ to $2 \times 10^{15}\,\text{cm}^{-2}$ due to acceptor removal [Fer+21].

After irradiation, all sensors of wafer 14 were characterized with the Transient Current Technique (TCT). Two studies were performed with the TCT setup (described in Section 5.1.3):

- **the gain deterioration study** to characterize the deterioration of the gain layer with increasing fluence and
- **the charge spreading study** to investigate how the induced charge propagates to the readout electrodes with increasing fluence.

Results obtained during the gain deterioration study are compared with results that were obtained using Van-der-Pauw test structures from the same wafer. The results of the measurements performed on test structures are not the focus of this work and are just included for a more complete picture of the behavior that the resistive layer exhibits.

13.2. Electrical Characterization

13.2.1. Before Irradiation

Before irradiation, all sensors were characterized regarding their IV/CV characteristics in a probe station (described in Section 5.1.1). The samples were biased with high voltage from the backside, the guard ring was grounded with an additional needle and the current flowing through the DC ring was measured. All measurements were performed at 20 °C and a relative humidity of at most 20%. Due to high noise in the low voltage region, Lowess smoothing [CL96] was applied to the IV curves. The bias voltage was increased in steps of 5 V up to the breakdown regime. A current compliance of 5 µA was set in the probe station to protect the sensors from irrevertible damage. After the IV measurement, the breakdown voltage was determined by applying the k-factor method [Bac+01]. The k-factor is defined as

$$K(I,V) = \frac{\Delta I}{\Delta V}\frac{V}{I}.$$

The method is based on defining a threshold for the k-factor, which is set to $k_{\mathrm{BD}} = 20$ in this work. This threshold is purely empirical and was chosen because it yielded the best results in this study. An early breakdown is defined as a breakdown voltage that is substantially lower than the median breakdown voltage of all sensors on a particular wafer. Sensors with early breakdowns are flagged as bad and were not eligible for further characterizations.

Capacitance-voltage measurements were performed with the same measurement setup, using a different current compliance of 30 µA which is a value that is typically used for capacitance measurements at this setup. All CV measurements prior to irradiation were performed at a frequency of 1 kHz and a temperature of 20 °C. The bias voltage was increased in steps of 0.5 V up to a voltage of 50 V because the CV characteristics were used to extract the depletion voltage of the gain layer, which was expected to be around 25 V. A logistic curve was fitted to the CV data to extract the gain layer depletion voltage V_{dep}.

13.2.2. After Irradiation

After irradiation with protons and neutrons, the sensors underwent a reception annealing of 80 min and 60 °C and were stored in a freezer subsequently to prevent any unwanted annealing. This annealing duration represents an equivalent annealing time of about two weeks at room temperature.

The same measurement setup was used to characterize the sensors electrically after irradiation. However, a lower temperature of −20 °C was used to reduce the leakage current and a relative humidity of at most 5% was used during the measurement. A lower humidity limit was chosen compared to the measurements on Phase-2 sensors presented in Part I of this thesis, since the RSDs tend to exhibit lower breakdown voltages due to higher electric fields resulting from the gain layer. A drier environment was chosen to reduce the risk of early breakdowns. For the IV measurements, the sensors were biased up to a voltage of 550 V and a current compliance of 50 µA was set. In order to increase the measurement resolution in the low voltage region, the bias voltage was increased in steps of 1 V up to a voltage of 60 V and in steps of 5 V until the maximum bias voltage was reached. The CV curves were measured with the same probe setup as before irradiation, but a maximum bias voltage of 60 V was chosen. The current compliance was set to 300 µA and the bias voltage was increased in steps of 1 V. In contrast to the pre-irradiation measurements, the CV measurements were performed at a frequency of 10 Hz. The reason for this choice is that measuring the capacitance at a frequency of 1 kHz yielded inconsistent and noisy results. It was found that the capacitance at a frequency of 10 Hz was stable and reproducible. A possible hypothesis for this behavior is that measuring at such a low frequency allows the charge carriers to be untrapped from radiation-induced traps during application of the AC small signal during the measurement.

The CV measurements after irradiation were also used to quantify the acceptor removal effect discussed in Section 3.1.3. Applying a bias voltage to the sensor causes the depletion region to expand through the gain layer, which leads to a drop in capacitance, as explained in Section 2.3.1. Choosing a consistent capacitance threshold C_{th} for all sensors allows for a comparison of gain layer depletion voltages between those sensors. Depending on the fluence, the gain layer depletion voltage varies, yielding a different threshold crossing voltage V_{th} for each sensor. This is shown in Fig. 13.1 for sensors of an arbitrary wafer irradiated with neutrons. For this study, an arbitrary $C_{\mathrm{th}} = 300\,\mathrm{pF}$ was chosen, which is a value that was found to be suitable for all sensors. The choice of this threshold introduces a systematic uncertainty in V_{th} of up to 5 V for the sensors investigated in this work, which affects all V_{th}-values in approximately the same way, due to the similar shapes of their CV curves. All V_{th}-values were extracted from the CV curves and normalized to the gain layer depletion voltage for an

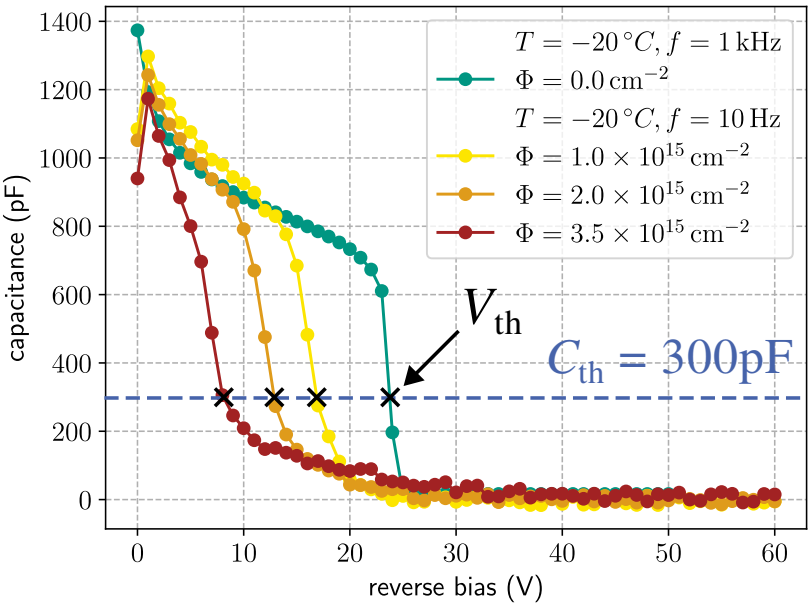

Figure 13.1.: Example of the procedure to extract the threshold crossing voltage V_{th} from the CV curve. The capacitance threshold $C_{\mathrm{th}} = 300\,\mathrm{pF}$ is shown in blue and the threshold crossing voltage V_{th} is defined as the voltage at which the capacitance crosses this threshold, shown in black. Details in main text.

unirradiated sensor $V_{\mathrm{GL},0}$. An exponential fit of the form

$$f(\Phi) = \frac{V_{\mathrm{th}}(\Phi)}{V_{\mathrm{GL},0}} = B\exp(-c\Phi).$$

with the fit parameters (B, c) and the particle fluence Φ was performed to extract the acceptor removal coefficient c. $f(\Phi)$ can be understood as a measure for the fraction of the gain layer that is active. The c coefficient describes the gain deterioration with increasing fluence. The method presented here is based on contemporary literature such as [CP24] which describes a method that is commonly employed with standard-design LGADs.

13.3. Transient Current Technique (TCT)

The following section describes the studies that were performed using the TCT setup. Prior to the TCT measurements themselves, the setup had to be calibrated and the laser focus had to be adjusted. The TCT setup itself as well as all calibration and adjustment procedures are described in detail in Section 5.1.3. All measurements described in the following were performed on already irradiated and reception-annealed sensors at a measurement temperature of about $-16\,°\mathrm{C}$. More details on why this temperature was chosen can be found in Section 5.1.3, as well.

13.3.1. Gain Deterioration Study

The gain deterioration study was performed to investigate how much the gain of the sensors decreases with increasing fluence. Only the DC-ring of a sensor was used to measure the induced signal, which drastically reduced the amount of unwanted annealing at RT during the bonding process to about 30 min. The sensors were biased with a voltage from 0 to 500 V

in steps of 10 V until 100 V and then in steps of 20 V until the maximum bias voltage was reached. The laser spot was visually aligned to the same point for every sensor of the same pitch. This laser shot point was located in the center right between the cross-shaped readout electrodes, about 300 µm away from the inner edge of the DC ring. At every bias voltage V, the laser was fired $n_{\text{pulse}} = 5000$ times, yielding 5000 events containing the induced signal pulse $S_{i,\text{raw}}(V,t)$ for that laser shot. A baseline correction was applied to the signal pulse $S_{i,\text{raw}}(V,t)$ by subtracting the time-averaged waveform from the waveform itself, yielding the corrected waveform $S_i(V,t)$. The average of all events $S(V,t) = 1/n_{\text{pulse}} \sum_i S_i(V,t)$ was calculated and the integral of the average signal pulse $S(V) = \int \mathrm{d}t\ S(V,t)$ was determined. This method of extracting the integral of the signal pulse is prone to jitter, since the signal pulse is not always triggered at the exact same time, so, the signal pulses are not perfectly aligned. However, the jitter was found to be negligibly small and even if it was not small enough, the jitter would be the same for all measurements and therefore not affect the results. The goal of this measurement is not a precise and absolute measurement of the gain, but rather a relative measurement of the gain deterioration with increasing fluence. The method used here is sufficient for this purpose but may not be suitable for an absolute measurement of the gain, where a method of correcting for the jitter would be necessary to obtain a precise value. The signal area $S(V)$ was compared for all 24 irradiated sensors after irradiation.

13.3.2. Charge Spreading Study

The charge spreading study was performed to investigate how the propagation of the induced charge in the resistive layer changes with increasing fluence. All investigated sensors for this study were 2×2 sensors and therefore, four electrodes with an additional DC-ring contact were used to measure the signal propagation on one AC-pad. The bonding process for one sensor took about 45 min of unwanted annealing at RT on average. In contrast to the gain deterioration study, the laser was not positioned on a single point but rather used to scan the entire sensor in steps of 20 µm in both the x- and y-direction. Reasons of choosing this pitch were on one hand, to ensure that the pitch was larger than the laser spot size and, on the other hand, to ensure that the entire sensor was scanned in a reasonable time. The time for a full scan was about two days for a single sensor with 50 events per point. Two quantities were extracted for each point in the scan matrix:

- the signal area $S(x,y)$ that was calculated in the same way as in the gain deterioration study introduced in the previous section, and
- the average signal amplitude $A(x,y)$ that was calculated in the same way as $S(x,y)$, but the signal amplitude was used instead of the signal area.

Using the discrete scalar fields $S(x,y)$ and $A(x,y)$ of each sensor, the charge spreading was analyzed.

Analysis

For each of the four electrodes and the DC-ring, the following analysis was performed: The four electrodes of the sensor were set manually to the positions A-D, as shown in Fig. 13.2a for the first channel of a sensor. Using the four electrode positions, a data mask was defined that enclosed the pixel. This data mask was used to define the area inside of the pixel that was used for the analysis. Since one such scan matrix was recorded for one channel of a sensor, the signal features a maximum that is centered around the corresponding electrode. This *signal electrode* is detected automatically by calculating the distance between the maximum of the signal map and the four electrode positions. Then, the *other electrode* is defined as the electrode that is

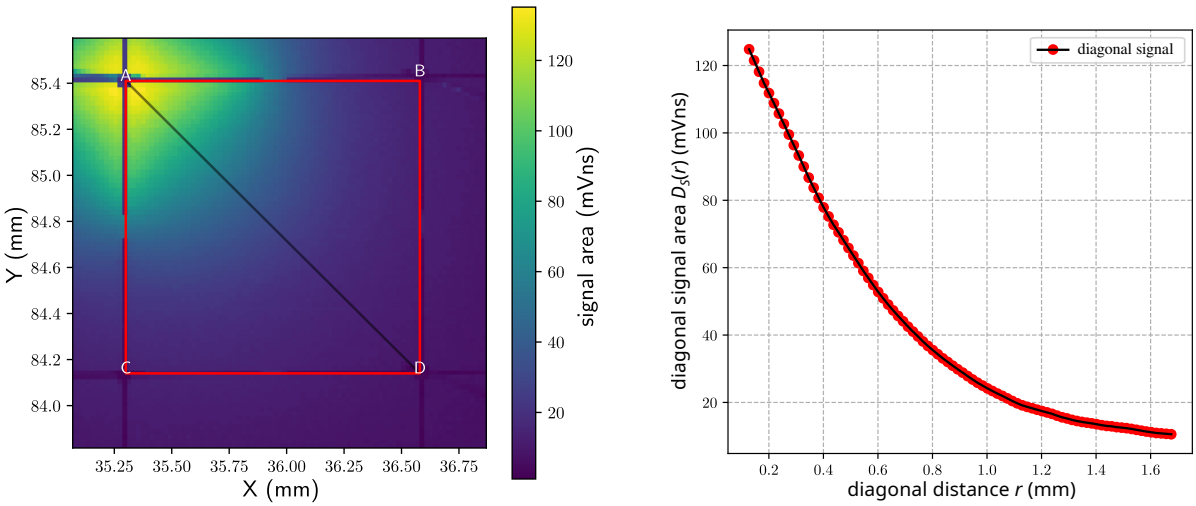

(a) **(b)**

Figure 13.2.: Example charge spreading analysis of channel one of a sensor. (a) shows the scan matrix $S(x, y)$ with the electrode positions annotated with letters A-D, the data mask in red enclosing the pixel and the diagonal line in black. (b) shows the points that were sampled along the diagonal line from the interpolated scalar field $S_{\text{int}}(x, y)$.

furthest away from the signal electrode, thus, on the opposite corner of the pixel. A diagonal line between the signal electrode and the other electrode was parameterized by the two coordinates of the two electrodes. The scan matrix was interpolated using a 2D cubic spline interpolation to obtain a continuous scalar field $S_{\text{int}}(x, y)$ and $A_{\text{int}}(x, y)$. The interpolation was performed using the `scipy.interpolate` package in Python [Sci25]. Sampling 100 points spaced evenly along the diagonal line, the signal area $S_{\text{int}}(x, y)$ and the signal amplitude $A_{\text{int}}(x, y)$ along the diagonal line were extracted. The *diagonal signal area* $D_S(r)$ as a function of the diagonal distance r along the line from the signal electrode for $S_{\text{int}}(x, y)$ is shown in Fig. 13.2b as an example.

14 Results

After introduction of the AC-RSD sensors and their design, as well as the methods and analysis procedures used to characterize them, this chapter presents the results of the irradiation tests performed on the AC-RSD sensors. Supplementary information on the IV and CV measurements that are not shown in the following sections can be found in Section A.3.

14.1. Electrical Characterization

IV and CV measurements were performed on the AC-RSD sensors before and after irradiation.

14.1.1. Before Irradiation

IV curves were measured for all sensors before irradiation to determine if the sensors were functional and to have a reference for the sensor characteristics. Figure 14.1 shows the IV curves of wafers four (FZ) and six (epi) before irradiation. Although IV characteristics for all wafers were recorded, only wafers four and six are shown here for demonstration. Green lines show the IV curves of sensors with normal characteristics, while red lines show the IV curves of sensors with early breakdowns. The qualitative behavior of the IV curves is similar for all wafers of the same substrate type. However, sensors with an FZ substrate showed a more distinct kink at the gain layer depletion voltage than sensors with an epi substrate. Moreover, sensors from an epi wafer exhibited lower leakage currents in full depletion than sensors from an FZ wafer by approximately two orders of magnitude. As explained previously, Lowess smoothing was applied to the IV curves to remove noise in the low voltage region. A greater amount of smoothing needed to be applied to the epi wafers than to the FZ wafers since epi wafers showed a higher noise in that region. The origin of this behavior is not yet understood but is likely related to how the SCR develops in the epi wafers compared to the FZ wafers. The median gain layer depletion voltage is marked with a blue dashed line and was precisely the same for all sensors, regardless of substrate type. It was extracted from the IV curves by the detection of the inflection point of the IV curve in the low voltage region. The median depletion voltage was found to be $V_{\mathrm{GL},0} = 26\,\mathrm{V}$ for all sensors, uncertainties were negligible. Using the K-factor method explained previously, the breakdown voltage of all sensors was extracted. The median breakdown voltage for each wafer was calculated and is shown as a red dashed line in Fig. 14.1. Median breakdown voltages were found to be $V_{\mathrm{BD,W3}} = 215\,\mathrm{V}$, $V_{\mathrm{BD,W4}} = 200\,\mathrm{V}$, $V_{\mathrm{BD,W6}} = 185\,\mathrm{V}$, and $V_{\mathrm{BD,W14}} = 210\,\mathrm{V}$. The uncertainty of all breakdown voltages was $\pm 5\,\mathrm{V}$ due to the voltage step size of the measurements. The high number of early breakdowns measured for wafer six significantly affected the median breakdown voltage of that wafer, skewing it to lower values. No claim can be made about why exactly there were more early breakdowns in wafer six than in the other wafers, which is why sensors with early breakdowns were also included in the median breakdown voltage calculation. Regardless of if the sensors had early breakdowns or not, all sensors were selected for subsequent irradiation since there was enough room for them to be included in the irradiation setups in one go. A deliberate decision was made, however, to exclude sensors with early breakdowns from the

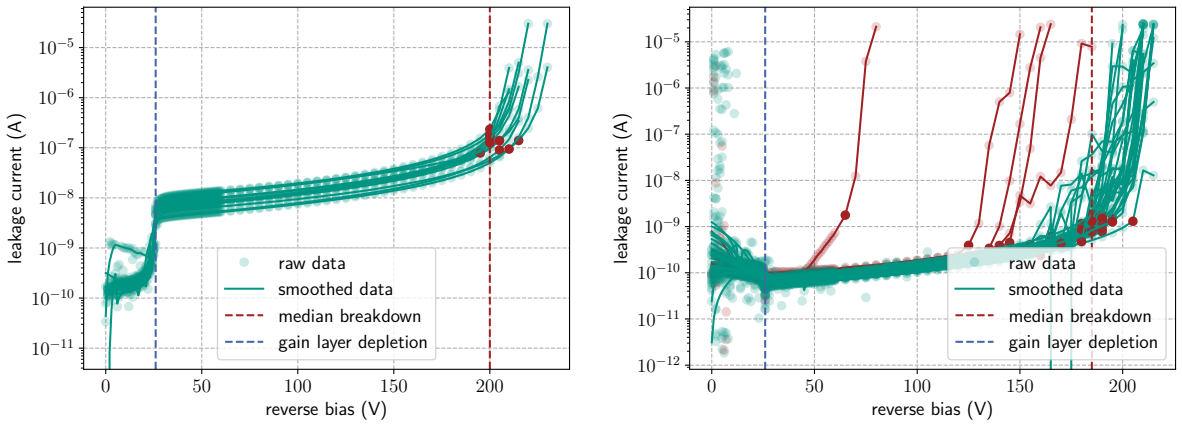

Figure 14.1.: IV curves of the AC-RSD sensors before irradiation for (a) FZ wafer four and (b) epi wafer six. Red lines show IV curves of sensors with early breakdowns, green lines show normal IV characteristics. Red points indicate the breakdown voltages extracted with the K-factor method. Details in main text.

measurements after irradiation to avoid any bias in the results and ensure that the results reflect the behavior of the sensors with typical characteristics.

Capacitance-voltage measurements were performed on all FZ wafers before irradiation to determine the gain layer depletion voltage $V_{\mathrm{GL},0}$ and examine the general depletion behavior of the sensors. Prior to the irradiation, CV measurements were only performed on wafers that used the FZ substrate, wafers three and four. The reason for this is that the epi wafers showed an inconsistent depletion behavior before irradiation. The exact reason for this is not yet understood, but considering that the epi wafers also showed a higher noise in the IV measurements, it is likely related to the SCR formation.

Having established that almost all sensors were functional and that the gain layer depletion voltage was the same for all sensors, the sensors were irradiated with neutrons and protons to study their radiation hardness.

14.1.2. After Irradiation

The same characterization procedure was performed on the sensors after irradiation with adjusted parameters as described in the previous section.

IV Measurements

The following section will discuss the IV measurements after irradiation, interpreting the results from different perspectives. First, the influence that the particle type and fluence have will be discussed using wafer six as an example. Additionally, the influence the wafer type and pitch size have on the IV characteristics will be analyzed. Then, the IV curves of all wafers will be compared to each other.

Figure 14.2 shows the IV curves of wafer six (epi) sensors after irradiation with neutrons and protons to different fluence values. Compared to the pre-irradiation IV curves, the post-irradiation IV curves show a significant increase in the leakage current, and as expected, the leakage current scales with the fluence. In Figure 14.2a, the curve of the sensor irradiated with the lowest fluence level overtakes the curve of the sensors irradiated to higher fluence levels at about $V = 400\,\mathrm{V}$. This overtaking effect was observed for all other wafers, regardless of the

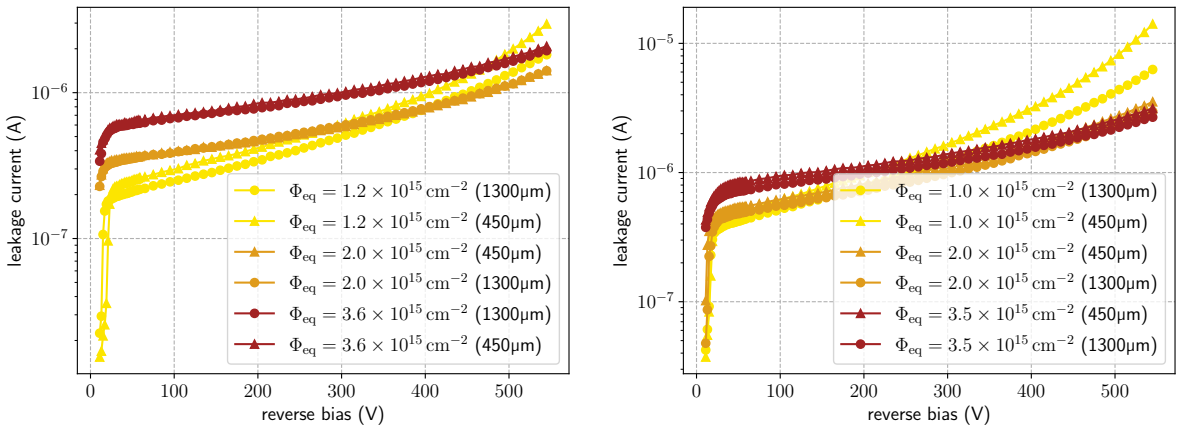

(a) **(b)**

Figure 14.2.: IV curves of wafer six sensors after irradiation with (a) protons and (b) neutrons to different fluence values.

substrate type. This behavior emerges due to the left over gain turning on at higher voltages and only appears for sensors irradiated to the lowest fluence level for proton irradiation. This is expected since the gain layer is expected to vanish only after about $\Phi_{eq} = 2 \times 10^{15}\,cm^{-2}$, which is close to the fluence of the middle fluence level. Inspecting Fig. 14.2b, the same behavior can be observed for the neutron-irradiated sensors, but the overtaking happens both for the lowest and the middle fluence level. This result was very surprising since it was not expected that the gain layer would survive the middle fluence level of $\Phi_{eq} = 2 \times 10^{15}\,cm^{-2}$. The author speculates that there are two possible explanations for this behavior:

- The estimated neutron fluence levels are not accurate and the actual fluence levels are lower than expected.
- The NIEL hypothesis is limited to relatively thick sensors without gain implants, demonstrating that complex behavior such as charge multiplication cannot be modelled with a single parameter.

Although the first explanation cannot be ruled out, especially considering that the equivalent proton fluences are higher than the neutron fluences, the second explanation is also plausible. The NIEL hypothesis is a simplification that does not take the different complex interactions for different particle types into account. Assuming that the NIEL hypothesis is valid, neutron irradiation seems to affect the gain layer less than proton irradiation, since the overtaking effect is visible for both the lowest and middle fluence levels for neutrons, while it is only visible for the lowest fluence level for protons. Both plots in Fig. 14.2 show that the leakage current is also not dependent on the pitch size, as both sensors with a pitch of 450 µm and 1.3 mm show virtually the same behavior for all fluence levels and particle types. Considering that leakage current generation happens in the bulk of the sensor, this result is expected.

Figure 14.3 compares the IV curves of all wafers after irradiation with protons and neutrons to the lowest fluence level of $\Phi_{eq} = 1 \times 10^{15}\,cm^{-2}$. All wafers show the same leakage current level, regardless of the substrate type. This is a very remarkable result since the FZ wafers showed a higher leakage current in the saturation region than sensors with an epi substrate before irradiation. It is hypothesized that this happens due to acceptor creation by irradiation damage for the epi wafers. Assuming that the substrate doping concentration of the epi wafers is lower than that of the FZ wafers prior to irradiation, acceptor creation would assimilate the

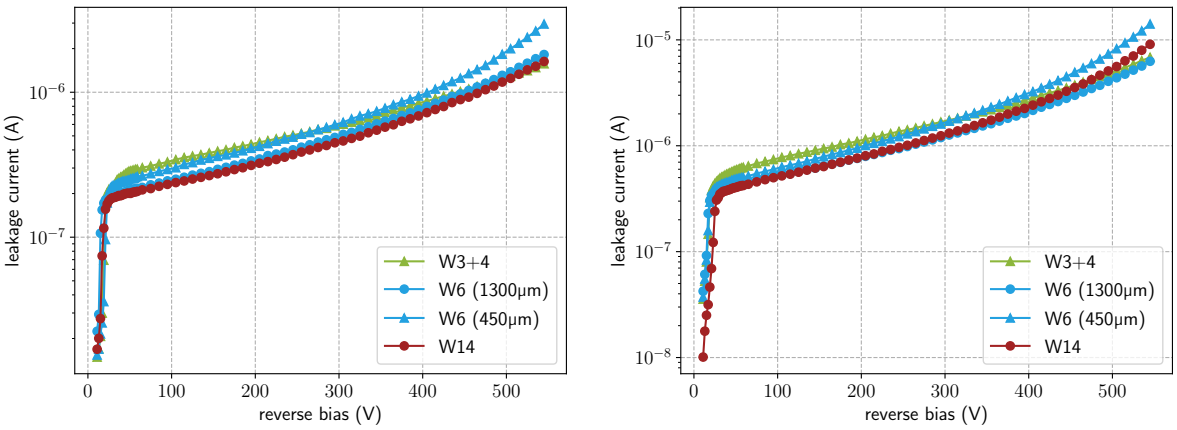

Figure 14.3.: Comparison of IV curves of all wafers after irradiation with (a) protons and (b) neutrons.

substrate doping concentration of the epi wafers to that of the FZ wafers, yielding the same leakage current level. However, this cannot be currently verified, but could be in the future if the substrate doping concentrations are disclosed. The more interesting finding, however, is that the overtaking effect that was observed while comparing the IV curves of the sensors is more pronounced for some wafers than for others. In particular, wafer six (blue) and 14 (red) show a more pronounced overtaking effect than wafers three and four (green). Considering that all examined wafers in this study possess virtually the same gain layer depletion voltage, the only significant difference that can be made out is the substrate type and n+ resistive layer doping concentration. As established, the overtaking effect is more pronounced the more gain is left over. Combining these two observations shows that the gain mechanism does not only depend upon the gain layer doping concentration but is a complex interaction of the gain layer and resistive layer doping concentrations.

CV Measurements

In this section, the CV measurements of the sensors after irradiation will be discussed. Again, different perspectives will be taken to analyze the results as with the IV measurements, focusing on the influence of the particle type, fluence and pad pitch first, followed by a comparison of the wafers. In addition, the acceptor removal coefficient c was extracted from the CV measurements using the method previously described. All fluences in this section are given in real particle fluences without NIEL scaling since it is not applicable for the CV measurements, as explained previously. Figure 14.4 shows the CV curves of wafer six (epi) sensors after irradiation with protons and neutrons to different fluence values. A clear scaling of the gain layer depletion voltage with the fluence can be observed for both particle types, as expected. Neutron irradiation seems to cause a significantly larger shift in V_{GL} than proton irradiation. This is best observed when comparing the middle proton fluence level and the lowest neutron fluence level, which are both $\Phi = 1 \times 10^{15}\,\mathrm{cm}^{-2}$. For proton irradiation, the capacitance drops at about $V = 8\,\mathrm{V}$, while for neutron irradiation, the capacitance drops at about $V = 17\,\mathrm{V}$. Another demonstration of NIEL scaling not applicable for this measurement becomes apparent when comparing both middle fluence levels, which are both $\Phi_{\mathrm{eq}} = 2 \times 10^{15}\,\mathrm{cm}^{-2}$ when the proton fluence is scaled accordingly. If NIEL scaling was applicable, the capacitance curves would be identical, which is not the case. The same observation applies to the other fluence levels. It is not surprising

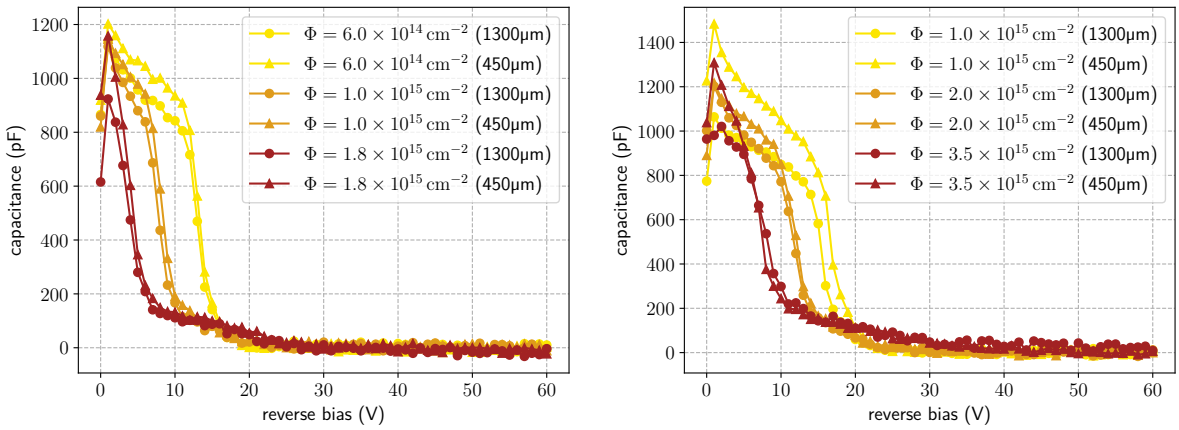

(a) **(b)**

Figure 14.4.: CV curves of wafer six sensors after irradiation with (a) protons and (b) neutrons to different fluence values.

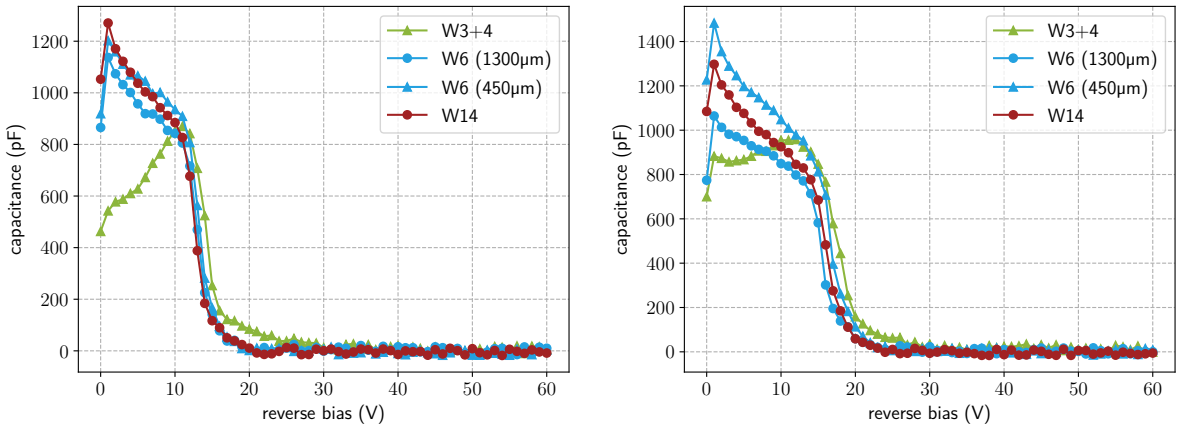

(a) **(b)**

Figure 14.5.: Comparison of CV curves of all wafers after irradiation with (a) protons and (b) neutrons.

that the neutron fluence causes a larger shift in the gain layer depletion voltage since neutron irradiation is expected to affect N_{eff} more than proton irradiation. Additionally, as observed in the IV measurements, the pad pitch has no significant influence on the capacitance behavior.

In Fig. 14.5, the CV curves of all wafers after irradiation with protons and neutrons to the lowest fluence level are compared. The same drop voltage is observed for all wafers, regardless of the substrate and particle type. However, the capacitance of FZ wafers three and four (green) rises before reaching V_{GL} and then drops again, while the capacitance of the epi wafers (blue and red) falls monotonically. In these plots, the lowest fluence levels are shown, corresponding to $\Phi_{\text{p}} = 0.8 \times 10^{15}\,\text{cm}^{-2}$ for protons and $\Phi_{\text{n}} = 1 \times 10^{15}\,\text{cm}^{-2}$ for neutrons. The effect is more pronounced for the proton-fluence $\Phi_{\text{p}} = 0.8 \times 10^{15}\,\text{cm}^{-2}$ and less pronounced (but still present) for the neutron fluence $\Phi_{\text{n}} = 1 \times 10^{15}\,\text{cm}^{-2}$ and vanishes for higher fluences. This indicates that this effect is related to the particle fluence and only occurs for FZ wafers. The reason for this behavior is not yet understood, but it is speculated that it is related to the SCR formation as was the case for the noise of the pre-irradiation IV measurements.

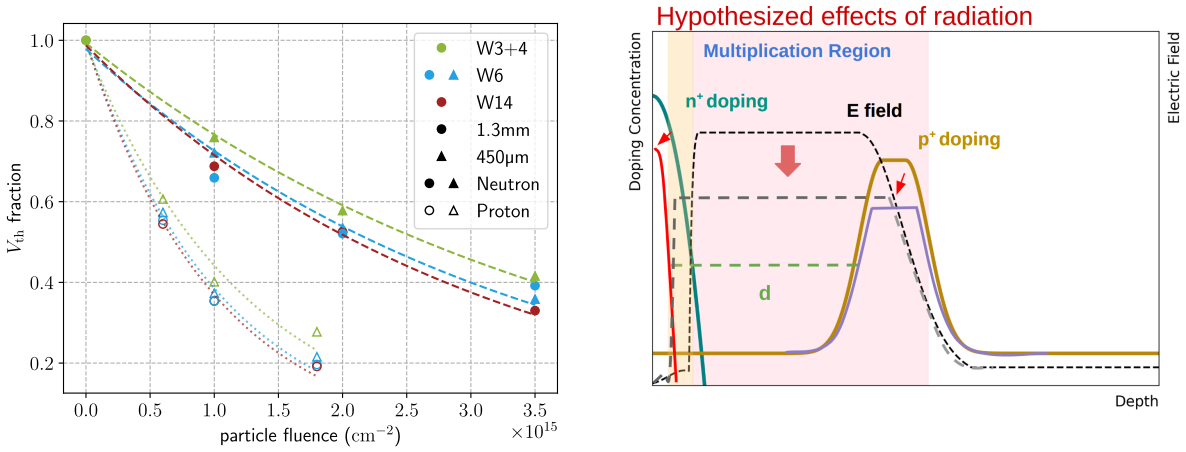

(a) **(b)**

Figure 14.6.: (a) Active gain layer fraction in terms of V_{th} as a function of particle fluence for all wafers and irradiation types. Dashed and dotted lines show the exponential fits used to extract c. (b) Graphic explaining the hypothesized effects involving the resistive layer leading to lower c values. More details in main text. Image by courtesy of Brendan Regnery [ER+25].

Figure 14.6a shows the fraction of active gain layer f expressed in terms of the threshold crossing voltage V_{th} (V_{th} fraction) as a function of the particle fluence for all wafers and irradiation types. The method used to extract the fraction of active gain layer is explained in the previous chapter. A threshold capacitance of $C_{\text{th}} = 300\,\text{pF}$ was used. The data points at the last fluence levels for both particle types were excluded from the fit since the gain layer is expected to be completely removed at these fluences which would lead to a saturation of V_{th} and is not modelled by the exponential fit. Using this method, the values for the acceptor removal coefficient c shown in Table 14.1 were extracted. The work in [Fer+21] gives acceptor removal coefficients for standard LGADs with similar gain layer designs of $c_{\text{n}} \approx 5 \times 10^{-16}\,\text{cm}^2$ and $c_{\text{p}} \approx 12 \times 10^{-16}\,\text{cm}^2$ for neutron and proton irradiation, respectively. Comparing the values in Table 14.1 that were found in this work to the values in [Fer+21] shows that the values are significantly lower. Taking the c values found in this study at face value, it would suggest a higher radiation hardness for the AC-RSD sensors than for similar devices investigated in [Fer+21]. However, it is very unlikely that devices with almost identical gain layer designs would show such a large difference in radiation hardness. Therefore, it is speculated that the lower c values are due to the fact that the coefficients were extracted from the capacitance measurements of the AC-RSD sensors, which are only sensitive to the evolution of the depletion zone through the sensor as a whole and not just the gain layer. The AC-RSD devices investigated in this study have a resistive n+ layer that has a much lower doping

Table 14.1.: Extracted c coefficients for all wafers and irradiation types given in units of $10^{-16}\,\text{cm}^2$.

Irradiation	W3+4	W6	W14
Neutron	2.6 ± 0.1	3.0 ± 0.3	3.2 ± 0.2
Proton	8.1 ± 0.7	9.5 ± 0.5	9.9 ± 0.4

concentration than standard LGADs. Therefore, the donor removal effect in the resistive layer is expected to be much more pronounced than in standard LGADs since the initial donor concentration is much lower. Figure 14.6b illustrates this effect schematically, where the n+ doping concentration of the resistive layer and the p+ doping concentration of the gain layer are shown, intially in green and gold lines, respectively. The electric field in the sensor is shown initially as a black dashed line. After irradiation, the donor removal effect in the resistive layer results in a lower concentration of donors (red line) and the acceptor removal effect in the gain layer leads to a lower concentration of acceptors (blue line). As a consequence, the multiplication region is wider than in standard LGADs, which is shown as the extension of the initial multiplication region (red shaded area) to the left (green shaded area). This means that the V_{GL} values extracted from the capacitance measurements tend to be higher, which in turn leads to lower c values. Due to the fact that the c coefficients, which were extracted in this study, not only characterize the acceptor removal for these devices but also the donor removal in the resistive layer, calling the extracted coefficient an *acceptor removal coefficient* seems difficult — *gain loss coefficient* would be a more appropriate name. At the time of writing, the author is not aware of any other work that investigated the interplay of donor and acceptor removal of LGADs with n+(+)-layer donor concentrations that are comparable to the ones in the AC-RSD sensors from this study. The work in [ER+25] further investigates the donor removal effect using Van der Pauw test structures specifically designed to measure the resistive layer. Upcoming publications will also present annealing studies on these structures, further investigating the evolution of donor removal in the resistive layer.

Summary of IV/CV Measurements

The IV and CV measurements of the AC-RSD sensors after irradiation show that the sensors are functional and that the gain layer is still present after irradiation with neutrons and protons to fluences of up to $\Phi_{\mathrm{eq}} = 2 \times 10^{15}\,\mathrm{cm}^{-2}$. Leakage current characteristics are not dependent on the substrate type or pitch size in magnitude, but the overtaking effect in the IV curves is more pronounced for sensors with a higher resistive layer doping concentration. The leakage current measurements also show that the gain layer is still present after irradiation with neutrons and protons to fluences of up to $\Phi_{\mathrm{eq}} = 2 \times 10^{15}\,\mathrm{cm}^{-2}$, which was not expected. The CV measurements show that the gain layer depletion voltage shifts with increasing fluence, while neutron irradiation causes a larger shift than proton irradiation due to higher effect on N_{eff}. The acceptor removal coefficient c was extracted from the capacitance measurements and was found to be significantly lower than standard LGADs with similar gain layer designs. This is likely due to the fact that the capacitance measurements are sensitive to the evolution of the depletion zone through the sensor as a whole and not just the gain layer. The lower c values are likely due to the donor removal effect in the resistive layer, which is expected to be more pronounced in the AC-RSD sensors than in standard LGADs.

14.2. Gain Deterioration

After the electrical characterization in the probe station, the sensors were tested in the TCT setup regarding their gain characteristics as a function of the applied bias voltage. Measurement settings were adjusted and calibrations were performed as described in Sections 5.1.3 and 13.3. All fluences in this section are given in real particle fluences since the NIEL scaling is not applicable for signal measurements that are sensitive to trapping and charge multiplication.

Figure 14.7 shows the area under the average signal pulse $S(V)$ as a function of the bias voltage V for all sensors irradiated with protons and neutrons. A number of $n_{\mathrm{pulse}} = 5000$ waveforms $S_i(V, t)$ were averaged to obtain the average signal pulse $S(V)$. In order to protect the

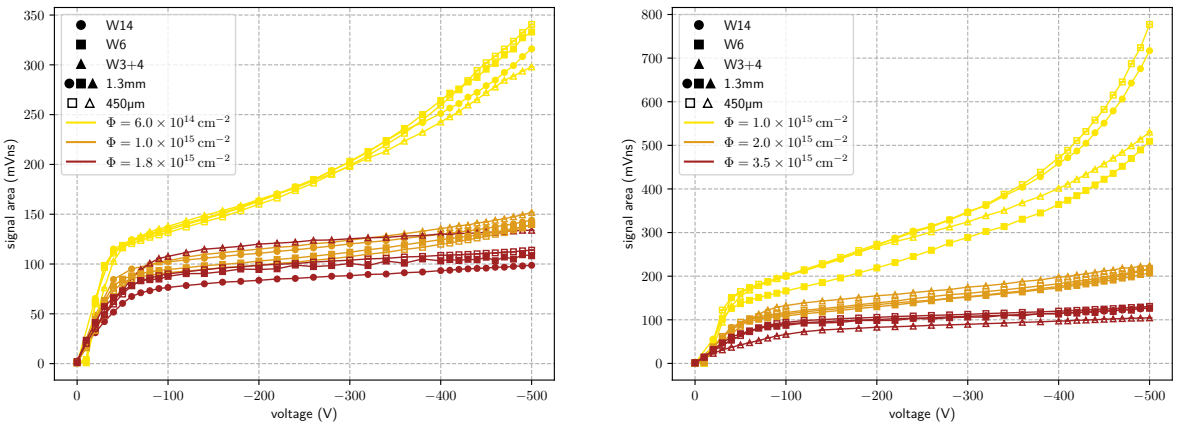

(a) **(b)**

Figure 14.7.: Area under the average signal pulse $S(V)$ as a function of the bias voltage V for (a) proton-irradiated and (b) neutron-irradiated sensors. An average of $n_{\text{pulse}} = 5000$ waveforms was used in the analysis.

sensors from damage, the bias voltage was limited to 500 V for all examined sensors, although in hindsight, this was not necessary since a current compliance limit was employed during the measurements. As expected, the signals from sensors irradiated with protons is significantly lower than neutron-irradiated sensors due to the introduction of more trapping centers by protons than neutrons. Comparing the highest fluence levels of both particle types (red) shows an identical behavior, with the signal area increasing up to a level of about 100 mV ns and almost saturation — the typical behavior of a PiN diode. This result indicates the complete absence of gain in both cases. Surprisingly, NIEL scaling does seem to apply at this fluence level, as the signals of the sensors irradiated with neutrons are on the same level as the signals of the sensors irradiated with protons. However, as soon as some gain is left over, like for instance in the middle (orange) and lowest (yellow) fluence levels, the signals of the neutron-irradiated sensors are significantly higher than those of the proton-irradiated sensors, even though the NIEL-scaled fluences are the same. This is a clear indication that NIEL scaling indeed does not apply for charge collection measurements of sensors with gain layers, as previously predicted. Moreover, the overtaking effect that was observed in the IV measurements is also present in the gain measurements of sensors irradiated with protons, indicating that some gain is still present in the sensors irradiated to the middle proton fluence level. Judging by the upward bend of the curves for middle neutron fluence levels, it seems that the gain layer is still present in these sensors as well, although no overtaking effect is observed since the signals of high neutron fluence levels are already lower than the signals of the middle neutron fluence level. The upward bend of the curves also indicates that, overall, more gain is left over in the sensors irradiated with neutrons than in the sensors irradiated with protons. Comparing the high-voltage bend at the end of the curves for the lowest fluence levels between the two particle types shows this very clearly. This result is consistent with the IV measurements, where the overtaking effect was also more pronounced for neutron-irradiated sensors. Combining the results of the IV and gain measurements suggests that the gain layer is more resistant to neutron irradiation than to proton irradiation, especially considering that the neutron fluences are significantly lower than the proton fluences. The gain turns on only at higher bias voltages for both particle types, judging by the low-voltage behavior of the curves until bias voltages of about 100 V for all fluence levels. Comparing just these parts of the curves between both particle types shows that they behave similarly, indicating that more voltage is required after irradiation to deplete the

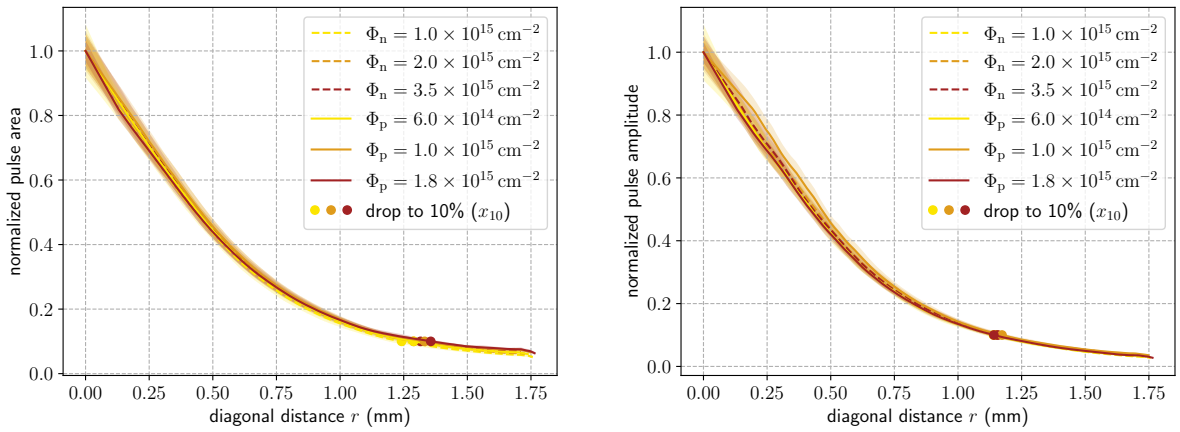

(a) **(b)**

Figure 14.8.: Normalized (a) diagonal signal areas $D_S(r)$ and (b) diagonal signal amplitudes $D_A(r)$ as a function of diagonal distance r. Curves belonging to proton-irradiated samples are shown as solid lines, neutron-irradiated ones are shown as dashed lines. Circles show x_{10} for each curve. Bands show the 95% confidence interval including all electrodes.

gain layer, which is consistent with the expectations. In addition to these observations, the gain deterioration does not seem to depend on the pitch size, since no correlation between the pitch size and the signal area can be observed.

In summary, the gain measurements show that the gain layer is still present after irradiation with neutrons and protons to fluences of up to $\Phi_{\mathrm{eq}} = 2 \times 10^{15}\,\mathrm{cm}^{-2}$. The gain mechanism of AC-RSD sensors are more resistant to neutron irradiation than to proton irradiation. A higher bias voltage is required to deplete the gain layer and turn the multiplication mechanism on after irradiation, which was expected.

14.3. Charge Spreading

After characterization of the gain deterioration, a study of the charge spreading was performed. The charge spreading measurements were exclusively performed on the AC-RSD sensors from wafer 14 due to a lack of time. Measurement settings were adjusted and calibrations were performed as described in Sections 5.1.3 and 13.3. Analysis methods are also described in Section 13.3. As in the previous section, fluences are given in real particle fluences.

14.3.1. Charge spread distance x_{10}

Propagation of the signal through the resistive layer was studied by measuring the signal area and amplitude as a function of the distance r from each of the four electrodes. Getting the point where the signal dropped to 10% of its maximum value yields a parameter that was named *charge spread distance* x_{10}, which is the metric that was used to quantify the charge spreading in the resistive layer among all tested samples. Naturally, the diagonal signal area $D_S(r)$ and amplitude $D_A(r)$ that were explained in Section 13.3.2 are expected to be lower the more the sensor was irradiated, leading to signal decays that are fluence-specific. To compare the charge spreading of different sensors regardless of the fluence, the signal area and amplitude were normalized to the maximum value of $D_S(r)$ and $D_A(r)$, respectively. This is shown in Fig. 14.8 for both the signal area and amplitude. Extracting the point where the normalized $D_S(r)$ and

Table 14.2.: Average charge spread distance $\overline{x_{10}}$ and average leak ratio $\overline{\psi}$ using (a) the signal area $D_S(r)$ and (b) the signal maximum $D_A(r)$. Uncertainties were calculated as the standard error of the mean resulting from averaging over all four electrodes.

(a) With D_S

fluence	n/p	$\overline{\psi}$	$\overline{x_{10}}$ (mm)
1.0×10^{15}	n	0.27 ± 0.03	1.24 ± 0.02
2.0×10^{15}	n	0.27 ± 0.02	1.29 ± 0.01
3.5×10^{15}	n	0.27 ± 0.02	1.32 ± 0.01
6.0×10^{14}	p	0.26 ± 0.02	1.29 ± 0.01
1.0×10^{15}	p	0.27 ± 0.01	1.33
1.8×10^{15}	p	0.26 ± 0.02	1.36 ± 0.02

(b) With D_A

fluence	n/p	$\overline{\psi}$	$\overline{x_{10}}$ (mm)
1.0×10^{15}	n	1.62 ± 0.20	1.15 ± 0.02
2.0×10^{15}	n	1.69 ± 0.11	1.16 ± 0.01
3.5×10^{15}	n	1.67 ± 0.16	1.16 ± 0.01
6.0×10^{14}	p	1.66 ± 0.18	1.14 ± 0.01
1.0×10^{15}	p	1.75 ± 0.11	1.17
1.8×10^{15}	p	1.76 ± 0.16	1.14 ± 0.01

$D_A(r)$ dropped to 0.1 defines the *charge spread distance* x_{10} for both quantities. These x_{10} points are shown in the aforementioned plots as circles. The x_{10} parameter is a measure of how far the induced charge spreads in the resistive layer. In theory, the area metric is expected to be a more accurate measure of charge collection per se since it contains more information about the whole signal shape, while the amplitude metric only considers the maximum value of the signal. However, for this particular study, the signal propagation through the resistive layer is the topic of interest. Depending on how far the charge spreads across the resistive layer, the signal amplitude will be affected more than the signal area. Therefore, a more accurate measure of charge spreading is expected to be the signal amplitude but the signal area is also useful to compare the results. Another reason advocating the use of the signal amplitude is that the signal pulse is bipolar for AC-RSD sensors, which makes extracting it more difficult. For a radiation-hard sensor design, x_{10} is expected to remain constant with increasing fluence. Extracting all x_{10}-circles from the plots and calculating the average over all four electrodes of each sensor yielded the average charge spread distance $\overline{x_{10}}$, shown in Table 14.2. Uncertainties in all $\overline{x_{10}}$ were calculated as the standard error of the mean resulting from averaging over all four electrodes. The $\overline{x_{10}}$ values remained constant with increasing fluence for both particle types when the signal amplitude metric was considered, which suggests that the charge spreading is not affected by the fluence. However, a slight increase in $\overline{x_{10}}$ is observed when the signal area metric is used, which suggests that the charge spreading is slightly affected by the fluence. Considering the limited number of sensors and fluences that were measured, this increase is not significant enough to draw any conclusions. Under the assumption that the amplitude metric is a more accurate measure of x_{10} and no significant changes are observed, it can be concluded that the charge spreading is not affected by radiation damage in the recorded fluence range.

14.3.2. Leak ratio ψ

In order to analyze how much of the charge that was deposited in a point within a pixel leaks outside the pixel, *the leak ratios* ψ_S for the signal area and ψ_A for the signal amplitude were extracted. The leak ratios are defined by summing the $S(x, y)$ and $A(x, y)$ values of the signal electrodes that are within the data mask and dividing the sum by the sum of all $S(x, y)$ and $A(x, y)$ values measured by the DC ring that are also within the data mask:

$$\psi_M(E) = \left. \frac{\sum_{x,y} M_E}{\sum_{x,y} M_{\mathrm{DC}}} \right|_{\mathrm{pix}},$$

where M is either S or A, $E \in \{1 \dots 4\}$ denotes the electrode number and the sum is taken over all points within the data mask/pixel. Averaging ψ over all four electrodes yields the average leak ratio $\overline{\psi}$. For the same reason as in the previous section, the signal amplitude metric is expected to be a more accurate measure of ψ than the signal area metric but both were analyzed for the sake of completeness. Table 14.2 shows the average leak ratios $\overline{\psi}$ for both metrics. The uncertainties in all $\overline{\psi}$ were calculated as the standard error of the mean resulting from averaging over all four electrodes. Average leak ratios $\overline{\psi}$ remained constant with increasing fluence for both particle types and metrics, which suggests that the signal containment is not affected by the fluence within the recorded fluence range.

14.3.3. Summary of Charge Spreading Measurements

The charge spreading measurements show that the charge spread distance x_{10} remains constant with increasing fluence for both particle types when the signal amplitude metric is used, which suggests that the charge spreading is not affected by the fluence. Moreover, the average leak ratios $\overline{\psi}$ also remain constant with increasing fluence for both particle types and metrics, which suggests that the signal containment is not affected by the fluence within the recorded fluence range. This result demonstrates an excellent radiation hardness of the AC-RSD sensors. Taking into consideration that no radiation-hardening techniques were applied to the AC-RSD sensors, the results of this study are very promising regarding the radiation hardness of the AC-RSD sensors.

15

Summary and Outlook: RSD Irradiation Testing

The second part of this thesis was dedicated to the investigation of the radiation hardness and charge sharing properties of AC-coupled Resistive Silicon Devices (AC-RSDs), a novel sensor concept for future 4D tracking detectors in colliders and beyond. These devices feature a resistive layer and are based on the concept of increased charge sharing to improve position resolution by increasing the intrinsic fill factor and reducing the number of readout channels required for a given resolution. The irradiation program focused on the characterization of AC-RSD sensors before and after irradiation, aiming to assess their suitability for use in high-radiation environments such as the HL-LHC in the scope of research and development for future timing detectors not necessarily limited to the CMS experiment.

AC-RSD sensors from four different wafers, provided by FBK and INFN, were characterized electrically before and after irradiation. The sensors were irradiated with protons and neutrons to fluences up to $\Phi_{\text{eq}} = 3.5 \times 10^{15}\,\text{cm}^{-2}$, covering the expected range for HL-LHC applications beyond Phase-2. IV and CV measurements were performed to assess sensor functionality, breakdown voltages, and gain layer depletion voltages. The sensors exhibited consistent gain layer depletion voltages before irradiation, and most were functional, with a small fraction showing early breakdowns.

After irradiation, all sensors showed increased leakage currents, as expected. The gain layer remained active up to the highest tested fluences despite prior expectation of gain deprecation from simulations [Fer+21], with the gain mechanism being more resistant to neutron irradiation than to proton irradiation. The characteristic overtaking effect in IV and gain deterioration measurements indicated that the gain layer survives even at intermediate fluence levels, especially for neutron-irradiated sensors. The acceptor removal coefficient c — or *gain loss coefficient*, a name proposed to describe the process more suitably — was extracted from CV measurements, quantifying the gain layer's response to irradiation.

Charge spreading studies were performed using TCT measurements on 2×2 AC-RSD sensors. The charge spread distance x_{10}, defined as the distance at which the signal drops to 10% of its maximum, was used as a metric for charge sharing. The results showed that the charge sharing properties of AC-RSDs are robust against irradiation, with only a moderate reduction in x_{10} at the highest fluences that was not deemed to be significant. No dependence on electrode pitch size was observed.

The results demonstrate that AC-RSD sensors maintain their gain and charge sharing capabilities after irradiation to fluences relevant for HL-LHC environments to some extent, even without dedicated radiation-hardening techniques. The findings highlight the potential of AC-RSDs for future timing and tracking applications, motivating further studies on optimization and large-scale production. Since the AC-RSD is a device that is based on increased charge sharing, high-rate tests are especially important for the AC-RSD concept and will be the focus of future studies. The high number of pileup events expected at the HL-LHC will require sensors that can handle high rates without significant degradation in performance.

Overall, the RSD irradiation tests presented in this thesis provide a broad assessment of the performance and radiation tolerance of AC-RSD sensors, supporting their suitability for next-generation high-energy physics detectors.

A Appendix

A.1. Definition of the quantities used in the *Bethe equation*

Table A.1.: Definition of quantities used in the *Bethe equation* Eq. (2.11).

symbol	quantity	value/unit
N_A	Avogadro's number	$6.023 \times 10^{23}\,\mathrm{mol}^{-1}$
r_e	class. electron radius	2.818 fm
m_e	electron mass	511 keV
z	projectile charge number	—
Z	absorber charge number	—
A	absorber atomic mass	in u
I	mean excitation number	in eV
β	relativistic beta factor v/c	—
γ	Lorentz factor $1/\sqrt{1-\beta^2}$	—
W_max	maximum possible energy transfer per collision	in MeV
$\delta\,(\beta\gamma)$	density effect correction	—

A.2. Supplementary Material for Part One: Irradiation Testing of Silicon Sensors for the CMS Phase-2 Upgrade

Table A.2.: List of measured samples per batch pre- (and post-) irradiation.

Batch	Babysensors	Diodes	MOS/GCDs	Campaign No.	Type
35719	3 (2)	3 (1)	3 (2)	2	2S
35955	2 (2)	2 (2)	2 (2)	1	PS-s
35958	2 (2)	2 (1)	2 (2)	1	2S
35960	3 (2)	3 (1)	3 (2)	2	2S
36236	3 (2)	3 (1)	3 (2)	2	PS-s
36237	3 (2)	3 (1)	4 (3)	2	PS-s
36698	2 (2)	1 (1)	2 (2)	1	2S
36699	2 (1)	1 (1)	2 (2)	1	2S
36700	2 (2)	2 (1)	2 (2)	1	2S
36701	4 (2)	4 (1)	5 (5)	1	2S
37083	3 (2)	3 (1)	3 (2)	2	2S
37084	2 (2)	3 (1)	5 (3)	2	2S
37901	3 (2)	3 (1)	3 (2)	2	2S
37907	3 (2)	3 (1)	3 (2)	2	2S
38202	3 (2)	3 (1)	3 (2)	4	2S
38712	3 (2)	3 (1)	4 (3)	2	PS-s
38921	2 (2)	3 (1)	3 (2)	2	PS-s
39563	3 (2)	3 (1)	3 (2)	4	PS-s
41353	3 (2)	3 (1)	3 (2)	3	2S
41355	3 (2)	3 (1)	3 (2)	3	2S
41727	3 (2)	3 (1)	3 (3)	4	PS-s
41728	3 (2)	3 (1)	3 (2)	3	PS-s
41729	4 (3)	3 (1)	3 (3)	5	PS-s
41742	3 (2)	3 (1)	3 (2)	3	2S
41759	3 (2)	3 (1)	3 (3)	5	2S
42245	3 (2)	2 (1)	3 (3)	5	2S
42248	3 (2)	3 (1)	3 (3)	5	2S
42652	3 (2)	3 (1)	3 (3)	5	2S
42899	3 (2)	3 (1)	3 (3)	5	PS-s
42904	3 (2)	3 (1)	3 (2)	5	2S
42909	3 (2)	3 (1)	3 (3)	5	2S
43259	3 (2)	3 (1)	3 (3)	5	2S

Table A.3.: Specifications for the electrical parameters of CMS Outer Tracker Sensors. Strips not passing all requirements are flagged as bad in the scope of SQC. Sensors with more than 20 flagged strips are rejected.

Parameter	Specification
full depletion voltage V_{FD}	$< 350\,\mathrm{V}$
current at 600 V I_{600}	$\leq 2.5\,\mathrm{nA\,mm^{-3}}$
breakdown voltage V_{BD}	$> 800\,\mathrm{V}, I_{800} < 2.5 \times I_{600}$
strip current I_{leak}	$< 10\,\mathrm{nA\,cm^{-1}}$
bias resistor resistance R_{poly}	$(1.5 \pm 0.5)\,\mathrm{M\Omega}$
coupling capacitance C_{ac}	$> 1.2\,\mathrm{pF\,cm^{-1}\,\mu m^{-1}}$
dielectric current I_{diel} (10 V)	$< 10\,\mathrm{nA}$
interstrip resistance R_{int}	$> 10\,\mathrm{G\Omega\,cm}$
interstrip capacitance C_{int}	$< 0.5\,\mathrm{pF\,cm^{-1}}$

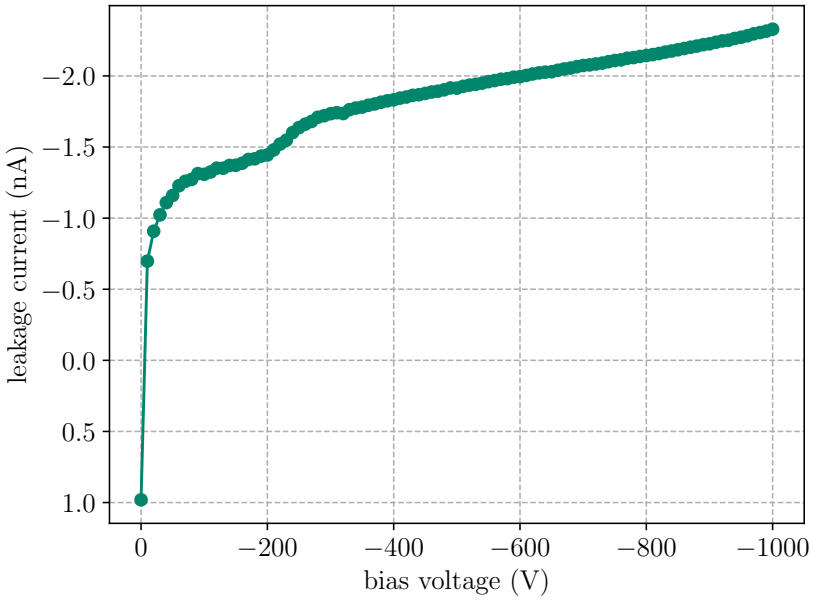

Figure A.1.: Sample IV curve of an unirradiated babysensor from batch 41355. The curve is different from a square root function and features a kink related to the evolution of the SCR as the sensor is depleted further.

A.3. Supplementary Material for Part Two: Irradiation Studies on Ultrafast Silicon Devices for Timing Applications

Table A.4.: Overview of the AC-RSD sensors used in this work. The lot number is a number uniquely identifying a location on the wafer. Fluences are quoted as particle fluences Φ, not equivalent fluences. If a sensor was used for the charge spreading study, it is flagged accordingly.

Lot	Wafer	Pitch (µm)	Particle	Φ (cm^{-2})	Charge spread?
3-3	W14	1300	neutron	1.0×10^{15}	Yes
5-6	W14	1300	neutron	2.0×10^{15}	Yes
3-6	W14	1300	neutron	3.5×10^{15}	Yes
6-4	W14	1300	proton	1.2×10^{15}	Yes
6-5	W14	1300	proton	2.0×10^{15}	Yes
4-5	W14	1300	proton	3.6×10^{15}	Yes
3-6	W3+4	450	neutron	1.0×10^{15}	No
2-6	W3+4	450	neutron	2.0×10^{15}	No
5-5	W3+4	450	neutron	3.5×10^{15}	No
12-5	W3+4	450	proton	1.2×10^{15}	No
2-6	W3+4	450	proton	2.0×10^{15}	No
3-5	W3+4	450	proton	3.6×10^{15}	No
3-6	W6	1300	neutron	1.0×10^{15}	No
4-6	W6	450	neutron	1.0×10^{15}	No
3-5	W6	1300	neutron	2.0×10^{15}	No
2-5	W6	450	neutron	2.0×10^{15}	No
6-4	W6	1300	neutron	3.5×10^{15}	No
2-3	W6	450	neutron	3.5×10^{15}	No
3-4	W6	1300	proton	1.2×10^{15}	No
3-3	W6	450	proton	1.2×10^{15}	No
6-6	W6	1300	proton	2.0×10^{15}	No
5-6	W6	450	proton	2.0×10^{15}	No
2-4	W6	1300	proton	3.6×10^{15}	No
3-4	W6	450	proton	3.6×10^{15}	No

A.3.1. IV Curves Before Irradiation

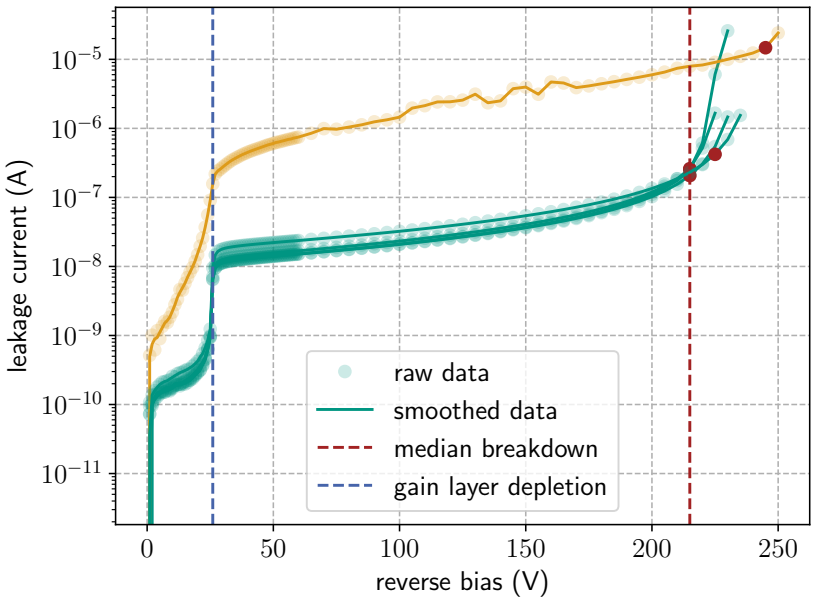

Figure A.2.: IV curves before irradiation of all tested W3 sensors. Curves belonging to sensors exhibiting typical behavior are shown in green. Atypical characteristics are shown in yellow. Red circles show the breakdown voltage extacted with the k-factor method.

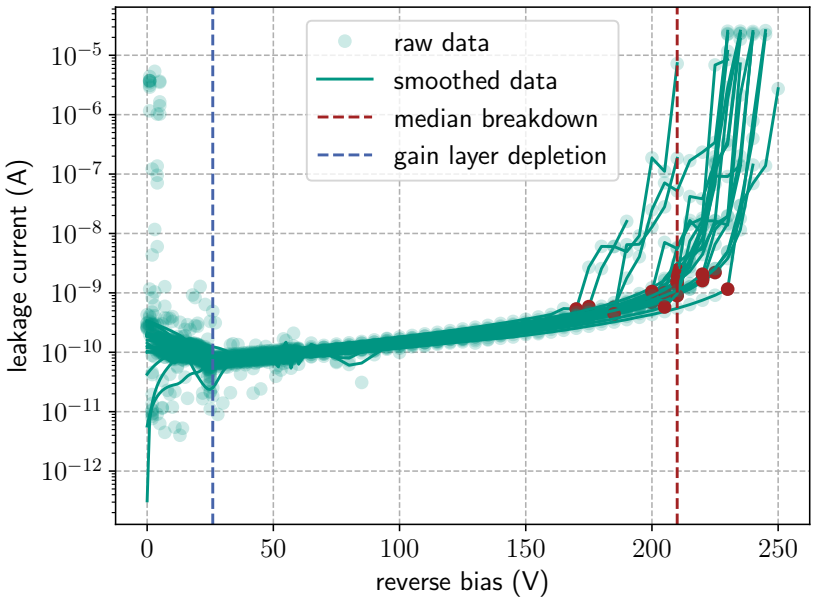

Figure A.3.: IV curves before irradiation of all tested W14 sensors. Curves belonging to sensors exhibiting typical behavior are shown in green. Red circles show the breakdown voltage extacted with the k-factor method.

A.3.2. IV Curves After Irradiation

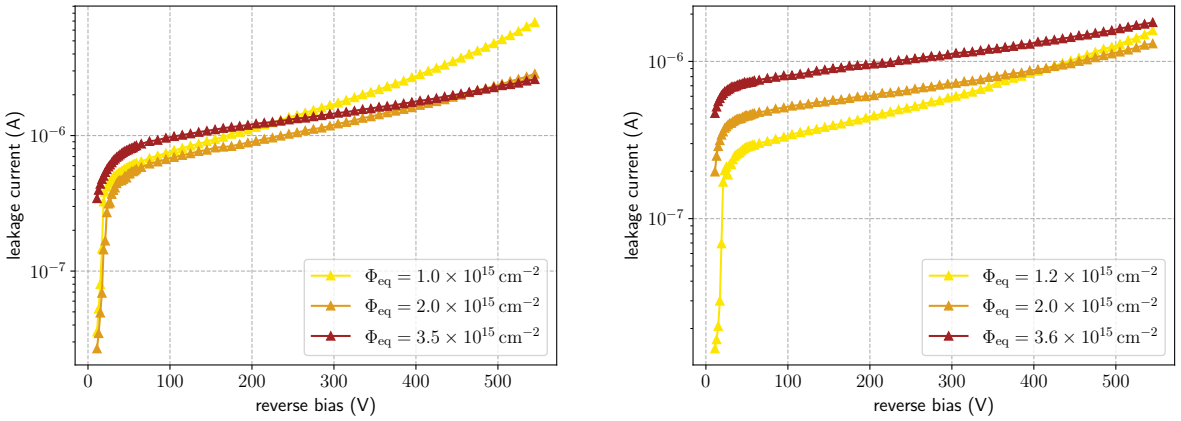

(a) **(b)**

Figure A.4.: IV curves after irradiation of all tested W3+4 sensors for different particle fluences. (a) neutron irradiated, (b) proton irradiated.

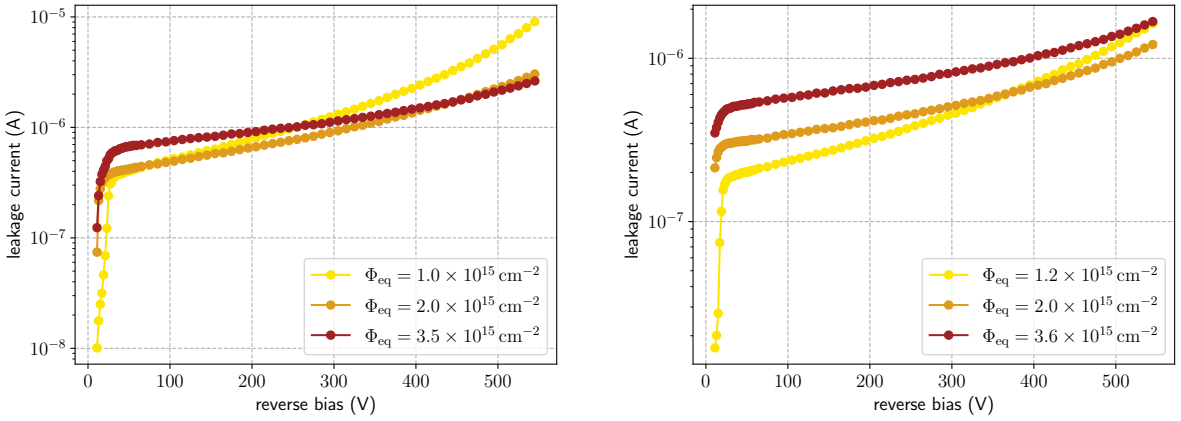

(a) **(b)**

Figure A.5.: IV curves after irradiation of all tested W14 sensors for different particle fluences. (a) neutron irradiated, (b) proton irradiated.

A.3.3. CV Curves After Irradiation

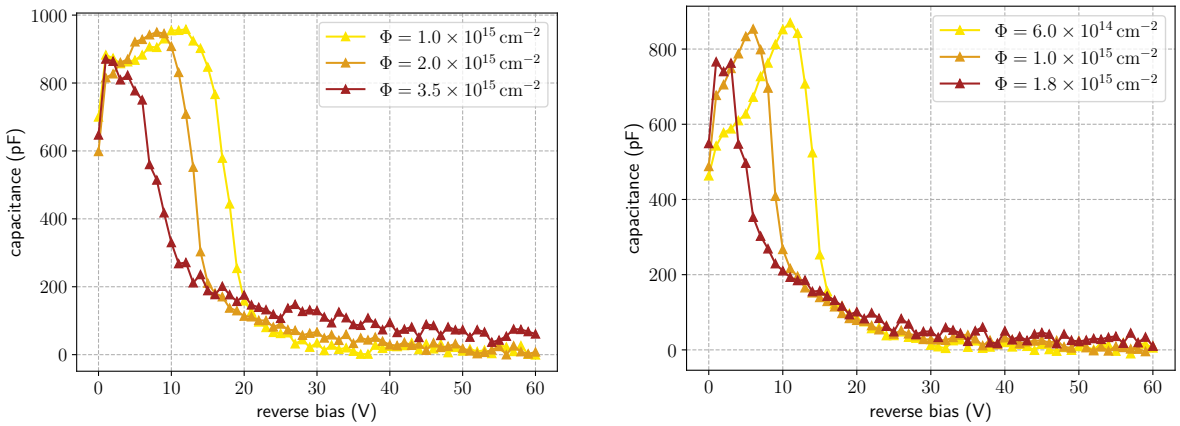

(a) **(b)**

Figure A.6.: CV curves after irradiation of all tested W3+4 sensors for different particle fluences. (a) neutron irradiated, (b) proton irradiated.

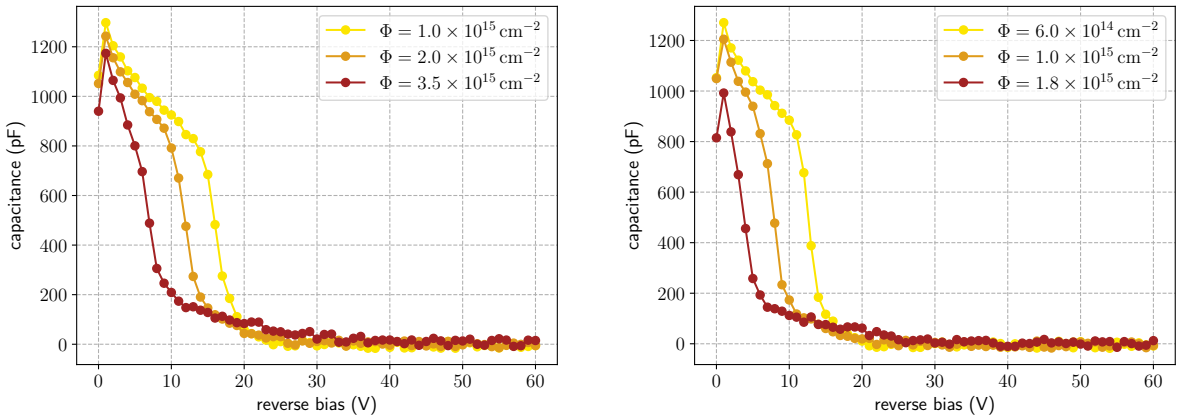

(a) **(b)**

Figure A.7.: CV curves after irradiation of all tested W14 sensors for different particle fluences. (a) neutron irradiated, (b) proton irradiated.

List of Figures

List of Tables

Bibliography

[Aad+12] G. Aad et al. *Observation of a new particle in the search for the Standard Model Higgs boson with the ATLAS detector at the LHC*. In: Physics Letters B 716.1 (Sept. 2012). ISSN: 0370-2693. DOI: 10.1016/j.physletb.2012.08.020 (cited on pp. 1, 31).

[Abe+20] O. Aberle et al. *High-Luminosity Large Hadron Collider (HL-LHC): Technical design report*. CERN Yellow Reports: Monographs. Geneva: CERN, 2020. DOI: 10.23731/CYRM-2020-0010 (cited on pp. 1, 31, 34).

[Ada+20] W. Adam et al. *Experimental study of different silicon sensor options for the upgrade of the CMS Outer Tracker*. In: Journal of Instrumentation 15.04 (Apr. 2020), P04017. DOI: 10.1088/1748-0221/15/04/P04017 (cited on p. 72).

[Alb22] A. Albrecht. *Pileup mitigation with timing – Forward timing meeting – 18.02.2022*. [Accessed 12-02-2025]. 2022 (cited on p. 40).

[ALi] ALiBaVa. *ALIBAVA SYSTEM CLASSIC*. https://alibavasystems.com/producto/alibava-system-classic/. [Accessed 17-03-2025] (cited on pp. 44, 60).

[ALI08] ALICE Collaboration. *The ALICE experiment at the CERN LHC*. In: JINST 3 (2008), S08002. DOI: 10.1088/1748-0221/3/08/S08002 (cited on p. 31).

[Alt+03] P. P. Altermatt et al. *Reassessment of the intrinsic carrier density in crystalline silicon in view of band-gap narrowing*. In: Journal of Applied Physics 93.3 (2003), pp. 1598–1604 (cited on p. 8).

[Arn+11] P. Arnolda et al. *NIEL Scaling: Comparison With Measured Defect Introduction Rate in Silicon*. In: IEEE Transactions on Nuclear Science 58.3 (2011), pp. 756–763. DOI: 10.1109/TNS.2011.2131154 (cited on p. 21).

[ATL08] ATLAS Collaboration. *The ATLAS Experiment at the CERN Large Hadron Collider*. In: Journal of Instrumentation 3.08 (Aug. 2008), S08003. DOI: 10.1088/1748-0221/3/08/S08003 (cited on p. 31).

[Bac+01] N. Bacchetta et al. *Improvement in breakdown characteristics with multiguard structures in microstrip silicon detectors for CMS*. In: Nuclear Instruments and Methods in Physics Research Section A: Accelerators, Spectrometers, Detectors and Associated Equipment 461.1 (2001). 8th Pisa Meeting on Advanced Detectors, pp. 204–206. ISSN: 0168-9002. DOI: https://doi.org/10.1016/S0168-9002(00)01207-9 (cited on p. 139).

[BB05] F. Berghmans and B. Brichard. *New Challenges for Radiation Tolerance Assessment: - from Deep Space Environments to Fusion Reactor Environments (Short Course Notebook - RADECS 2005)*. English. Ed. by A. Fernandez Fernandez. 1st ed. Vol. 1. Score = 10. RADECS Association, Sept. 2005 (cited on p. 12).

[Bet30] H. Bethe. *Zur Theorie des Durchgangs schneller Korpuskularstrahlen durch Materie*. In: Annalen der Physik 397.3 (1930), pp. 325–400. DOI: https://doi.org/10.1002/andp.19303970303. eprint: https://onlinelibrary.wiley.com/doi/pdf/10.1002/andp.19303970303 (cited on p. 10).

[Bic88] H. Bichsel. *Straggling in thin silicon detectors*. In: Rev. Mod. Phys. 60 (3 July 1988), pp. 663–699. DOI: 10.1103/RevModPhys.60.663 (cited on p. 11).

[Blo29] F. Bloch. *Über die Quantenmechanik der Elektronen in Kristallgittern*. In: Zeitschrift für Physik 52 (1929), pp. 555–600. URL: https://doi.org/10.1007/BF01339455 (cited on p. 3).

[Bro] Broadcom. *RabbitMQ — one broker to queue them all*. https://www.rabbitmq.com/. [Accessed 12-06-2025] (cited on p. 66).

[CAE] CAEN. *DT5742 - Product page*. https://www.caen.it/products/dt5742/. [Accessed 19-03-2025] (cited on pp. 49, 60).

[Car24] N. Cartiglia. *Signal formation in LGAD detectors*. https://indico.cern.ch/event/1439336/contributions/6242124/attachments/2977561/5242005/DRD3_Landau_NC.pdf. [Accessed 12-06-2025]. 2024 (cited on p. 52).

[CCS02] D. Campbell, A. Chilingarov, and T. Sloan. *Frequency and temperature dependence of the depletion voltage from CV measurements for irradiated Si detectors*. In: Nuclear Instruments and Methods in Physics Research Section A: Accelerators, Spectrometers, Detectors and Associated Equipment 492.3 (2002), pp. 402–410. ISSN: 0168-9002. DOI: https://doi.org/10.1016/S0168-9002(02)01353-0 (cited on pp. 123, 127, 130).

[Cen+15] F. Cenna et al. *Weightfield2: A fast simulator for silicon and diamond solid state detector*. In: Nuclear Instruments and Methods in Physics Research Section A: Accelerators, Spectrometers, Detectors and Associated Equipment 796 (2015). Proceedings of the 10th International Conference on Radiation Effects on Semiconductor Materials Detectors and Devices, pp. 149–153. ISSN: 0168-9002. DOI: https://doi.org/10.1016/j.nima.2015.04.015 (cited on pp. 14, 17).

[CER] CERN Collaboration. *The HL-LHC project — High Luminosity LHC Project*. https://hilumilhc.web.cern.ch/content/hl-lhc-project. [Accessed 01-02-2025] (cited on pp. 34, 35).

[CER25] CERN Collaboration. *CERN70, Inspiring the Future*. https://cern70.cern/. [Accessed 29-05-2025]. 2025 (cited on p. 29).

[Cha+12] S. Chatrchyan et al. *Observation of a New Boson at a Mass of 125 GeV with the CMS Experiment at the LHC*. In: Phys. Lett. B 716 (2012), pp. 30–61. DOI: 10.1016/j.physletb.2012.08.021. arXiv: 1207.7235 [hep-ex] (cited on pp. 1, 31).

[Chi11] A. Chilingarov. *Generation current temperature scaling*. Tech. rep. Version 1. Lancaster University, 2011. URL: https://rd50.web.cern.ch/doc/Internal/rd50_2011_001-I-T_scaling.pdf (cited on p. 9).

[Chy58] A. G. Chynoweth. *Ionization Rates for Electrons and Holes in Silicon*. In: Phys. Rev. 109 (5 Mar. 1958), pp. 1537–1540. DOI: 10.1103/PhysRev.109.1537 (cited on p. 14).

[CL96] W. S. Cleveland and C. Loader. *Smoothing by Local Regression: Principles and Methods*. In: *Statistical Theory and Computational Aspects of Smoothing*. Ed. by W. Härdle and M. G. Schimek. Heidelberg: Physica-Verlag HD, 1996, pp. 10–49. ISBN: 978-3-642-48425-4 (cited on p. 139).

[CMS08] CMS Collaboration. *The CMS experiment at the CERN LHC. The Compact Muon Solenoid experiment*. In: JINST 3 (2008). Also published by CERN Geneva in 2010, S08004. DOI: 10.1088/1748-0221/3/08/S08004 (cited on pp. 33, 34).

[CMS17] CMS Collaboration. *The Phase-2 Upgrade of the CMS Tracker*. Tech. rep. Geneva: CERN, 2017. DOI: 10.17181/CERN.QZ28.FLHW (cited on pp. 32, 35–38).

[CMS19] C. CMS. *A MIP Timing Detector for the CMS Phase-2 Upgrade*. Tech. rep. Geneva: CERN, 2019. URL: https://cds.cern.ch/record/2667167 (cited on p. 40).

[CMS23a] CMS Collaboration. *CMS Outer Tracker FLUKA Simulations*. https://cms-tklayout.web.cern.ch/cms-tklayout/layouts-work/recent-layouts/OT801_IT701/irradiation_Outer.html. [Accessed 12-06-2025]. 2023 (cited on pp. 38, 82, 83).

[CMS23b] CMS Collaboration. *OT801_IT701 - Info — cms-tklayout*. https://cms-tklayout.web.cern.ch/cms-tklayout/layouts/recent-layouts/OT801_IT701/. [Accessed 12-02-2025]. 2023 (cited on p. 36).

[Com23] A. H. Compton. *A Quantum Theory of the Scattering of X-rays by Light Elements*. In: Phys. Rev. 21 (5 May 1923), pp. 483–502. DOI: 10.1103/PhysRev.21.483 (cited on p. 12).

[Con+15] D. Contardo et al. *Technical Proposal for the Phase-II Upgrade of the CMS Detector*. Tech. rep. Upgrade Project Leader Deputies: Lucia Silvestris (INFN-Bari), Jeremy Mans (University of Minnesota) Additional contacts: Lucia.Silvestris@cern.ch, Jeremy.Mans@cern.ch. Geneva, 2015. DOI: 10.17181/CERN.VU8I.D59J (cited on p. 37).

[Cor] I. S. Cordasco. *flake8: Your Tool For Style Guide Enforcement*. https://flake8.pycqa.org/en/latest/. [Accessed 12-06-2025] (cited on p. 60).

[CP24] M. Centis Vignali and G. Paternoster. *Low gain avalanche diodes for photon science applications*. In: Frontiers in Physics Volume 12 - 2024 (2024). ISSN: 2296-424X. DOI: 10.3389/fphy.2024.1359179 (cited on p. 141).

[Dem00] W. Demtröder. "Halbleiter". In: *Experimentalphysik 3: Atome, Moleküle und Festkörper*. Berlin, Heidelberg: Springer Berlin Heidelberg, 2000, pp. 455–474. ISBN: 978-3-662-05904-3. DOI: 10.1007/978-3-662-05904-3_14 (cited on pp. 4, 5, 7, 9).

[Doc25] Docker Inc. *Docker homepage*. https://www.docker.com/. [Accessed 31-05-2025]. 2025 (cited on pp. 60, 62).

[Ein05] A. Einstein. *Über einen die Erzeugung und Verwandlung des Lichtes betreffenden heuristischen Gesichtspunkt*. In: Annalen der Physik 322.6 (1905), pp. 132–148. DOI: https://doi.org/10.1002/andp.19053220607. eprint: https://onlinelibrary.wiley.com/doi/pdf/10.1002/andp.19053220607 (cited on p. 12).

[Eli19] U. Elicabuk. *Charakterisierung von n-in-p Streifensensoren für das Phase-2-Upgrade des CMS-Detektors*. 2019 (cited on p. 101).

[ER+25] U. Elicabuk, B. Regnery, et al. *Irradiation Studies of the Resistive AC-coupled Silicon Detector (RSD/AC-LGAD)*. In: (Apr. 2025). arXiv: 2504.13098 [physics.ins-det] (cited on pp. 150, 151).

[Fan+19] J. Fang et al. *Understanding the Average Electron–Hole Pair-Creation Energy in Silicon and Germanium Based on Full-Band Monte Carlo Simulations*. In: IEEE Transactions on Nuclear Science 66.1 (2019), pp. 444–451. DOI: 10.1109/TNS.2018.2879593 (cited on p. 5).

[Fer+05] A. Ferrari et al. *FLUKA: A multi-particle transport code (Program version 2005)*. In: (Oct. 2005). DOI: 10.2172/877507 (cited on p. 38).

[Fer+19] M. Ferrero et al. *Radiation resistant LGAD design*. In: Nuclear Instruments and Methods in Physics Research Section A: Accelerators, Spectrometers, Detectors and Associated Equipment 919 (2019), pp. 16–26. ISSN: 0168-9002. DOI: https://doi.org/10.1016/j.nima.2018.11.121 (cited on p. 23).

[Fer+21] M. Ferrero et al. *An Introduction to Ultra-Fast Silicon Detectors: Design, Tests, and Performances*. June 2021. ISBN: 9781003131946. DOI: 10.1201/9781003131946 (cited on pp. 15–18, 139, 150, 157).

[Fer40] E. Fermi. *The Ionization Loss of Energy in Gases and in Condensed Materials*. In: Phys. Rev. 57 (6 Mar. 1940), pp. 485–493. DOI: 10.1103/PhysRev.57.485 (cited on p. 10).

[Fis20] R. Fischer. *Bestrahlungstests an Siliziumstreifensensoren für das Phase-2-Upgrade des CMS-Spurdetektors*. 2020 (cited on pp. 104–106).

[FLU] FLUKA Collaboration. *FLUKA Simulations for Radiation Levels in Tracker and ECAL Regions for Phase II*. https://twiki.cern.ch/twiki/bin/view/CMSPublic/FlukaPhaseIITrackerECALv630x. [Accessed 12-02-2025] (cited on p. 39).

[GK23] D. Groom and S. Klein. *Passage of Particles Through Matter*. In: PDG (2023). URL: https://pdg.lbl.gov/2024/reviews/rpp2024-rev-passage-particles-matter.pdf (cited on pp. 10, 11).

[Gre08] M. A. Green. *Self-consistent optical parameters of intrinsic silicon at 300K including temperature coefficients*. In: Solar Energy Materials and Solar Cells 92.11 (2008), pp. 1305–1310. ISSN: 0927-0248. DOI: https://doi.org/10.1016/j.solmat.2008.06.009 (cited on p. 13).

[Gut+12] M. Guthoff et al. *Geant4 simulation of a filtered X-ray source for radiation damage studies*. In: Nuclear Instruments and Methods in Physics Research Section A: Accelerators, Spectrometers, Detectors and Associated Equipment 675 (2012), pp. 118–122. ISSN: 0168-9002. DOI: https://doi.org/10.1016/j.nima.2012.01.029 (cited on pp. 55, 56).

[Ha98] J. L. Hintze and R. D. N. and. *Violin Plots: A Box Plot-Density Trace Synergism*. In: The American Statistician 52.2 (1998), pp. 181–184. DOI: 10.1080/00031305.1998.10480559. eprint: https://www.tandfonline.com/doi/pdf/10.1080/00031305.1998.10480559 (cited on p. 93).

[Ham23] Hamamatsu Photonics K.K. *HPK Website*. https://www.hamamatsu.com/eu/en.html. [Accessed 12-06-2025]. 2023 (cited on p. 70).

[Har24] F. Hartmann. *Basic Principles of a Silicon Detector*. Springer Nature Switzerland, 2024. ISBN: 978-3-031-59720-6. DOI: 10.1007/978-3-031-59720-6_1 (cited on p. 17).

[Hen06a] Hennig, Markus A. *Dotierung im zweidimensionales Siliziumkristallgitter mit Aluminium*. https://de.m.wikipedia.org/wiki/Datei:Schema_-_p-dotiertes_Silicium.svg. [Accessed 12-06-2025]. 2006 (cited on p. 6).

[Hen06b] Hennig, Markus A. *Dotierung im zweidimensionales Siliziumkristallgitter mit Phosphor*. https://de.m.wikipedia.org/wiki/Datei:Schema_-_n-dotiertes_Silicium.svg. [Accessed 12-06-2025]. 2006 (cited on p. 6).

[Hor19] J. L. Horowitz. *Bootstrap Methods in Econometrics*. In: Annual Review of Economics 11.Volume 11, 2019 (2019), pp. 193–224. ISSN: 1941-1391. DOI: https://doi.org/10.1146/annurev-economics-080218-025651 (cited on p. 113).

[HTA24] A. Hayrapetyan, A. Tumasyan, and W. Adam. *Development of the CMS detector for the CERN LHC Run 3. Development of the CMS detector for the CERN LHC Run 3*. In: JINST 19.05 (2024), P05064. DOI: 10.1088/1748-0221/19/05/P05064. arXiv: 2309.05466 (cited on pp. 31, 32).

[Huh02] M. Huhtinen. *Simulation of non-ionising energy loss and defect formation in silicon*. In: Nuclear Instruments and Methods in Physics Research Section A: Accelerators, Spectrometers, Detectors and Associated Equipment 491.1 (2002), pp. 194–215. ISSN: 0168-9002. DOI: https://doi.org/10.1016/S0168-9002(02)01227-5 (cited on p. 20).

[ise] iseg. *SHR — Switchable High Precision AC/DC Desktop High Voltage Power Supply*. https://iseg-hv.com/files/media/docitems_file_20240423111613.pdf. [Accessed 12-06-2025] (cited on p. 60).

[Jow18] J. Jowett. *Colliding Heavy Ions in the LHC*. In: (2018), TUXGBD2. DOI: 10.18429/JACoW-IPAC2018-TUXGBD2 (cited on p. 29).

[La 19] A. La Rosa. *The CMS Outer Tracker for the High Luminosity LHC upgrade*. In: (Dec. 2019). DOI: 10.48550/arXiv.1912.02061 (cited on p. 38).

[Lac91] T. Lackner. *Avalanche multiplication in semiconductors: A modification of Chynoweth's law*. In: Solid-State Electronics 34.1 (1991), pp. 33–42. ISSN: 0038-1101. DOI: https://doi.org/10.1016/0038-1101(91)90197-7 (cited on p. 15).

[Lan44] L. D. Landau. *On the energy loss of fast particles by ionization*. In: 1944. URL: https://api.semanticscholar.org/CorpusID:118136651 (cited on p. 11).

[LHC08] LHCb Collaboration. *The LHCb Detector at the LHC*. In: JINST 3 (2008). Also published by CERN Geneva in 2010, S08005. DOI: 10.1088/1748-0221/3/08/S08005 (cited on p. 31).

[Lop22] E. Lopienska. *The CERN accelerator complex, layout in 2022. Complexe des accélérateurs du CERN en janvier 2022*. In: (2022). General Photo. URL: https://cds.cern.ch/record/2800984 (cited on p. 30).

[LS06] S. Löchner and M. Schmelling. *The Beetle Reference Manual - chip version 1.3. 1.4 and 1.5*. Tech. rep. LHCb, 2006. URL: https://www.kip.uni-heidelberg.de/lhcb/Publications/BeetleRefMan_v1_3.pdf (cited on pp. 44, 46).

[Man+20] M. Mandurrino et al. *Analysis and numerical design of Resistive AC-Coupled Silicon Detectors (RSD) for 4D particle tracking*. In: Nuclear Instruments and Methods in Physics Research Section A: Accelerators, Spectrometers, Detectors and Associated Equipment 959 (2020), p. 163479. ISSN: 0168-9002. DOI: https://doi.org/10.1016/j.nima.2020.163479 (cited on p. 135).

[Man+22] M. Mandurrino et al. *The second production of RSD (AC-LGAD) at FBK*. In: JINST 17.08 (2022), p. C08001. DOI: 10.1088/1748-0221/17/08/C08001. arXiv: 2111.14235 [physics.ins-det] (cited on p. 135).

[Man17] M. Mandurrino. *TCAD Simulation of silicon detectors – A validation tool for the development of LGAD*. https://indi.to/TfhND. [Accessed 12-06-2025]. 2017 (cited on p. 135).

[MDN21] J.-O. Müller-Gosewisch, A. Dierlamm, and A. Nürnberg. *Influence of surface damage and bulk defects on the interstrip isolation of p-type silicon strip sensors*. In: Journal of Instrumentation 16 (July 2021), P07004. DOI: 10.1088/1748-0221/16/07/P07004 (cited on pp. 84, 118).

[Men+24] L. Menzio et al. *First test beam measurement of the 4D resolution of an RSD pixel matrix connected to a FAST2 ASIC*. In: Nucl. Instrum. Meth. A 1065 (2024), p. 169526. DOI: 10.1016/j.nima.2024.169526. arXiv: 2402.01517 [physics.ins-det] (cited on p. 135).

[Men23] L. Menzio. *Development of Resistive Silicon Detectors for 4D tracking*. PhD thesis. Universita degli Studi di Torino, 2023. URL: https://www.researchgate.net/publication/374633102_Development_of_Resistive_Silicon_Detectors_for_4D_tracking (cited on pp. 17, 23, 40, 133–136).

[Men25] L. Menzio. *DC-Coupled Resistive Silicon Detectors – A Status Update*. https://indico.cern.ch/event/1533252/contributions/6487520/attachments/3058468/5408090/DC-RSD_status_DRD3_LM.pdf. [Accessed 12-06-2025]. 2025 (cited on p. 135).

[MMO90] W. Maes, K. M. D. Meyer, and R. V. Overstraeten. *Impact ionization in silicon: A review and update*. In: Solid-state Electronics 33 (1990), pp. 705–718. URL: https://api.semanticscholar.org/CorpusID:15686146 (cited on p. 15).

[Mol18] M. Moll. *Displacement Damage in Silicon Detectors for High Energy Physics*. In: IEEE Transactions on Nuclear Science 65.8 (2018), pp. 1561–1582. DOI: 10.1109/TNS.2018.2819506 (cited on p. 123).

[Mol99] M. Moll. *Radiation damage in silicon particle detectors: Microscopic defects and macroscopic properties*. Ph.D. Thesis (Advisor: G. Lindstrom); Dissertation, Universität Hamburg, 1999. Dissertation. Universität Hamburg, 1999, p. 251. DOI: 10.3204/PUBDB-2016-02525 (cited on pp. 9, 19, 20, 22, 24, 26, 27, 75, 86, 103).

[Mov] M. Movsisyan. *Flower Documentation*. https://flower.readthedocs.io/en/latest/. [Accessed 12-06-2025] (cited on p. 66).

[Mül21] J.-O. Müller-Gosewisch. *Investigation of Radiation Damage in Silicon Sensors for the Phase-2 Upgrade of the CMS Outer Tracker*. PhD thesis. Karlsruhe Institute of Technology (KIT), 2021 (cited on pp. 8, 26, 55, 72, 84, 86, 88, 90, 107).

[Pal] Pallets. *Welcome to flask*. https://flask.palletsprojects.com/en/stable/. [Accessed 12-06-2025] (cited on p. 59).

[Per11] H. Perrey. *Jets at Low Q2 at HERA and Radiation Damage Studies for Silicon Sensors for the XFEL*. PhD thesis. Universität Hamburg, 2011 (cited on p. 78).

[pyl] pylint-dev. *pylint3.3.7 at pypi*. https://pypi.org/project/pylint/. [Accessed 12-06-2025] (cited on p. 60).

[Pyt] Python Software Foundation. *Black: The Uncompromising Code Formatter — on github*. https://github.com/psf/black. [Accessed 12-06-2025] (cited on p. 60).

[Ram39] S. Ramo. *Currents Induced by Electron Motion*. In: Proceedings of the IRE 27.9 (1939), pp. 584–585. DOI: 10.1109/JRPROC.1939.228757 (cited on p. 13).

[Ruz+99] A. Ruzin et al. *Comparison of radiation damage in silicon induced by proton and neutron irradiation*. In: IEEE Trans. Nucl. Sci. 46.5 (1999), pp. 1310–13. DOI: 10.1109/23.795808 (cited on pp. 24, 25).

[RWC25] G. van Rossum, B. Warsaw, and A. Coghlan. *PEP 8 – Style Guide for Python Code — peps.python.org — peps.python.org*. https://peps.python.org/pep-0008/. [Accessed 31-05-2025]. 2025 (cited on p. 60).

[Sci25] SciPy Developers. *SciPy — scipy.org*. https://scipy.org/. [Accessed 11-06-2025]. 2025 (cited on p. 143).

[Sen+22] M. Senger et al. *Characterization of timing and spacial resolution of novel TI-LGAD structures before and after irradiation*. In: Nucl. Instrum. Meth. A 1039 (2022), p. 167030. DOI: 10.1016/j.nima.2022.167030. arXiv: 2204.08739 [physics.ins-det] (cited on p. 134).

[Sho38] W. Shockley. *Currents to conductors induced by a moving point charge*. In: J. Appl. Phys. 9.10 (1938), pp. 635–636. DOI: 10.1063/1.1710367 (cited on p. 13).

[Sir+17] A. Sirunyan et al. *Particle-flow reconstruction and global event description with the CMS detector*. In: Journal of Instrumentation 12.10 (Oct. 2017), P10003. DOI: 10.1088/1748-0221/12/10/P10003 (cited on p. 40).

[Sol] A. Solem. *Introduction to Celery*. https://docs.celeryq.dev/en/stable/getting-started/introduction.html. [Accessed 12-06-2025] (cited on p. 66).

[Ste] R. Steerenberg. *Accelerator Report: The excellent 2024 LHC run ended abruptly*. https://home.cern/news/news/accelerators/accelerator-report-excellent-2024-lhc-run-ended-abruptly. [Accessed 01-02-2025] (cited on p. 31).

[Str71] J. Strutt. *XV. On the light from the sky, its polarization and colour*. In: The London, Edinburgh, and Dublin Philosophical Magazine and Journal of Science 41.271 (1871), pp. 107–120. DOI: 10.1080/14786447108640452 (cited on p. 12).

[SŽT12] L. Snoj, G. Žerovnik, and A. Trkov. *Computational analysis of irradiation facilities at the JSI TRIGA reactor*. In: Applied Radiation and Isotopes 70.3 (2012), pp. 483–488. ISSN: 0969-8043. DOI: https://doi.org/10.1016/j.apradiso.2011.11.042 (cited on p. 55).

[Ter] Terahertz Technologies Inc. *TIA-950 O/E Converter*. https://scitec.uk.com/fibreoptics/pdf/tia-950_datasheetweb.pdf. [Accessed 21-03-2025] (cited on p. 52).

[The07] TheNoise. *Pn-junction-equilibrium (no title provided)*. https://commons.wikimedia.org/wiki/File:Pn-junction-equilibrium.svg. [Accessed 12-06-2025]. 2007 (cited on p. 8).

[The17] The CMS Collaboration. *Technical proposal for a MIP timing detector in the CMS experiment Phase 2 upgrade*. Tech. rep. Geneva: CERN, 2017. DOI: 10.17181/CERN.2RSJ.UE8W (cited on p. 40).

[Tuk77] J. Tukey. *Exploratory Data Analysis*. Addison-Wesley series in behavioral science Bd. 2. Addison-Wesley Publishing Company, 1977. ISBN: 9780201076165. URL: https://books.google.de/books?id=UT9dAAAAIAAJ (cited on p. 93).

[TuS] TuSimple. *Naive UI — A Vue 3 Component Library*. https://www.naiveui.com/en-US/os-theme. [Accessed 12-06-2025] (cited on p. 62).

[Van80] V. Van Lint. *Mechanisms of Radiation Effects in Electronic Materials*. A Wiley-Interscience publication Bd. 1. Wiley, 1980. ISBN: 9780471041061. URL: https://books.google.de/books?id=NwxTAAAAMAAJ (cited on p. 19).

[VL00] A. Vasilescu and G. Lindstroem. *Displacement damage in silicon, on-line compilation*. In: (2000) (cited on pp. 20, 21).

[Vue] Vuetify. *Vuetify — Vue Component Framework*. https://vuetifyjs.com/en/. [Accessed 12-06-2025] (cited on p. 63).

[Wit23] F. Wittig. *Qualification of Silicon Sensors for the Phase-2 Upgrade of the CMS Outer Tracker*. PhD thesis. Karlsruhe Institute of Technology (KIT), 2023 (cited on pp. 38, 95, 101).

[Wun92] R. Wunstorf. *Systematische Untersuchungen zur Strahlenresistenz von Siliziumdetektoren fpr die Verwendung in Hochenergiephysik-Experimenten*. PhD thesis. University of Hamburg, 1992 (cited on p. 27).

[You] E. You. *Vue.js — The Progressive JavaScript Framework*. `https://vuejs.org/`. [Accessed 12-06-2025] (cited on p. 63).

[Žon+99] D. Žontar et al. *Time development and flux dependence of neutron-irradiation induced defects in silicon pad detectors*. In: Nuclear Instruments and Methods in Physics Research Section A: Accelerators, Spectrometers, Detectors and Associated Equipment 426.1 (1999), pp. 51–55. ISSN: 0168-9002. DOI: `https://doi.org/10.1016/S0168-9002(98)01468-5` (cited on p. 55).

[Zyk] Zyklotron AG. *Zyklotron AG Homepage*. `https://www.zyklotron-ag.de/`. [Accessed 21-03-2025] (cited on p. 55).

Acknowledgments — Danksagung

If you've read this far: good job! Don't be like me during the writing of my thesis; take a break. You've earned it! Let me take this opportunity to thank all the people who have helped me during my PhD journey.

Wenn du es bis hierher geschafft hast: gut gemacht! Sei nicht wie ich während des Schreibens meiner Dissertation; gönn dir eine Pause. Du hast sie dir verdient! Ich möchte diese Gelegenheit nutzen, um allen Menschen zu danken, die mich während meiner Promotion unterstützt haben.

Zuerst danke ich meiner Mutter, Birsen, die immer hinter mir stand, mich unterstützt und selbst in den schwierigsten Zeiten an mich geglaubt hat. Von ihr lernte ich Stärke, Ehrgeiz und Geduld. Ohne sie wäre ich nicht der Mensch, der ich heute bin.
Thank you, Franzi, my forever-partner, for nourishing me, showing me the world, true love, and myself. You taught me to take a step back and enjoy life. You are my safe haven, you are my best friend and btw: your painting rocks! ♡

Thank you, Brendan, for being a great friend and mentor. You taught me how to be a better researcher and navigate the insanities of academia. Our late-night measurements led to all of this, give yourself a pat on the back!
Paul, Joscha, das hier geht an euch! Wer Freunde wie euch hat, hat keine Feinde mehr. Das nächste Mal Catan kriegt ihr einmal extra Getreide.

Alexander Dierlamm, du warst mir nicht nur der beste Team-Chef, sondern hattest immer ein offenes Ohr für mich in meinen dunkelsten Zeiten. Deine Arbeit und dein Einsatz werden oftmals nicht genug gewürdigt und das würde ich daher hiermit gerne tun.
Jan-Ole Müller-Gosewisch würde ich gerne für das Fundament danken, das seine Arbeit für die meine gelegt hat.
A special thanks to the team at INFN, especially Luca, Nicolò, Marco and Roberta. This is what I call a great collaboration. Continue being absolute rockstars of science!
Thanks to my working group. I am grateful for all the support and the great time we had together. In particular thanks to Ulrich for true leadership in times of crisis, Tobias for putting up with my endless questions about mechanical engineering, and Lea for helping me with printing this thesis.
Ein spezieller Dank geht nochmal raus an die Jungs aus der E-Werkstatt, besonders Waldemar, der mir beim Bonden der RSD-Sensoren stets mit Rat und Tat zur Seite stand und last but not least an Bernd für seine stets gewissenhafte Arbeit rund um Elektronik und Bestrahlungen. Ihr habt in dieser Leistungsgesellschaft die Menschlichkeit nicht vergessen.

Never forget: the best is yet to come! Strive for perfection, don't forget to enjoy the ride, and take care of yourself and your loved ones. Umut out!

Declaration

I declare that the work in this dissertation was carried out in accordance with the requirements of the University's Regulations and that it has not been submitted for any other academic award. Except where indicated by specific reference in the text, the work is the candidate's own work. Work done in collaboration with, or with the assistance of, others is indicated as such.

Karlsruhe, June 2025

Umut Elicabuk